MONASH University

High-Throughput Perovskite Solar Cell Materials Discovery
Maciej Adam Surmiak
(M.Sc.Eng. B.Eng.)

A thesis submitted for the degree of *Doctor of Philosophy* at
Monash University in 2021
Faculty of Engineering
Department of Chemical and Biological Engineering

July 2021

„Das Leben ist schnell, die Kunst ist langsam, die Gelegenheit spröde, die Ausführung unzuverlässig und das Urteil parteiisch."

- *Johann Heinrich Füssli*

Copyright notice

Abstract/Zusammenfassung/Preambuła

New generation photovoltaics (PV) materials, in particular solid-state metal-halide perovskites, have the potential to contribute towards the future of renewable energy (RE) production. The discovery of perovskite solar cells (PSCs) offers a price competitive, lightweight alternative, and/or enhancement to the state-of-the-art silicon solar cells (SSCs). The last decade of intensive PSC research around the world allowed by 2021 for the realization of PSCs with power conversion efficiency (PCE) of 25.5%, only ~0.6% less than the top SSC. The PSC potential and competitiveness are evident, even though there are unmitigated long-term limitations that hinder their transition to the commercial market. In order to realize their full potential, the PSCs need to meet PV market product stability and lifetime expectations. Unlike the SSC, the solution-processed perovskites are a group of hundreds of thousands of materials in which complex and various chemical compositions, material additives, and fabrication strategies allow for the alteration, improvement and realization of PSC. Additionally, adjacent charge-transporting layers (CTLs) and various electrodes further expand the number of potentially efficient PSCs. Therefore, it is a non-trivial task to screen all these materials and configurations to find which ones are promising, reproducible, efficient and stable candidates. The systematic investigation of compositions, CTLs, electrodes, and fabrication protocols need to be predicted, prepared and characterized to ensure that all the extracted information is tracked, trustworthy and accurate.

This doctoral thesis focuses on combinatorial high-throughput methodologies that accelerate the discovery of industry-ready candidates for the solar cells of tomorrow. A novel perovskite film fabrication method was developed in this research, making it possible to fabricate perovskite compositional space without human interference in a closely controlled environment. Subsequently, an automated additive concentration screening for better performance and stability of perovskite films was investigated. Furthermore, the ligand-modified, scalable low-temperature deposition of nickel oxide nanoparticles via the employment of the Tesla-valve microfluidic mixer was developed. Moreover, a combinatorial high-throughput PSC characterization setup for standardized and accelerated precise PSC

measurements was proposed, serving as the accelerator for rapid screening and discovery of perovskite materials. Lastly, a modular perovskite solar panel prototype was developed to enable real-world application and stability data acquisition of PSCs that can contribute to current and future research efforts and commercialization of PSCs.

Abstract/**Zusammenfassung**/Preambuła

Die neue Generation von Photovoltaikmaterialien, insbesondere Metall-Halogenid-Perowskite, haben das Potential zur zukünftigen Energieproduktion aus erneuerbaren Energien beizutragen. Die Entdeckung von Perowskitsolarzellen (PSZ) ermöglicht eine preiskompetitive, leichte Alternative und Verbesserung derzeitiger Siliziumsolarzellen. Das letzte Jahrzehnt weltweiter intensiver PSZ-Forschung hat in 2021 zu einer Effizienz von 25.5% geführt, nur ~0.6% tiefer als die höchsten Effizienzen von Siliziumsolarzellen. Das Potential und die Wettbewerbsfähigkeit von PSZ sind offensichtlich, ihre beschränkte Langzeitstabilität haben jedoch bisher ihre Kommerzialisierung verhindert. Um ihr volles Potential auszuschöpfen müssen PSZ marktgerechte Stabilitäten und Laufzeiten erreichen. Im Gegensatz zu Siliziumsolarzellen sind PSZ eine Gruppe von Hunderttausenden von Materialien, bei welchen komplexe und chemische Kompositionen, Zusatzstoffen und Fabrikationsstrategien eine Änderung, Verbesserung und Realisierung von PSZ ermöglicht. Angrenzende Ladungsträgermaterialien und verschiedene Elektroden erweitern die Zahl potenziell effizienter PSZ. Deshalb ist es eine nicht-triviale Aufgabe, all diese Materialien zu erforschen und die vielversprechenden, reproduzierbaren, effizienten und stabilen PSC-Kandidaten zu finden. Die systematische Erforschung von Kompositionen, Ladungsträgern, Elektroden und Fabrikationsprotokollen müssen vorhergesagt, zubereitet und charakterisiert werden, wobei sichergestellt werden muss, dass die gesammelten Daten aufgezeichnet, zuverlässig und präzise sind. Diese Doktorarbeit ist auf kombinatorische highthroughput Methoden fokussiert, die die Suche nach industrierelevanten Kandidaten für die Solarzellen von Morgen beschleunigen. Es wurde eine neue Methode zur Fabrikation von Perowskitschichten entwickelt, welche es ermöglicht, einen kombinatorischen Raum von Perowskiten ohne menschlichen Einfluss und in kontrollierter Umgebung zu generieren. Danach wurde eine auf automation basierte Untersuchung von Konzentrationen von Zusatzstoffen durchgeführt, um die Leistung und Stabilität von Perowskitschichten zu untersuchen. Außerdem wurde eine ligandmodifizierte, skalierbare Tieftemperaturauftragung von Nickeloxid Nanopartikeln durch Verwendung eines Teslaventils entwickelt. Zusätzlich wurde ein kombinatorischer highthroughput PSZ Charakterisierungsaufbau für standardisierte, beschleunigte und präzise PSZ Messungen

entwickelt, die der beschleunigten Untersuchung und Erforschung von Perowskitmaterialien dient. Schließlich wurde ein Perowskitsolarmodulprototyp entwickelt um reale Stabilitätsdaten von PSCs zu sammeln.

Abstract/Zusammenfassung/**Preambuła**

Rozwój nowej generacji materiałów fotowoltaicznych, w szczególności, perowskitów organo-metaliczno-halogenkowych, przyniosło realna szanse na dalszy rozwój odnawialnych źródeł energii (OZE). Wynalezienie perowskitowych ogniw słonecznych (POS) pozwoliło na opracowanie ekonomicznej i ultralekkiej alternatywy dla najnowocześniejszych ogniw krzemowych (Si). W czasie ostatniej dekady, dzięki intensywnym badaniom na całym świecie, POS niemal dorównały sprawności najlepszych ogniw krzemowych, PCE=25.5% (zaledwie o ~0.6% mniej niż Si). Korzyści i potencjał POS jest oczywista, jednak technologia ta jest ograniczona ze względu na wrażliwość i niestabilność materiału. W przeciwieństwie do krzemu, POS wytwarzane są z wieloskładnikowych roztworów, dzięki czemu możliwa do otrzymania jest niezliczona ilość kompozycji tych materiałów. Dodatkowo, liczne metody wytwarzania warstw perowskitowych mają wpływ na jakość i wydajność POS. Szeroki wybór materiałów, w tym podłóż, materiałów przewodzących nośniki (dziury, elektrony), domieszkowań, oraz elektrod pozwala na zrealizowanie wydajnych kompozycji POS. Potencjalnie istnieją wciąż nieodkryte, bardzo stabilne i wydaje POS. Dlatego kluczowe dla rozwoju POS są systematyczne badania nad możliwymi strukturami i metodami produkcyjnymi. Generowane w tym celu kompozycje materiałowe, dane pomiarowe, procesy wytwarzania, oraz ich analiza, muszą być zaplanowane, dokładne i powtarzalne. Niniejsza rozprawa doktorska przedstawia kombinatoryczne i wysokowydajne metody pozwalające na odkrywanie i doskonalenie kolejnych prototypów POS gotowych do produkcji na masową skalę. Opracowana w prezentowanej tezie nowa metoda wytwarzania warstw perowskitowych umożliwia produkcję szerokiej gamy możliwych kompozycji perowskitowych. Procesy te są zautomatyzowane i odbywają się w pełni kontrolowanym środowisku. Techniki automatyczne zostały zastosowane do badań przesiewowych nad stężeniami roztworów perowskitowych w celu poprawienia wydajności i stabilności otrzymanych warstw. Również, nowa metoda wytwarzania nanocząsteczek tlenku niklu oraz mikrofluidiczny zawór Tesli zostały wykorzystane w skalowanej, niskotemperaturowej fabrykacji POS. W dalszej części przedstawiono nowatorską technikę pomiarową POS, która umożliwia dokładne i ustandaryzowane pomiary dla szybkich testów przesiewowych materiałów perowskitowych. Ostatni rozdział eksperymentalny poświęcony jest prototypowi

modułowego panelu perowskitowego, który pokazuje zastosowanie tej technologii w rzeczywistych warunkach. Otrzymane pomiary nad stabilnością zbudowanego prototypu są unikatowym zbiorem danych służącym dalszemu rozwojowi oraz komercjalizacji POS.

Acknowledgements

I would like to thank Professor Udo Bach, a strong man that gives the ground and pulls you up, giving the chance to excel. I will never forget our conversations. Without You Professor, I would be a different man, and thanks to You I will be a better man.

I would like to highlight people who helped me throughout the studies and without whom my work would have never been finalized.I would like to thank for the marathon, last moment help Ms Jane Moodie. I would like to thank all my co-workers and particularly thank the group of Renewable Energy Laboratory which helped me with their expertise: Prof. Salvy Russo, Dr Sebastian Führer, Dr Kevin Rietwyk, Dr David McMeekin, Dr Sonia R Raga, Dr Boer Tan, Dr Jianfeng Lu (*The Greatest Master of all times – thanks for teaching me how to make PSC*), Dr Tian Zhang, Dr Anthony, Dr Doojin Vak, Dr Dechan Angmo, Dr Andrew Scully, Dr Tuncay Alan, Dr Nastaran Meftahi, Prof. Salvy Russo, Dr Gaveshana Sepalage, Prof. Jacek Jasieniak, Dr Dorota Bacal, Dr Xiongfeng Lin, Mr Siqi Deng, Ms Monika Michalska, Mr Hao Deng (amazing help with microfluidic devices), Dr Jason Brenker, Dr Nick Scarrat, Dr Anton Tadich, Mr Iain Strachan and all the other people from RE laboratory at Monash University, MCEM, MCN, Australian Synchrotron, ANFF-SA. The author acknowledges the use of facilities at CSIRO Flexible Electronics Laboratory and would like to thank especially Mrs Regine Chantler, Dr. Mei Gao, Dr. Doojin Vak, Dr. Chuantian Zuo, Dr. Dechan Angmo, Dr. Anthony Chesman, and Dr. Andrew Scully. The author wants to acknowledge invaluable help in semiconductor related topics received from Mr. Dan Smith and for fullerene thermal evaporation from Dr Ash Dyer, both from MCN. I want to thank my friends in Australia, US, UK, Germany and

Poland who supported me throughout the times or been a part of my journey, particularly: Elena, Michał, Sławomir, Paulina, Tomasz, Aniela, Anna, Adam, David, Dominika, Piotr, Alexandra, Arthur, Bill, Horace, Diana Szarlota, Paweł, Lukas, Nyalie, Thomas, Anya, Mitra, Kinga, Rohan, Toon, Robert, Carol, Marek, Zosia, Kate, Hana, Dijon, Kira, Cezary, Beata, Mateus, Carl, Pegah, Kamil, Alexandra, Mathias, Roberto, Piotr, Viviane, Matt, Konrad, George, Kevin. And my family: sisters (Agata (Spark of Life), Marta (Black Lightning), Anna), brothers (Grzegorz, Jacek). Grandma Stefania (our legendary Babcia and our Polish teacher) and the most importantly my amazing Mum, who has gone through a difficult time and I could not be with You that time, but I am really glad that I still have You and I love You so much for all that you gave me over the years. *In memoriam:* my beloved Father, Officer Captain Przemyslaw Adam Surmiak (1956-2018), Bachelor Degree (Economy) in Poznan, Master Degree (National Defence Academy) in Warsaw, Officer of Poland's Armed Forces, who served at 78th Rocket Regiment of the Air Defence and later at Military Unit of Air Force. *You were taken so unexpectable from us, without any warning.* I remember Your voice, strong and reassuring, like a sword cutting right through and getting to the core of each topic. I was inspired by You; I had all tools to shape my future. Thank You for all help in the last battle, a small scar but I won myself back. We had so much despite having so little, the true wealth was Our countless conversations. My last words before you passed away were that I love You…You knew it.

Peer-reviewed Publications during enrolment

[1] **Surmiak, M.A.,** Zhang, T., Lu, J., Rietwyk, K.J., Raga, S.R., McMeekin, D.P. and Bach, U. (2020), High-Throughput Characterization of Perovskite Solar Cells for Rapid Combinatorial Screening. Sol. RRL, 4: 2000097. https://doi.org/10.1002/solr.202000097

[2] Michalska, M. (F-A), **Surmiak, M.A.,** Maasoumi, F., Senevirathna, D.C., Chantler, P., Li, H., Li, B., Zhang, T., Lin, X., Deng, H., Peiris, T.A.N., Rietwyk, K.J., Chesman, A.S.R., Alan, T., Vak, D., Bach, U. and Jasieniak, J.J. (2021), Microfluidic Processing of Ligand-Engineered NiO Nanoparticles for Low-Temperature Hole Transporting Layers in Perovskite Solar Cells. Sol. RRL. https://doi.org/10.1002/solr.202100342

[3] Ruan, S.; **Surmiak, M.-A.;** Ruan, Y.; McMeekin, D. P.; Ebendorff-Heidepriem, H.; Cheng, Y.-B.; Lu, J.; McNeill, C. R., Light induced degradation in mixed-halide perovskites. Journal of Materials Chemistry C 2019, 7 (30), 9326-9334.

[4] Rietwyk, K. J.; Tan, B.; **Surmiak, A.;** Lu, J.; McMeekin, D. P.; Raga, S. R.; Duffy, N.; Bach, U., Light intensity modulated photoluminescence for rapid series resistance mapping of perovskite solar cells. Nano Energy 2020, 73, 104755.

[5] Eghlimi, A.; Jubaer, H.; **Surmiak, A.;** Bach, U., Developing a Safe and Versatile Chemiluminescence Demonstration for Studying Reaction Kinetics. *Journal of Chemical Education* **2019,** *96* (3), 522-527.

Publications under review

[6] "A High-Throughput Exploration of the $BA_2MA_{(n-1)}Pb_nX_{3n+1}$ Ruddlesden-Popper Perovskite Compositional Space" **Maciej Adam Surmiak**, Sebastian O. Fürer, David P. McMeekin, Jianfeng Lu, Kevin James Rietwyk, Sonia Ruiz Raga, Hao Deng, Caria Evans, Dechan Angmo, Anthony Chesman, Doojin Vak*, and Udo Bach*

[7] "Machine Learning-Enhanced High-Throughput Fabrication and Optimization of Quasi-2D Ruddlesden-Popper Perovskite Solar Cells" **Maciej Adam Surmiak**, Nastaran Meftahi, David P McMeekin, Sebastian O Fürer, Kevin Rietwyk, Jianfeng Lu, Sonia Ruiz Raga, Caria Evans, Monika Michalska, Hao Deng, Tuncay Alan, Dechan Angmo, Doojin Vak, Anthony Chesman, Andrew J Christofferson, David A Winkler, Salvy Russo* and Udo Bach*

[8] "Perovskite Solar Panel Prototype – a step by step fabrication of an environmental aging station" **Maciej Adam Surmiak**, Monika Michalska, Tian Zhang, Sebastian Fuhrer, David McMeekin, Boer Tan, Jie Zhao, Nirmal Peiris, Narendra Pai, Kevin Rietwyk, Gaveshana Sepalage*, Jacek J. Jasieniak, Udo Bach*

Declaration for a thesis including published works

I hereby declare that this thesis contains no material which has been accepted for the award of any other degree or diploma at any university or equivalent institution and that, to the best of my knowledge and belief, this thesis contains no material previously published or written by another person, except where due reference is made in the text of the thesis. This thesis includes (2) original papers published in peer reviewed journals. The core theme of the thesis is combinatorial high-throughput perovskite solar cell materials discovery. The ideas, development and writing up of all the papers in the thesis were the principal responsibility of myself, the student, working within the Department of Chemical Engineering, under the supervision of Prof. Udo Bach and Prof. Salvy Russo (RMIT). The inclusion of co-authors reflects the fact that the work came from active collaboration between researchers and acknowledges input into team-based research. The inclusion of co-authors reflects the fact that the work came from active collaboration between researchers and acknowledges input into team-based research.)

In the case of (6,7) my contribution to the work involved the following:

In the case of (6,7) my contribution to the work involved the following:

Thesis chapter	Publication title	Status	Nature and percentage contribution	Co-author names and contribution	Co-authors Monash student
6	Microfluidic Processing of Ligand-Engineered NiO Nanoparticles for Low-Temperature Hole-Transporting Layers in	Published	45% Planned the paper, surveyed the literature, designed experiments, sample preparation, collection of experimental data, processing and analysis of all the data, writing and editing the manuscript with	(45% Monika Michalska), all the others 10% Fatemeh Maasoumi, Dimuthu C. Senevirathna, Paul Chantler, Hanchen Li, Bin Li, Tian Zhang, Xionfeng Lin,	Yes

			figures, responding to reviewers with revisions.	Hao Deng, Naresh Chandrasekaran, T. A. Nirmal Peiris, Kevin James Rietwyk, Anthony S. R. Chesman, Tuncay Alan, Doojin Vak, Udo Bach, Jacek J. Jasieniak)	
7	High-Throughput Characterization of Perovskite Solar Cells for Rapid Combinatorial Screening	Published	90% Planned the paper, surveyed the literature, designed the system and experiments, sample preparation, collection of experimental data, processing and analysis of all the data, writing and editing the manuscript with figures, responding to reviewers with revisions.	10% (Tian Zhang, Jianfeng Lu, Kevin James Rietwyk, Sonia Ruiz Raga, David Patrick McMeekin, Udo Bach)	No

I have not renumbered sections of submitted or published papers in order to generate a consistent presentation within the thesis.

Student signature: Maciej Adam Surmiak

 SIGNATURE REMOVED

Date: 30.07.2021

The undersigned hereby certify that the above declaration correctly reflects the nature and extent of the student's and co-authors' contributions to this work. In instances where I am not the responsible author I have consulted with the responsible author to agree on the respective contributions of the authors.

Main supervisor signature: Prof. Udo Bach

 SIGNATURE REMOVED

Date: 30 /07/2021

List of abbreviations

2DRP quasi-2D Ruddlesden-Popper

AFM Atomic Force Microscopy

AZO Aluminium Doped Zinc Oxide

RPM Revolutions Per Minute

PID Proportional Integral Derivative

CBZ Chlorobenzene

CTL Charge Transporting Layer

EQE External Quantum Efficiency

FF Fill Factor

GIWAXS Grazing Incidence Wide Angle X-ray Scattering

GO Graphene Oxide

ITO Indium Tin Oxide

J_{SC} Short-Circuit Current Density

ML Machine Learning

MoOx Molybdenum Oxide

NREL National Renewable Energy Laboratory

OPV Organic Photovoltaics

P3HT Poly(3-hexylthiophene-2,5-diyl)

PCBM Phenyl-C61-butyric acid methyl ester

PCE Power Conversion Efficiency

PEIE Polyethylenimine Ethoxylated

PESA Photoelectron Spectroscopy in Air

PSP Perovskite Solar Panel

PV Photovoltaics

RE Renewable Energy

V_{OC} Open-Circuit Voltage

XPS X-ray Photoelectron Spectroscopy

XRD X-ray Diffraction

Contents

1 Introduction

1.1 Thesis structure

This doctoral thesis focuses on the combinatorial high-throughput perovskite solar cell material discovery approaches for rapid fabrication, testing and analysis. This work aims to speed up progress in photovoltaics, and reveal key information about solar cell devices.

The **first chapter** starts with a discussion and current goals for the world's energy consumption in the view of catastrophic climatic degradation, which it is hoped can be stopped and even reversed. What on the surface may look completely unrelated to this doctoral thesis, if omitted would make this work incomplete or even generic. The importance of solar cell technology for addressing the climate change is highlighted. Also the current status of existing classes of photovoltaic devices is outlined. **Chapter 2** provides the rationale for this research work, it starts with the theory behind photovoltaics, including an overview of the current state-of-the-art, followed by a brief history of perovskite discovery including the most significant breakthroughs. The differences between perovskite solar cells and other technologies are explored. The reader is provided with the concept of perovskite tunability ,various architectural designs of perovskite solar cells, and the address of current issues related to the perovskite solar cell stability. Finally, the aspect of combinatorial high-throughput research is reviewed. The **third Chapter** provides for the reader an outline of all materials, methods, and instrumentations used in this research. The author provides here all details related to precursors, substrates, depositions, annealing, post-annealing and entire solar cell preparation protocols. All steps in producing the films and samples are described in detail. **Chapter 4** presents the results of the first stage of the research. The reader is introduced to combinatorial high-throughput (cHTR) setup for perovskite film fabrication. A pathway for an automated system dedicated to the discovery of new perovskite-based solar cell materials is described. In detail, the topic of environmentally stable quasi-2D Ruddlesden-Popper perovskite crystals, highlighting the origins of their superior stability versus their 3D counterparts is investigated. The automated method for microfluidically mixed precursor

solutions and deposition technique (drop-casting) of quasi-2D Ruddlesden-Popper perovskites is presented. The extraction and creation of convenient-to-read heatmaps with various optoelectronic and performance metrics that allow for narrowing down the optimization are proposed. **Chapter 5** presents further developments with the use of the cHTR film deposition system. The optimization of the quasi-2D Ruddlesden-Popper perovskites via the employment of additives, solvents, and surfactants is studied. The optimization combined with standardized sample preparation methodology was analyzed. The details related to film formation and tunability of precursor solution crystallization mechanisms and their impact on the device performance are discussed. **Chapter 6** focuses on the charge transporting layer optimization using the developed high-throughput microfluidic mixing approach presented in previous chapters. Insights into the low-temperature ligand-exchanged nickel oxide (NiO_x) nanoparticle film preparation method are presented. An inexpensive and quick film improvement and material quality validation methodology of microfluidically fabricated films based on a field-effect transistor (FET) are given. A microfluidic mixing enhanced dispersion deposition technique based on multi-pillared multistage inverted Tesla-valve and T-junction is explored. In **Chapter 7**, a unique, parallel 16-channel rapid cHTR solar cell testing system for rapid data harvesting and electrical characterization is presented. A novel approach for solar cell device development compatible with the system is investigated. Finally, **Appendix A** provides technical details and methodology for the modular construction of prototype perovskite solar panels (PSPs). Accessible data acquisition and testing solution in real-world conditions is presented. A pathway for a long-term stability testing station that can further the perovskite research and serve the research community as a great data gathering tool is described. The thesis is concluded in **Chapter 8**.

1.2 Rationale behind tool development for climatic adaptation

From the beginning of mankind, people used energy to perform their everyday tasks, initially with their own muscles, and later with the help of domesticated draught animals. The demand for produce, commodities, and transport reached far beyond the capabilities of

farmers or haulers, so naturally this limited population growth. Numerous civilizations were rising and falling over that time, usually conquering each other with smarter tools, better armies, and stronger food supplies. Rivalry, development, and survival lasted through the epochs and the "modus-operandi" was not significantly changed. Fast forward to the XVII century in disproportionally densely populated Europe, the tools were designed and built for sake of easing the daily tasks or production of goods. The first mechanized solutions were developed in order to increase output. Despite a couple of previous attempts in the XII century, only about 300 years ago mankind entered a new era – the Industrial Revolution. In the fifth edition of *The Industrial Revolution in World History* Stearns discusses many socio-economical aspects which shaped the world that we know now. The production of food, armaments, construction resources, and commodities was speeded up and perfected. Most importantly, the living standard of the population advanced. The industrial revolution, until today, takes over region by region, country by country, continent by continent. Places without sophisticated technology are being reshaped by that universal transformation – the demand-driven symbiosis of a growing population and energy-driven machinery. We began a large-scale, mechanized production phase which impacted every aspect of our life. Most importantly it enabled humans to produce a surplus of commodities and food, significantly increasing their wellbeing.[1] The population count rocketed exponentially, increasing the demand for commodities, goods, and food. The amplified consumption caused unforeseen progress in all aspects of our livelihood but at the same time, this progress requires more raw materials and energy to be sustained. The entire world, as we know it now, needs the energy to run. Therefore the source of energy must be constant and stable. In the early industrial revolution days, people learned that energy can be carried by heat and the easiest way to get the heat is to burn the fuel. That particular observation leads to a pivotal discovery – the construction of the first steam engines, where heat energy obtained from burning fuel was converted into mechanical movement. From the beginning of the combustion machinery's existence, its fuel needed to be timely delivered. Firstly, people were using self-harvested wood or straw, soon they replaced them with more energy-dense coal. Later on by natural gas and crude oil. **Figure 1** illustrates exponential and rapid growth over the last two centuries of all energy sources consumption (besides the "traditional biomass"). Remarkably, from 1800 to the end of the II World War, the growth only doubled whereas from the 1950s until today we can observe >700 % increase in global energy demand.

Figure 1: Global direct primary energy consumption direct primary energy consumption does not take account of inefficiencies in fossil fuel production. Published online at OurWorldInData.org.

1.3 Energy intensive economy impacts

Unfortunately, coal, gas, and crude oil are fossil fuels that originated from living organisms. They are formed by complex and slow reactions which take millions of years and as such their formation cannot be sped up and they cannot be self-regenerated merely making them a single-use source causing intensive pollution when they are processed. The demand for fossil fuels continues to grow. In some regions of the world, the exploitation of natural resources has been so intense that almost their entire known reserves were already excavated and processed or exported. Of course, such intensive mining came with environmental damage. Most fumes, ashes, and exhaust gases were simply piped out to the atmosphere, part-exchange products were directly ending up in water basins or rivers and in some cases, the mining leftovers were stored outside mines significantly changing surroundings and causing pollution to nearby located environments. Such rapid demand caused an extremely hefty

environmental price. However, humans have not thought about global changes, and sometimes those who voiced the problem were silenced, and often deliberately ignored.[1] Another aspect is that just within ~200 years, for the first time in the history of Earth, the actions of a living species polluted the atmosphere with "greenhouse" gases (for example carbon dioxide, methane, nitrous oxide, or chlorofluorocarbons) to an extent similar to a natural disaster.[1] Once known for beneficial change, the industrial revolution became a direct existential threat for many other species which inhabit this planet, not forgetting the very mankind itself. **Figure 2** shows that barely a fraction of deaths were caused by air pollution (obviously this is only one of many causes, but certainly this one concerns all of us). It can be seen that deaths caused by household air pollution decreased but outdoor air particulates almost doubled their grim effect on the population.
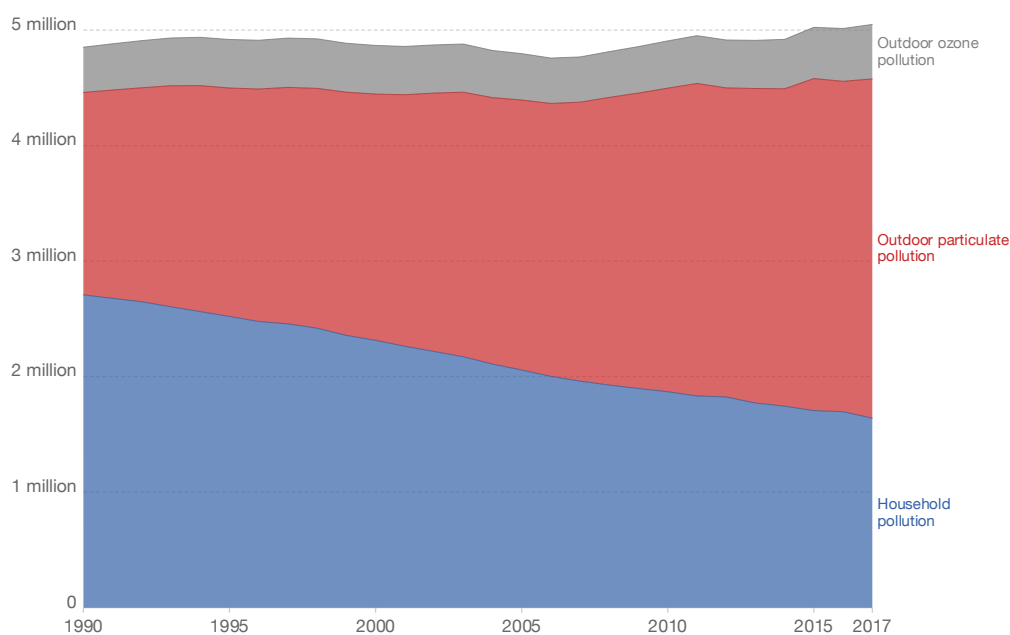
Figure 2: Number of deaths from air pollution (Global Burden of Disease Collaborative Network. Global Burden of Disease Study 2017 (GBD 2017) Results. Seattle, United States: Institute for Health Metrics and Evaluation (IHME), 2018). Published online at OurWorldInData.org.

The pollution accelerated the naturally occurring on Earth temperature cycle. Our direct and indirect products severely damaged the atmosphere, waters, and lands. However, humanity fight against this existential problem, and this time the solution needs to be functional globally. It is evident that the population growth is nowhere near its plateau region. It can be seen in **Figure 3** that the current 7 billion people will increase by 40% just in the next-

generation lifespan. These numbers indicate that the demand for energy will surpass previous heights and the attached environmental price if not addressed now can cause a massive, global disaster.
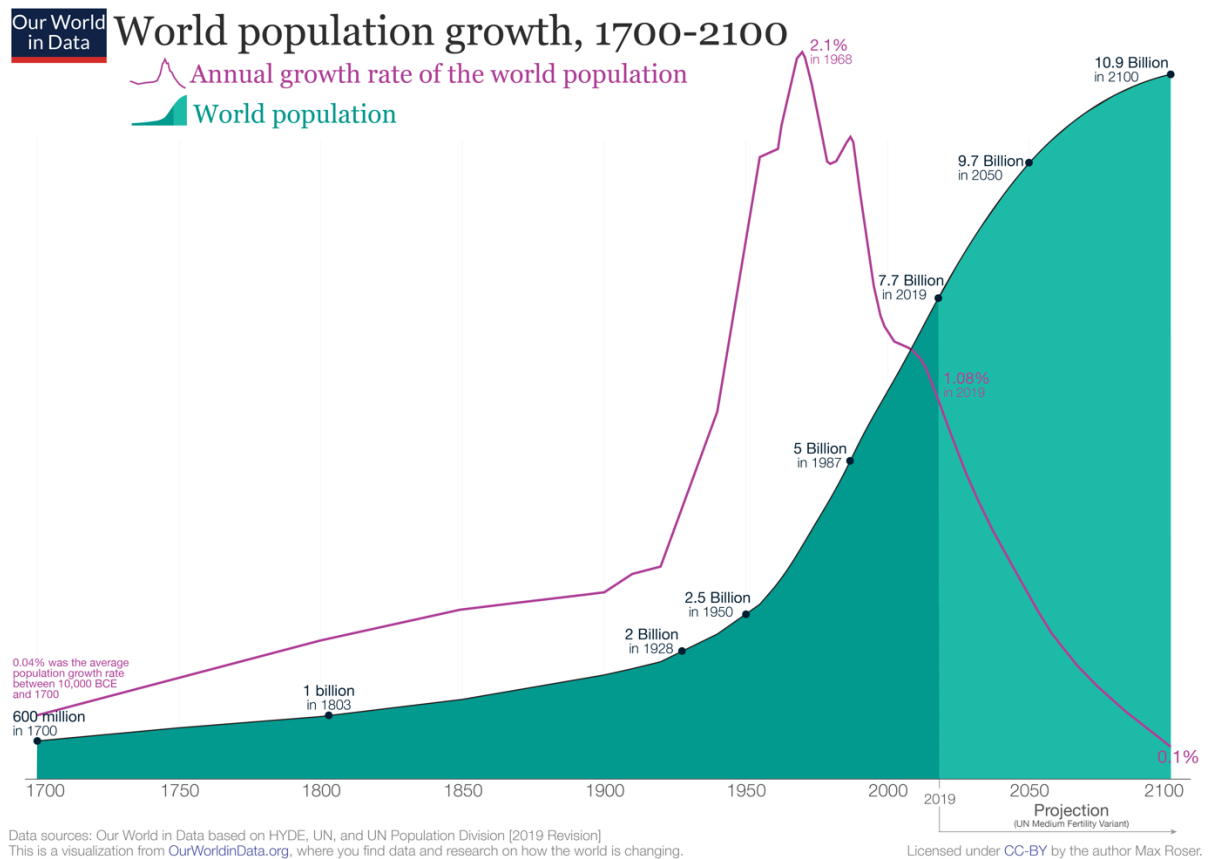
Figure 3: Projections from 2020 through to 2100 based on HYDE and UN, and UN Population Division. Published online at OurWorldInData.org.

At the beginning of the 20th century, we started noticing environmental degradation. Usually, the post-industrial horizon instigated considerations, later on, the tangible observations were correlated to chemistry and matter and demarcated the problem. Finally, we acknowledged the negative climate changes. Beginning from the 20th century, the climate change and pollution became finally recognized, multiple movements and policies were globally initiated. Various countries' administrations formed alliances towards measured eradication of fossil fuel utilization or at least intelligent management of strategic resources. Contrary to the last century, the social changes brought mutual language and understanding. Economies are based on collaborations and cooperation instead of warfare. The global economy allowed mankind to take a clever and beneficial decision. The causes which were dividing people yesterday, now are bringing people together. Globalization is indeed a miracle, mankind

became unified and connected like never before, it allows us to act globally and impact the entire world uniformly in a fast time. There are hundreds of international arrangements that guard the ecosystem, mainly through education and restriction of certain practices known for pollution or destructive impact. One of the big examples is a reduction of refrigerant use, notoriously known as ozone layer contaminants.[1] Humanity has proven that they recognized the issue which affects all of us and took sufficient counteractions in order to preserve the environment. We are responsible for pollution but we are also responsible for the restoration of harmony in the environment. Currently, to ensure economical progress, energy utilization, clean and sustainable growth of economies, and wellbeing of communities. Intelligent management of resources that are accessible now and limitation of unnecessary consumption allows for better usage of them. All that is set in place and or is currently being improved across the planet. We need to ensure that next generations will get the same chance of leading livelihood like we do (or better) and we will not run out of energy sources. Importantly, we cannot harm our ecosystem to the point beyond recovery. Therefore, the main, common, and universal goals for the entire humanity are to ensure a continuum of life with its steady development that will not trigger detriment to nature and allow future generations to enjoy their lives in a clean world. In the age of rapid industrialization and global progress towards an unified lifestyle where hunger, poverty, disease, and premature death are greatly eliminated, energy plays a pivotal role. It can be seen in **Figure 4**, that through the implementation of policies the harmful CO_2 emissions (currently levelling at 50 Gt) can be not only limited but reduced or even inverted (we would start cleaning the atmosphere by absorbing the CO_2 in some pathways by 2060) despite the anticipated population growth and energy demand increase.

Global greenhouse gas emissions and warming scenarios

– Each pathway comes with uncertainty, marked by the shading from low to high emissions under each scenario.
– Warming refers to the expected global temperature rise by 2100, relative to pre-industrial temperatures.

Annual global greenhouse gas emissions
in gigatonnes of carbon dioxide-equivalents

150 Gt

No climate policies
4.1 – 4.8 °C
→ expected emissions in a baseline scenario if countries had not implemented climate reduction policies.

100 Gt

50 Gt

Greenhouse gas emissions up to the present

Current policies
2.7 – 3.1 °C
→ emissions with current climate policies in place result in warming of 2.7 to 3.1°C by 2100.

Pledges & targets (2.4 °C)
→ emissions if all countries delivered on reduction pledges result in warming of 2.4°C by 2100.

0

2°C pathways
1.5°C pathways

1990 2000 2010 2020 2030 2040 2050 2060 2070 2080 2090 2100

Figure 4: Potential future emissions pathways of global greenhouse gas emissions (measured in gigatons of carbon dioxide equivalents) in the case of no climate policies, current implemented policies, national pledges within the Paris Agreement, and 2 °C and 1.5 °C consistent pathways. High, median and low pathways provide the range for a given scenario. Published online at OurWorldInData.org.

1.4 New potential of energy sources

How can that be achieved? The policies themselves cannot produce energy and stop the emissions. We need to find a way for energy production, distribution and utilization which is not harming our habitat. In the 20th century, we began the competition of pioneering cleaner and newer energy sources. For example, nuclear energy brought a new standard for electricity production but still has many problems. Firstly, the catastrophic failure can permanently pollute the surroundings, it was both caused in the past by human error[2] or natural disaster,[3] secondly the nuclear waste needs to be stored safely for thousands of years which pose significant problems.[4] Hence, nuclear energy may co-exist with conventional fossil fuel power plants but it will not fully replace them, and in the long run, nuclear fuel is not a

fully renewable source. Nevertheless, there are sources that can generate the energy needed for modern living at a very little environmental price - specifically renewable energy (RE) sources. RE needs a broader back-story that points to the reason why the RE is better than conventional fossil fuels. In the age of rapid population growth, mechanization of nearly all manufacturing divisions, sky-rocketing need for energy, and appearance of new global players that develop at a much quicker rate than western European or northern American equivalents, we need to rethink the current status quo of energy production and distribution. Especially the new global development "power-houses" (commonly referred to India or China but also previously underdeveloped, now emerging central European markets called Visegrád group (Poland, Czechia, Slovakia, and Hungary), southern American countries such as Brazil or African nations such as Ghana or Nigeria are a place for new solutions. As can be seen in Figure 3, the United Nations predicts that the earth's population will reach ~10 billion by 2060, denoting the increasing requirement for low-cost energy displays no signs of decelerating. Indeed, it is predictable to escalate by up to 50% over the 25 years. As aforementioned, the international hubs for energy utilization remain altering. This intensification and further scattering of pollution sources would be catastrophic from a conservational standpoint, especially if fossil fuels persist as the central energy source. The effort towards ecological and reliable systems for energy generation and distribution are the main drivers of today's large-scale development projects. As it was stated beforehand, the emerging hubs for energy use are predominantly positioned in geographical zones where widespread transport grids are not commonplace, ushering the opportunity to operate ecological substitutes aimed at the main percentage of these essential energy increase additions. For example in Australia, regardless of being considered as a fully developed "western" nation in terms of socio-economics, differences between heavily underdeveloped parts of the world and Australian rural areas are very little.[4-5] There are tactics and projects implemented that can change the Australian outback communities into the scattered energy producers, moreover clean RE producers.

1.5 Renewable energy

The Australian Renewable Energy Agency (ARENA) described RE as "produced using natural resources that are constantly replaced and never run out."[1] There is indeed RE's obligation to satisfy clean policy requirements, it must be: enough to cover the peak demand (+ small surplus), commonly accessible, and most importantly stable and safe in the long run. Preferably, the RE needs to be transformable into easy to transport, refinement-free, and widely storable electrical energy. Nature around gives the answer to what can be the best energy source locally: solar radiation, wind energy, water such as tidal or rivers, and biomass that can be grown rapidly and then reused, or some more sophisticated such as heat from geothermal wells. It was known for centuries that solar irradiation can be efficiently used. In ancient Rome or Greece people made use of solar energy by designing the vernacular architecture in a beneficial way; to utilize shade and sun-exposed parts of the building as either cold storages or warm and dry spaces.[6] Another RE source, wind, has been taken advantage of in multiple applications for centuries. For example, by bakers in wind mills[7] and by seamen to thrust their vessels.[8] Hydro energy was also utilized across the globe. Similar to wind, the river's currents were harnessed to propel the mills.[9] The biomass energy surprisingly gave birth to alchemists and evolved into an energy source, especially after people discovered fermentation or alcohol refinement.[10] Even the aforesaid complex geothermal energy was utilized; for example ancient baths.[11] Those examples support the very simple theory – people naturally and uniformly (do not belong to any particular culture or geographical location) notice certain relationships in nature. Mankind can utilize local and accessible resources adjusted to appropriate forms and applications. Currently, the form of energy utilization has evolved too, especially the fact that energy from all RE sources can be converted into electrical energy. Thus it can then be distributed locally or even for hauled to distant end-users or perhaps stored to be readily available. Contrastingly to the ancient functions, solar energy now can be harnessed, converted, and delivered everywhere. For instance with energy harvested from solar panels. Nowadays wind energy is usually acquired by wind turbines and converted from mechanical to electrical energy, stored at peak wind hours, and distributed in quiet times.[12] Hydro energy is usually converted by water dams on rivers or creeks which use the flow of water to propel very efficient water turbines with

similar, however more predictable effect to wind turbines.[13] Also mentioned biomass has been developed further[14] – nowadays the compost or manure can be harnessed into combustible gas production or even certain species of plants can be produced by highly effective farming and converted to a range of materials.[11, 15] Finally, geothermal energy utilization has evolved into a very efficient, inexpensive form of RE that can be harvested, converted, and stored.[16-17] Consequentially, there is a growth in RE participation in the global energy balance. **Figure 5** indicates current trends in RE. The map shows very positive (from the RE perspective) trends in South America and Africa. Moreover, there is visible rapid growth in RE participation in countries that had not held any other sources.

Share of electricity production from renewables
Renewables includes electricity production from hydropower, solar, wind, biomass. and waste, geothermal, wave and tidal sources.
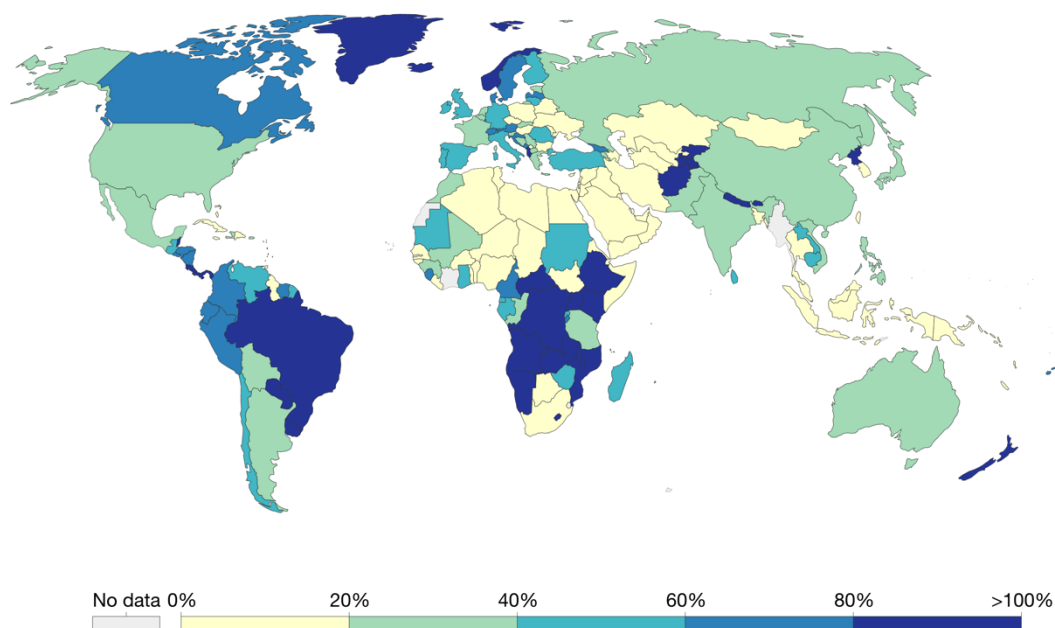
Source: Our World in Data based on BP Statistical Review of World Energy & Ember (2021)   OurWorldInData.org/energy • CC BY

Figure 5: Renewables includes electricity production from hydropower, solar, wind, biomass. and waste, geothermal, wave and tidal sources. Published online at OurWorldInData.org

1.6 Future of Renewable Energy

Another reason why RE has not been adopted everywhere as a dominating energy source is its dependence on weather and geographical localization. From an economical perspective, the RE dependence means that the energy shortage is more likely to happen; a huge setback if the country/region is heavily industrialized and reliant on the energy to run factories or cities. For instance, tidal energy depends on the waves and requires regions to have access to the sea, or hydropower dams indeed can be empty at certain times of the year. Wind energy can see quiet periods but gusts need to blow with significant speed, to at least break the inertia of massive propeller arms. There is also a limitation to where they can be constructed excluding most of the metropolitan areas or heavily populated by birds or other flying animals regions.[1-2] Geothermal installations are usually permanent and can significantly impact the environment – as for now this particular type also is strictly limited to best localizations.[3-4] Their application mostly excludes individual households from having their own installation for different purposes than simple heating. Biomass is usually contemplated as a first-step alternative that is directly employable and compatible with existing fossil fuel-consuming systems. Referring back to Figure 5, there is one particular type of energy that was omitted in terms of drawbacks. Solar energy. It can be subdivided into a couple of groups: photovoltaics (PV)[5], solar-thermal converters[6,] or solar-fuel chemical systems.[7-8] It can be seen in **Figure 6**, how heavily global economies are investing in solar energy generation. Solely the US and China added last year between 25 to 50 TWh per year of infrastructure, whereas India, Australia and Mexico oscillated between 10 to 25 TWh per year.[2] Very distinct and perhaps to some extent counterintuitive is the lack of available data or slow uptake along the equator and especially in the central part of Africa.

Figure 6: Shown is the change in solar energy generation relative to the previous year, measured in terawatt-hours. Published online at OurWorldInData.org.

Solar-thermal energy generation harnesses solar energy in the form of heat. It takes advantage of visible and infrared radiation to then produce steam to drive a turbine.[1-2] Some applications use direct heat exchangers with solar vacuum tubes for convection[3] or thermoelectric phenomenon.[4] Some solar fuels are created directly from solar or thermal energy through photochemical reactions.[5] In other words, the sunlight energy can be converted into electricity through a direct photo-electrochemical reaction, which will form a fuel that can be stored, transported, and utilized to generate electricity. Unfortunately, each energy conversion process is flawed by the efficiency limitation (losses). Remarkably, photovoltaics (PVs) directly converts solar irradiation into electrical energy. The significant losses related to the aforementioned reactions can be circumvented. Direct photo-creation of electricity makes PV exceptionally appealing for the future of RE. The electrical energy can be produced, stored by residential investors or/and commercial entities. It can be transported over pre-existing grids or consumed directly. Indeed, the solar radiation is never-ending, free (at least until the existence of the Sun – which means beyond our species' existence), and abundant. Solar panels do not have any moving parts nor do they require extensive or

specialized maintenance. Solar panels as an alternative source of energy have another, very important advantage – they receive strong public support and are considered harmless for the environment.[6] In fact, the International Energy Agency 2021 Renewable Energy Market Update[3] revealed that RE sources were the only types of energy for which demand increased during the global pandemic. Noteworthy, the demand for other conventional fossil energy sources was stagnant or declined. In 2020, the RE global additions increased by 45% accounting now for almost 280 GW.[3] The PV developments also broke new records, it is estimated in the IEA update that the annual additions reach 162 GW and will grow almost 50% by 2022 in comparison to 2019 (pre-pandemic).[3] We will focus on PVs from this point onwards and the discovery of new materials used in PV is the main focus of this thesis.

2 Literature review

A large amount of work has been conducted in the last 10 years on the novel subgroup of PV perovskite solar cells. Of these, the developments of the perovskite compositions, architectures, and properties have attracted the most attention. Studies in the field of perovskite solar cell materials can be divided into three main areas:

(i) perovskite working mechanisms, material development and synthesis, optimization, and compositional modifications;

(ii) fabrication methods, device architectures, and measurements;

(iii) the elucidation of the new subgroups of perovskites and the compositional screening prospects.

These areas of investigation will be reviewed. Moreover, a brief summary of the photovoltaics, the origins of solar cells and position of perovskite in the hierarchy of available PVs will provide essential background, and will give an insight into the basic material functionalities.

2.1 Background

2.1.1 Semiconductors for photovoltaics

Semiconductors are the cornerstone of modern electronics and are found across microchips, lasers, sensors, and solar cells. Broadly, electrical materials can be split into three categories: metals, isolators, and semiconductors. Electrical conductivity is a measure of freely transportable electrons within the material. Metals are materials that typically exhibit electrical resistivity (at temperature of 300 K) ranging from 10^{-2} to 10^{-8} Ω-m, with insulators typically 10^{-11} to 10^{-20} Ω-m positioning semiconductor conductivity between them. However, the electrical properties of semiconductors can be altered by applying voltage bias or

introducing foreign elements (dopants) into the crystal structure to achieve a number of properties. Number of the semiconductor properties achieved with careful doping/crystal engineering, for example: electrical signal amplification, fast switching, and most importantly energy conversion. Semiconductors are at the center of photovoltaics, devices that convert optical energy into useful electricity. At the beginning of the 20th century, Planck and Einstein developed principles of quantum mechanics that described light as a "particle" possessing energy E and momentum p (proportional to the wave vector and direction of the motion of photon). Light can be described as a particle or/and a wave. Since it is beyond the scope of this doctoral thesis, only a brief introduction will be provided on how photons can be converted to electrons and vice-versa upon interaction with the material. The energy and the momentum are given in Equations 1 and 2:

$$E = hv = \frac{hc}{\lambda} \tag{1}$$

where h is the Planck constant, v is the frequency of light wave, c is the speed of light, and λ is the wavelength of light, and therefore the momentum can be expressed as:

$$p = \frac{h}{v} \tag{2}$$

In other words, upon the collision of quantum particles, the transfer of kinetic energy can occur. The "wave of corpuscles" (dualism of corpuscle-wave) can be also described as a wave due to diffraction and constructive/destructive interference, but it is important that the light (or even a single photon) carries energy (E) that interacts with materials. The relationship is expressed as:

$$E(w) \overset{\text{def}}{=} \frac{p^2}{2m} \overset{\text{def}}{=} \frac{\hbar^2 w^2}{2m} \tag{3}$$

where $\hbar$ is the reduced Plank constant, w is the wave, p is the particle momentum, and m is the particle mass.

Important for this research is the interaction between the irradiation and material that allows the harvesting of the photon-carried energy. Some semiconductors can generate both voltage and current upon exposure to light. Therefore in simple terms, they become light-to-electrical energy converters or photovoltaic (PV) devices.

2.1.2 Light to power conversion

In principle, the photon energy (E_{photon}) gets converted into electrical energy $E_{electrical}$ if the bandgap energy of the material is lower than E_{photon}. The intended origin of E_{photon} is the Sun. As a central star in our planetary system, the Sun, only within on second emits omni-directionally power of 3.846×10^{26} W. Significant part of it is in the form of electromagnetic radiation (visible and invisible light). The energy emitted from the Sun needs to overcome multiple obstacles as it travels from the Sun to the Earth's surface (~150 000 000 km) which significantly limit its energy. Especially upon entering the Earth's atmosphere losses due to scattering and atmospheric gases absorption occur (as a side note thanks to them there is life on Earth). Hence, the optimal path, that is a ratio between the path length (L) and zenith path (L_p)) from the Sun to the Earth's atmosphere is defined as an air-to-mass coefficient (AM) given by :

$$AM = \frac{L}{L_p} = \frac{1}{cos\ z}$$
(4)

where z is the zenith angle.

Depending on the exact location of the measurement, three spectra can be distinguished. The three solar irradiance spectra are: extra-terrestrial (AM 0) of intensity ~1350 W m^{-2}, global terrestrial (AM1.5G) of intensity 1000 W m^{-2} , and direct terrestrial (AM1.5D) with intensity 900 W m^{-2} (see **Figure 7**). The AM1.5G serves as a world standard for all solar cell electrical performance characterization. Realistically, precisely built solar simulators (of the spectrum as close as possible to the Sun) calibrated for solar cell active areas with the standardized

AM1.5G maintained at the temperature 25 °C serve as the light source for electrical characterization of solar cells.
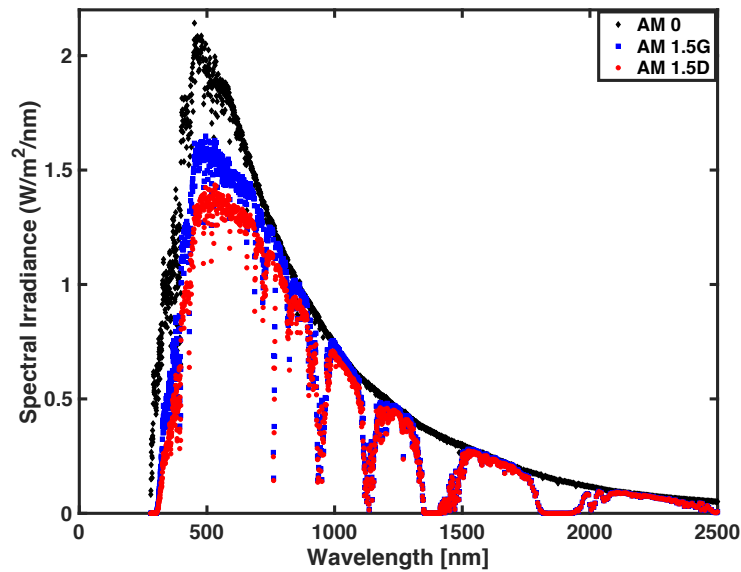
Figure 7: Solar irradiance terrestrial spectra. Black: extraterrestrial spectrum denoted as AM 0, Blue: global terrestrial spectrum denoted as AM1.5 G , and Red: direct terrestrial spectrum denoted as AM1.5 D. Image plotted from the raw data acquired from Open Access Source National Renewable Energy Laboratory. https://www.nrel.gov/grid/solar-resource/spectra-am1.5.html

In order to test the sample, the incremental voltage bias is applied (usually from 0 V to 1.2 V with a step size of tens of mV) whilst simultaneously the photocurrent is measured. These two simple electrical parameters plotted against each other contain key information about the solar cells. Naturally, to compare the overall solar cell efficiency the power conversion efficiency (PCE) measure is calculated as in Eq.5:

$$PCE = \frac{Maximum\ power\ output}{Incident\ light\ flux \times active\ area\ of\ cell} = \frac{Power_{generated\ power\ output}}{Power_{incident\ power\ density}} \tag{5}$$

This efficiency equation that is universal for all PV devices will be used to describe the characterization of the samples throughout this thesis.

2.1.3 Photovoltaics history

The PV effect was discovered in the mid-19th century by Becquerel and its working principle remains unchanged. A PV device consists of a photoactive material (absorber) and two electrodes, and upon light irradiation voltage and current are observed. This elegant effect is true for all semiconductors, however not all semiconductors are equally good for PV applications. The Schockley-Quassier Efficiency Limit (SQEL) defines the maximum efficiency of the single-junction SC whilst excluding all the other efficiency loss mechanisms besides the radiative recombination.[4] The SQEL theoretical solar conversion efficiency is limited to ~33.7%, Thus, the only candidate semiconductors with a bandgap > 1 eV belong to the group of potentially useful absorbers for the SCs.

PV technology has been intensively researched since the 1950s. Multiple semiconductors (organic, inorganic, hybrid), as well as dopants for them, CTLs, and multiple charge-extracting electrodes, have been investigated. If the family of materials or architecture differs significantly from one another, a distinctive subgroup is created. The certified research achievements in the form of scientific communication or from certified commercial records are gathered in Best Research-Cell Efficiencies by the American National Renewable Energy Laboratory (NREL), see Figure 12. There are 5 subdivisions of solar cells: multijunction cells, single-junction gallium arsenide (GaAs), crystalline (silicon) Si cells, thin-film technologies, and emerging PVs. Altogether, there are ~29 subgroups of SCs. See the **Figure 8** for the NREL chart.

Figure 8: Best Research-Cell Efficiency Chart by NREL from 1976 until 2021. Image Reproduced from Open Access

Source: nrel.gov/pv/cell-efficiency.html

Despite the differences in the physical and/or chemical realization of SCs, three main mechanisms cross-link them all: power conversion efficiency (PCE), production cost (commercial realization) and operational lifetime. First, PCE is defined as the maximum power (the product of photovoltage and photocurrent) generated from an active area of SCs under 1 Sun illumination (AM 1.5 100 mW cm^{-2}). Next, the production cost indicates the basic monetary figure for a levelized cost of electricity (LCOE) and cost of energy (COE), and it is centrally important for successful SCs. It usually leads to estimation of the present worth of a particular SC technology subgroup which can be directly compared with other energy sources. Lastly, the operation lifetime is a measure of SCs stability, standardized by the International Electrochemical Commission (IEC 61215-1: 2021) which clearly indicates the design requirements for the photovoltaic modules (panels) to last for at least 15-20 years.

These three mechanisms serve as an indication for the commercial market value of certain SC technologies. Undoubtedly, most commercialized SCs are based on crystalline silicon and make up approximately 90% of the entire PV market. The state-of-art single-junction device reached a PCE of 26.1 %, an average price of ~$0.3 per W, and a lifetime of ~15-20 years.[1] During the last decade, advanced manufacturing processes have reduced the production costs to such an extent that PV generated and fossil fuels generated energy are comparative with each other in terms of final LCOE and COE, while new PV installations are predicted to cost around ~$25 per MWh in the EU and USA and half that cost in China or India.[2] Broadly speaking, it is evident that most of those financial calculations are based on silicon solar panels and the majority of other subgroups of PV devices are simply not considered as cost-effective enough. Extensively deployed solar farms (solar panels fixed across large designated areas with high irradiation for better energy yield) have become a major competitor to traditionally coal-fired power stations. However, the silicon SC technology clearly has its limitations.[3]

2.1.4 Emerging PV technology

Developed by Polish chemist Jan Czochralski, the Si wafer fabrication technique (Cz)[4] dominates Si crystal production, however this process has a number of limitations. It is

energy-intensive and this lengthens the energy pay-back time. Cz silicon crystal ingots need to be cut into very brittle wafers and the process of preparation requires 99.9999% purity and post-processing (doping and electrode deposition). In addition, Si has a very low absorption coefficient, requiring a thickness of at least a couple of hundred micrometres for efficient light harvesting. Such prepared Si wafers require significant encapsulation, a translucent cover, and a solid, rigid frame in order to be deployed, and in the case of a mechanical crack at a critical spot, the entire module usually stops working.

Other problems come from financial and transportation perspective. Heavily subsidized markets dominate the production of Si wafers used for the PV industry, and centralization of the production of PV Si wafers causes transportation bottlenecks and does not promote the diversity required for technological progress.[5-6] Usually, Si solar panel farms need to be deployed on non-arable land, distant from major population agglomerations in cities.[7] Small, typically suburban residential roof-top electrical energy enhancements are hard to implement in vertical, high-rise metropolitan environments, thus generating the additional loss of energy that is required for its transportation.[8] During the deployment, solar panels need to be mounted at a specific angle and the energy production usually starts after a specific irradiation threshold is reached, further limiting their application. Importantly, it takes 2-3 years of Si panel operation to produce the equivalent energy to that consumed on the panel production.

These drawbacks can reduce the potential use of PV technology, despite the upheaval of RE in the market. Another PV subgroup is needed to fill the gaps that cannot be addressed by Si SCs. A deployment space close to the energy recipients in cities that could be greatly utilized is buildings and public spaces with modern curvature, making potentially flexible solar cells a highly sought-after candidate. Another possibility could be light-weight and flexible SCs which could be installed on existing older buildings where rigid, heavy panels cannot be mounted. An image of Building Attached Photovoltaics (BAPV), where new generation solar panels are attached to the windows or façades of existing constructions is shown in **Figure 9**.
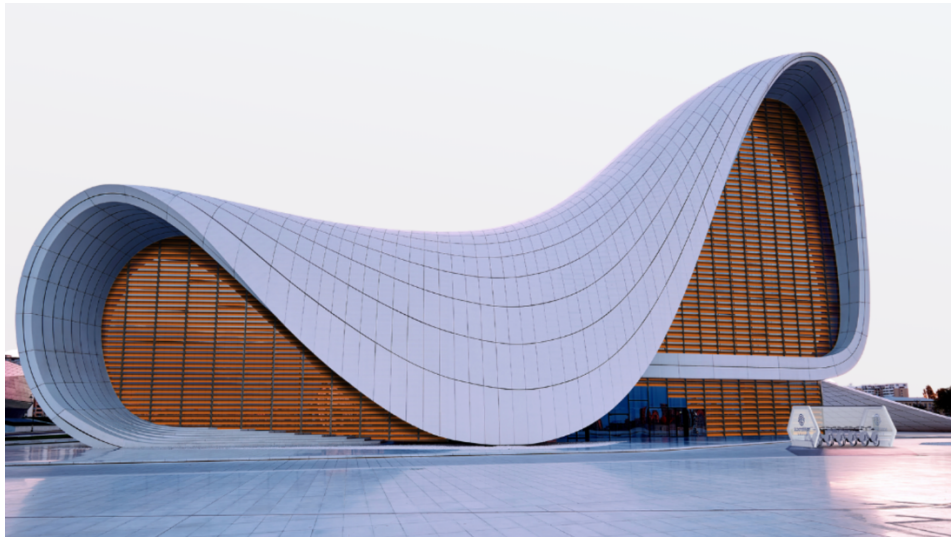
Figure 9: Conceptual image of BAPV. Image reproduced with permission of Dr. O. Malinkiewicz, sauletech.com.

Rather than using gray Si SCs, colorful or semi-transparent devices could be integrated into windows, walls, or glass panes across metropolises generating energy and thus adding more possibilities to modern architecture, and reducing the need for inner-city electrical grids and distribution power substations.

One of the technology subclasses outlined in the previously illustrated NREL chart under emerging technologies is a subgroup called perovskite solar cells (PSCs) which at the moment are the most promising alternatives to Si SCs. After the initial breakthrough in PSCs (PCE = 3.8%[9]), intensive research has led to significant improvements in PSCs with PCE = 25.5% achieved by 2020[10-11], which is only 0.6% less than the best performing research single-junction Si SC.[11-12] The cost of perovskite solar panels if the technology reaches full commercialization is estimated to be multiple times lower than the cost of current state-of the art silicon panels.[1] The significant advantages of PSCs are their low-temperature, solution-processability which makes them significantly less energy intensive to fabricate than Si SCs. PSCs have a direct, easily tuneable band gap. They can be colorful, semitransparent and still generate meaningful energy. They possess a light-weight architecture, they are around ~800 nm thick and they can be built on flexible substrates. Their short, invested energy pay-back is predicted to be counted in days or months instead of years.[2] Thus, perovskite solar cells are the most promising and exciting materials for the entire PV industry.

2.2 Perovskites

2.2.1 Perovskite crystals

German scientist Gustav Rose in 1839 first discovered a new type of crystal called calcium titanate ($CaTiO_3$) in the Ural Mountains[3] and named it "perovskite" after the famous Russian mineralogist, Lev Perovski. The unique crystal structure of $CaTiO_3$ was later investigated in 1926 by Victor Goldschmidt[13] who defined a size tolerance factor for different moieties of the crystal that allow the growth of certain crystal structures. Later studies, especially those with X-ray diffraction, on materials with a perovskite crystal structure revealed the full crystal structure which is rarely ideally cubic. The structure more often occurs as orthorhombic, tetragonal or rhombohedral structure usually depending on the crystallization temperature and ingredients.

The general chemical formula for perovskite crystals is expressed as ABX_3, where A and B stand for two different cations and X is the anion bonding A and B. The size of the elements or compounds in perovskite crystals needs to meet the Goldschmidt tolerance factor G_{tf}, given by the Eq.6:

$$G_{tf} = \frac{R_A + R_X}{\sqrt{2}(R_B + R_X)} \qquad (6)$$

where R_A, R_B, R_X are the radii of the ions A, B, and X, respectively. The perovskite crystal formation will be preserved if the G_{tf} value is close to unity. Some examples of the elements that can form perovskite are for the A: calcium (Ca), potassium (K), sodium (Na), strontium (Sr) or cesium (Cs); for the B: copper (Cu), titanium (Ti), nickel (Ni), cobalt (Co), iron (Fe), manganese (Mn), palladium (Pd), chromium (Cr), cadmium (Cd), tin (Sn), germanium (Ge), europium (Eu), ytterbium (Yb), lead (Pb) or CH_3NH_3, and NH_2CHNH_2. **Figure 10** illustrates the structure of the perovskite crystal and illustration of the crystal unit cell.
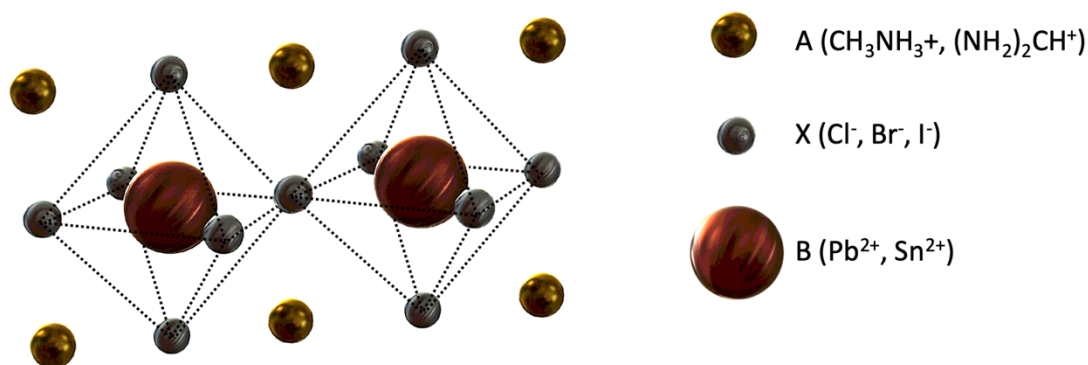
Figure 10: Left: Perovskite unit cells (two adjacent units for illustration of shared vertices). Right: Example of A-site, B-site and X-site ions commonly used in solar cell applications.

The rarely occurring perfect cubic crystal unit cell has a structure in which the A atom sits at the cube-corner position (0,0,0), the B atom moves to the body-center position (0.5,0.5,0.5) and the X atom occupies the center positions (0.5,0.5,0), (0.5,0,0.5) and (0,0.5,0.5). Such a crystal structure allows perovskite to form crystals with numerous interesting properties. One example is strontium titanate ($SrTiO_3$) that exhibits a dielectric constant ε of ~900 and resistivity of $G\Omega$ which makes it applicable in high-voltage (HV) capacitors. Interestingly in 1987, Poglitsch and Weber determined many of the perovskite crystal structures originating from the Guinier-Simon photographs[14], providing insights into the "methylammoniumtrihalogenoplumbates". The measurements are provided in **Table 1**.

Perovskite	Phase	Temperature (K)	Crystal system	Space group	Lattice (pm)	Volume (10^6 pm^3)
$CH_3NH_3^+PbCl_3^-$	α	>178.8	Cubic	$Pm3\,m$	$a = 567.5$	182.8
	β	172.9–178.8	Tetragonal	$P\,4/mmm$	$a = 565.6$	180.1
					$c = 563.0$	
	γ	<172.9	orthorhombic	$P\,222_1$	$a = 567.3$	357.0
					$b = 562.8$	
					$c=1118.2$	
$CH_3NH_3^+PbBr_3^-$	α	>236.9	Cubic	$Pm3\,m$	$a = 590.1\,(1)$	206.3 (260K)
	β	155.1–236.9	Tetragonal	$I\,4/mcm$	$a = 832.2(2)$	819.4
					$c = 1183.2(7)$	
	γ	149.5–155.1	Tetragonal	$P\,4/mmm$	$a = 589.4(2)$	–
					$c = 586.1\,(2)$	
	δ	<144.5	orthorhombic	$Pna2_1$	$a = 797.9(1)$	811.1
					$b = 858.0(2)$	
					$c = 1184.9(2)$	
$CH_3NH_3^+PbI_3^-$	α	>327.4	Cubic	$Pm3\,m$	$a = 632.85(4)$	253.5
	β	162.2–327.4	Tetragonal	$I\,4/mcm$	$a = 885.5(6)$	992.6
					$c = 1265.9(8)$	
	γ	<162.2	orthorhombic	$Pna2_1$	$a = 886.1(2)$	959.5
					$b = 858.1(2)$	
					$c = 1262.0(3)$	

Table 1: Temperature-dependent structural data of CH$_3$NH$_3$PbX$_3$ (X = Cl, Br, I). Reproduced with permission from Elsevier.[14]

Notably, the organic complexes typically form perovskites via weak interactions (van der Waals or H bonding). Because of this, such perovskites have high electro- and photo-luminescence, increased polarizability, offer current conducting properties, and from a mechanical perspective can form highly plastic texture.

2.2.2 Discovery of perovskite solar cells

In the early 90s, hybrid organic-inorganic perovskites were applied in field of electron transistors (FET) by David Mitzi in the IBM corporation laboratories. However, until 2009 they were not applied in any PV application. As mentioned in the previous section, in its most simplified definition, an SC is a stack of materials with a centrally located absorption material which is excited by energy-carrying photons causing electron promotion from VB to CB (leaving a hole in CB). These negatively and positively (electron-hole pair) charged carriers are extracted from the material to the external circuit in the form of photogenerated current.

While the operational principle of the solar cells remains the same throughout all PV subclasses and subgroups, the exact mechanisms may vary slightly . Unlike the Si SC, in PSCs, the built-in asymmetric electronic field utilized for efficient carrier extraction does not originate from crystal doping but from the strong electronic field induced by strongly WF-mismatched interfacial materials in the form of charge-transporting layers (CTLs). These CTLs directly sandwich the perovskite layer. As a result, the built-in mismatch separates the electron-hole pairs causing the potential difference between electrodes adjacent to CTLs, and the current can be extracted to the external load each time the light shines on the active photon-absorbing perovskite layer.

 2009 marked the breakthrough which spread quickly around the world and generated many thousands of PV-related projects. In that year, Miyasaka *et al*. reported the first perovskite-based dye-sensitized solar cell (DSSC) that employed a electrolyte hole transporting material.[9] In their work, nanoparticles (NPs) of methylammonium lead iodide $CH_3NH_3PbI_3$ and methylammonium lead bromide $CH_3NH_3PbBr_3$ were deposited on top of the electron transporting layer (ETL) consisting of titanium oxide (TiO_2) resulting in an efficiency of 3.8 %. This concept and the charge extraction can be seen in **Figure 11**. Miyasaka's DSSC was followed up and improved by Park et al. in 2011 resulting in PCE = 6.5%. A new DSSC was reported by Kantzidis et al. when they replaced the typically liquid electrolyte with a solid $CsSnI_3$ reporting PCE = 10%. In 2012 two independently working groups lead by Snaith and Miyasaka and by Park and Grätzel published works on solid-state perovskite solar cells which

utilized   2,2',7,7'-tetrakis(N,N'-di-p-methoxyphenylamine)-9,9'-spirobifluorene   (spiro-OMeTAD) instead of liquid electrolyte for efficient hole transport. Interestingly, Snaith and Miyasaka replaced the mesoporous TiO_2 layer with an Al_2O_3 scaffold-like insulating layer of similar size without hindering the current extraction.
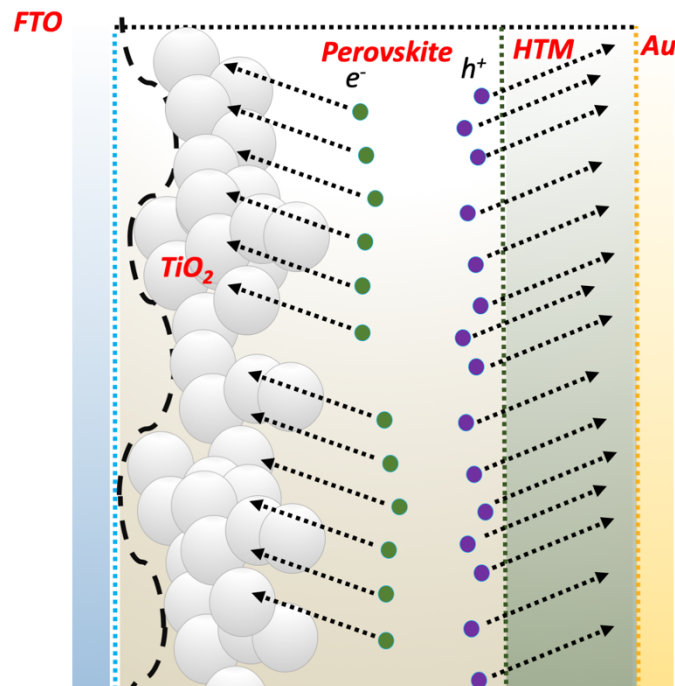
Figure 11: Perovskite solar cell with a mesoporous TiO_2 ETL layer. In the mesoscopic structure, electrons can be extracted efficiently via the TiO_2 layer.[15]

in 2013 Grätzel perfected morphologically solar cells via a new approach to the material deposition. The technique based on a two-step method was ground breaking. The first step was the lead iodide (PbI_2) formation directly on a TiO_2 scaffold, then followed by complementary treatment with CH_3NH_3I solution in order to form $CH_3NH_3PbI_3$, which yielded independently certified PSCs with PCE of 14.1 %. Snaith (2012) did not use a scaffold but employed thermal co-evaporation of the precursor materials forming a morphologically compact, thin film of $CH_3NH_3PbI_{3-x}Cl_x$ and reported PCE of 15.4 %. Both works demonstrated that perovskite materials are highly versatile, tuneable and applicable in different architectures. These achievements were astonishing and inspired the entire PV (especially DSSC[7-8]) community so that researchers around the world began investigating perovskites

aiming to enhance the efficiency by employing different materials, deposition techniques and modifications.

2.2.3 Efficiency race around the world

Since 2013, new PSCs have been extensively developed. Importantly, a huge improvement in PSC efficiency was reported in between 2013 and 2015 when a modification of the halide content $CH_3NH_3PbI_{3-x}Br_x$ (x: iodide-bromide ratio) was found to be viable for the perovskite film improvement. Some studies focused on the morphological improvements, usually slightly improving the reported efficiency.

However, the achievement of greater efficiency is not just a trivial quality improvement. In 2015 it became evident that there are other underlying problems, Snaith *et al*. reported transient behavior of PSCs called hysteresis that was unique in the entire PV field.[16] They revealed that the *J-V* performance curves are different if measured "forward" from short circuit point (J_{sc}) to open circuit point (V_{oc}), and respectively in "reverse". Snaith noticed that certain pre-biasing of the solar cell and exposure to simulated light directly prior to the performance measurement could momentarily increase efficiency, see **Figure 12** for the hysteresis effect.
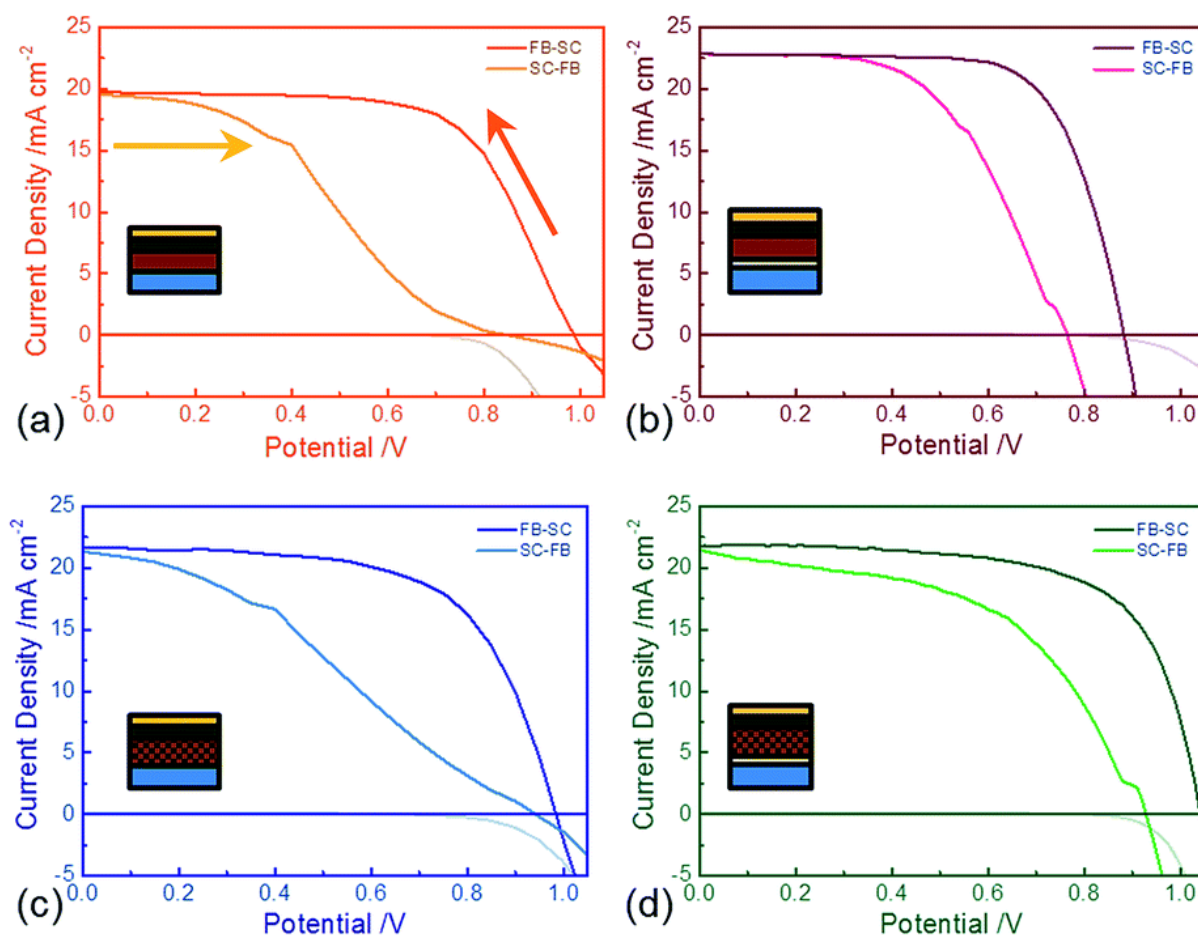
Figure 12: Forward bias to short-circuit (FB–SC) and SC–FB J–V curves of perovskite solar cells with different structures measured under simulated AM1.5, 100 mW cm−2 solar irradiance of the best performing solar cells for each type. Devices are scanned at 0.38 V s−1 after holding the devices at 1.4 V forward bias under illumination for 5 seconds. (a) Planar structure without a titania compact layer, (b) planar structure with a titania compact layer. (c) Mesoporous structure on an Al2O3 scaffold without a titania compact layer, (d) mesoporous structure on an Al2O3 scaffold with a titania compact layer. Corresponding dark currents (FB–SC) are plotted underneath the x-axis. The arrows indicate the scan directions. The inserted diagrams indicate cross-sections of each device configuration. Reproduced with permission from RSC.[16]

The PSCs hysteresis puzzled researchers and the following studies focused on understanding the origin of such an effect. Some answers rose after a study published by Lin *et al.* who measured ε of perovskite crystals ($CH_3NH_3PbI_3$) which proved that the perovskite crystals behaved anomalously, and had much lower binding energies than had been calculated earlier. This finding highlighted the difference between the suspected excitonic conductor-like behavior and more ionic nature of perovskites.

Since then, multiple groups have tackled the origins of hysteresis and resolved some of the strong transient issues.[17] On the other hand, from the perspective of new CTL materials other than perovskites, the use of poly[bis(4-phenyl)(2,4,6-trimethylphenyl)amine] as a HTL resulted in a PCE of 17.9%. This sparked another race towards screening all possible CTLs and their employability in PSCs.[18] Also numerous studies focused on novel fabrication techniques of PSCs. The Ho-Baillie group reported a new gas quenching fabrication technique for rubidium-incorporated perovskite films. In this study, the deposition followed by an inert gas quenching for solvent removal allowed for rapid nucleation for dense, dendritic form free perovskite films achieving PCE of 20% for 65 mm^2 devices.[19] An interesting fabrication method based on solvent extraction for rapid nucleation was reported by Xiao *et al.* In this method, droplets of anti-solvent removed the residual precursor solution solvent whilst the spin-coating dynamic process distributed the perovskite precursor solution, thus achieving a reproducible methodology for highly efficient PSCs.

Another advancement in efficiency improvement was related to studies of large perovskite crystal growth. Nie *et al*. developed a method called "hot casting" where the precursor solution was pipetted onto the mildly preheated substrate before spin-coating. This allowed for >1 mm perovskite crystal grain size which was significantly greater than the widely reported grain sizes of approximately 200-500 nm. Larger grains increased the probability of charge diffusion and extraction without encountering obstacles within the bulk of the material, and translated into an improved PCE.

Multiple new phases of perovskite were developed over time and created the potential for property enhancement and development. Interestingly, Saliba *et al.* in 2016 incorporated rubidium (Rb) and cesium (Cs) cations into mixed organic cation and mixed halide perovskite composing very stable (~300 hours), strongly absorbing perovskite film which as a device exhibited a PCE of almost 20.6%. Follow-up studies focused on perovskite doping with use of potassium (K), europium (Eu) and many other elements facilitating better morphology, growth, mobility and absorption.

The increase in the understanding of PSCs and high efficiency was of great interest to all researchers in the PV field. It was found that some of the concepts and discoveries known in

organic photovoltaics (OPV) and DSSC could be directly employed in PSCs.[9] The inventor of DSSC, Prof. M.Grätzel in 2017 said "This is a really unique event in the history of photovoltaics, and that is what has created a lot of excitement. I have been told that 10 000 researchers are now working in this field worldwide, from just a few in the beginning."[20] In the same year, the excitement of researchers in the field was expressed by H. Snaith who stated "To put it into context, we had been working for about 5 years previously, squeezing the efficiency of the solid-state dye cell up from 5 to 6%, and then all of a sudden, we reached, what was at the time our end goal, our key target of getting to 10% efficiency, with the solid-state hybrid cell just like that. That was quite a surprise and a shock."[21] **Figure 13** illustrates the rapid upheaval of the perovskite papers.
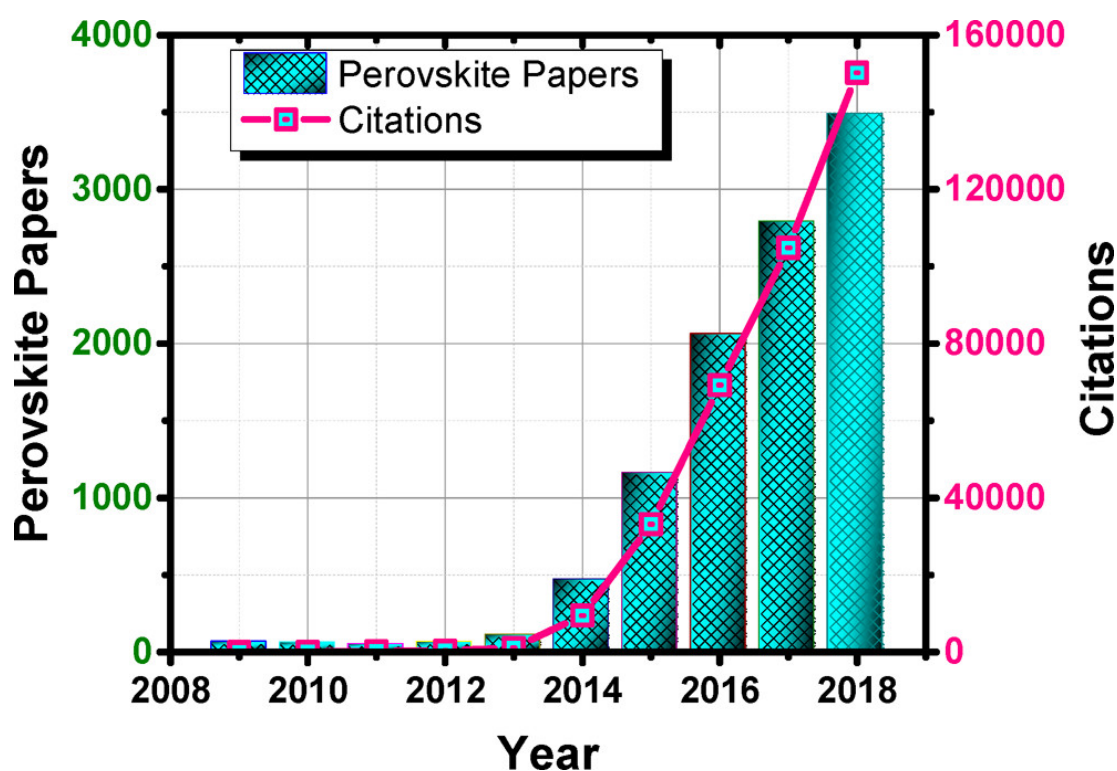
Figure 13: Rise of perovskite research as viewed through the published papers and their citation impact during 2009–2018 (Source: Web of Science, Clarivate Analytics March 3, 2019).

2.2.4 Architectures of PSCs

Many different PSC types have been investigated in the last decade including: flexible PSCs,[10] organic, inorganic, or hybrid PSCs,[11] lead-free PSCs,[12] p-i-n or n-i-p PSC,[13] low dimensional PSCs (Ruddlesden-Popper, Dion-Jacobson),[14] double PSCs,[14] back-contact PSCs,[15] tandem perovskite-perovskite[16] or silicon-perovskite SC,[17]and even first attempts of p-n homo and heterojunction PSC[18-19]. However, the main architecture of PSC can be in general divided into two categories. Namely, the planar (n-i-p) and inverted (p-i-n) configurations can be distinguished. The planar structure contains of the transparent substrate (flexible polymer or rigid glass), a transparent conductive oxide employed for electron collection and transport, the n-type ETL, perovskite film, the p-type HTM (sometimes referred as HTL), and a top metal or organic electrode functioning as charge extracting contact. The PSC with such geometry is also referred as a n-i-p PSC. The inverted geometry means that the ETL and HTM/HTL are flipped relative to the perovskite layer creating a p-i-n structure. Within some other known architectures, ETL and HTL materials are not present. In **Figure 14**, the most common and efficient architectures are presented.

Figure 14: The device architectures of the perovskite solar cells: (a) the planar PSC without ETL, (b) the planar PSC with compact ETL, (c) the mesoporous PSC without compact ETL, and (d) the mesoporous PSC with compact ETL. Reproduced with permission from RSC.[22]

Importantly, the n-i-p or p-i-n architectures are readily employable in modular designs. Shown in **Figure 15** is an image of 4 cm^2 PSC, modular interconnection of the n-i-p archit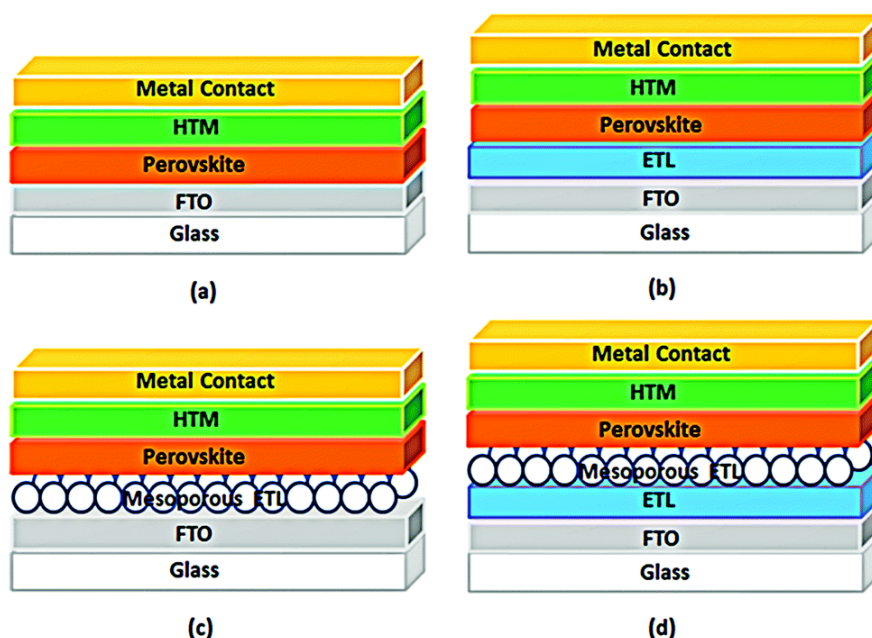ecture, and a typical n-i-p architecture PSC cross-section. This design allows for modular interconnections required for scalability and application in perovskite solar panels.
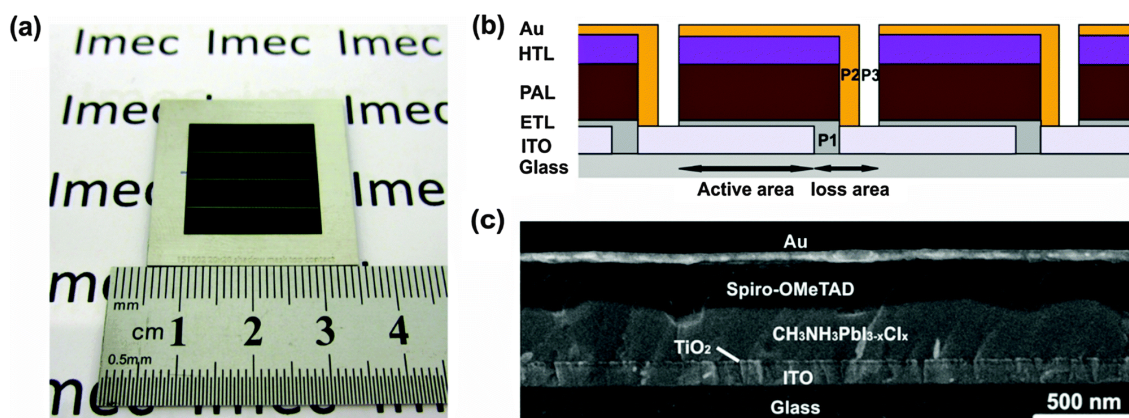
Figure 15: (a) Photograph of the backside of the perovskite module consisting of 4 sub-cells with a total aperture area of 4 cm^2. (b) Scheme of the interconnection of the sub-cells in the perovskite thin-film solar module with the patterning of the ITO bottom contact (P1), the series connection of adjacent cells (P2) and the Au top contact patterning (P3). ETL: electron transport layer; PAL: perovskite active layer; HTL: hole transport layer. (c) Cross-section SEM image showing the actual layer structure of a device. Reproduced with permission from RSC.[23]

2.3 Performance assessment

2.3.1 Bandgap energy alignment

As was explained previously, the incident light is absorbed by perovskite crystal, where the energy conversion occurs. Photons are absorbed by perovskite, producing the electron-hole pairs. At the molecular level, the electron is promoted from the valence band (VB) to the conductive band (CB) generating an electron vacancy (hole) in the VB. The energy difference between the CB and the lowest unoccupied molecular orbital (LUMO) of ETL generates the electronic driving force inducing the electron transport. The excited electron moves through the crystal structure towards the ETL.[24] Simultaneously, the energy difference between the CB and highest occupied molecular orbital (HOMO) drives the transfer of holes from the

perovskite into the HTL.[25] Ultimately, the electron reaches the cathode, and the hole finds its way to the anode. Notably, the energy mismatch between the HOMO and LUMO determines the maximum theoretical open circuit voltage. Critical for the efficient PSC is the charge transport within its structure. Thus the energy alignment between adjacent layers in the perovskite architecture is not trivial. The charge transfer needs to be as seamless as possible, especially at the material interfaces that can effectively block the transport if not matched correctly. Some of the known causes of low PSC efficiency due to incorrect bandgap alignment originate from high trap state density, poor charge mobility, and defect driven charge recombination. There are numerous materials which are applicable and **Figure 16** shows some of the energy levels of these materials.[26]
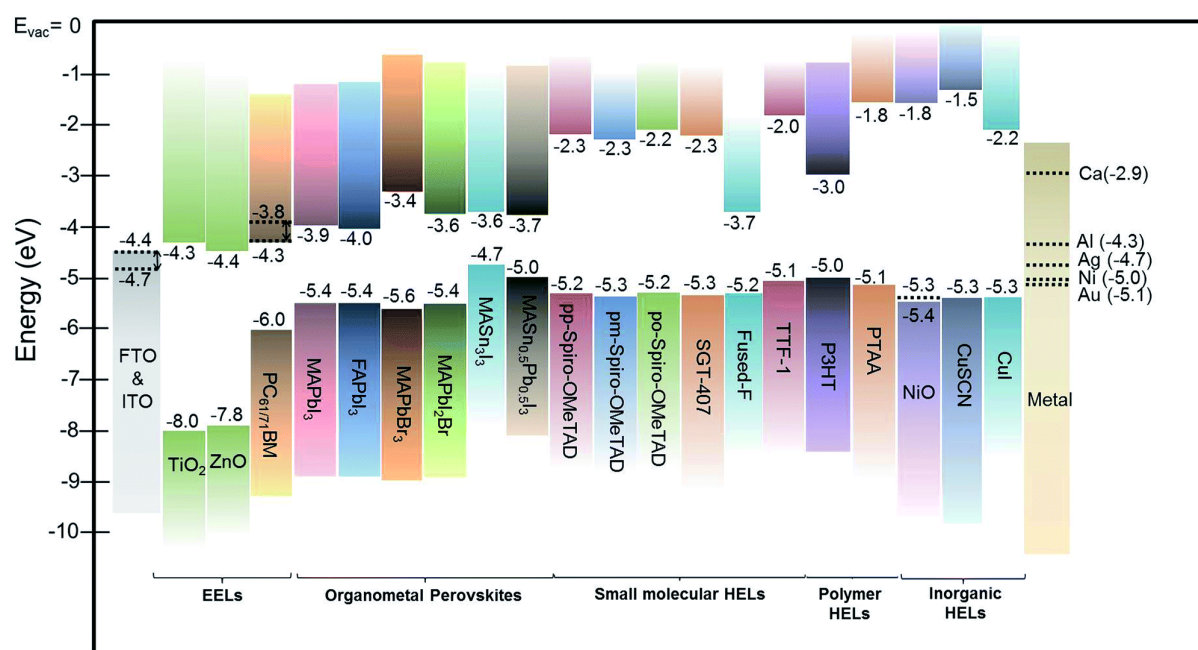
Figure 16: A summarized energy level diagram of representative organometal perovskites and charge-extraction interlayers. The dotted lines represent the WF of the materials.[27]

2.3.2 Characterization of SC

In the majority of the scientific reports, the electrical efficiency measurement serves as a pinnacle of the new PSC concept verification. Typically, the maximum power at the voltage at

which the solar cell generates its maximum power is recorded as well. The measurements are performed by performing the voltage bias sweeps with a certain step time, iteration, settling or dwell time (the time for each voltage step to stay at a certain bias) from ~0V to ~1.2V and extracting the photocurrent (I_{SC}). Because the solar cell area is limited the photocurrent density-voltage (J-V) characteristic data can be extracted. However, in order to explain the working mechanism, the equivalent circuit model of the practical SC needs to be introduced (see **Figure 17**).
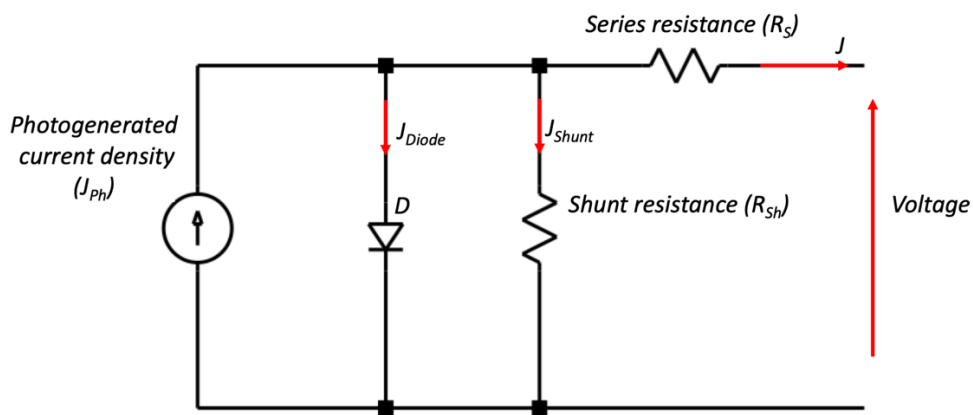
Figure 17: Circuit diagram representing the solar cell photocurrent generation known as "single diode equivalent circuit".

J_{Ph} is the photo-generated current density (area dependent), J_{Diode} is the dark saturation current density of the SC, and J_{Shunt} is the shunt resistance originated from the current leakage. It is worth noting that the Rs arises from the contact resistance between the layer-electrode interfaces. Typically the characterization test starts from the measurement under dark condition. The net current density flow through the connected load under bias voltage (V_b) is expressed by Eq.7:

$$J(V_b) = J_R(V_b) - J_{Th}(V_b) \tag{7}$$

where J_R is the recombination current density in function of the bias voltage, caused by the recombination of the diffusing minority carriers with the majority carriers. J_{Th} is the thermally

generated current caused by the drift of the minority carriers. The J_R can be also determined by Eq.8:

$$J_R(V_b) = J_{R,V_b=0} \exp \frac{eV_b}{kT} \qquad (8)$$

where k is the Boltzmann constant, T is the temperature in K. Hence, the J_{Th} is not strongly dependent on the potential barriers of the SC junction, but rather caused by the thermally generated minority carriers, and can be determined as in Eq.9:

$$J_{Th}(V_a) \cong J_{Th,V_b=0V} \qquad (9)$$

Thus, in the absence of voltage bias (V_b= 0V), it follows the relationship in Eq.10:

$$J(0) = J_R(0) - J_{Th}(0) = 0 \qquad (10)$$

Hence, the external current density is determined by Eq.11:

$$J(V_b) = J_R(V_b) - J_{Th}(V_b) = J_{sat} \left[exp \left(\frac{qV_b}{kT} \right) - 1 \right] \qquad (11)$$

where J_{sat} is the saturated current density in dark condition, that can be determined by Eq.12:

$$J_{sat} = J_{Th,V_b= 0V} = en_i^2 \left(\frac{D_P}{L_P N_D} + \frac{D_N}{L_N N_A} \right) \qquad (12)$$

where D_P,D_N are the hole and electron diffusion coefficients, respectively, N_A,N_D are the concentrations of acceptor and donor atoms, respectively, L_P,L_N are the minority carrier diffusion lengths for hole in a p-type medium and electron in a n-type medium, respectively. Therefore under the illumination, J_{Ph} depends on the electron generation rate (*eG*), and the minority carrier diffusion lengths, and follows Eq.13:

$$J_{Ph} = eG (L_P + L_N) \qquad (13)$$

The net total SC current density is effectively the superposition of the thermal-generated, photo-generated, and the recombination currents. It can be expressed by Eq.14 as:

$$J(V_b) = J_{sat}\left[exp\left(\frac{eV_b}{nkT}\right) - 1\right] - J_{Ph} \qquad (14)$$

where n is the ideality factor. Notably, the SC dark diode current uses the n instead of the Boltzmann approximation. The ideality factor defines the junction quality in respect to the type of the recombination. If the n is close to unity, then the carrier recombination in the depletion zone is negligible, meaning that the dominant current originates from the charge diffusion. The ideality factor greater than 2 represent bi-molecular recombination in the semiconductor bulk or at the interfaces.

2.3.3 Current density vs bias voltage curve

Using the externally extracted photocurrent from the PSC performance assessment, the current density (J) in function of applied bias (V) curve can be drawn. There are two types of J-V curves: the forward direction J-V curve (from no bias or slightly below 0 V), the reverse direction J-V curve (from higher voltage to 0 V (or slightly below). Both the J-V curves can be performed under dark or light conditions. In **Figure 18** the typical *J-V* characteristic is illustrated and the key components of that curve. The I cartesian quadrant is arbitrarily used for the plot, as some reports show the J-V curve in the III cartesian quadrant.
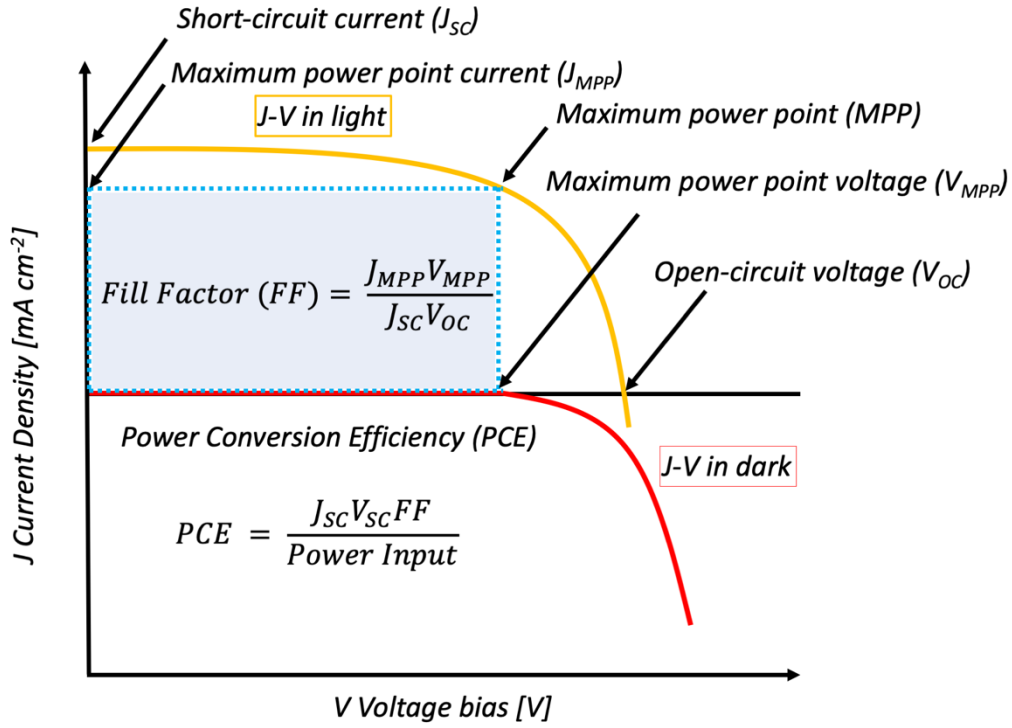
Figure 18: The current-voltage (J-V) characterization curves for photovoltaic devices. Yellow: condition called "light" when the device is subject to measurement under illumination, and Red: condition "dark" when the device is measured without illumination. The blue dotted area designates power achievable from the solar cell.

There are two distinct curves in the figure 18. The orange curve represents the *J-V* characteristics in light conditions (under illumination), and the red one characterizes SC in dark conditions (with no light at all). The open-circuit voltage (V_{OC}) is defined as the voltage level at which the SC produces no photo-current. Broadly speaking, V_{OC} of the SC originates from the splitting of the hole and electron quasi-fermi energetic levels initiated by photon, which directly defines the maximum electrical bandgap of the absorbing semiconductor. The V_{OC} is explained by the Shockley equation (Eq.15) below:

$$V_{OC} = \frac{nkT}{e}\left(\frac{J_{SC}}{J_0} + 1\right) \tag{15}$$

where the J_0 depends on the recombination mechanisms of SC. The maximum theoretical V_{OC} determines then the maximum radiative bandgap of the semiconductor. Practically, the measured V_{OC} is lower that the theoretical one, it reflects the losses of the charge recombination, imperfection of the light source or the material defect density (trap states). The J_{SC} is the photocurrent of the SC at the 0V (short-circuit), it depends on the *eG*, L_P and L_N. The eG is correlated to the absorption profile and the light spectrum, simultaneously

depending on the photon flux incident to the SC. Practically, the J_{SC} is extracted through the electrodes, at which the charge recombination can occur hindering the collection. The FF is the ratio of the maximum extracted power from the SC with specific working area and the product of the measured J_{SC} and V_{OC}. The **Figure 19** represents the idealized J-V curve with effects of two the parasitic resistances (shunt and series) which cause the performance losses.
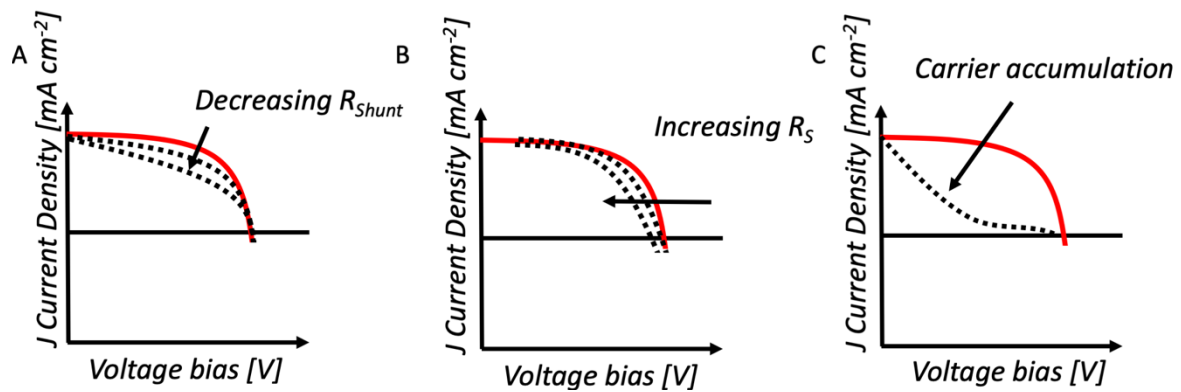
Figure 19: The J-V characteristic curve with bolstered impact of particular parasite resistance in order to visualize information of solar cell.

To a certain degree, they can be read from *J-V* characteristics, and typically they are revealed as a visible deformation of the ideal *J-V* presented in Figure 19. The first mechanism is related to the shunt resistance, that originates from material imperfections. In the *J-V* curve it occurs as the J_{SC} region slopes steeply. At certain situations the shunt resistance can form weak "hot" spots in the PSC, and cause catastrophic short-circuit, ultimately leading to the device failure.[28] The second mechanism involves the series resistance of electrodes and leads connecting the PSC, in some cases it can also reveal poor electrical contact or the measurement instrument probes. In other words, when the series resistance increases, the *J-V* curve in the neighborhood of the V_{OC} point becomes less "quadratic". Predominantly, the increase of series resistance causes the PSC to negatively impact operation, decrementing the overall PCE.[29]   The third mechanism is related to the charge carrier accumulation phenomenon at the material interfaces, and reveals, for example, information about underperformance of CTLs or electrodes.[30]

2.3.4 Characterization algorithms

The assessment of the PSC performance remains a non-trivial task, and unfortunately the lack of standards and volatile environmental conditions cause misinterpretation or errors.[31] The main sources of error in the measurements may be subdivided into a number of groups, including: an imperfect light source serving as a baseline for calculations, incorrect PSC working area definition, or wrong measurement protocol. The most comprehensive categorization would usually encompass all the parametrization aspects required for the complete and trustworthy reporting that even in case of underreporting or exaggeration could be reviewed and challenged in the form of a case study.[31]

In order to perform a correct test, a proper light source is required. As mentioned in the background paragraph, the simulated light source needs to fulfil the requirement of:

- spectral content,
- temporal stability,
- spatial uniformity.

Figure 20 illustrates how the real 1 Sun spectrum corresponds to the simulated 1 Sun spectrum:
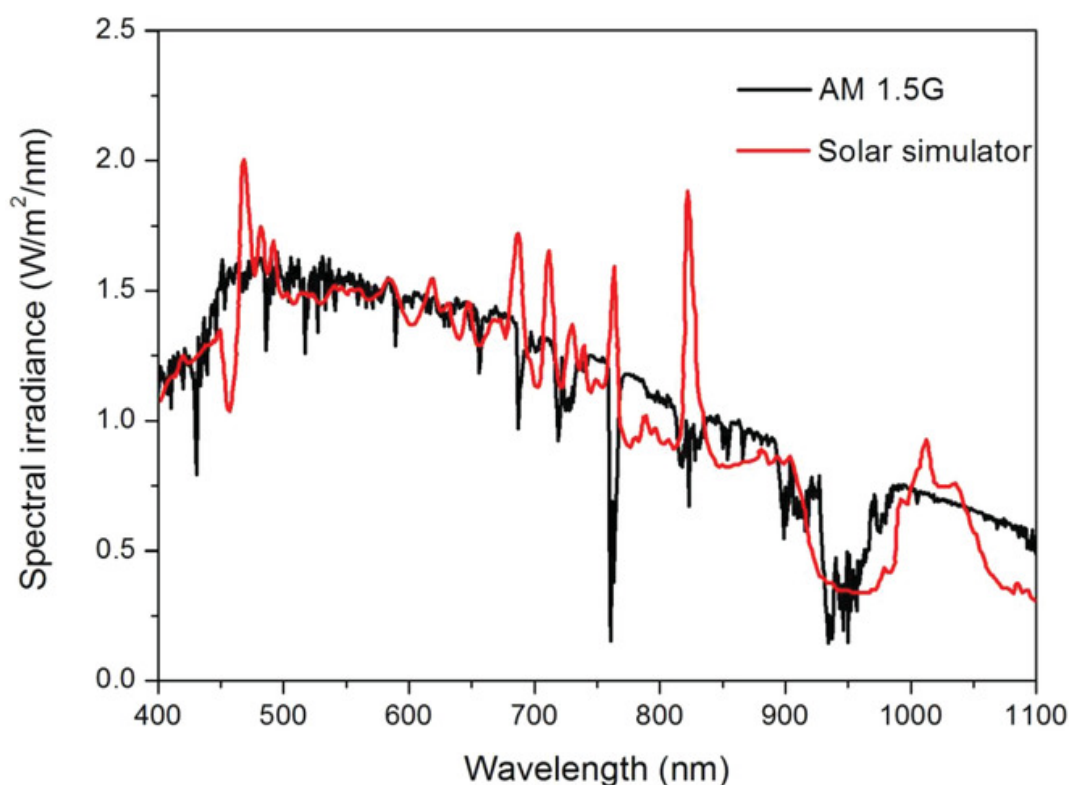
Figure 20: Spectra comparison between AM 1.5G (black curve) and a solar simulator from Wacom Electric Co. Ltd (red curve). Illustration reproduced with permission from Wiley and sons VCH.[32]

which is defined by IEC 60904-9 Edition 2 and ASTM E927-10 standard and sub-divided into certain classes of solar simulators, as shown in **Table 2**.

Table 2: Solar simulator Class defined by the IEC and ASTM.

Solar Simulator Class	Spectra match (1 – full match)	Irradiance Spectral non-uniformity	Temporal Stability
Class A	0.75 – 1.25	2 %	2 %
Class B	0.6 – 1.4	5 %	5 %
Class C	0.4 – 2.0	10 %	10 %
no Class	<0.4 or >2.0	>10 %	>10 %

Another important aspect is a correct understanding of PSC positioning under such solar simulators. There are multiple reports which do not take into account problems related to bottom transparent substrate reflections (especially if the samples are handled on

contaminated hot-plates), edge effects artificially pumping the photogenerated current in case of an absence of the shadow mask or of a non-perpendicular position of the solar cell under the solar simulator.[33] A typical light path is illustrated in **Figure 21**.
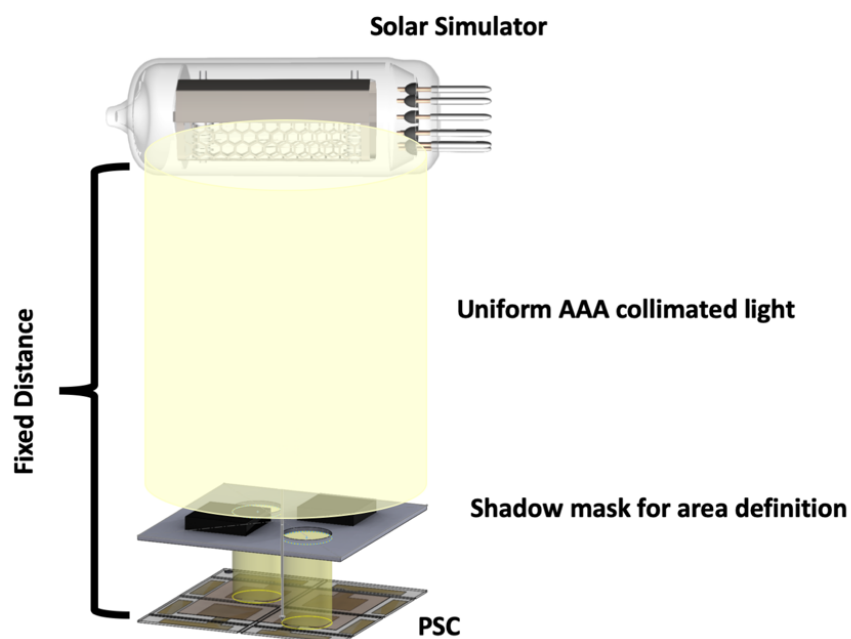
Figure 21: Illustration of the correct PSC positioning under the simulated light source. The PSC must be within the collimated light area at specific distance (illumination must be equivalent to 1 Sun), the shadow mask defines the illuminated area (purposefully there is a difference however the mask should be placed on the solar cell without any room in between.

The PSCs sample is placed under the light source and positioned within a known distance from the lamp in order to ensure that the 1 Sun illumination has the correct intensity at the perovskite film level. Importantly, the shadow mask is applied on top of the device for definition of the active area. This ensures that the photocurrent is collected from that specific PSC area, and serves as a reference area for *J-V* measurements. Importance of the shadow masks was comprehensively studied in Dye-Sensitized Solar Cells (DSSCs) and Organic Solar Cells (OSCs),[43-44] where the unmasked devices allowed to observe various edge effects causing artificial PCE improvements.

Finally, the measurement algorithm plays a crucial role. The new types of PSCs typically exhibit some degree of transient effects.[34] Some of them were discussed in the previous paragraphs, hence the *J-V* curve protocol needs to be transparent and reported each time. Unlike other technologies, PSCs must be subject to bespoke measurement protocols in order

to extract proper measurement data, which in detail means that the electrical setup needs to at least allow for:

- voltage range, direction, and step control[32]
- dwell time (also known as settling time and measurement delay)[35]

Due to such differences, there is ongoing discussion about the relevance of the *J-V* curve. Usually the argument is that the MPP is very "volatile" (see **Figure 22**), and therefore the proper time based tracking of MPP can reveal real performance.[36]
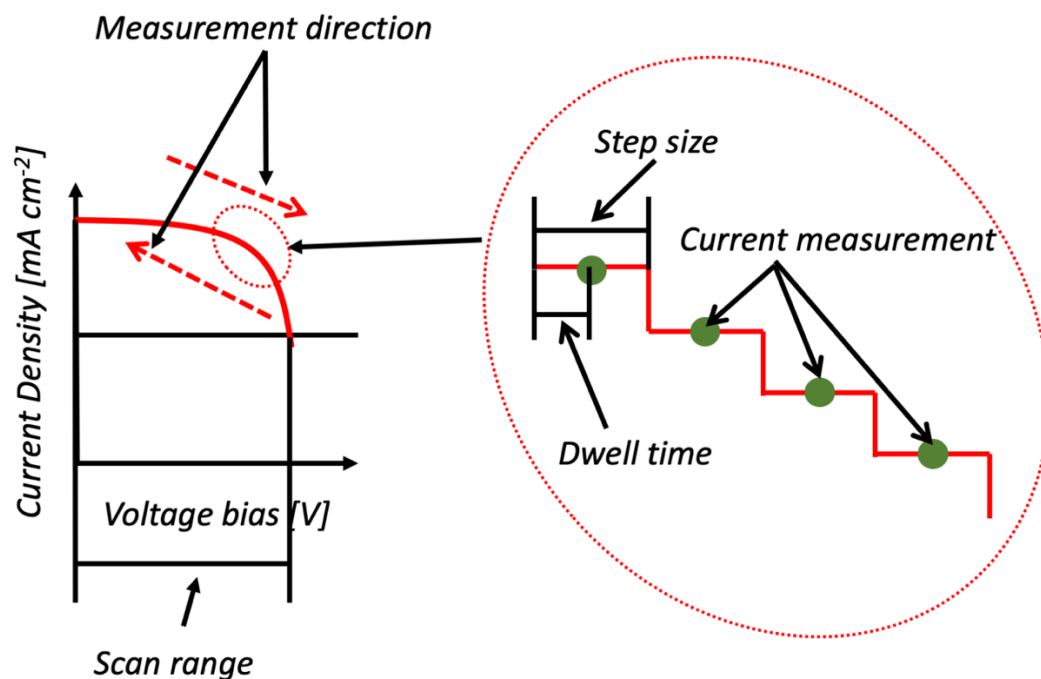
Figure 22: Bolstered J-V curve with providing the illustration of important for the correct measurement pre-sets.

Some of further problems are related to the device pre-conditioning (**see Figure 23**).[37] These activities affect the measurement outcome by simply altering the ionic structure of the perovskite crystal (for example voltage bias applied directly before the measurement (still in dark condition) can introduce ionic movement causing the extra current gain which would not exist otherwise). Another pre-conditioning method which is not often reported is called light-soaking, where the solar cell is placed (soaking under voltage bias or with no bias) under 1 Sun solar simulator for light exposure. This treatment can momentarily induce various

effects such as charging, and light-induced degradation or even cause some charge accumulation that can be immediately extracted and skew the results. Hence, the best and trustworthy approach is to track and report all the parameters related to the PSC measurements.
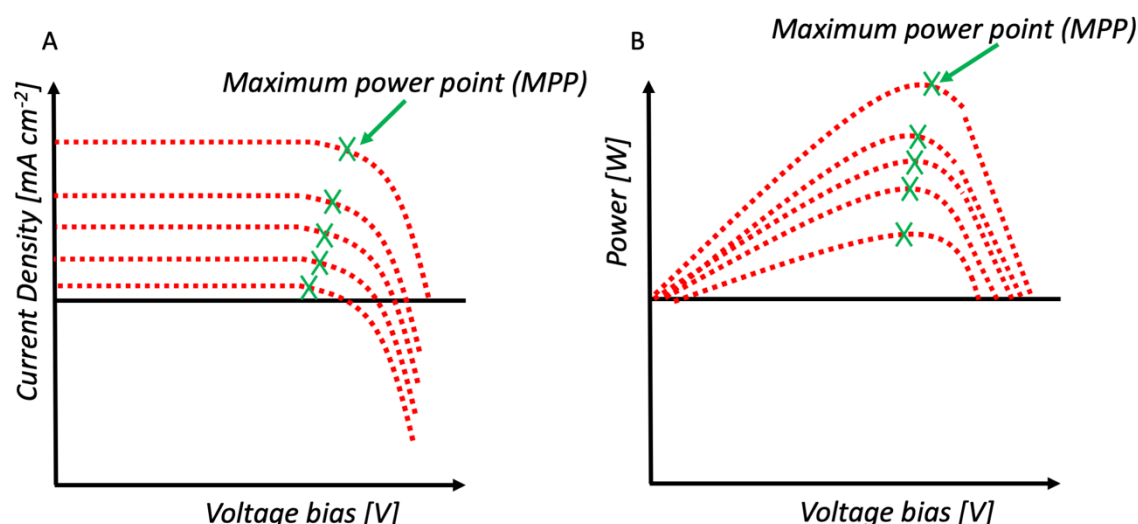
Figure 23: MPP of the PSC. A) The power point "travels" with the light intensity drop hence it can be difficult to compare the performance with multiple curves. B) The MPP in terms of the power tracking usually is considered more definite metric.

2.4 PSC stability problem

In this section, in order to provide an understanding of recent progress related to the stability issues, studies of degradation mechanisms are critically reviewed. First, the premature degradation mechanisms are introduced. Next, the work on of a new subgroup, namely low dimensional perovskites, more stable perovskites is reviewed. Finally, recent progress in stability and efficiency of the new subgroup is highlighted.

2.4.1 Premature degradation

From the very beginning of the PSC upheaval, it was relatively easy to fabricate a device that could eclipse with its performance all the PCE achievements of DSSC or OPV. However, the major limitation for PSCs is the lack of long-term stability. The technology can only be widely

adopted if it is commercially viable for investors and producers, and PSCs at the moment suffer degradation, and do not last for the PV industrial standard life-span of 25 years.

There are three major limitations intrinsic to the perovskite crystal features that cause premature degradation: thermal degradation, ion migration and water ingress. Thermal degradation is mitigated by compositional engineering, for example FA cations improve the decomposition energy threshold.

Ion migration is actually the most sophisticated degradation mechanism and can be addressed by doping the A-site ions with alkali dopant or incorporation of molecular additives. It is a sophisticated mechanism as intrinsically the multidimensional halide-metal perovskites are in fact mediums for ion migration.[38] However, this undesired effect is still avoidable or perhaps can be strongly suppressed.[39] For instance, it can be impeded by passivation of the grain boundaries, more uniform films or filling the packing density in the crystal lattice via utilization of ion substitution mechanisms. Li *et al*. improved stability of crystals by the use of crosslinking alkyl phosphonic acid ω-ammonium chlorides. Through the hydrogen bonding of the -PO(OH)$_2$ and -NH$_3^+$, terminal groups at the grain boundaries demonstrated a significant improvement of the perovskite resistance to degradation.[40]

The water ingress can be mitigated at the fabrication step by use of a dry fabrication environment or employment of anhydrous precursors. Similarly, dopant free, molecular CTLs have become a crucial development pathway for highly stable devices. Yu *et al*. demonstrated that carefully prepared CTLs with inorganic, uniform, high-quality nickel oxide (NiO$_x$) serves as a water blocking and yet functional layer that possesses superior hole mobilities.[41] After the film is fabricated, a number of encapsulation mechanisms can be introduced to avoid the moisture penetration. Remarkably, the introduction of aliphatic bulky spacer cation (for example butylammonium) in the crystal structure of perovskite allows moisture-repelling layers to be directly incorporated into the perovskite crystal. **Figure 24** shows the gradual decomposition of perovskite crystals due to the degradation mechanisms.
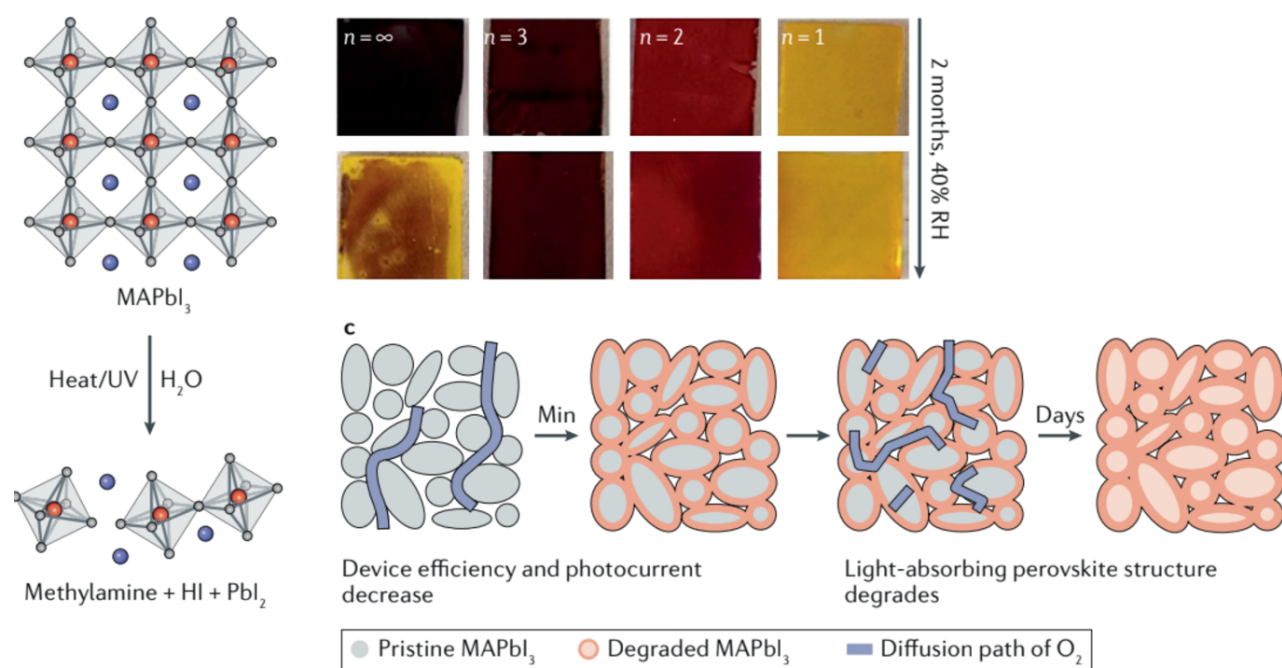
Figure 24: 3D perovskite degradation mechanism. Figure reproduced with permission from Springer Nature Review Materials[42]

Unfortunately, these problems are not easy to overcome and are often not easy to directly observe. Besides these three major problems, there exist several other material degradation mechanisms reported such as: halide originated segregation[24-27], UV-light degradation[27-28], ionic effects caused by voltage bias[29], collapse of complex organic structures,[30] and metal electrode migration induced effects.[31] Optical, crystallographic film characterization techniques or device electrical measurements may be a good indicator of the outcome of the degradation, however further visualization techniques are employed to better understand this phenomenon, and alternative materials can then be eventually tested which can elongate the device lifetime. Multiple studies demonstrated the intralayer diffusion in PSCs by using inductively couple plasma mass spectrometry (ICPMS) and depth-profiling X-ray photoelectron spectroscopy, but they do not show the time-dependent mechanism; rather they reveal the suspected outcome. Domanski *et al*. used dynamic visualizations to show that the crystal structural and optical changes are not the critical causes of the dramatic PSC performance losses, and that the CTLs and metal electrodes also have a significant impact on the overall PSC lifetime.[39] They employed time of flight secondary ion mass spectroscopy (ToF-SIMS) elemental depth profilometry to characterize the degradation mechanism at the interfaces. Their methodology visualized the ion migration and most importantly the

migration of metal into the perovskite layer, allowing them to propose use of buffer metal layer which suppressed this effect. In **Figure 25** the ToF-SIMS diffusion profiles can be seen.
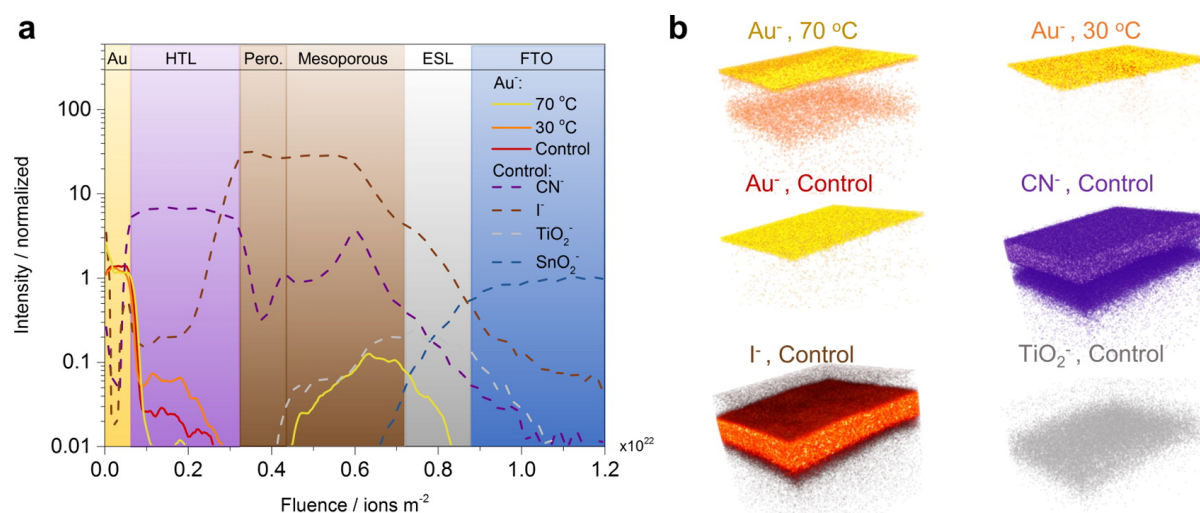
Figure 25: ToF-SIMS depth profiles of the aged PSC devices. (a) Profile showing the concentration of selected species across the control device. The profile of Au– is compared to that of the devices aged at 30 and 70 °C. (b) Reconstructed elemental 3D maps for the ions traced in the depth profile. The xy dimensions of the analyzed area are 10 × 10 μm. Reproduced with permission from RSC[39].

In summary, it is clear that premature degradation of perovskites causes a significant barrier for this technology. While some causes of decomposition are easily mitigated through better fabrication, there are still inherent issues that can be overcome using better perovskites, CTL materials, substrates or electrodes.

2.4.2 Low dimensionality for stable perovskite

In an exciting step forward for this emerging PV technology, studies of quasi-2D perovskites have reported great improvements in previously hindered stability. As briefly indicated above, the highly efficient, three-dimensional organic-inorganic perovskites with n numbers -> ∞ are unstable. However, the incorporation of bulky spacer cations into the perovskite structure allows perovskites to form more stable, quasi-two-dimensional (quasi-2D) layered perovskites. Compared with the typical ABX_3 structures, the quasi-2D perovskites are a preeminent group of semiconductors with a similar tunability of photophysical properties, high power conversion and marketable stability.[43] Unlike in the traditional perovskite counterparts, the employment of both hydrophobic and functional spacer cations effectively

isolates the perovskite crystals from water, simultaneously forming a exciton dense quantum-well superlattices. There are two subgroups of the quasi-2D perovskites: Ruddlesden-Popper (RP) which typically contain monovalent organic cations and allow for the staggered arrangement. The alternating inorganic layers of $[BX_6]^{4-}$ are shifted along the *ab-plane* with ((1/2),(1/2)) displacement, whereas the organic cation forms the alternating spacers,[44] and Dion-Jacobson (DJ) perovskites which have a divalent organic cations which do not form staggered structures, but rather eclipsed arrangements of inorganic halide layers without the displacement of $[BX_6]^{4-}$ groups.[45] Additionally, there are a number of the derivative material-specific quasi-2D perovskite subgroups distinguished; for example alternating cations in the interlayer space (ACI)[46] or the alkyl diammonium cations (ADC).[47] However, both ACI and ADC are usually referred as part of the RP or the DJ family.

The main structural differences between traditional ABX$_3$ are exhibited in the crystal formation and the type of the bulky cation in RP and DJ. The crystal structures can be described as in the Eq.16-17:

$$RP: R'_2 R_{n-1} B_n X_{3n+1} \tag{16}$$

$$DJ: R' R_{n-1} B_n X_{3n+1} \tag{17}$$

where R is the bulky monovalent spacer cation, and R' is the bulky monovalent or divalent spacer cation. In **Figure 26** a typical crystal structure of DJ and RP perovskites is presented.
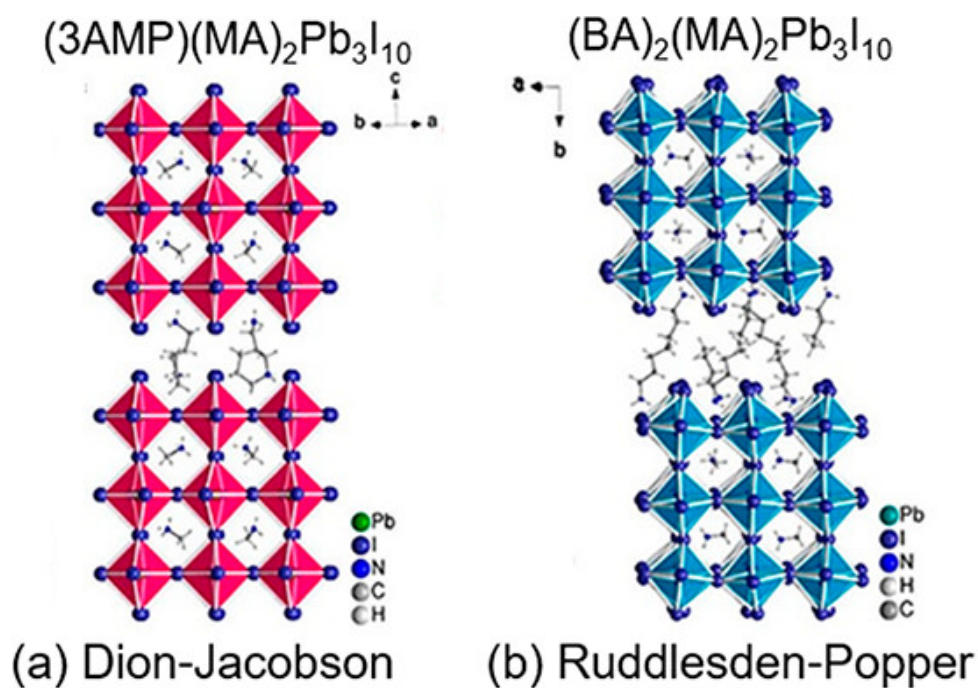
Figure 26: Crystal structural of typical (a) Dion–Jacobson, (b) Ruddlesden–Popper. Reproduced with permission from ACS.[48]

2.4.3 Quasi-2D perovskite tunability

In addition to the significant advantage that the quasi-2D perovskites have in solving stability issues, such a low-dimensional crystal construction provides many more benefits. The first advantage, the *GTF* limitation of ABX_3 is "relaxed" allowing for a multitude of new compositions. This structural flexibility allows for the exploration through material compositional engineering. For instance, the n-number relationship between the dimension and photo-properties brings in another degree of freedom in terms of tunability. The quasi-2D structures exhibit similar to the ABX_3 feature and property tunability. For example, quasi-2D perovskites are subject of intensive bandgap engineering,[49] exciton binding energy and dynamics modulation,[50] charge carrier transport and electron-photon coupling modifications,[51] and dielectric constant variation.[52] In **Figure 27** some of the potential benefits are shown such as (a) stepwise absorption onset tunability, (b) band gap energy level engineering prospects, (c) layered crystal structure realization, and (d) organized charge transport pathways.
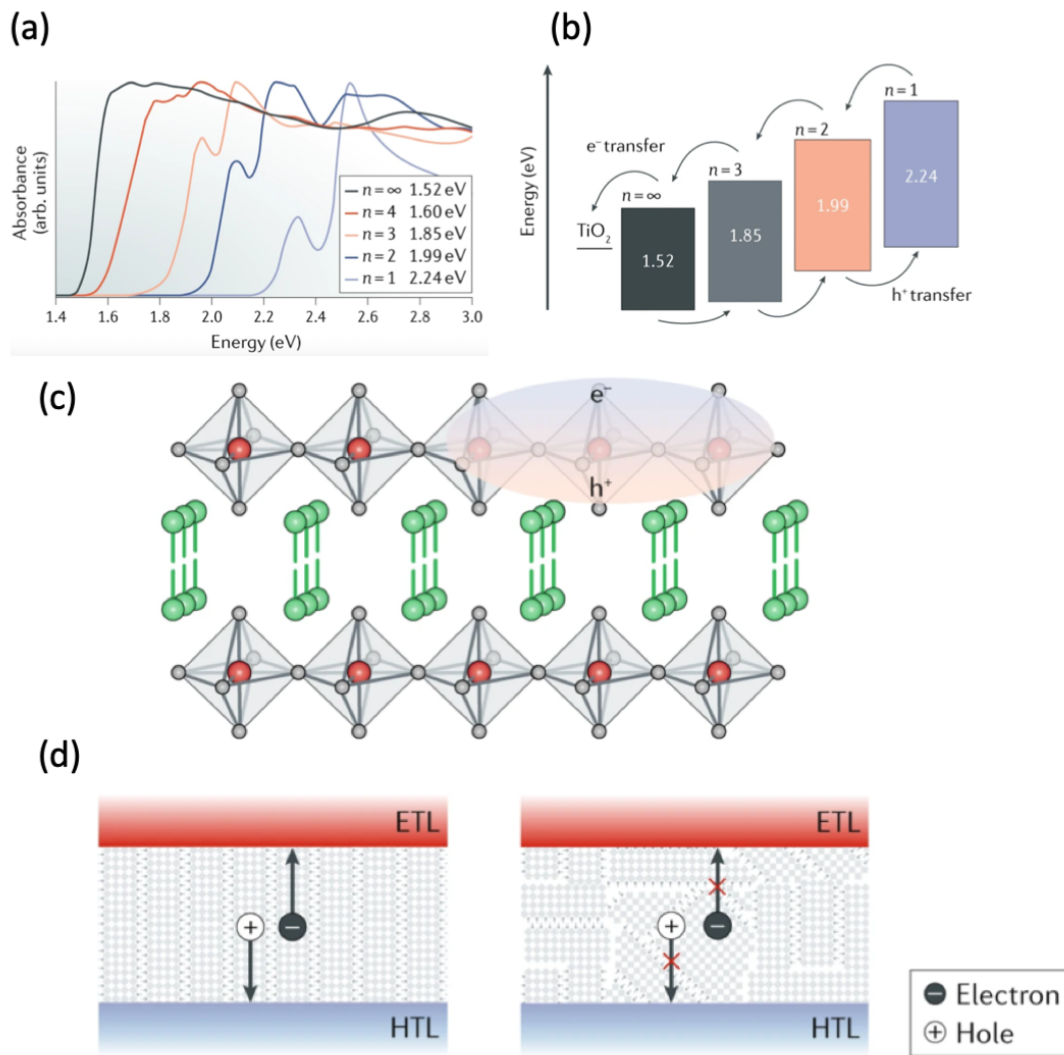
Figure 27: (a) Absorption of low dimensionality perovskites (where n is the number of perovskite layers following $R_2MA_{n-1}Pb_nI_{3n+1}$. (b) Energy levels and bandgaps of the $R_2MA_{n-1}Pb_nI_{3n+1}$ perovskites with different n. The electron-transfer and hole-transfer pathways are depicted. The conduction band minimum for TiO_2 is also shown. (c) Structure of a 2D perovskite highlighting the exciton (electron–hole pair). (d) With vertical stacking (left), charges are transported through the inorganic planes to the electron-transport layer (ETL) and hole-transport layer (HTL). With a random and horizontally oriented perovskite structure (right), there is not a direct pathway for charge transport to the ETL and HTL. Illustrations reproduced with permission of Springer Nature.[42]

Thus, the discovery of highly tuneable quasi-2D perovskites has provided great opportunity for the development of commercialization-ready candidates with precisely engineered, desired properties.

2.4.4 Quasi-2D perovskite PSC application

The employment of low dimensional perovskite in devices has also been successful and provided a new promise towards the stable and efficient perovskite PV. Analogically to the ABX$_3$, the quasi-2D perovskites began from the low efficiency prototypes and over the years of intensive research their current record PCE (> 20%) is commercially viable. In 2014 Smith *et al*. and in 2015 Cao et al. reported PSCs with a PCE of a little over 4%, whereas only a year later in 2016, Tsai *et al*. reported a PCE of 12.52% in an hysteresis-free device. In 2020 Lian *et al*. presented co-evaporated devices with PCE above 18%,[53] and in 2021 Lai *et al*. employed fluorinated benzylammonium iodide as bulky cation spacer achieving a PCE of 20.12%.[53] Despite the overall PCE lower than the ABX$_3$, the long-term power output typically doubles the maximal one achieved with the traditional perovskites. In the **Figure 28** the PSC realized only with quasi-2D perovskite material can be seen.

Figure 28: Fully quasi-2D PSC. (a) Inverted (p-i-n) PSC structure, (b) cross-sectional SEM image of the PSC, typically the quasi-2D perovskites have 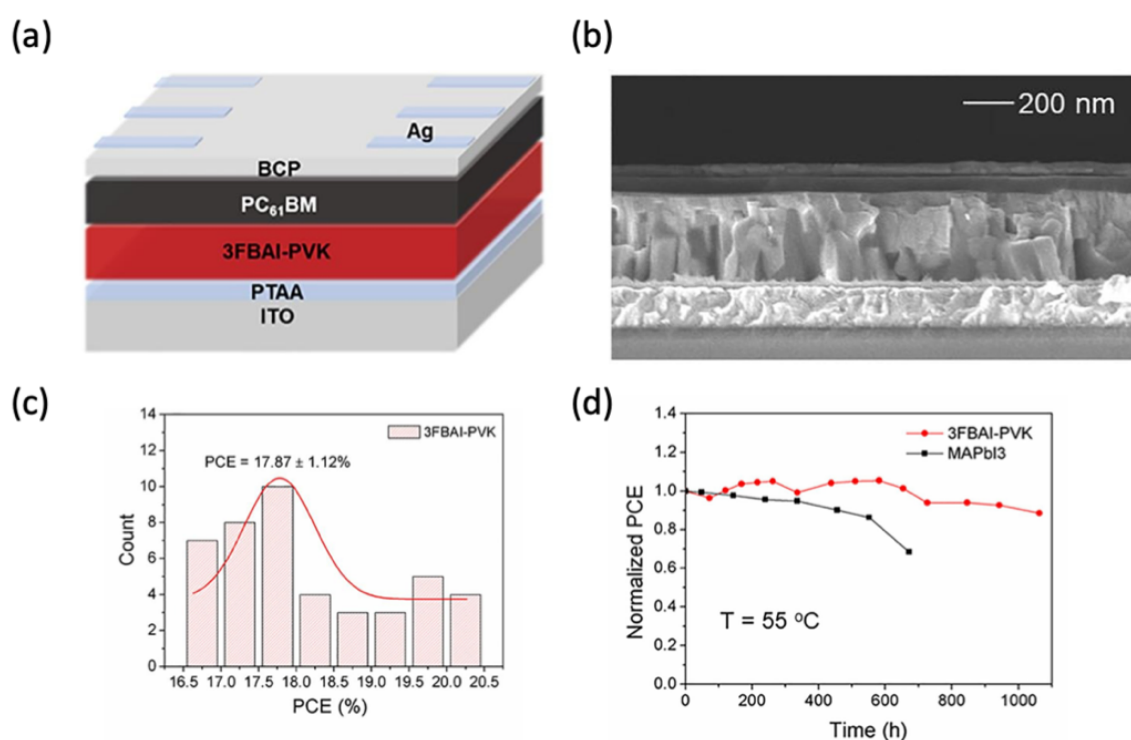elongated grains, (c) distribution of PCE in the Lai et al. study, and (d) long-term comparison of the traditional ABX$_3$ perovskite and quasi-2D. Images reproduced with permission of Elsevier.[54]

Thus, low dimensional quasi-2D perovskites due to low hole-electron recombination rate, high absorption coefficients, strong photoluminescence, and superior stability are regarded as next-generation perovskites. In order to fully take advantage of that new perovskite subgroup, large scale, accurate and reproducible combinatorial screening is urgently required.

2.5 Compositional exploration of perovskites

In this paragraph, a recent developments related to perovskite compositional material discovery are critically reviewed. Firstly, the idea of iterative compositional screening is described. Secondly, the compositional screening is divided into the chemical composition search, morphological exploration and performance studies. Next, the combinatorial high-throughput discovery through automated compositional screening is introduced. Finally, the potential of prediction, computational search and importance of database generation and feedback for further improvements are outlined.

2.5.1 Material library generation

A number of studies have investigated the composition of perovskites. These studies can be grouped as studies into metal halide perovskite crystals, architectures of perovskite employment in devices, stability testing or various additives impact investigations. However, as described previously unlike the other PV materials, perovskites are highly tuneable. The traditional methyl ammonium lead iodide ($CH_2NH_3PbI_3$) can be altered and mixed in myriad ways. Remarkably, it turned out that the pure $CH_2NH_3PbI_3$ is not the best perovskite candidate. Multiple studies have shown that the mixed-halide perovskites can have significantly better the results. For example, the full or partial replacement of methyl ammonium (MA) with formamidinium (FA), or iodide (I) with bromide (Br) allows perovskites to form with different bandgaps and film morphologies. Often caesium (Cs) or rubidium (Rb) are incorporated for better stability, efficiency and material properties. The iodide can be

replaced with halides other than Br, for example chloride (Cl) which was found to improve the crystal grain sizes. Hence, compositional changes have been reported to greatly improve crystallographic properties, emissions and absorptions. Jacobsson *et al.*[55] found that small changes in the material composition also have a large effect on the device performance. They investigated the exchange of small amounts of iodide to bromide, and MA to FA creating the compositional space shown in **Figure 29**.
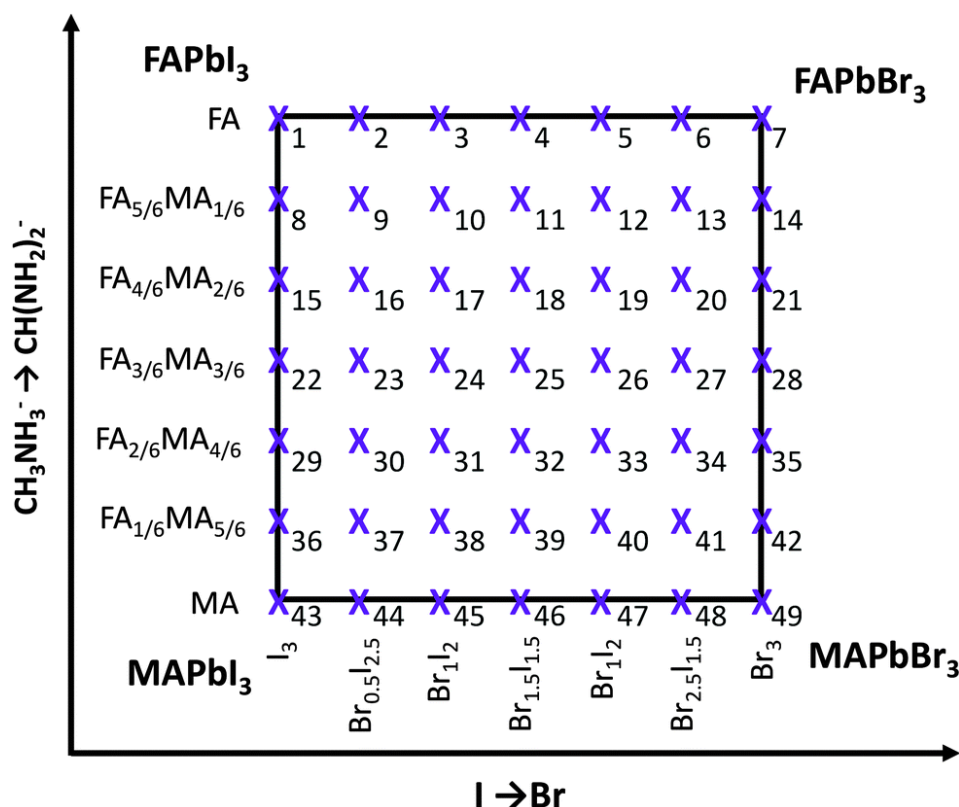
Figure 29: A graphical illustration of the compositional matrix with markings for all the compositions explored. The numbers next to the crosses represent the key between the intended perovskite compositions and sample numbers. Reproduced with permission from RSC.[55]

2.5.2 Perovskite crystal property tunability

As elaborated above, the compositional change can simultaneously involve variations in the organic ions and halides. Hence, the investigation of mixed perovskites can provide detailed information of new, never discovered materials. Fortunately, the "small-step" composition variation allowed for predictable to certain degree crystal properties. For example, in their

study Jacobsson *et al*. discovered efficient compositions, yet never previously reported that then served as a great starting point for other researchers to even further reduce step-size or modify some of the variations. Screenings of the optoelectronic properties are important in optimizing further device efficiency, and allow the search for the highest performing devices to be narrowed down and accelerated. It comes from the simple fact that film or crystal characterization requires significantly less effort than the complete device screening. For example Jacobsson *et al*. demonstrated that higher Br participation resulted in the bandgap increase, without depending on the MA or FA percentage. They reported that the Br rich perovskites turned out have narrower excitonic peak, corresponding to higher binding energy and that the organic cations have lesser impact on the bandgap than the inorganic halides. The trends are presented in **Figure 30** a-c. Furthermore, the new perovskites need the determination of their bandgaps from the light absorption point of view. For most direct bandgap semiconductors, the square of the absorption forms a linear function of the photon energy. Hence, the band gap energy can be approximated from the absorption onsets, and corresponds directly to the device V_{OC} trends. Thus the compositional studies provide great insights into the evolution of these properties, and allow the excitonic energy offsets (usually couple of meV) to be visualized, usually unnoticed in the devices. Further, it was found reference that the energy increase is strongly exhibited with halide exchange, but completely independent to the organic ions ratio, see Figure 30 d-f. That exploration of perovskites with a small compositional changes also allows crystal properties to be correlated with device performance. For instance, low performance was found to be strongly correlated to strong sub-bandgap photoemission. It was indicated by Friend *et al.* and Hoke *et al.* that such behavior can indicate the perovskite phase separation.[56-57] Also, in these studies it was observed that for example FA-based perovskites with halide variations, the two photoluminescence peaks representing two phases after some time merge into one. This observation allows potential stability problems related to ion diffusion and phase segregation to be pinpointed. Remarkably, such phase segregation mechanisms were also attributed by them to performance limiting recombination centers. Hence, the evolution of such curves that are shown in Figure 30 g-I can point to the compositions that have potential for improvement or should be avoided.
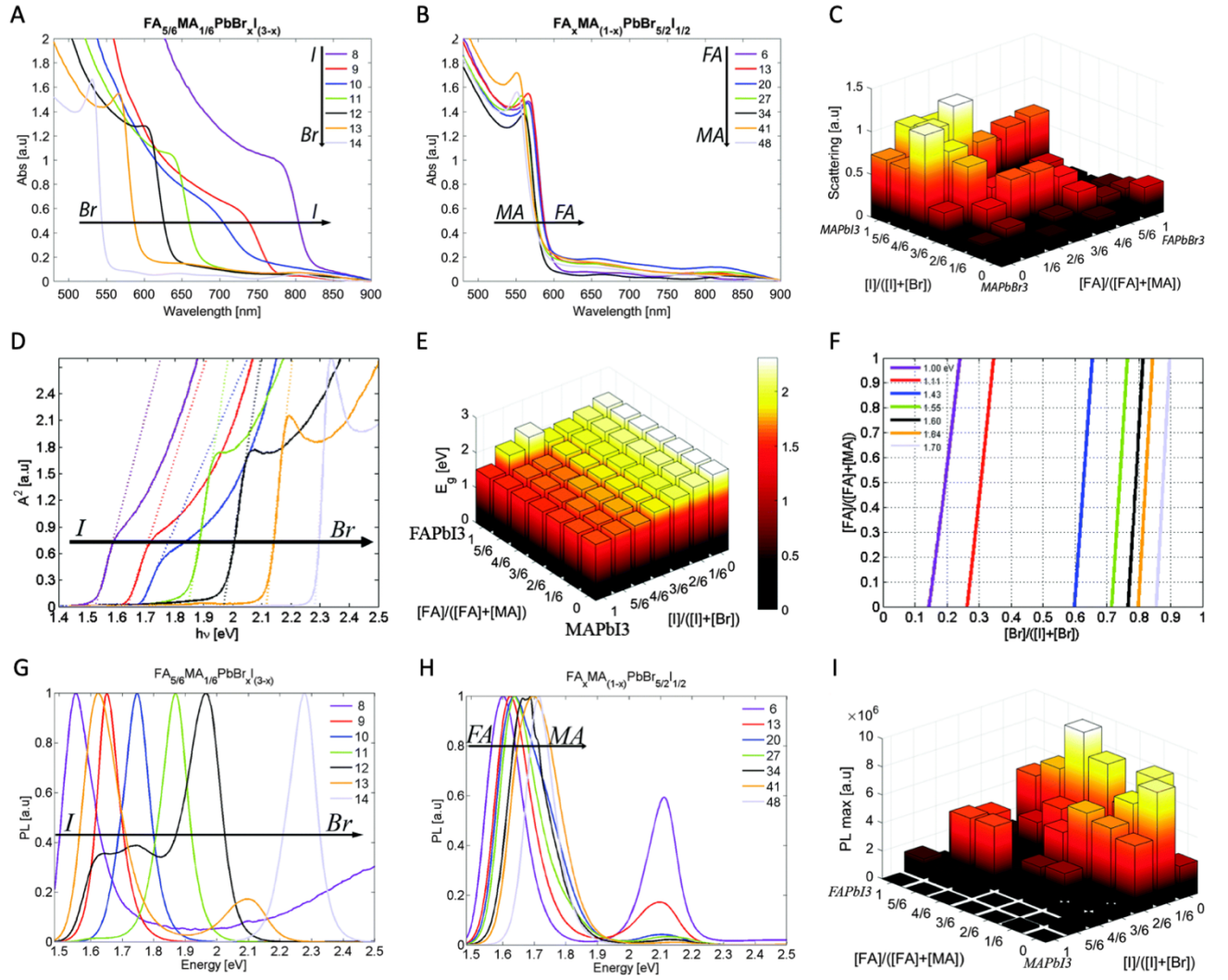
Figure 30: Measurements corresponding to compositional map presented in Figure 24. (a) Optical absorption as a function of wavelength for a subset of the samples, corresponding to samples 8–14, FA$_{5/6}$MA$_{1/6}$PbBr$_x$I$_{(3-x)}$ where the I/Br-ratio is changed. The background due to scattering is removed. (b). Absorption for the subset of samples corresponding to FA$_x$MA$_{1-x}$PbBr$_{5/2}$I$_{1/2}$ where the MA/FA-ratio was changed. (c) The height of the background in the absorption measurements as a function of composition. (d) Illustration of band gap determination for samples 15–21 which goes from no bromide to only bromide. (e) A bar plot of the band gaps in the compositional space explored. (f) Illustration of where in the explored compositional space the ideal band gap for a top cell is found with respect to the band gaps of several possible bottom cells. (g) Normalized PL spectra while the iodine/bromide ratio is changed. (h) Normalized PL spectra while the FA/MA ratio is changed. (i) Maximum emission intensity as a function of composition. Reproduced with permission of RSC.[55]

2.5.3 Morphological exploration

The morphological impact of the perovskite film directly defines the device performance, so there have been a number of investigations into the effect of the morphology of perovskites. Effectively the PSC can be viewed as a large heterojunction. The perovskite film typically infiltrates the CTL, ultimately acting as an embedded light absorber and photo-charge generating medium. As early as in 2013, Eperon *et al.* investigated the impact of morphological control on the performance in solution-processed planar heterojunction PSCs.[58] They found multiple correlations between the film quality and the resulting device performance. For instance, if the perovskite film is blemished with pin-holes, the light will pass right through without being absorbed, thus lowering the overall available photocurrent. Also if the perovskite film has nonuniform coverage, the ETL and HTL can effectively connect to each other without the perovskite causing shunt paths that cause local increase of charge recombination locales (so-called hot-spots). Each of the hot-spots mimics a parallel diode, that locally lowers FF and V_{OC}. Ultimately, this leads to electrical and light induced degradation of the device. Hence, poorly made perovskite film can result in very low efficiency devices despite the presence of perovskite films having promising optoelectronic properties. For compositional screening of new perovskites, it is important to find a way to successfully optimize the resulting perovskite films. McMeekin *et al.*[59] investigated tunability of colloidal precursor solutions for FA-Cs mixed-cation lead halide perovskites. They found that by adding hydrohalic acids the colloids present in $[HC(NH_2)_2]_{0.83}Cs_{0.17}Pb(Br_{0.2}I_{0.8})_3$ can be further dissolved. This increased the nucleation site concentration causing the growth of highly ordered, textured perovskite films allowing for crystal micro-strain reduction and increase in charge-carrier mobilities to > 20 $cm^2V^{-1}s^{-1}$. Solvent engineering has also been reported to provide morphological control of perovskite films, ultimately enabling the development of specialized blends for new types of perovskites which facilitate growth of good quality films. In the case of the compositional screening it would be crucial to develop a blend that allows for highly versatile film formation, as it can be seen in **Figure 31** that the organic cation and halide manipulation drastically impacts the morphology.
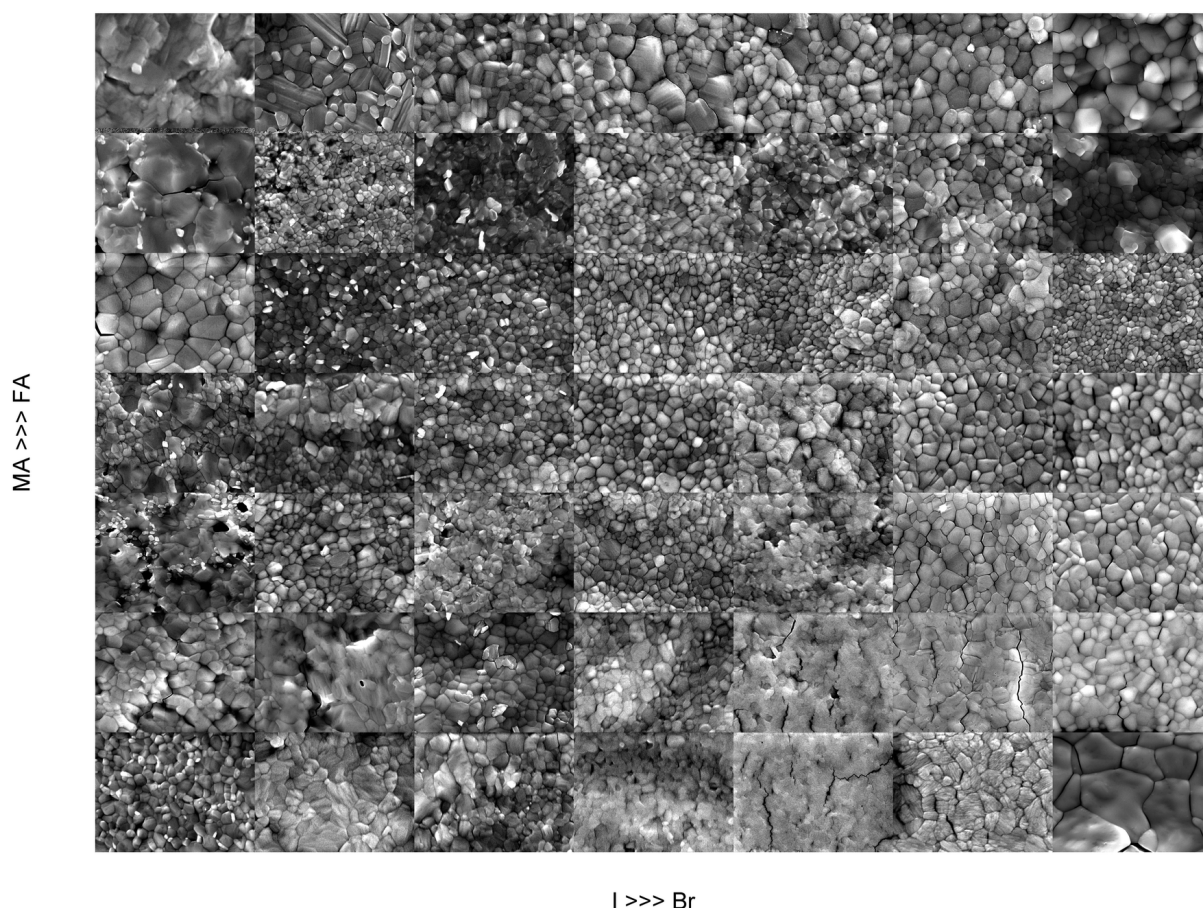
Figure 31: SEM images of the $FA_xMA_{(x-1)}Pb(I_xBr_{(x-1)})_3$ films of different compositions. The panels are in the same order as in the samples in Fig. 24. The width of each sub-panel is 3.9 μm. The composition for the best device corresponds to the panel that is second from the left in the third row from the top. Reproduced with permission from RSC.[55]

2.5.4 Compositional space of device performance

As it was explained in previous paragraphs, the optoelectronic properties of the films or crystals correspond to the PSC device performance. A compositional set of optoelectronic or morphological data can be obtained to estimate the impact of certain modifications on the resulting PSC performance. The compositional engineering does not need to be limited only to particular material variation e.g. mixed-halide perovskite ratios. There are studies which reflect on the fabrication environmental impacts, for instance the fabrication of a range of samples in function of temperature or humidity. Other studies present the impact on the PSC performance in compositional spaces in function of the precursor solution molarity,[60] perovskite film thicknesses,[61] post-treatment,[62] additives,[63] electrode type,[64] substrate type,[65] and many other possible variants. The most important rule for this studies is to control

the iterations and to fix all the conditions. From the analyzed samples, the evolution patterns can be distinguished. Those usually serve as a good indication for follow up studies. Further analysis of certain impacts or behaviors allow possible drawbacks to be determined or improved. The linear or convex patterns in perovskite performance compositional spaces have been observed in many cases, which is very promising and allows conclusions to be drawn. It is worth noting that the accurate control of external conditions whilst preparing such performance compositional spaces allow the physical origins of the degradation processes to be determined. In **Figure 32** the compositional space of gradual organic cation and halide exchange is presented.
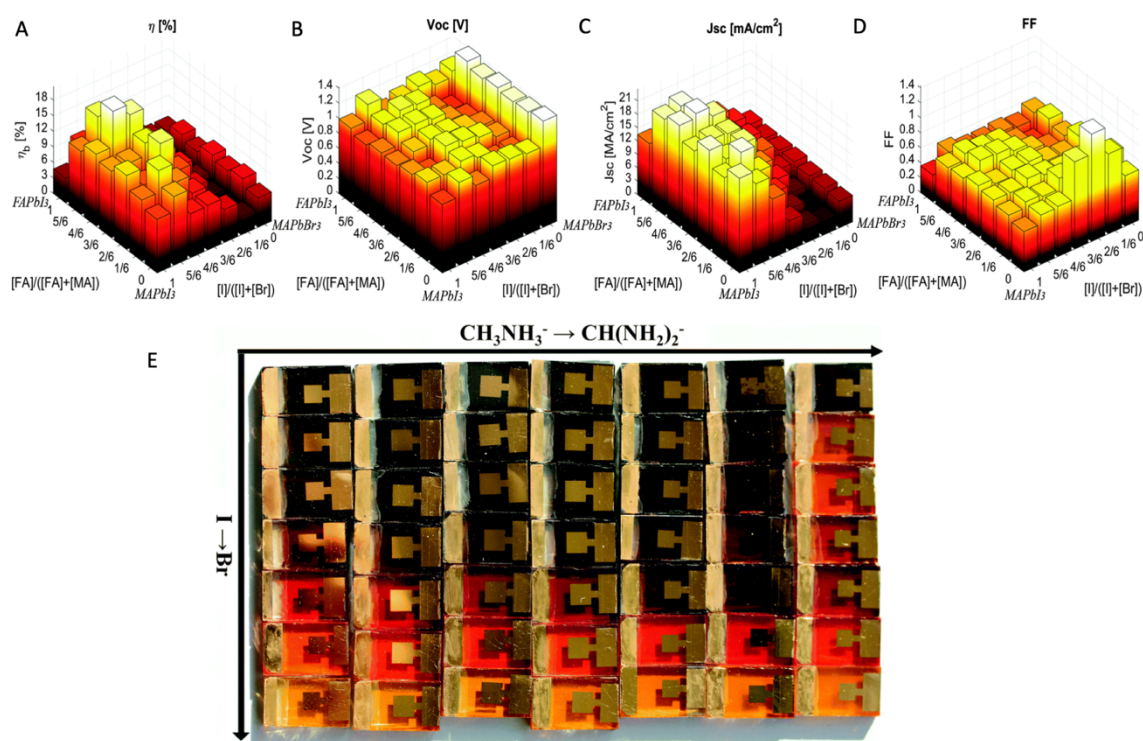
Figure 32: Device parameters for cells of different compositions in space of $FA_xMA_{(x-1)}Pb(I_xBr_{(x-1)})_3$. (a) η; (b) Voc; (c) Jsc; and (d) FF. (e) refers to the map from Figure 29. Reproduced with permission from RSC.

2.5.5 Combinatorial high-throughput methodologies for perovskite solar cell materials discovery

As reviewed previously in recent years, the number of perovskite-related peer-reviewed projects has reached an unprecedented level. The research community has realized that even more can be done to advance the technology, but this will require significantly more

resources, "labor" and time. Therefore, given this increase in resource requirement, advances will be best made by replacing predominantly manual methods with an automated approach that creates the potential for combinatorial high-throughput (cHTR) screening combined with direct data feedback analysis. Thanks to significantly reduced time and costs, the automatization of research tools has recently gained significant attention. As described in the Introduction to PSC paragraph, the multiparameter perovskite system is a perfect candidate for bespoke screening approaches. The traditional approach, where a researcher fabricates small samples across multiple processes can significantly slow down and hamper PV discovery due to unavoidable anthropogenic errors. The ultimate setback is caused by omitting certain experiments due to lack of time. Another problem arises from untraceable or irreproducible fabrication protocols; research reporting without great detail causes multiple errors in follow up studies, which in the worst case can even divert the focus to a potentially incorrect pathway. Hence, the proposition of accelerated, quantitative, and versatile sample prediction, production, and data extraction is critical to advancing this field of research.

cHTR techniques can ensure the optimal (or even maximal) progress in PV and explore ultimately the entire parameter space of metal halide PSCs. With hypothetically millions of formulas for "optimum candidate" and in light of possibly hundreds of investigation groups across the world working on the PSC, a significant amount of time and resources can be saved. Moreover, the quality of the data and inter-research group data exchange can be improved to further push the discovery status and ultimately provide a state-of-art recipes segregated in the outcome library. **Figure 33** shows how cHTR technique converges towards discovery.
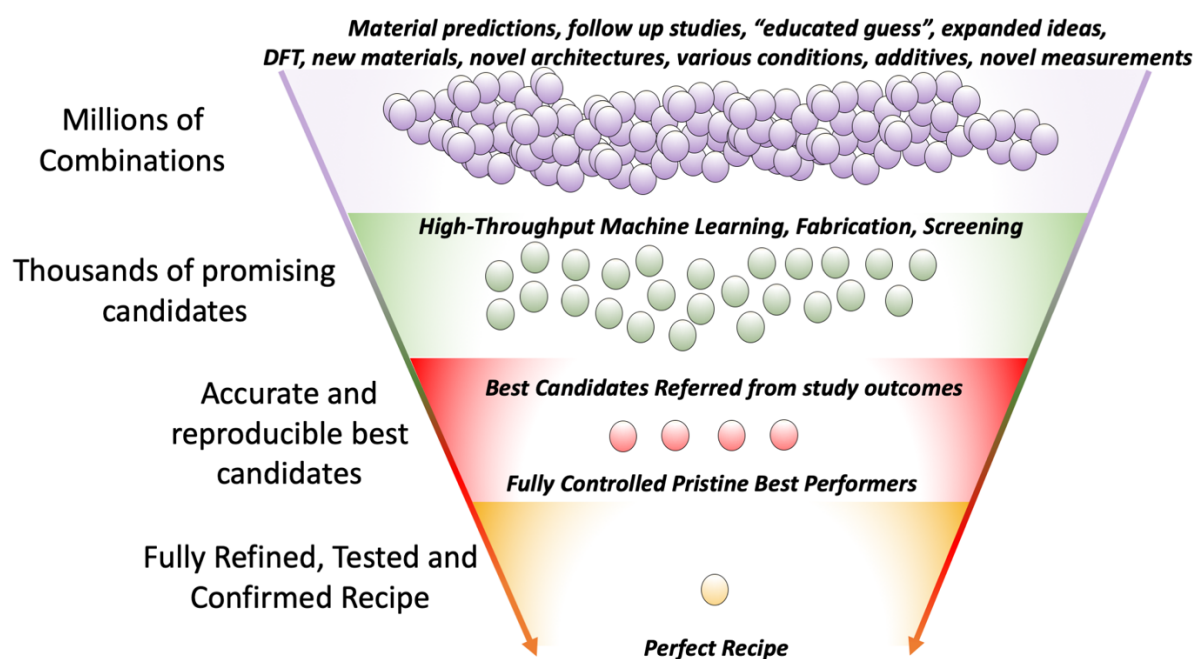
Figure 33: Motivation behind the High-Throughput Perovskite Materials Discovery – the amount of potential perovskites, time and money required to research and find perfect candidate usual "perovskite topic" continues its sky-rocketing rise, however the number of commercially viable and broadly available product "Perovskite Solar Panel" as of beginning of 2021 is equal to 0.[66]

The productivity of research resources plays a key role in the discovery processes. Most researchers start from reading corresponding history, literature and begin their own journey towards their first "home-made" PSC. The evident problem lays in the amount of relevant literature, which currently exceeds approximately 3000 PSCs-related publications. Moreover, such reporting can cause overlapping research or competition called "onion" research.[4] It results in an average of ~10 new "perovskite" publications per day which is not a rate that can be "consumed" with a manual research methodology. Moreover, it is impossible to reproduce or replicate most studies and hence upheaval in publication output may counter the progress in PV.[5]

2.5.6 Prediction of new perovskite compositions

As it was mentioned in previous paragraph – the productivity in view of myriad of compositions plays a great role in perovskite study. The concept of new PSC or new materials aiding PSC performance (for example substrates, CTLs, or electrodes) usually originates from pre-existing studies (especially if a significant gap in knowledge has been identified).[6] There were very few unprecedented breakthroughs in the form of an idea that has never been tested before. Overall, significant advances in perovskite technology have evolved through the advancements.[7] Importantly, perovskite research field has already matured enough to not report novel, unverified,[8] or erroneous achievements[9-10] so eager as during the first years the study[11-12], enforcing the rule that the progress requires verifiable proof. Hence, the vital question is what will be the result of a particular composition/fabrication/additive/mixture employed in a PSC (or derived to other utilizations of perovskite), or simply where to start the new PSC developments to maximize the progress. The two most promising ways to find new PSCs come from the density functional theory (DFT) and the use of Machine Learning (ML) models. Ultimately, the outcomes of DFT or ML can be justified in terms of accuracy via synthetic routes. These approaches are outlined in the following subsections. **Figure 34** shows the "educated guesses" for possible new PSCs originating from existing literature harnessed with machine learning (ML) prediction. It presents compatible A- and B-site cations with a number of theoretically formable perovskites likely to work as PSCs.

Figure 34: Considered to be a High-Throughput methodology: Machine learning estimation (based on literature and gathered so far knowledge about perovskite) of number of formable perovskites (without counting the variation caused by different CTLs, fabrication processes or conditions, electrodes, additives or mixed-perovskites (at various proportions). If there are millions of available perovskites, the number of unverified or unknown yet stable and efficient perovskite solar cell ready materials can be infinitely high. Image reproduced under permission from ACS.[67]

2.5.6.1 Density functional theory for perovskites

As indicated in previous paragraph the potential number of known ABX_3 variations not considering the halide ions, indicates hundreds of thousands of possibilities just for the active material selection. In addition, since the perovskite crystal can perform differently and depends on hundreds of factors, there is a near infinite number of combinations. Despite

these ML predictions, the standard approach in research remained as manual sample fabrication, characterization and analysis. Typically, the researcher is able to formulate and test only a few new concepts over months or even years.[14] Extraction of meaningful statistical results from carefully prepared batches of solar cells remains tedious and erroneous. Often, these results end up forgotten in the stack of new publications and only a few potential candidates may gather enough attention to be noted and improved upon.[15] Interestingly, due to the recent publication count and widely accessible material study outcomes, advanced computational studies may play a pivotal role in the future of PSC technology. Computer-aided density functional theory (DFT) simulations provide an effective approach to analyze the physical mechanics of the perovskites. These simulations can potentially resolve multiple electronic and optoelectronic properties, and their results could be used to investigate the causes of defects or underperformance. In addition, such simulations greatly aid the design of new perovskite structures clearly aimed at high-efficiency and stable solar cells. There are multiple reports presenting van der Waals corrections (vdWs), crystal structure, electronic properties, or spin-orbital couplings (SOCs) essential for further enhancement of density functional theory (DFT) computations.[16] Usually extracted from classical, laboratory-based-outcomes, the sources of defects in perovskites allow for determination of the electron-hole diffusion path and length. Other reports provide a great starting point and correlation relationship between V_{oc} and bandgap.[17] DFT studies create the possibility of testing and verifying different defects in order to computationally tune features of perovskite crystals. They provide a fast way to test the potential of various chemical compositions and indicate potential candidates. The ferroelectric domains in perovskite crystals play a key role in further improving their PV properties, while charged perovskite domain walls (p-type and n-type) serve as segregated pathways for the motion of carriers. The compositional screening data serves as a fantastic canvas for the DFT refinements that can significantly reduce time and resources required for discovery. Hence, the synergy between laboratory-based results and computational studies can flourish pushing the progress even further. **Figure 35** presents an example of the DFT discovery protocols based on metal halide perovskite molecular behavior extracted from previous experimental studies.
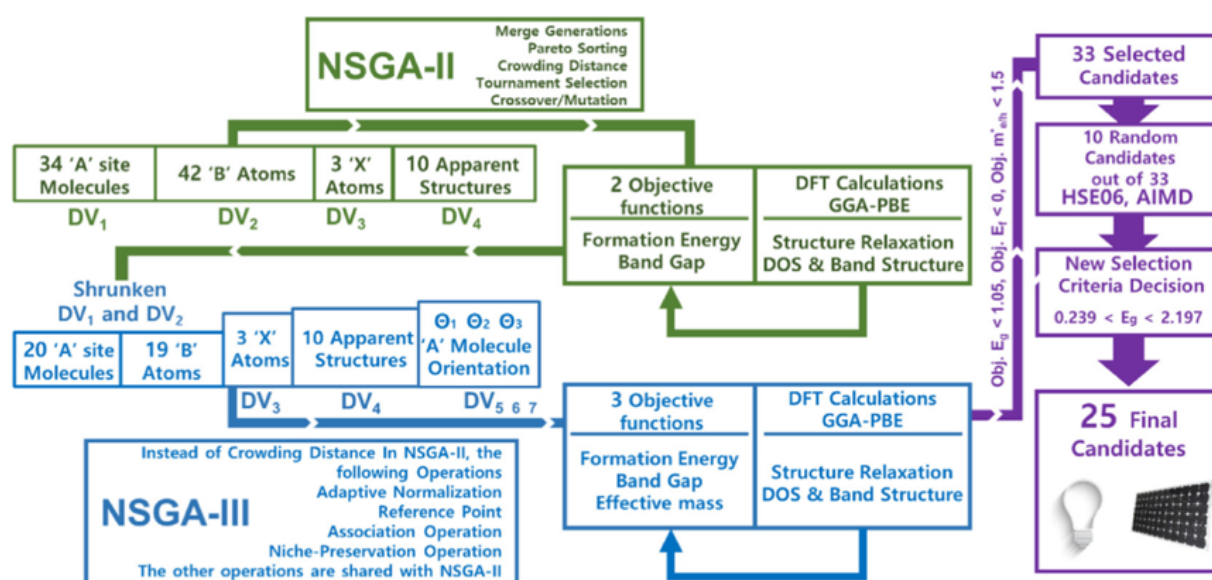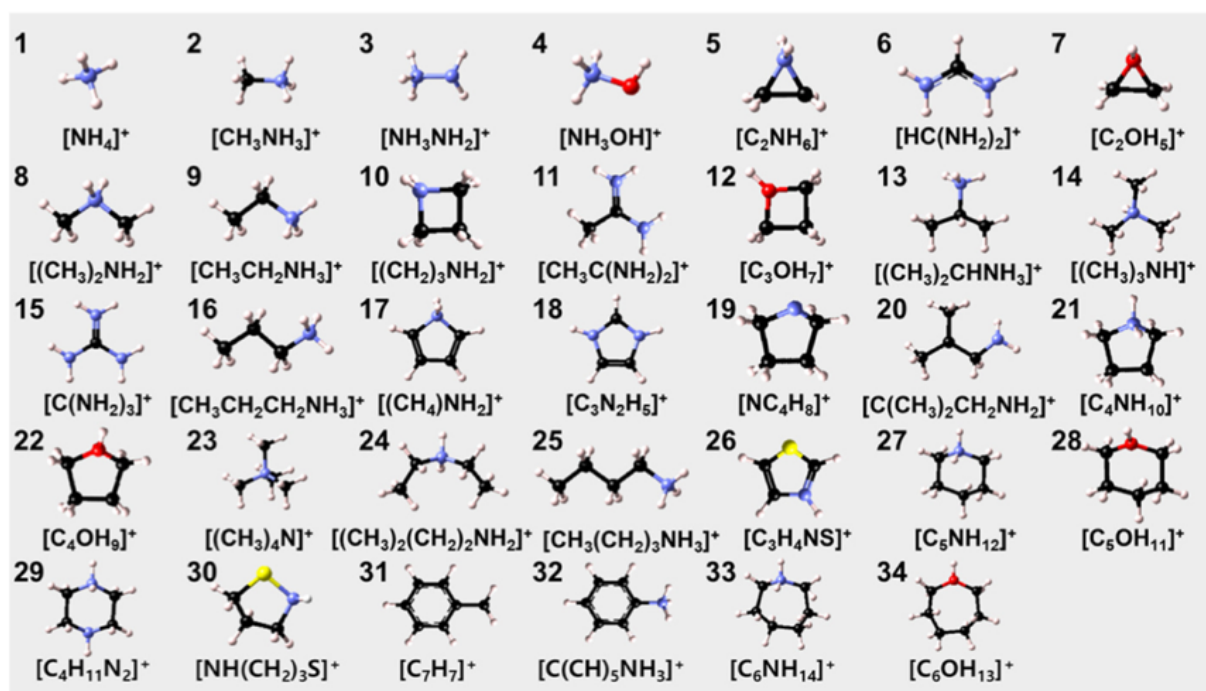
Figure 35: An inexpensive, fast computational methodology to discover large volume of novel perovskites based on density functional theory (DFT) proposed by Lee et al.[68] Top: Molecule candidates and apparent structure types with the corresponding chemical formul. Bottom: Workflow for Machine Learning enhanced material discovery involving DFT-calculations. The outcomes can be treated as good propositions for applicational verification. Image reproduced with permission of ACS. [68]

2.5.6.2 Machine learning

While DFT provides computationally complete material information, it involves modeling of quantum chemistry, usually followed by convoluted calculations. Unfortunately, the DFT outcomes are erroneous to a certain extent; however, without DFT, research is limited to trial/error studies. There is another computational approach already mentioned in previous paragraph which is beneficial to PSC research – ML. First of all, it does not require much computational power nor quantum chemistry in order to conduct experimental works. Also, it limits the trial/error experiments by providing "educated" feedback from the existing correlations between the material change and the resulting parameter change. Hence, ML models are built for the prediction of desired parameters upon the data extracted from previous results.[19] The outcomes from one of ML studies are presented in **Figure 36**.
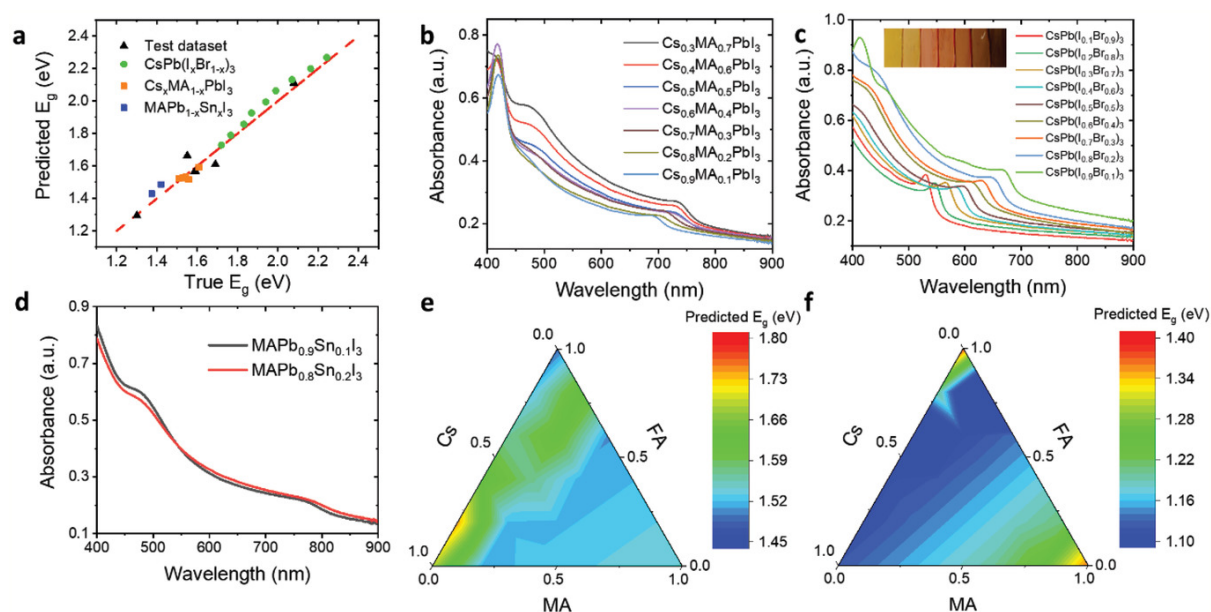
Figure 36: Performance of the PSC material design model by the ANN algorithm showing the correlation between the true data and predicted results. b–d) are the absorption spectra of the synthesized perovskite solar cell material $Cs_xMA_{1-x}PbI_3$, $CsPb(I_xBr_{1-x})_3$, and $MAPb_{1-x}Sn_xI_3$, respectively, with different fractions of "x" based on ML predictions. The inset of (c) is the image of real samples we fabricated (from left to right: x = 0.1–0.7). e,f) Ternary contour plots of Cs/MA/FAPbI_3 and Cs/MA/FASnI_3 showing the predicted bandgaps with different ratio of Cs/MA/FA while fixing Pb = 1, I = 3 and Sn = 1, I = 3, which provides the trend that Sn gives a smaller bandgap than Pb. Image reproduced with permission from Wiley.[69]

ML models can guide the synthesis of new perovskites with parameters similar to or better than the ones which serve as a base.[20] Mostly, ML approaches are developed to find the correlation between perovskite material properties and results. Typically, new test sample recipes that are not included in the ML training data, are fed to ML model to test the predictability or quality of it. Many ML algorithms do not involve detailed aspects of PSC, for example, the electrical data is correlated with the perovskite crystal composition, but the crystal grain size, fabrication conditions are omitted or minimized. Especially they can be "thrown out" if the input datasets are large. For example, the root mean square error or so-called good Pearson's coefficients methods can output valuable instructions for the next iterations of designing PSC devices or materials.[21] As was mentioned before, large datasets can contain much more information than a single datapoint, moreover, the human analysis of myriad plots and datapoints is not efficient and often difficult.[22] Hence, ML algorithms based on the artificial neural network (ANN) are employed to find certain relationships and help to correlate such findings with the material property or preparation method. This approach serves as a relevant starting point for future discoveries.

2.5.6.3 cHTR synthesis of perovskites

The material predictions described previously can significantly reduce the discovery time and costs, however the accuracy of the predictions usually depends on the quality of the computational model that is generated in part from the data received from the real experiments. Hence, the proper DFT or ML outcome verification is highly deserved. There are numerous methods for perovskite material synthesis.[23-24] As the different methodologies for obtaining perovskite-related materials/ compounds is not the focus of this thesis, these different methodologies will only be briefly mentioned here. The high-throughput material synthesis can lead to the generation of tens of thousands of novel perovskite compositions without the need for full solar cell device fabrication. The idea of perovskite synthesis usually is related to a single crystal or single compound film fabrication.[25] It is worth to mention that there are various other than PSCs optoelectronic perovskite devices that can benefit from new crystals, such as lasers, x-ray detectors, photosensors, or light-emitting diodes (LEDs). However, from the perspective of cHTR discovery, the majority of defining optoelectronic

properties (carrier lifetime, mobility, diffusion length, trap density, optical absorption, photoluminescence, energy band gap) can be directly measured without the need to fabricate the device. The commonly applied synthesis methods include: slow evaporation, inverse temperature crystallization, droplet-pinned crystallization or antisolvent vapor-assisted formation as shown in **Figure 37**.
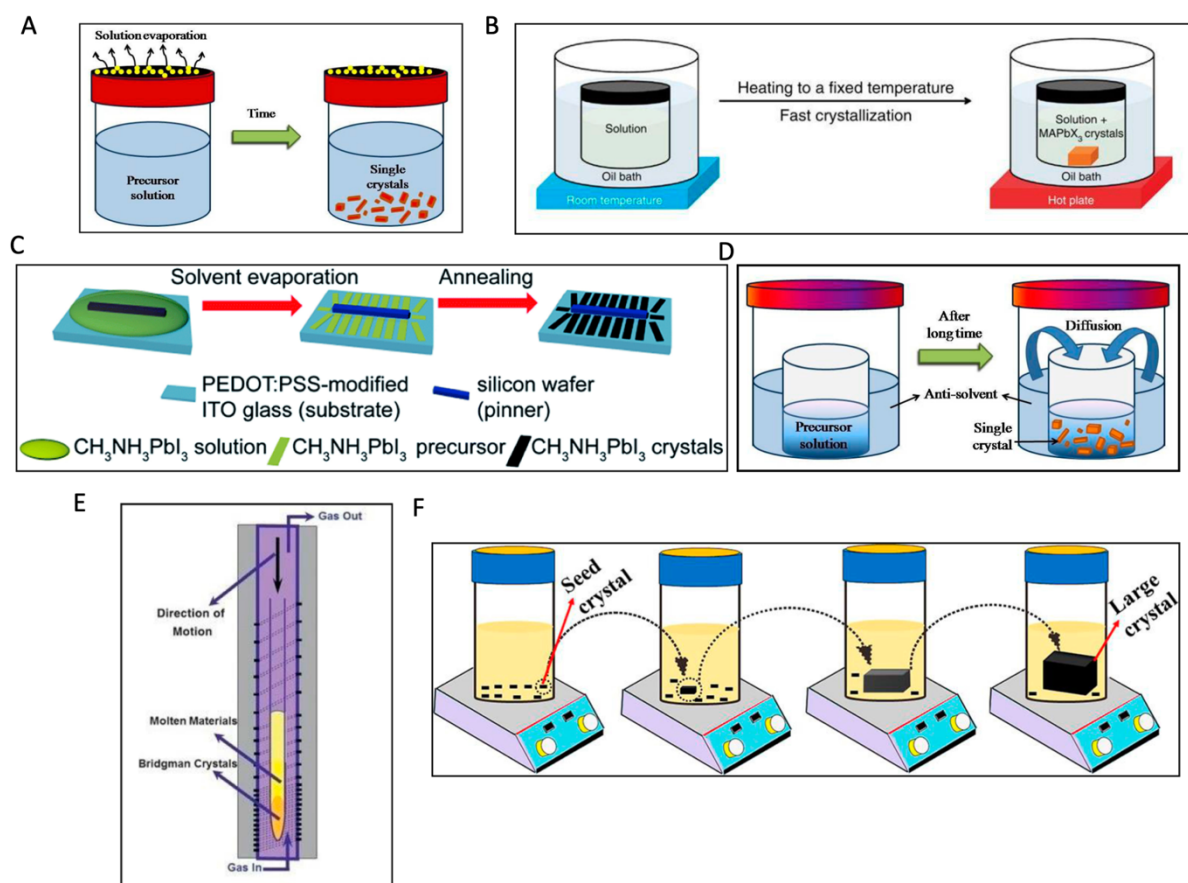
Figure 37: Synthesis methodologies used for perovskite single crystal fabrication. A) Slow evaporation (SE). B) Inverse temperature crystallization (ITC). C) Droplet-pinned crystallization (DPC). D) Anti-solvent vapor-assisted crystallization (AVC). E) Bridgman method. F) Modified inverse temperature crystallization (MITC). Images reproduced with permission from Elsevier.[70]

The common characteristic of all such methodologies (besides single crystal formation) is the fact that they consume a lot of time and resources. To successfully synthetize a new crystal, the requirements are pristine precursor solutions, complex temperature cycling, and specific environmental conditions (for example inert, dry atmosphere). However, in principle, such

synthesis is fairly simple, and by miniaturization and accurate precursor solution design, high-throughput crystallization robots could be developed. One of the first approaches was presented by the Brabec group[27] **(see Figure 38)** where the authors built a system that can not only produce the crystals but also it can immediately afterwards screen the resulting samples for their optoelectronic parameters (photoluminescence and absorption).
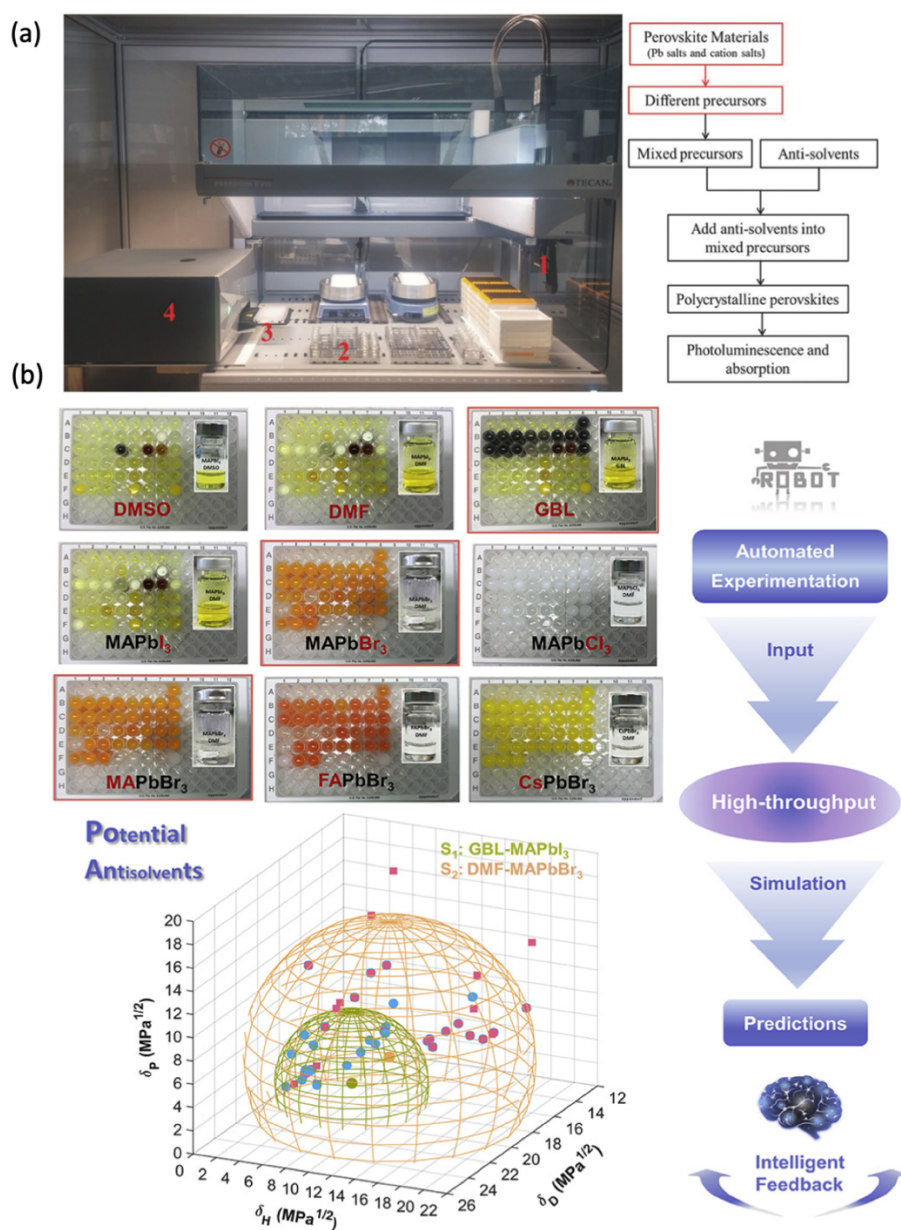
Figure 38: High throughput robotic crystallization system. (a) Working principle flow diagram. Four pipetting fingers, solution region, 96-well plate, and spectrometer are labelled as 1, 2, 3, and 4, respectively. In the flow chart, parts in the red box and in the black box are manual and automatic processes, respectively. (b) Brabec group high-throughput screening of antisolvents for lead halide perovskites using their robotic platfrom.[71] Reproduced with permission from Wiley.[72]

Hence the combination of both approaches , ML/DFT and their realization through synthesis, remains the most accurate development pathway. This mechanism through synthesis and characterization is explored in another study in 2020 by Li et al.[29] who employed the ML prediction driven inverse temperature crystallization (ITC) methodology. They showed **(Figure 39)** that from 45 organic ammonium cations, they were able to perform 8172 metal halide perovskite reactions. This further proved certain predictions and provided a detailed library of crystal characteristic data useful for numerous DFT and ML studies, and for the broader research community.
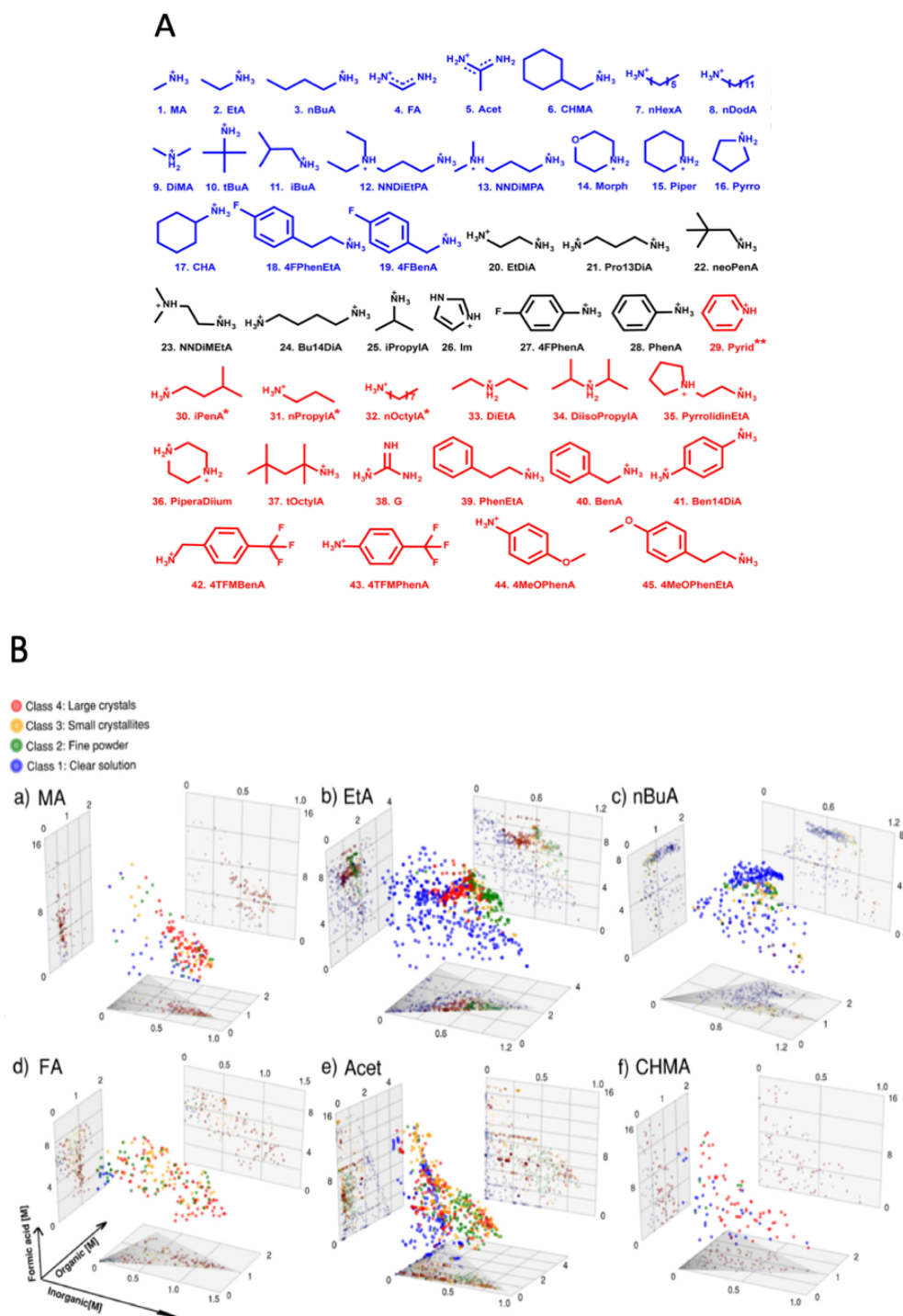
Figure 39: A: Chemical structures of the organo-ammonium cations studied including previously unknown/not matching the literature compounds. B: Crystal quality of 2295 lead iodide perovskite reactions as a function of the organic cation and the concentrations of the organic, inorganic (PbI2), and formic acid precursors. Organic precursors are methylammonium iodide (a), ethylammonium iodide (b), n-butylammonium iodide (c), formamidinium iodide (d), acetamidinium iodide (e), and cyclohexylmethylammonium iodide (f). Light gray boxes show two-dimensional projections of the data. Dark gray triangles illustrate the accessible experimental space in the organic–inorganic plane, as constrained by precursor solubilities. Image reproduced with permission of ACS.[73]

2.5.7 The prospects of high-throughput PSC fabrication

This review has established that new materials can be first predicted and subsequently synthetized. However between the optoelectronics trends and the PSC application there are still significant differences caused by the interaction of each PSC layer. Still some of the trends visible in perovskite crystals or films can be revealed via compositional screening of fully-made devices. For example, the manual fabrication of large parameter space screening related to wide bandgap exploration and tandem silicon-perovskite devices was demonstrated in 2017 by Jacobsson *et al*.[30] Despite fabricating first films and then PSCs, it was unfortunately not precise, or reliable, and it is subject to multiple errors caused by manual handling. Remarkably, Chen *et al*. used a simple robotic system to create a compositional map for the $FA_{1-x}Cs_xPb(I_{1-x}Br_x)_3$ perovskite system in order to find the optimum composition for a wide-bandgap material for tandem solar cell applications.[27] Unfortunately, at that time the characterization remained manual added unnecessarily a lot of error. cHTR fabrication is not only important to ensure that the perovskite film quality is sufficient for solar cell fabrication. cHTR systems in PSC research can help to screen the large parameter space and extract segregated verified and reliable information. Ideally, they can also be harnessed to create a compositional variety of perovskite materials.[31-33] Importantly, as reported in the literature, cHTR applications have mostly been used to synthesize perovskite materials.[27-29, 34-36] Some of the reported cHTR approaches developed include: miniature crystallization cuvettes,[27] ink-jet sprays for larger film fabrication,[37] solvent screening pipettes for multiple concentration study[38] and spray-pyrolysis nozzles for CTL thickness variations.[39] For example Zaban's group has built a system that allows for fabrication of "perovskite libraries" and then automatically such "libraries" are characterized. Their system records all possible PV datapoints into a concise, reliable, and trustworthy material library.[40-42] In **Figure 40**, it is shown that by modifying the thickness and composition of the device, this group achieved a systematic, automatized compositional screened libraries.

This was an early attempt at perovskite library generation via fabrication of large substrate with multiple top electrodes which allowed for scanning and extracting multiple *J-V* curves. The data is easily readable thanks to the heatmap-style color coding. Although some would

argue that the thickness modification or vapor treatment leaves a significant gap, The Zaban group research paved a way towards future data presentation and the prediction -> synthesis -> standardized fabrication -> automated measurement approach with easily readable large data libraries.
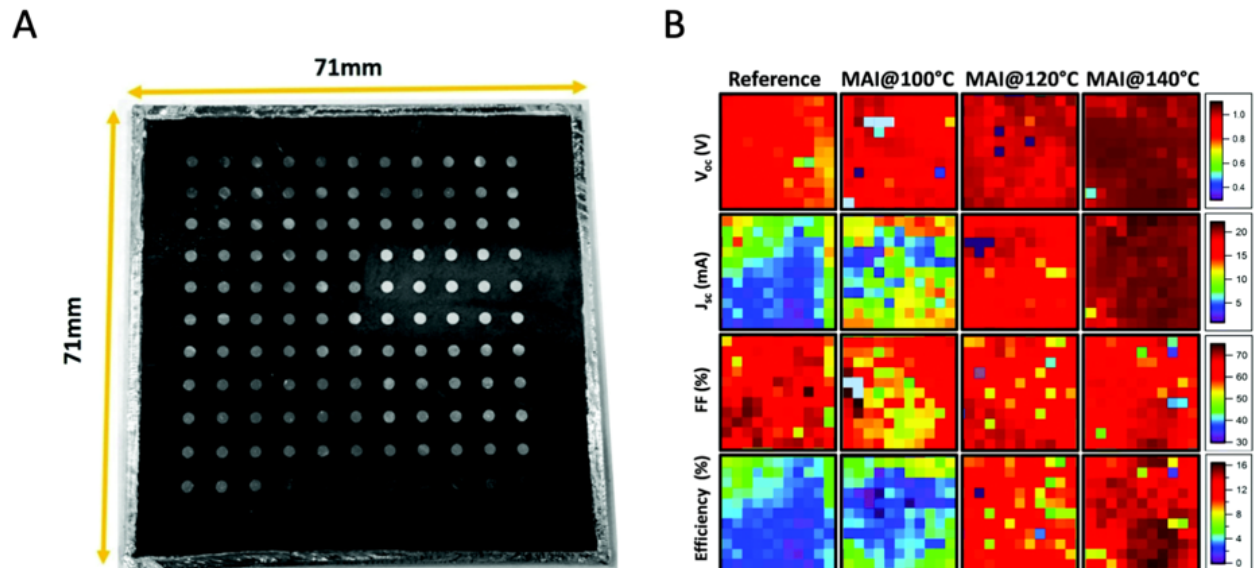
Figure 40: Multiple solar cells for a proper concept validation: The authors knew that certain perovskite works well, but believed that modification of certain process can increase their parameters of interest. In this particular case they fabricated A) a library of solar cells, which was subjected to 2-step synthesis of perovskite by exposing the perovskite films to MAI vapor and resulted in B) heatmaps of performance data. Gouda et al. [74] reproduced with permission from RCS Nanoscale.

Despite these promising attempts, these instruments still remain unreachable for many due to their costs or their limited applicability. Until now, there were very few attempts of creation of commonly accessible data libraries where researchers are able to view a trustworthy perovskite recipes. Fabrication techniques followed by manual handling, performance characterization and analysis leave significant room for misinterpretation. In order to build a comprehensive cHTR system equal importance must be placed on predicting, fabricating, and characterizing new perovskite materials.

2.6 Summary

The rapid evolution of metal halide PSCs has intensified in recent years, especially in view of the first commercialization attempts. The review presented in this chapter establishes that PSC research efforts in this field have focused on achieving greater stability rather than greater efficiency. Moreover, predominantly erroneous, manual handling, preparation and characterization of PSCs can limit research progress and discovery of new, reproducible PSC compositions.

2.7 Research aims

From the review, it is clear that these shortcomings must be addressed to further advance this field. This thesis addresses some of the gaps outlined previously. The fabrication and demonstration of high performing PSC devices have often suffered from barely reproducible recipes. This is because the majority of the research community is focused on fabricating PSCs using nonscalable, untraceable, manual fabrication methodologies, and measurement techniques. Typically, due to the time-consuming, expensive, and time-dependent investigations of often highly unstable materials, the lengthy research efforts achieved only a couple of ground breaking results. Additionally, only a few of the highest-grade laboratories can afford to use specialized equipment for material synthesis, precursor solutions, device fabrication, and characterization.

Hence, the overall aim of this thesis is to explore, develop and employ cHTR systems and techniques for rapid, reproducible, and accurate perovskite solar cell materials discovery. The specific aims of the work carried out to achieve this broad research aim are as follows.

1. The first aim is to propose a perovskite film fabrication system which is capable of *in-situ* mixing and deposition of the perovskite precursor solutions. The proposed cHTR system must allow for the perovskite compositional screening. The system needs to vary, control and track fabrication conditions. The samples must be standardized,

high quality, and ideally, the human intervention during the deposition must be minimized. The system must be able to generate perovskite films that are directly employable in PSC devices.

2. The next aim is to expand the automated deposition and mixing system for automatic optimization of the most promising perovskite films. The system needs to be enhanced beyond pure perovskite precursor solutions and screen the impact of additives on the PSC film quality. The system must generate reproducible and precise samples. The extracted data needs to indicate the potential paths for the sample quality improvement.

3. Another aim is to develop a technique for cHTR fabrication of CTL films used in PSC devices. The technique must be adaptable for large-scale fabrication and must produce pristine samples in low-temperature processes.

4. One more aim is to fabricate and characterize PSCs using a rapid cHTR measurement protocol. This protocol must be compatible with the currently available fabrication steps, although it must significantly improve the productivity, controllability, and precision of the PSC measurements. The measurement protocol must remain "open", meaning that the researcher can adjust the protocol to the samples, especially in view of the transient and unpredictable material behavior of PSCs.

5. Our final aim is to engineer and propose an inexpensive method of acquiring the stability information about the solar cell modules or panels. The goal is to build a prototype that provides the functional way of employing the PSCs in real-world application scenarios and can be shared with broader PSC community.

3 Experimental methods

A short overview of the materials, experimental methods and characterization techniques used in the research is provided here. The overview begins with a description of the materials, and then it is followed by the key processes utilized for the fabrication of this thesis PSCs. The substrates, CTL, electrodes, and deposition details involved in these processes are also outlined. Further details of particular experimental methods, instrumentation and analysis parametrization relevant to the work and reported in each chapter is provided in this chapter and/or in the specific chapter.

3.1 Materials

Butylammonium iodide (n-, iso-, tetra-) was purchased from Greatcell Solar. Oleic acid (OA, 90%), nickel (II) acetate tetrahydrate (Ni(ac)$_2$ · 4H$_2$O, 98%), Me$_3$OBF$_4$ (95%), 1-octadecene (ODE, 90%), oleic acid (OA, technical grade 90%), 4-hydroxybenzoic acid (HBA, 99%), anhydrous ethanol (EtOH, 99.5%), toluene (99.5%), hexane (anhydrous, 95%), 2-propanol (IPA, 99.5%), chloroform and chlorobenzene (CF and CBZ, anhydrous 99.8%), 1,2-dichlorobenzene (DCB, anhydrous, 99%), *N*,*N*-dimethylformamide (DMF, anhydrous, 99.8%), dimethyl sulfoxide (DMSO, anhydrous, 99.9%), gamma-butyrolactone and acetonitrile (GBL and ACN, 99.5%) were purchased from Sigma Aldrich. Lead bromide (PbBr$_2$, 99.999%) were purchased from Alfa Aesar. Formamidinium iodide (FAI), and methylammonium bromide (MABr) were purchased from Greatcell Solar. Sodium oleate (NaOA, 97%), and lead iodide (PbI$_2$, 99.999%) were purchased from TCI and Sigma -Aldrich. PEDOT:PSS was purchased from Sigma-Aldrich and Hereaus. [6,6]-Phenyl-C61-butyric acid methyl ester (PCBM) was purchased from 1-Material. All materials were used as received without further purification. If materials are not listed here, then particular description will be provided with source and purity.

3.2 Sample preparation

*Noteworthy contribution: The author of this thesis designed the new patterned substrate (see **Figure 41**) that completely replaced the previously used manual laser patterning and cutting. Importantly for the Renewable Energy Laboratory at Monash University, from the deployment of the work further presented in Chapter 7, a standardized methodology is now employed at this laboratory.*
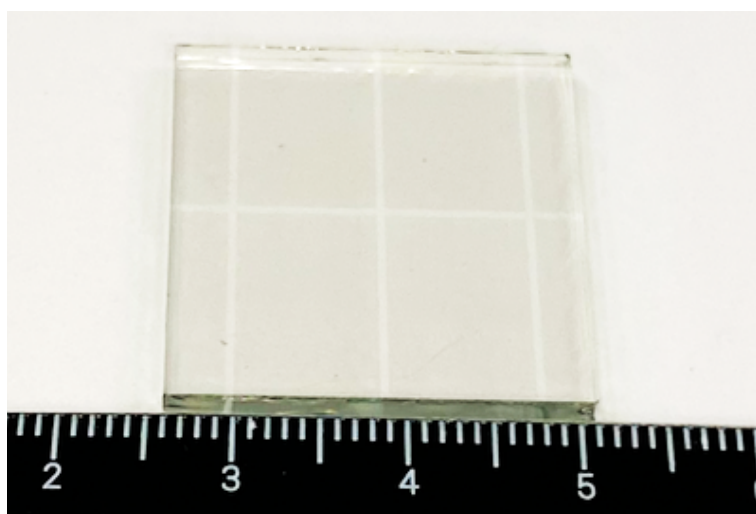
Figure 41: Digital photograph of the pre-patterned substrate sample according to the design Surmiak et.al. The thickness is 2.2 mm. The visible etch lines (0.5 mm) define the 4 individual solar cells, more details can be found in Chapter 7.

All devices were fabricated on pre-patterned and formatted fluorine-doped tin oxide (FTO) coated soda lime glass (Latech Singapore, 25 x 25 mm, thickness of 2.2 mm), indium-doped tin oxide (ITO) coated soda lime glass (Keivo, 25 x 25 mm, thickness of 1.1 mm), aluminium zinc oxide (AZO) soda lime glass (Huanyu 25 x 25 mm, thickness of 2.2 mm), see **Figure 42** for comparison. The substrates were cleaned in a following sequence (photographs and more details can be found in Appendix A):

- Nitrogen (N_2) gun blow
- Mili-Q water (resistivity of 18.2 MΩ cm^{-2}) ultrasonic bath (10 minutes)
- Hellmanex in Mili-Q water 2% solution ultrasonic bath (10 minutes)
- Mili-Q water (resistivity of 18.2 MΩ cm^{-2}) ultrasonic bath (10 minutes)

- Acetone (pure, laboratory grade) ultrasonic bath (10 minutes)

- Isopropyl alcohol (pure laboratory grade) ultrasonic bath (10 minutes)
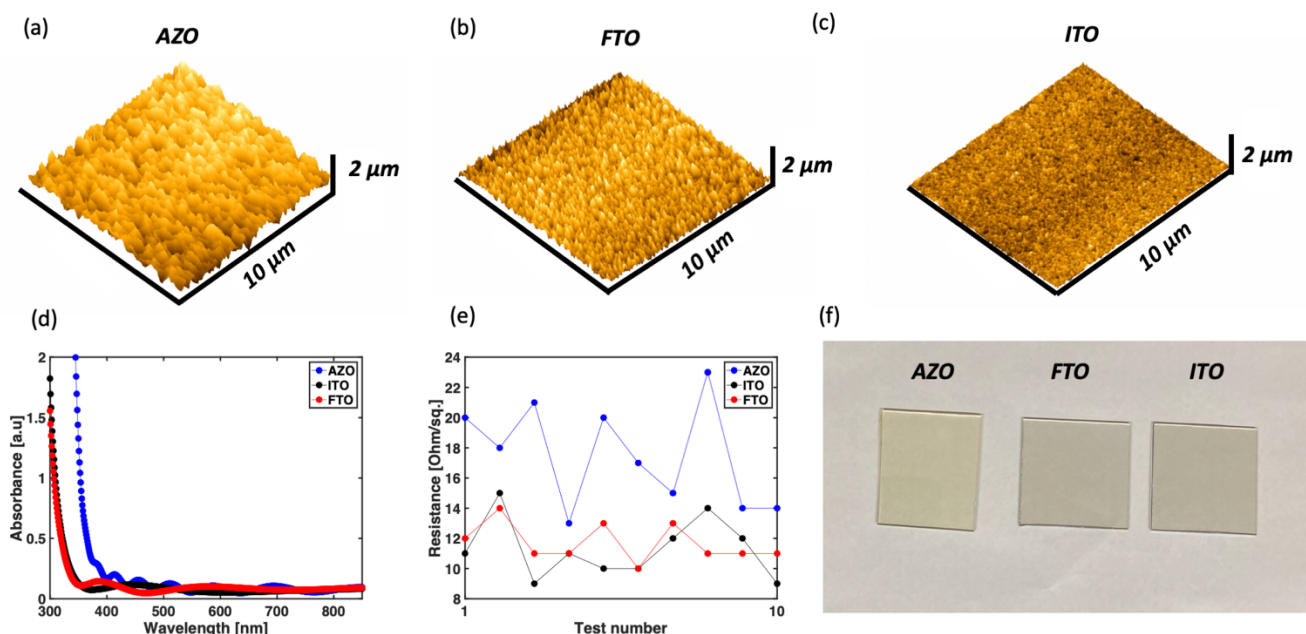
Figure 42: Relative comparison of roughness using AFM after cleaning procedure, the z-axis is set on 2 μm to provide uniform scale: (a) AZO, (b) FTO, and (c) ITO. (d) UV-vis absorbance comparison, (e) 4-point probe sheet resistance comparison, and (f) digital photograph of the substrates. Product datasheet declarations: FTO 10 Ω sq-1, ITO 10 Ω sq-1, and AZO 15 Ω sq-1.

3.2.1 Electron transporting material

In the research, inorganic and organic electron transporting materials were employed that will be referred to throughout this thesis as electron transporting layers (ETLs).

Inorganic:

Compact titanium oxide (TiO_2) – all layers were prepared with fully automated spray-pyrolysis system using masking area shadow masks and stainless steel temperature equalizer contributed as a part of work of the author. The preparation of the stock solution for spray pyrolysis: Cleaned FTO substrates were oxygen plasma treated for 15 minutes (in ambient

conditions) and carefully placed inside the rebates on the temperature equalizer and shadow masked accordingly to ensure that the active area is exposed and the electrode area is masked. The equalizer was placed on the hot-plate inside of the spray system and PID controlled hotplate was subsequentially used to bring the temperature with a gradual ramp for 30 minutes to 500 °C. Titanium diisopropoxide bis(acetylacetonate) (TAA) stock solution, also known as: TYZOR® AA organic titanate, $Ti_{(acac)}2O_iPr_2$, diisopropoxytitanium bis(acetylacetonate) was diluted with GB grade IPA (anhydrous, inside the GB) TAA:IPA 1:19 and cooled down to 5 °C. The TAA solution was loaded into programmable syringe pump and sprayed over the surface (spraying distance 15 cm). The substrates were subsequentially (after spray) annealed for 30 minutes and naturally cooled down to RT.

Mesoporous titanium oxide (TiO_2) – the commercially available titania paste transparent (NR30) was diluted NR30:ethanol (1:6). The dispersion was stirred overnight and sonicated. The FTO substrate with compact-TiO_2 was masked with Kapton tape and the substrate was vacuum mounted on spin-coater. Aliquots of 100 µL were pipetted on top of the substrate and spin-coating was undertaken (ramp 2000 RPM, speed 4500 RPM for 30 seconds). After the deposition the tape was removed and the substrate was subsequentially annealed in 100 °C for 15 minutes and subsequentially brought to 500 °C for 1 hour (ramp of 20 minutes), after the annealing the substrates were cooled down naturally.

Tin oxide (SnO_2) – 22.5 mg of tin(IV) chloride pentahydrate ($SnCl_4\ 5H_2O$) was dissolved for 1 hour at RT in 1 mL of IPA (anhydrous) and stored inside of GB. Subsequentially, FTO or ITO substrates directly after cleaning were oxygen plasma treated (15 minutes for FTO, 10 minutes for ITO) in order to remove residual organics and change the surface property to more hydrophilic. The substrates were vacuum mounted inside of the GB and aliquots of 80 µL were spin-coated (acceleration 500 RPM, speed 2500 RPM for 30 seconds). The substrates were annealed in two step process in N_2: 100 °C for 15 minutes and then 200 °C for 60 minutes.

Organic:
3'H-cyclopropa[1,9][5,6]fullerene-C60-Ih-3'-butanoic acid 3'-phenyl methyl ester, known also as phenyl-C61-butyric acid methyl ester ($PC_{61}BM$) - 10 mg of $PC_{61}BM$ (>99.5% Osilla Ltd) was

dissolved in 1mL of anhydrous CBZ inside of the GB. The solution in vial was stirred and shaken for 4 hours in dark inside of GB. The vial was transferred to fabrication GB where through needle was pumped into the syringe, subsequentially the needle was replaced with 0.45 μm (polytetrafluoroethylene) PTFE filter and solution was filtered directly prior the deposition.

Fullerene (C_{60}) – approx. 1 g of (C60-Ih)[5,6]fullerene (C60) was placed in the high temperature glass crucible inside of Ångstrom® glovebox thermal evaporator. The evaporation rate was set to 0.1 Å s^{-1} and typically up to 20 nm was deposited using thermal evaporation through shadow mask.

3.2.2 Hole transporting material

In this thesis, we have employed inorganic and organic hole transporting materials, further referred to as hole transporting layers (HTLs) sourced and prepared accordingly:

Inorganic:

Nickel Oxide (NiO_x) - nickel oxide nanoparticles were synthesized using modified method developed by Liang *et al.*[89] Ni(ac)$_2$ · 4H$_2$O (0.5 mmol), NaOA (oleic acid) (0.2 mmol), 1-dodecanol (DOD) (3 mmol), OA (1 mmol), and octadecene (ODE) (4 ml) were mixed sequentially in a "tree-neck" round bottom flask which was connected to a Schlenk line. It was magnetically mixed, outgassed and brought to 110 °C for 30 minutes under vacuum.[8] Upon fully dissolved precursors, the temperature was ramped to 235 °C in 10 minutes. The reaction was kept for 2 hours under N$_2$. After 2 hours brought back naturally to RT, precipitated with a mixture of acetone and ethyl acetate (1:1), and centrifuged at 5000 RPM for 5 minutes. The supernatant was decantated. The solids were dissolved in 30 mL of a nonpolar solvents: hexane or toluene. The solute was subsequentially centrifuged to precipitate impurities. The NiO NPs from the supernatant were precipitated (30 mL of ethanol (EtOH)) and centrifuged again (5000 RPM for 10 minutes). The dark-green wet solids were dry hot air dried (70 °C for 5 hours). Subsequentially, the product was dispersed in a nonpolar solvent: 1:1:1, CBZ:toluene:hexane to a concentration of 15 mg mL^{-1}. Further details about

ligand-engineering and microfluidically-enhanced deposition of the NiOx NPs can be found in Chapter 6.

Organic:

Poly(3,4-ethylenedioxythiophene) polystyrene sulfonate (PEDOT:PSS) - the water-based solution was further dissolved 1:1 in mili-Q® water (18.2 MΩ, RT). On pre-cleaned, oxygen plasma treated substrates 100 µL aliquots were statically spun (acceleration 4000 RPM, speed 4000 RPM) for 25 seconds.

Poly(3-hexylthiophene-2,5-diyl) (P3HT) – precursor solution was prepared inside of GB. 30 mg of powder was taken and dissolved in 1 mL of CBZ. The solution was magnetically stirred overnight (12 hours) in elevated temperature (60 °C). It was filtered directly before the deposition with syringe mounted 0.45 µm teflon filter. Aliquots of 90 µL were deposited onto cleaned ITO/FTO substrates or perovskite films, and spun subsequentially following the procedure: acceleration of 1000 RPM, speed of 1500 RPM for 45 seconds, followed by acceleration of 3000 RPM, speed of 3000 RPM for 30 seconds. The substrates were annealed directly after the deposition for 10 minutes in 100 °C inside of GB.

Poly[bis(4-phenyl)(2,4,6-trimethylphenyl)amine (PTAA) – precursor solution was prepared inside the GB. 5 mg of PTAA powder was taken and dissolved in 1mL of CBZ. The solution was magnetically stirred overnight (12 hours) at RT. It was filtered directly before the deposition with syringe mounted 0.45 µm teflon filter. Aliquots of 60 µL were deposited onto cleaned ITO/FTO substrates or perovskite films, and statically spun (meaning deposited on immobilized substrate) subsequentially following the procedure: acceleration of 5000 RPM, speed of 5000 RPM for 30 seconds. The substrate was annealed directly after the deposition for 10 minutes in 100 °C inside of GB.

Poly[N,N'-bis(4-butylphenyl) -N,N'-bis(phenyl)-benzidine] (poly-TPD) - precursor solution was prepared inside the GB. 5 mg of poly-TPD powder was taken and dissolved in 1mL of CBZ. The solution was stirred overnight (12 hours) at RT. It was filtered directly before the deposition with syringe mounted 0.45 µm teflon filter. Aliquots of 70 µL were deposited onto cleaned ITO/FTO substrates or perovskite films, and statically spun (meaning deposited on

immobilized substrate) subsequentially following the procedure: acceleration of 5000 RPM, speed of 5000 RPM for 30 seconds. The substrates were left to dry without annealing inside of GB.

2,2',7,7'-tetrakis(N,N-di-p-methoxyphenyl-amine)-9,9'-spirobifluorene (spiro-OMeTAD) – inside the GB: stock solution A (SSA): 520 mg bis(trifluoromethanesulfonyl)imide (LiTFSI) was dissolved in 1 mL of acetonitrile (ACN) and left on shaker for 1 hour at RT. Stock solution B (SSB): 300 mg of cobalt complex FK269(III) was dissolved in 1 mL of ACN and left on shaker for 1 hour at RT. Into new vial 72.3 mg of spiro-OMeTAD was weighted, 28.8 µL of 4-tert-butylpyridine (TBP) was pipetted, 17.5 µL of SSA and 6.4 µL of SSB was pipetted in, followed by 1 mL of CBZ. The spiro solution was left on shaker for 3 hours to fully dissolve.

Layer fabrication: Onto perovskite layer (at RT) typically 40 µL of the spiro solution is dynamically spin-coated – meaning that the substrate is spinning whilst solution is pipetted at acceleration of 3000 RPM and at speed of 3000 RPM for 30 seconds. The substrates were left to dry without annealing inside of GB for 30 minutes.

3.2.3 Perovskite precursor preparation

All perovskite active layers were fabricated using two main deposition routes (spin-coating and drop-casting). All precursor solutions were prepared in the strictly controlled nitrogen (N_2) glovebox (O_2 below 0.1 ppm, H_2O below 0.01 ppm). Prior material preparation the glovebox was purged for 30 minutes to avoid any solvent vapor contamination.

3.2.4 Perovskite layer fabrication

Spin-coated perovskite (in Chapter 6): The precursor solution was prepared using the following precursor salts: formamidinium iodide (FAI) (99.9%, Sigma-Aldrich), cesium iodide (CsI) (99.999%, Sigma-Aldrich), lead iodide (PbI_2) (99.999%, Sigma-Aldrich), lead bromide ($PbBr_2$) (99.999%, Sigma-Aldrich). The salts were opened in the GB and all steps were

continued under strict GB conditions, the solution was prepared according to recipe: PbI_2 (0.88 mmol), $PbBr_2$ (0.22 mmol), FAI (0.83 mmol), and CsI (0.17 mmol), 1 mL blend (4:1 volume/volume) of anhydrous N,N-dimethylformamide (DMF) and dimethyl sulfoxide (DMSO). The perovskite precursor solution was magnetically stirred and subsequentially shaken overnight until fully dissolved forming a clear yellow solution at RT. Aliquots of 40 μL cm^{-2} of perovskite precursor solution were pipetted onto substrates, then spin-coated following a 2-step program (acceleration 1000 RPM, speed 1000 RPM) for 10 seconds and then (acceleration 2000 RPM, speed 5000 RPM) for 30 seconds. 110 μL of chlorobenzene (CBZ) was pipetted dynamically onto the spinning film 5 seconds before end of the spin. The substrates were immediately transported on the preheated to 100 °C hot-plate and annealed for 1 hour, later on naturally brought back to RT.

3.2.5 Electrode

The metal electrodes: thermally evaporated (Au, Ag) inside of the GB (Korean Glovebox Evaporator) or inside of the GB in clean room Class 1000 (Ångstrom Engineering EvoVac), sputtered (Ag, Au) in clean room Class 1000 (Intlvac Nanochrome AC/DC Sputter Anatech Hummer BC-20 RF/DC Sputter) or evaporated using electron-beam (Ag, Al, Ni, Ti, Cu, Ge, Au) (E-beam Intlvac Nanochrome II) evaporation. Typically the electrodes were from couple of nm to approx. 100 nm thick.

The organic electrodes: commercially available carbon paste was dipped into ethanol/isopropanol blend and ultrasonically shaken overnight, carefully ground into a powder Reticulated Vitreous Carbon (known as Glassy Carbon) was added into carbon paste and ground together inside of the milling machine for 7 consecutive days. Such paste was further transferred with automatic doctor blading system on vacuum class aluminum foil with 120 nm of copper (Cu). The foil with carbon paste was dried in GB on hot plate for 2 hours at 120 °C. The foil was cut and placed directly on spiro-OMeTAD coated perovskite and pressed with hydraulic press. More fabrication details can be found in Appendix A.

3.3 Characterization

3.3.1 Hole mobility characterization technique based on field effect transistor

Field Effect Transistors (FET) were measured inside the cleanroom Class 1000 using a self-balancing probe station (Signatone WL-1160RF) combined with an Agilent B2902A Precision Source/Measure Unit. Device characterization results were calculated and fitted using the Igor® script.

3.3.2 Solar cell electrical performance characterization

For the *J-V* performance and maximum power point (MPPT) measurements we used AAA 1 Sun ABET 3000 Solar Simulator and 4-wire sense technique utilizing BioLogic® VMP3 source-measure unit (SMU) employing high-throughput characterization system developed by Surmiak et al. See **Figure 43** and chapter 7 for more details.

Figure 43: Digital photograph of operating high-throughput characterization setup used in Renewable Energy Laboratories at Monash University built by author. More details can be found in Chapter 7.

3.3.3 Incident Photon to Charge Carrier Efficiency (IPCE)

Incident Photon to Charge Carrier Efficiency (IPCE) spectra were achieved by measuring the PSCs with custom-made setup. Namely, Keithley 2400 Source Meter worked as source-measure unit (SMU) and as a light source a 300 W xenon lamp with an Oriel Cornerstone 260¼ m monochromator. Such produced photon flux was co-referenced through a calibrated silicon solar cell (obtained commercially from Peccell Technologies). To ensure perpendicular light orientation vs the PSC a custom-made printed circuit board was built to position the substrate. Author has built and flocked the Faraday cage and PCB, see **Figure 44**.
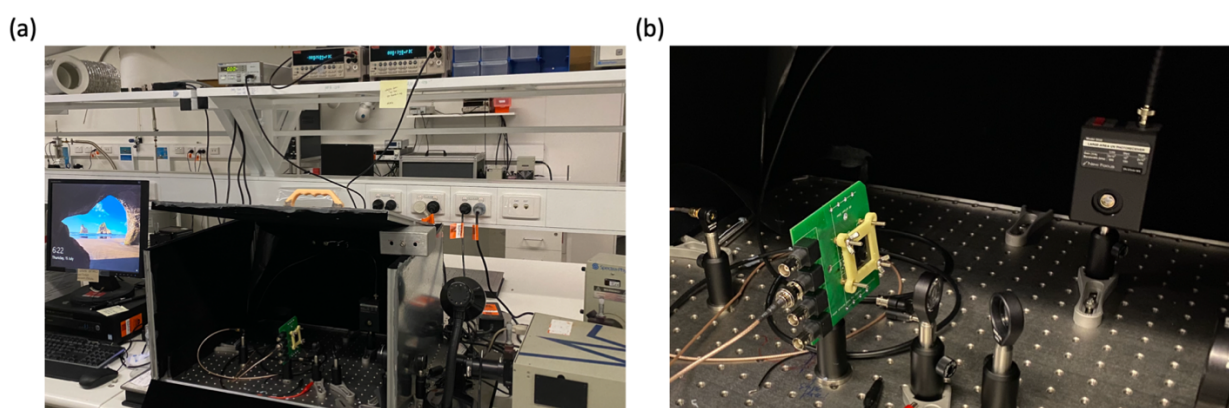
Figure 44: IPCE home-built setup at RE laboratories (a) Faraday cage with flocked interior (b) PCB board designed to allow easy connection of PSCs according to author's design.

3.3.4 Atomic Force Microscopy (AFM)

Atomic Force Microscopy (AFM) scans were measured on a Dimension Icon (Veeco) in air at RT. Chromium-platinum-coated Si conductive probes (ElectriMulti75-G, BudgetSensors) were used for the scans. The scanning area and scanning rate were 5 x 5 or 10 × 10 µm at 0.5 Hz. Grain cluster size of the films, RMS roughness was fitted and scans were levelized by Gwyddion® software.

3.3.5 Photoelectron Spectroscopy in Air (PESA)

Photoelectron spectroscopy in air (PESA) measurements were performed using a Riken Keiki AC-2 spectrometer. For all samples, a power intensity of 20 nW was used.

3.3.6 Ultra-violet photoelectron emission spectroscopy (UPS)

Ultra-violet photoelectron emission spectroscopy, was performed using Al K-alpha and He (I) source (21.21 eV) with pass energy of 200 eV (50 eV for narrow scan) and 3 eV were used to emit X-ray and UV photons, respectively. The measurements were conducted with a chamber pressure below 5.0×10^{-8} Torr. The work function was determined directly from the secondary cut-off energy through the relation: Work Function = 21.21 − Secondary Cut-Off Energy.

3.3.7 Photographs

The photographs of films were taken in flocked (using Stuart Semple pitch black paint) faraday-cage built by author. The camera uses was Nikon D90 Nikon AF-P DX Nikkor 18-55mm f/3.5-5.6G variable aperture objective, the system used Nikon SLR Control add-on in LabView® and bespoke Python® code for home-built linear stage movement developed by author, see **Figure 45**.
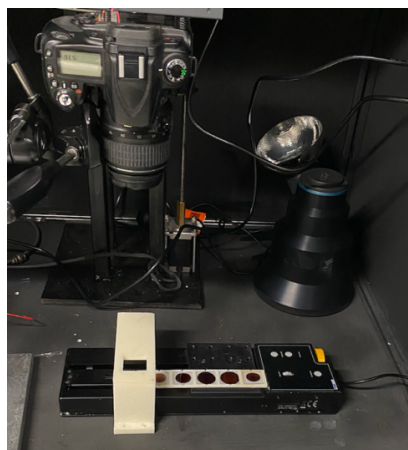
Figure 45: Photographs of the perovskite films were taken with simple 3D-printed, automated jig.

3.3.8 Infrared Thermal Measurements

All thermal pictures were taken using FLIR X6540SC camera controlled by thermography system (IrNDT IRX Box Automation Technology GmbH). The studies were conducted using dark/light lock-in thermography.

3.3.9 Scanning Electron Microscopy (SEM)

The top-view morphology was obtained by FEI NOVA FEGSEM or FEI Magellan 400 FEGSEM. The perovskite device cross-sections were prepared on glass substrates and coated with 2 nm RF sputtered iridium where applicable (films only) to drive the charge out. Scans were taken with various voltages and currents applicable at the moment.

3.3.10 X-ray Powder Diffraction (XRD)

X-ray diffraction (XRD) patterns were gathered with a Bruker D8 Advance Diffractometer (range from 5° onwards) or Bruker D2 Phaser Diffractometer (range from 2° onwards) with a Cu Kα X-ray tube at 40 kV and 40 mA and with a step size of 0.02° and 0.8 s per step.

3.3.11 Device stability measurements

PSC devices were aged and measured simultaneously inside of ATLAS SC3 340 MHG climate chamber using in-house made 20-channel custom parallel real-time measurement system based on Osilla Xtralien X200 source-measure units developed by author. The voltage step was ranged from 10 to 50 mV s^{-1}, no bias conditioning or light soaking was applied, MPPT was developed by author basing on perturb-observe algorithm.[75] The test conditions were set to 1 Sun, 25 °C and relative humidity of 40%. The devices were always encapsulated in GB prior testing. The metal shim nonreflecting shadow mask was mounted to limit working area of the devices to 0.16 cm^2. The author developed PCB boards with spring loaded pins in order to ensure perpendicular to the light source position of the devices inside of the chamber.

3.3.12 Transient voltage decay

Transient photovoltage (TPV) decay measurements were accomplished employing an in-house built system by illuminating solar devices with a constant background intensity high-power white light-emitting diode (Thorlabs MWWHL3). A light perturbation was delivered by a Kingbright L-7104VGC-H LED (465 nm wavelength) triggered by a signal generator (Agilent 33533A). A pulse width of 2 μs was chosen for the perturbation with the rise and fall times of the LED to be <100 ns measured using a Thorlabs DET10A/M Si photodetector. The transient response of the solar cell under test was recorded on an Agilent DSO-X 3032A (DOSC). For transient photovoltage measurements, solar cells were connected with the termination of 1 MΩ to achieve open-circuit condition. The intensity of the background LED was changed to achieve different V_{OC} conditions. To measure the transient photocurrent response, the device was connected to the DOSC with a 50 Ω termination to achieve a short-circuit condition. The LED intensity was verified and calibrated to correspond to *J-V* curves achieved under specific ND filtered light as a fraction of a 1 Sun AAA simulated light (ABET 3000 solar simulator). The *J-V* curves were obtained using system designed by the author of this work which is described in Chapter 6.

3.3.13 X-ray Photoelectron Spectroscopy (XPS)

X-ray photoelectron spectroscopy (XPS) analysis was performed on Thermo Scientific Nexsa Surface Analysis System with monochromatic Al Kα X-ray (1486.6 eV), using a 40 eV pass energy for the high-resolution narrow scans.

3.3.14 Fourier-Transformed Infrared Spectroscopy (FTIR)

The scans were obtained on a Thermo Scientific Nicolet 6700 FT-IR spectrometer with a Smart iTR[TM] Attenuated Total Reflectance (ATR) Sampling Accessory. A typical measurement consisted of 16 scans that were later averaged into a single figure with a resolution of 4 cm^{-1}. The powder was prepared in a sealed GB environment and distributed on the tool in strict PPE.

3.3.15 Thermogravimetric Analysis (TGA)

The analysis was conducted using Mettler Toledo Thermogravimetric Analyser 2 Star System at CSIRO Clayton. N_2 was used during the analysis at 40 mL min^{-1} rate and cell gas at 20 mL min^{-1} at a temperature ramp rate of 10 K min^{-1} from 25-500 °C.

3.3.16 Contact angle (CA)

The pictures and analysis were gathered using a Contact Angle System OCA (Dataphysics). Typically precursor solutions/dispersion or solvents of volume 3.5 µL were dispensed at dosing rate of 1 µL s^{-1}. All were performed in strict PPE and exhaust system at RT in air.

4 High-throughput Exploration of the BA$_2$MA$_{(n-1)}$Pb$_n$X$_{3n+1}$ Ruddlesden-Popper Perovskite Compositional Space

4.1 Context and Motivation

It is worth reiterating that due to the rapid upheaval in conventional ABX$_3$ PSC research the PCE reached a record of 25.5% in 2021.[13] Despite their advantages over state-of-art silicon solar cells (26.1%),[1] such as low fabrication costs,[2] low energy payback time during the manufacturing process,[3] and band-gap tunability[4], there remain significant challenges, namely, long-term operational stability[5], poor reproducibility[6] and anomalous hysteretic behavior.[7-11] External degradation mechanisms caused by oxygen or moisture degradation[12] can be minimized using encapsulation,[13] additives[14] or moisture- and oxygen-free fabrication environments[15], but are unable to address intrinsic degradation mechanisms still remain reported. These include halide segregation[16-19], UV-light induced degradation[19-20], ionic movements[21], decomposition of complex inorganic-organic structures[22] and problems induced by electrical stress.[23] For commercialization of PSCs to be realized, research focus should not be limited to maximizing the efficiency on the a smaller laboratory scale, but should be expanded to routinely include inexpensive materials that are deposited with industry-compatible production methods. Typically, most electron and hole accepting layers, along with the perovskite layer itself, are deposited by spin-coating[24-30], which is not suitable for large-scale perovskite panel applications.[31] To overcome this hurdle, a number of deposition techniques have been employed for PSC fabrication, such as blade-coating[27, 32], spray deposition,[33] roll-to-roll deposition,[76 34-35] ink-jet printing[36-37] and vacuum deposition techniques.[38-39] While these methods provide a pathway towards commercialization, several challenges still remain. In particular, small variations in wettability, thickness, roughness and morphology causes non-uniformities over large areas,[40-41] these cause shunts, or even pinholes, which can short-circuit the device.[42-43] There exist many trade-offs between each deposition techniques; for instance, large-area vacuum deposition techniques allow for accurate thickness control while limiting the number of voids, however, they suffer from low deposition rates and require high-vacuum, causing often uncontrollable phase transformations.[44-46] A thought-provoking technique was presented in 2019 by Zuo *et al.*, who used drop-casting for quasi-2D

perovskite fabrication that can be potentially enhanced at very low cost into a cHTR system. Zuo *et al.* demonstrated that low molar concentrations of the perovskite precursor solution could allow for its spreading across the substrate and forming a "self-assembled", vertically oriented, highly crystalline (**Figure 46**), and efficient perovskite films.[46] Their work provided a new path for the development of an emerging group of excellent PSCs in terms of stability and still highly efficient RP. Most importantly from the perspective of this thesis, the drop-casting methodology has been never used for compositional screening of RP PSCs.
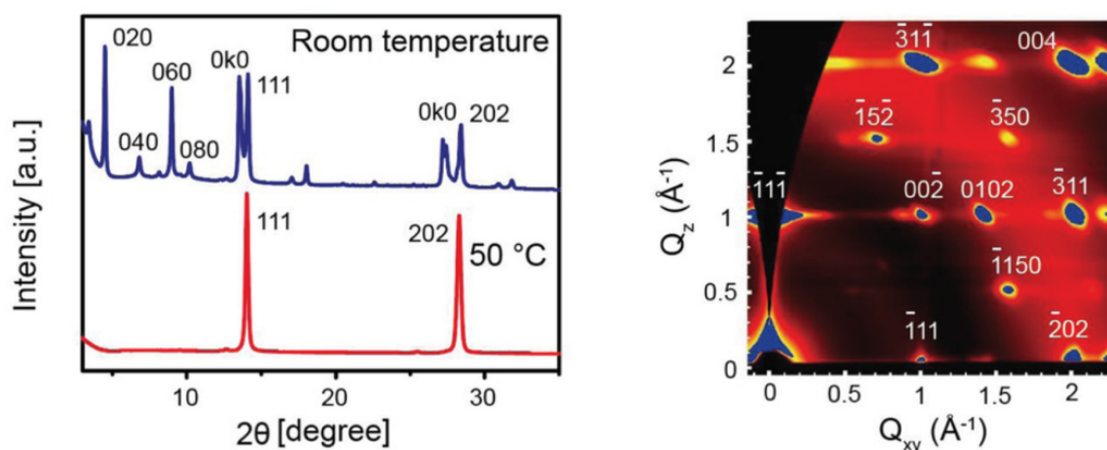
Figure 46: Drop-casted, vertically "self-assembled" perovskite crystals. Left: XRD diffraction pattern of the drop casted perovskite, right: Grazing-incidence wide-angle X-ray scattering (GIWAXS). Image reproduced with permission from John Wiley and Sons.[77]

In this chapter, the focus will be on the development of the inexpensive, yet precise and reproducible methodology of cHTR compositional screening for perovskites. The role and promise for enhanced stability of emerging low-dimensional RP PSCs will be briefly discussed. This will be followed by the system design, where the deposition, film formation and compositional space library generation of this study will be explained. The results of this study will be then presented and discussed, and then the concluding words together with the future outlook will be given.

4.2 Quasi-2D Ruddlesden-Popper perovskites

The compositional screening of RP-PSCs space requires a brief reiteration of its potential. Ruddlesden-Popper perovskites (RPPs) are a related material class, which in the past has shown promise to be more resilient to environmental stress than conventional ABX_3 perovskites. In this work, we study RPPs with the general formulae $R_2(MA)_{n-1}B_nX_{3n+1}$, where the R^+ stands for a large cation which typically does not satisfy the Goldschmidt Tolerance Factor (*GTF*) rule, methylammonium cation (MA^+), B^{2+} metal cation, and halide anions (X^-). The quasi-2D structure of RPPs is shown schematically on **Figure 47**. Due to their large size, the R^+ a cation cannot be incorporated into the three-dimensional perovskite lattice. Instead, they assemble into layers creating separation slabs dividing structure similar to the one found in ABX_3 perovskites. The dielectric mismatch of organic and inorganic components creates a favorable environment for the formation of quantum wells and barriers,[51] generating an excellent perovskite for excitonic phenomena.[52-54] Like their ABX_3 counterparts, RPPs have easily tunable band gaps,[55] can be solution-processed,[56] and exhibit high device PCE of ~17-20 %.[57-58]
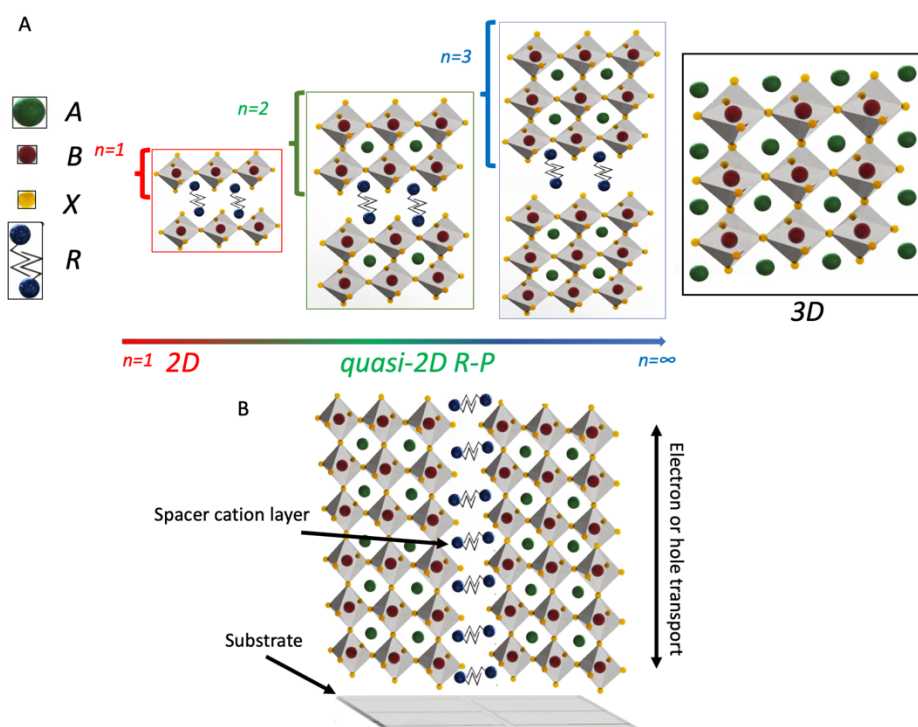

Figure 47: Schematic representing crystal structure evolution of 2D to 3D perovskites. A) The layered crystal octahedra structure where its shape is driven by an increase in layer count (n-number). The strict 2D-perovskite

has the chemical formula R_2BX_4, the quasi-2D Ruddlesden-Popper structure $R_2A_{n-1}B_nBX_{3n+1}$ and the conventional perovskite ABX_3. B) Schematic of perpendicular to substrate quasi-2D perovskites where the photogenerated carriers are transported vertically. Van der Waals forces between the alkyl chains keep the spacer cation layers together and enable the charge transport within the "packing" stacks of the perovskite crystals.

Further studies by Stoumpos *et al*. provided a strong reference for 2D R-P perovskite crystal properties through a systematic change of the precursor stoichiometry, namely by producing RPP crystals ranging from stochiometric index (n) = 1, 2, 3, 4, and ∞, further studying the crystallographic and photophysical properties of them **(see Figure 48).** For example photoluminescence (PL) and UV-vis absorption spectroscopy study,[55] revealed that the RPP bandgap tuned by changing the chemical composition.[59] Figure 48 provides an illustration of the RPP property tunability simply in the function of n-number increase. As can be seen from the photo in this figure panel D, the crystals were prepared manually in vials, hence there is a desire to see whether the same trends can be observed in the perovskite films.
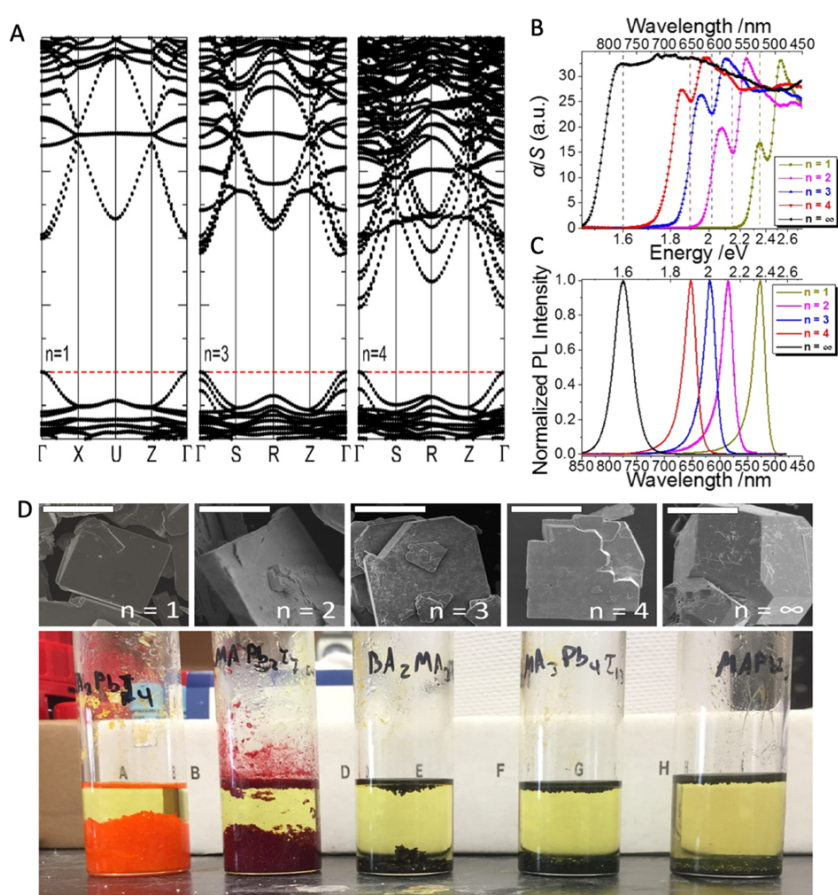

Figure 48: Dimensional tailoring of the Quasi-2D Ruddlesden-Popper perovskites. On the top left: electronic band structure of the polar configurations for Γ(0,0,0)-X/S(1/2,0,0)-U/R(1/2,0,1/2)-Z(0,0,1/2)-Γ(0,0,0) path. Perovskites: n = 1, 3, 4. Image reproduced with permission of ACS Chemistry of Materials.[78]

4.3 System design

To the best of my knowledge this is the first time that an automated drop-casting technique is developed for the purpose of high-throughput screening of solar cell materials. Especially in light of the reproducibility problems of manually spin-coated PSCs that are hindered by manual pipette aliquots, approximated process parameters and assumed but not measured environmental conditions[48] are likely to impact the optimization of PSCs.[49] Partial or complete removal of manual handling reduces discrepancies and errors.[50] The drop-casting technique is compatible with combinatorial high-throughput research (cHTR) approach. Key fabrication parameters can be controlled, allowing for highly reproducible results. Thus, the aim of this study is to develop it further and expand to be compatible with rapid compositional screening. In this study, the compositional space of $BA_2MA_{(n-1)}Pb_nX_{3n+1}$ quasi-2D R-P perovskites, where BA^+ acts as the bulky spacer cation and MA^+ as the lattice organic cation was explored. This was achieved by utilizing the cHTR system shown in Figure 51, where two precursor solutions of neat 3D ($MAPbX_3$) and 2D (BA_2PbX_4) perovskite solutions of identical molarities were mixed. For any given ratio of the solutions, the n-number of the resulting quasi-2D R-P perovskite can be calculated according to Eq. 18, where n is the number of 3D units within the unit cell. The n-number can be calculated from the ratio of the mole fractions of the 2D- and 3D-precursor solutions according to Eq. 19-21. To extend this library, the second screened parameter was the halide composition, where I^- was gradually replaced with Br^-. It is well known that RPP precursor solution crystallizes into a layered structure where 3D "packed" <100> crystal faces are suspended between spacers organized alternatively as ligands replacing the A-site cation.

The general study formula was derived from well-known quasi-2D R-P PSC perovskite formula: $R_2A_{n-1}M_nX_{3n+1}$[79] The following formulas will define the combinatorial compositional space:

$$BA_2PbX_4 + (n-1)MAPbX_3 \rightarrow BA_2MA_{n-1}Pb_nX_{3n+1} \tag{18}$$

$$n = \frac{\chi_{3D}}{\chi_{2D}} + 1 \tag{19}$$

$$\chi_{2D} = \frac{n_{2D}(BA_2PbX_4)}{n_{total}(BA_2PbX_4 + MAPbX_3)} \tag{20}$$

$$\chi_{3D} = \frac{n_{3D}(MAPbX_3)}{n_{total}(BA_2PbX_4 + MAPbX_3)} \tag{21}$$

where X is the halide (I or Br), χ_{2D} is the mole fraction of 2D perovskite, χ_{3D} is the mole fraction of 3D perovskite and n is the stoichiometric index represented as a function of the mole fractions.

4.3.1 Precursor solution pre-mixing

The exploration of the compositional changes requires a precise pre-deposition mixing technique. Importantly, the crystallization mechanisms of two precursor solutions are different, which is unacceptable for the compositional screening. It is important to thoroughly pre-mix all precursor solutions prior the casting. The manual mixing (on the shaker or with a use of a stir bar in a vial) is sufficient, however this approach leaves a room for volume mismatch related errors (pipetting error) and requires significant amount of time and manual handling. Hence, the microfluidic pre-mixing (MFP) is optimal for preparation of ready to cast,

on-demand pristinely mixed precursor solutions. **Figure 49** illustrates the crystallization effect of unmixed and mixed precursor solutions.
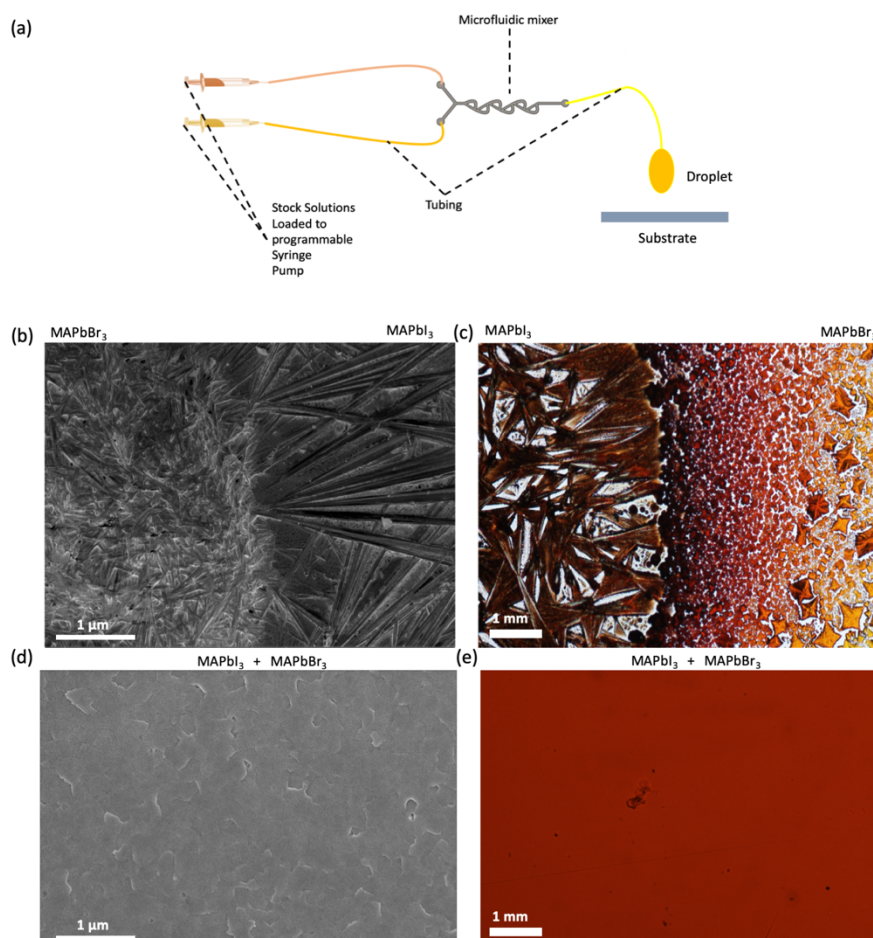
Figure 49: Illustration of mixing of the perovskite precursor solution directly prior the deposition. Precursors used: (0.4M) MAPbI$_3$ and (0.4M) MAPbBr$_3$, both with 1 wt % of MACl additive. Deposition in air on preheated to 40 °C soda lime glass substrate (10 minutes of oxygen plasma treatment prior) (a) Conceptual illustration of the single drop-casting cavity with directly pre-mixed precursor. (b-e) SEM micrograms and optical images (Nikon optical microscope, 50x) of films: two precursor solutions casted through a simple Y-connector tube (b,c), and (d-e) pre-mixed and then casted using microfluidic approach.

In this study we have used a microfluidic mixer based on an inverted Tesla valve principle combined with mixing enhancing micro-pillars[16] and T-junction passive MFPs.[17-18] This promotes rapid turbulent mixing, rather than laminar flow, allowing for complete mixing of the solutions. Microfluidic mixing in tesla valves is achieved by forcing the liquid flow through the valve against the preferred flow direction.[80-81] In combination with the MFPs, a programmable syringe pump drives the needle deposition system to deposit a precisely set 8

µL of precursor solution onto a central part of the substrate. All deposition parts are made of flexible polydimethylsiloxanes (PDMS) and rigid polytetrafluoroethylene (PTFE), which are chemically inert to the solvents commonly used for precursor solutions: dimethylformamide (DMF) or dimethyl sulfoxide (DMSO).[19-22] In the **Figure 50** the principle mechanical details of the mixing system are presented.
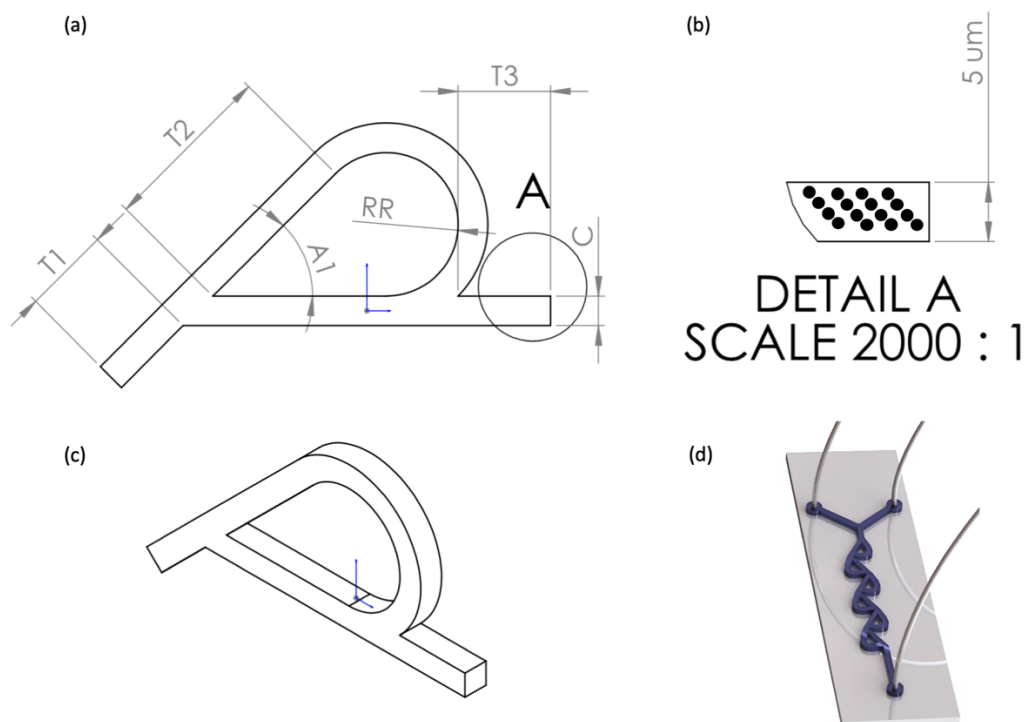
Figure 50: Single stage of Tesla-valve and key optimization parameters. (a) T1,T2, and T3 are inlet and outlets lengths proportional 1:2:1. The reverse flow is realized though T1 towards T3. The A1 angle be adjusted to increase the flow, the RR is the loop radius, (b) detailed micropillars for enhancement of the mixing, each has diameter of 1 µm, distance 1 µm, pitch 0.5 µm, (c) the single stage Tesla valve 3D view, and (d) the 3D illustration of tubular connections, top 120° T-junction for inlets, bottom for outlet.

4.3.2 cHTR deposition

This fabrication system (see **Figure 51**) allows precisely the stoichiometry of the deposited precursor solution to be tuned by adjustment of the relative mixing volumes between two different perovskite precursor solutions using programmable simultaneously-run dual syringe pumps and a multi-staged Tesla microfluidic mixer. Simultaneous variation of the MA$^+$ to BA$^+$ ratio and the Br$^-$ to I$^-$ ratio allows for the creation of a 2D-compositional map with the n-

number and the halide ratio as the two variables. For simplicity, the halide ratio is expressed as the mole fraction of I⁻ with $\chi = 1$ to pure Br⁻ with $\chi = 0$. This allowed the results as a 2D heatmap of the n-number of the formed R-P perovskite on the x-axis and the mole fraction of I⁻ on the y-axis to be presented. The precursor deposition head travels over to a singular film-forming cavity for drop casting; the head temporarily encloses the cavity reducing the evaporation rate, ensuring undisrupted (by premature drying) spread of the precursor solution. To ensure homogeneous mixing of the two precursor solutions prior to deposition, the system used microfluidic passive mixers (MFP).[15] The thoroughly mixed, homogeneous precursor solutions are subsequently deposited on mildly preheated (60 °C) poly(3,4-ethylenedioxythiophene) polystyrene sulfonate (PEDOT:PSS)-coated indium tin oxide (ITO) glass substrates using a blunt needle attached to a robotic head controllable in a XYZ direction. After the average spread time (~10 s), the gas valve triggers and gently opens the gas flow that dries the precursor solution. The freshly made film is gas-quenched with a uniform N_2 stream for 2 minutes. Control of the gas flowrate deposition head allows for rapid solvent evaporation, inducing the nucleation of the perovskite crystal to ultimately form well-textured and highly crystalline films.[13] The head moves over to the next position on the hot plate and repeats the steps. After the deposition of all intended films, the hotplate enters the post-annealing stage by increasing (ramping 5 °C per minute) the temperature to 100 °C and then naturally cools down back to RT.
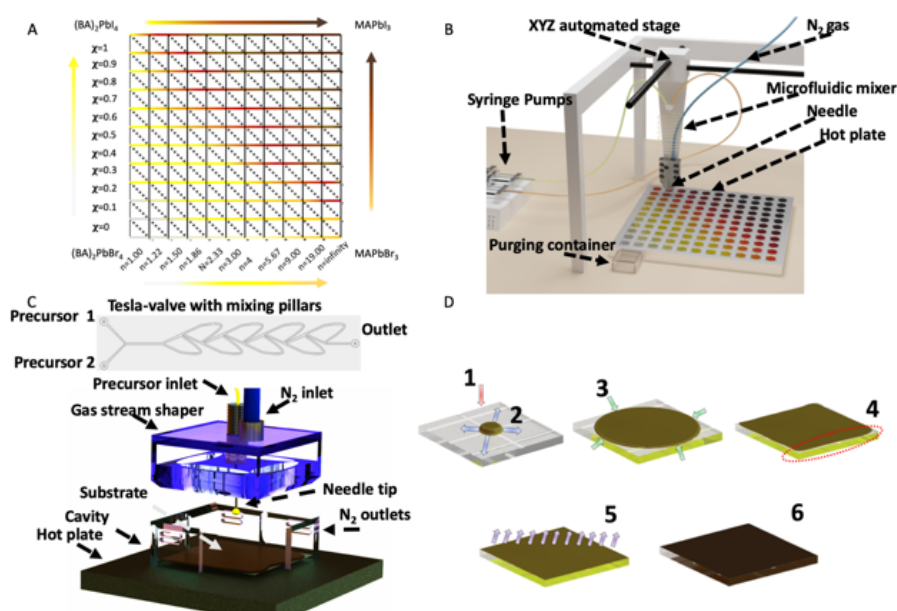
Figure 51: The combinatorial high-throughput spin-coating free perovskite film deposition system. A) Compositional matrix for the $BA_2MA_{(n-1)}Pb_nX_{3n+1}$ perovskite system. B) A conceptual view of the key components and working principle of the cHTR system C) The deposition head with the film crystallization cavity. Top inset: the multi-staged microfluidic inverted Tesla valve. D) The spreading and crystallization mechanism: (1 – red arrow) – syringe pump stroke pushes the droplet onto the substrate; (2 – blue arrow) isotropic movement distributes precursor; (3 – green arrow) precursor reaches the edge (4) causing the van der Waals surface tension to break and the solution to spread along the edge; (5) solvent evaporation and (6) timely application of N_2 quenching gas facilitates film formation.

To enable controlled moisture and oxygen-free environment, the robotic platform was placed inside a N_2-filled glove box. Such design allowed for an uniform temperature gradient inside of the cavity (**Figure 52**), which was a great benefit for controllable crystallization which cannot be achieved with manual, uncovered deposition.
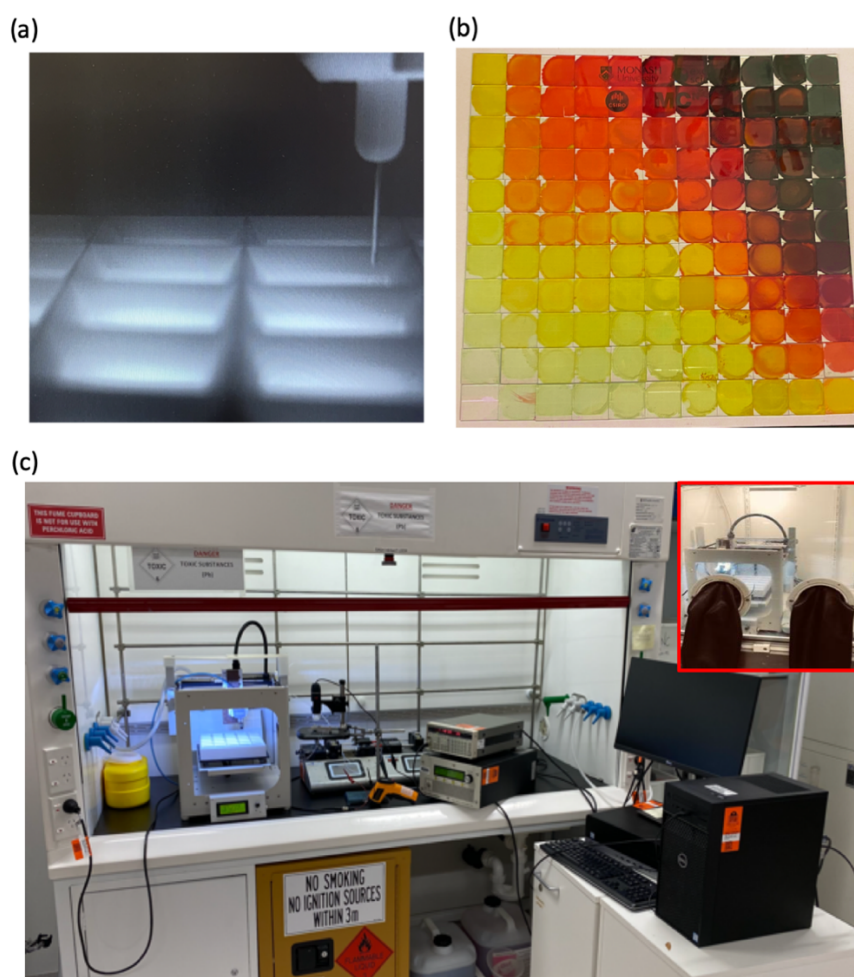
Figure 52: (a) Thermal image of the deposition cavity at 100 °C, (b) Drop-casted matrix of films produced with cHTR drop-casting robot. (c) The cHTR deposition system used for this study (inset: the same system built inside of the glove box).

4.4 Results and Discussion

This methodology lead to pin-hole free films with grain sizes of > 1 µm and a root-mean-square (RMS) roughness of ~1.1 nm for an area of 10 x 10 µm **(see Figure 53).**
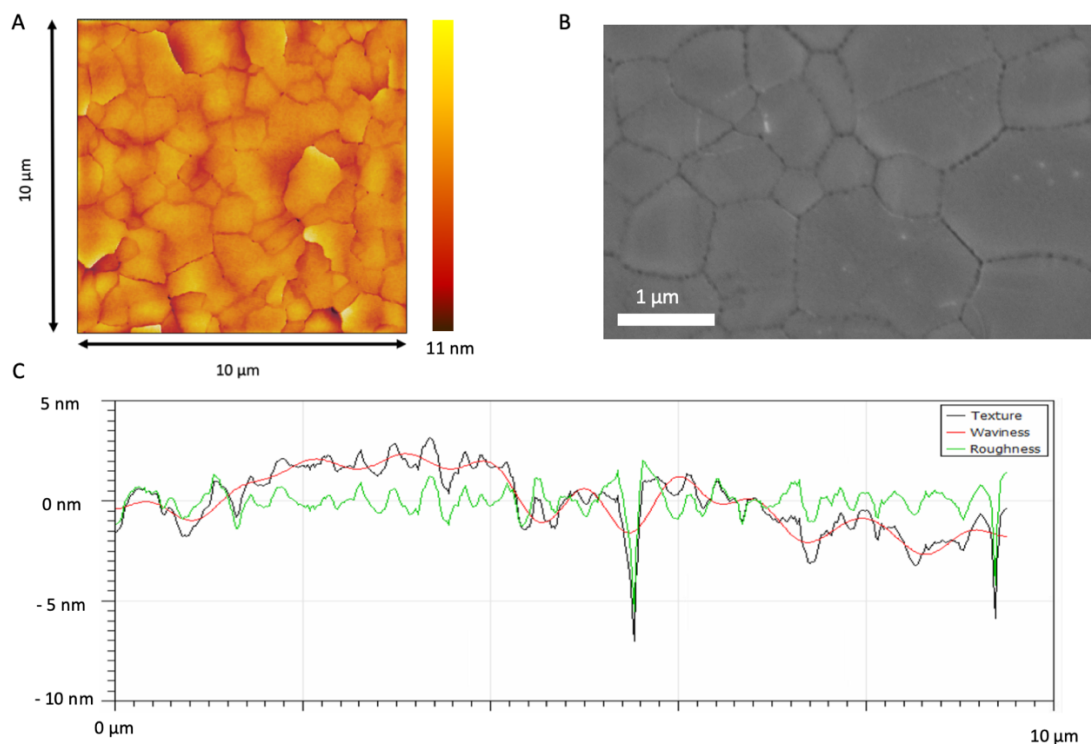
Figure 53: A) AFM topographical image of a perovskite film (n = 5.57, χ = 0.8). B) SEM microgram exhibiting a perovskite film (n = 9, χ = 0.9) with compactly packed grains with an average of ~800 nm. C) typical RMS measurement accomplished in program Gwyddion® using function "calculate roughness parameters" across 10 µm.

The morphological quality of crystal grains and resulting films is sufficient for solar cell fabrication.[82-83] From these were extracted PL, UV-vis, PESA and XRD measurements. The optoelectronic and crystallographic properties of thin films of the $BA_2MA_{(n-1)}Pb_nX_{3(n+1)}$ perovskite systems are presented as heatmaps in **Figure 54**. The steady-state photoluminescence (PL) maxima are shown in Figure 54A and show a clear redshift for both an increase in iodide incorporation into the perovskite lattice (χ =0 to χ =1) and increasing n-number of the RP-perovskite. The PL of the neat 2D- and 3D-perovskites agree well with previous reports,[25-28] showing a PL of ~520 nm for BA_2PbI_4 (n= 1 and χ = 1), ~419 nm for BA_2PbBr_4 (n= 1 and χ = 0), ~774 nm for $MAPbI_3$ (n= ∞ and χ = 1) and ~568nm for

MAPbBr$_3$ (n= ∞, χ = 0). In addition, the PL peaks of films for n= 1,3,4 and χ = 0 correspond to previous reports of single crystal studies and further confirmed the accuracy of our cHTR system.[29] Moreover, for χ = 0.7 and n= 4, we obtained perovskite films with PL emission peaks and photophysical properties more suitable for photovoltaic applications,[13] in agreement with previous studies.[14, 25]
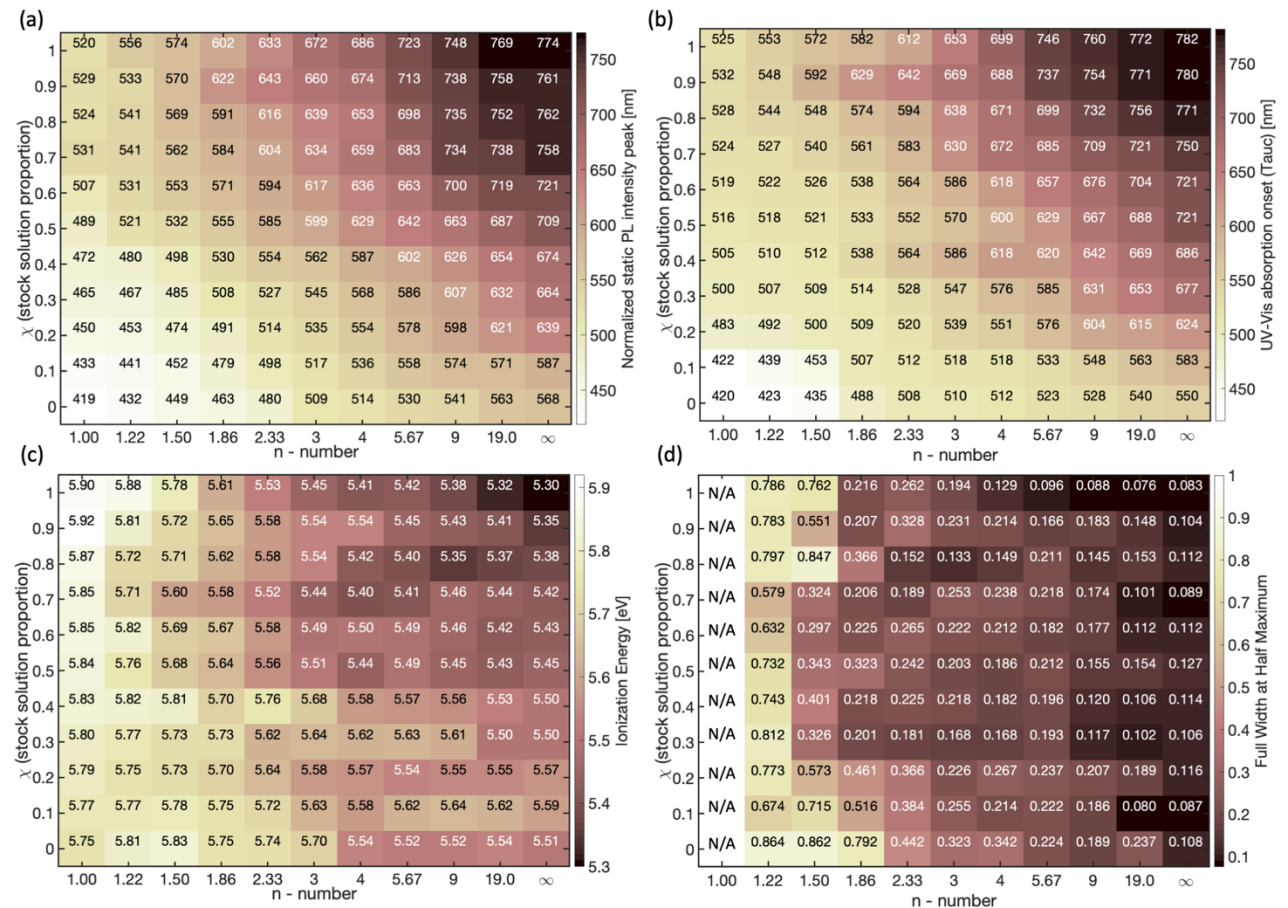
Figure 54: Optoelectronic and crystallographic properties of thin films of the BA$_2$MA$_{(n-1)}$Pb$_n$X$_{3n+1}$ perovskite system deposited with our cHTR system. A) Steady-state photoluminescence (PL) maxima (nm). B) Optical absorption (UV-vis) onsets (nm), approximated from Tauc plots. C) Ionization energy (eV) from photoelectron spectroscopy in air (PESA) measurements. D) Crystallinity of the perovskite films expressed as the full width at half maximum (FWHM) of the ABX$_3$ perovskite peak at ~14°, a smaller number represents a greater crystallite size. Examples of the data and data extraction process can be found in Appendix D.

The absorption onsets are shown in Figure 54B and follow similar trends to the PL, with a continuous redshift with increasing iodide concentration and n-numbers. This is in agreement with previous reports,[25-26] which observed a narrowing of the bandgap with an increase in the

n-numbers for R-P perovskites between n= 3.00 and n= ∞. A narrower bandgap allows for lower energy photons to be absorbed, thus increasing current densities, however, since these photons thermalize at lower energy, a lower V_{OC} is expected. This trade-off also occurs when varying n-numbers, where the number of superposition of stacked 3D units separated by BA dictates the material's properties. Figure 54C summarizes the ionization energy (IE) determined by Photoelectron Spectroscopy In Air (PESA) measurements as a function of the n-number and χ. We observed that both the introduction of MA^+ and the introduction of Br^- lower the ionization energy of the resulting perovskite material. However, it is worth noting that the n-number has a greater impact on the IE than the variation in halide from I^- to Br^-, noted as χ. For example, from the pure 2D BA_2PbI_4 (n=1, χ= 1) to the pure 3D perovskite $MAPbI_3$ (n=infinity, χ =1) the change in IE is 0.59 eV, whereas from 2D BA_2PbI_4 (n=1, χ =1) to 2D BA_2PbBr_4 (n=1, χ =0) it is 0.14 eV. The degree of texturing and crystallinity was determined using x-ray diffraction (XRD) analysis (Figure 54D). The XRD patterns correspond with previous reports, with diffraction peaks located at 2θ = ~19.1°, ~6.8°, and ~13.9° able to be assigned to $BA_2MA_{(n-1)}Pb_nX_{3(n+1)}$ relevant for our compositional space n= 1, 3, 4, thus confirming the formation of layered quasi-2D R-P perovskites.[26-28] We identify neat 3D perovskites, with peaks located at 2θ = ~14.9°, ~28.5° and ~43.1°[29] associated with $MAPbI_3$ (n = ∞) and $MAPbBr_3$ (n = ∞) peaks located at 2θ = ~14.9°, ~30.5°[30], validating our methodology (on Figure 39). The peak around ~14° is characteristic for $MAPbX_3$ 3D perovskites and appears in all films apart from the neat 2D perovskite films (n= 1). In order to compare the crystallinity of the various compositions, we extracted the full width at half maximum (FWHM) of the main XRD peak assigned to the 3D $MAPbX_3$ perovskite (see Figure 38E), located between 2 angles of ~14.2° for the (110) $MAPbI_3$[31] peak and 14.9° for the (100) $MAPbBr_3$.[30] This FWHM heatmap allows for quick visualization of the degree of crystallinity of the 3D component throughout the entire compositional library. Thus, we established that films with lower n-numbers tend to be less crystalline in the 3D structure. Significant broadening of the 3D peak occurs for n-numbers lower than n= 4. To study the impact of optoelectronic and crystallographic properties on the device performance we prepared perovskite solar cells using the drop-casted perovskite films from the cHTR setup. Following the optical and structural characterization of the needle-coated perovskite films, the layer of phenyl-C61-butyric acid methyl ester ($PC_{61}BM$) was spin-coated on top, and then layers of C_{60}, bathocuproine (BCP) were evaporated in a single-vacuum session consecutively, finally a Ag layer was evaporated,

which served as electron selective and charge collection electrodes (**see Figure 55**). All layers were incorporated into well-established, inverted p-i-n architecture comprised of: ITO|poly(3,4-ethylenedioxythiophene):polystyrene sulfonate (PEDOT:PSS)|$BA_2MA_{(n-1)}Pb_nX_{3(n+1)}$|phenyl-C61-butyric acid methyl ester ($PC_{61}BM$)|C_{60}|bathocuproine (BCP)|Ag.[32-36]
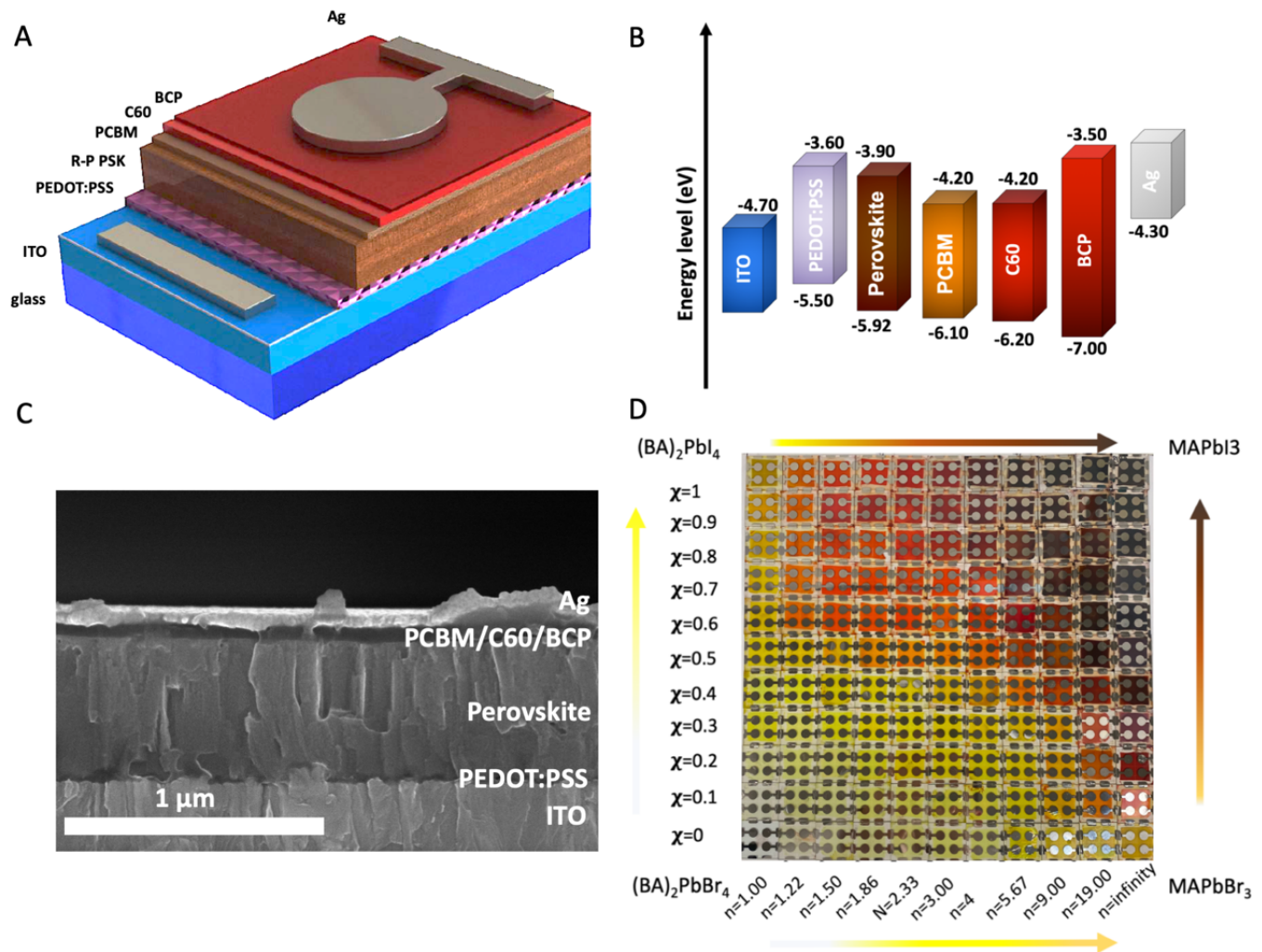
Figure 55: R-P perovskite solar cells. A) Schematic view of the p-i-n perovskite solar cells produced (inverted structure: ITO|poly(3,4- ethylenedioxythiophene):polystyrene sulfonate (PEDOT:PSS)| $BA_2MA_{(n-1)}Pb_nX_{3(n+1)}$ | phenyl-C61-butyric acid methyl ester ($PC_{61}BM$) | C_{60} | bathocuproine (BCP) | Ag; active area: 0.16 cm^2), B) Energy level diagram of the functional layers within the PSCs. C) A cross-sectional SEM image of a device. D) A top-view image of a series (121 substrates, 484 devices) of devices spanning the entire $BA_2MA_{(n-1)}Pb_nX_{3(n+1)}$ compositional space corresponding to the compositions presented in Fig. 38A.

In total, the system fabricated three sets of 121 samples, where each sample contains four individual solar cells, corresponding to a total of 1452 PSC devices. The automated and

controlled needle drop-casting allowed for uniform and highly reproducible films across the active area where the electrode was later evaporated. **Figure 56** shows the photovoltaic performance parameters (V_{oc}, J_{sc}, PCE, and FF) for the $BA_2MA_{(n-1)}Pb_nX_{3n+1}$ compositional space. The photovoltaic performance of the PSCs was characterized with previously reported cHTR measurement setup[37] which allowed for a reduction in the measurement time from hours to minutes. The short-circuit current (J_{SC}) increases with higher n-numbers and χ of iodide, consistent with the red-shift of the absorption onset and the associated increase in light-harvesting efficiency. Solar cells composed of RPPs with high n-numbers (n> 9), and high iodide mole fractions (χ >0.8) showed larger J_{SC} values than their $MAPbX_3$ counterparts (n=∞) despite their inferior light-harvesting properties. The highest J_{SC} value was observed for a pure iodide quasi-2D R-P PSC (χ= 0.9, n= 19). This could be attributed to improved film quality upon the addition of a small amount of BA and Br. Whilst high bandgap materials usually hold the promise of increased V_{OC}, the opposite trend is observed here. The V_{OC} of quasi-2D R-P PSCs were found to decrease with decreasing n-number and I-mass-fraction but stabilizes to ~0.9-1.1 V for χ> 0.7 and n> 3. This illustrates that bandgap-engineering is in itself is insufficient to guarantee improved V_{OC}, with it also being dependent on a number of other parameters, such as the adjacent charge-transporting materials[38-39] and their built-in potential,[40] the quality of the deposition,[41-42] which is likely to cause recombination or carrier diffusion/tunnelling effects,[43] and intra- and inter-grain potential barriers.[44] It was also observed that $MAPbX_3$ PSCs show the highest voltages for pure $MAPbI_3$ and $MAPbBr_3$, while the mixed halide analogues around χ= 0.5 show slightly decreased voltages. The highest FFs of about 64.6% were observed for n= 9 and/or χ= 0.9. This is higher than the FF observed for pure $MAPbI_3$ (59.7%). Similar to the trend noted for V_{OC} and J_{SC}, there could be observed a sharp decrease in FF values with decreasing χ and n. The PCE as a product of J_{SC}, V_{OC}, and FF follows a similar trend, with low efficiencies for low n and χ values. Remarkably, quasi-2D R-P PSCs with small additions of BA and Br showed the highest efficiencies of up to ~11.5%, significantly outperforming $MAPbI_3$ (PCE= 9.7%). The maximum performance for MA can be observed at n> 9 and χ> 0.7 , indicating that a small amount of BA improves the perovskite. Similar to other reports,[30] the small Br⁻ content improved the V_{OC} whilst lowering the J_{SC} (mainly due to narrower absorption which in case of increased content resulted in significant PCE drop). Interestingly, lowering the χ for purely 3D and n = 19, the trend shows improved V_{OC} upon Br⁻ content increase, however, the BA combined with Br⁻ for χ<0.4

drastically lowers the V_{OC} due to the wide bandgap and low current caused by the low absorption. The highest performing devices were obtained with perovskite compositions located in the upper-right corner of the compositional space, coinciding with previous reports of 2D quasi-RP perovskites.[45-46]
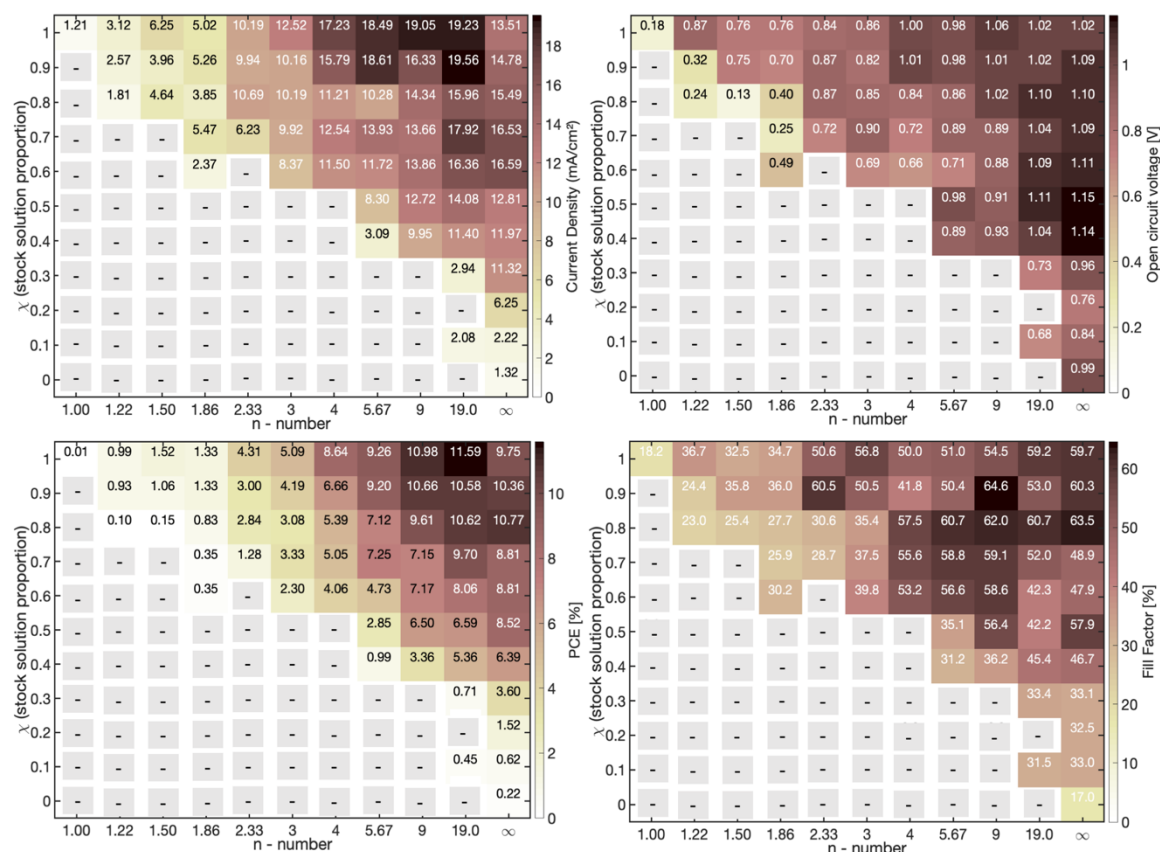
Figure 56: Photovoltaic performance. Performance heatmaps representing working champion devices. The dash-line represent samples which were excluded from the heatmap due to short-circuit. (A) Short-circuit current density (B) Open-circuit voltage. (C) Power Conversion Efficiency and (D) Fill factor. Examples of the data and data extraction process can be found in Appendix D.

The overall trend indicated that we obtained an increase in performance towards the top right corner of the compositional space heatmaps, mostly due to the bandgap narrowing. Remarkably, we noted that the pure 3D PSC resulted in worse performance than the adjacent candidates with a slight addition of BA or MA; it is attributed mainly to fewer pinholes (BA is known to facilitate better crystallization required to fully transition to perovskite phase and removal of the residual solvent),[25] better V_{OC} induced by small Br content,[26-27] and the inherent thermal instability of volatile MA cations.[28] The top left corner illustrates how widening the bandgap and elevating the ionizing energy results in lower device performances.

A number of reports[29-31] observed significant gains in perovskite film quality and resulting device performance when adding excess PbI_2 to the precursor solution to improve their optoelectronic properties. Therefore, using the high-throughput system, a systematic study of adding excess PbI_2 to the $BA_2MA_{(n-1)}Pb_nX_{3n+1}$ perovskite system was conducted. The parameter screening experiment was repeated with an excess of lead iodide present. The ratio between Pb and A was kept constant (with the A = BA + MA), yielding to $MA_{(1-n)}BA_nPbX_3$ (with n = 0-1). The PV trends were similar to what was described in Figure 41, highest V_{OC}, J_{SC}, FF, and PCE were observed for pure iodide (χ = 1) RP PSCs with n between 4 and 8. Again the record PCE for the quasi-2D Ruddlesden-Popper (~14.5 %) was significantly higher than that for the pure $MAPbI_3$ compound (~9.6 %) and superior to that achieved in the absence of PbI_2 (see above). As shown in **Figure 57**, the compositional space with PbI_2 excess follows similar trends, although, in good agreement with previous reports, PbI_2 improved the electrical properties and yielded better results allowing for champion PCE of ~14.5% for 0.16 cm^2.
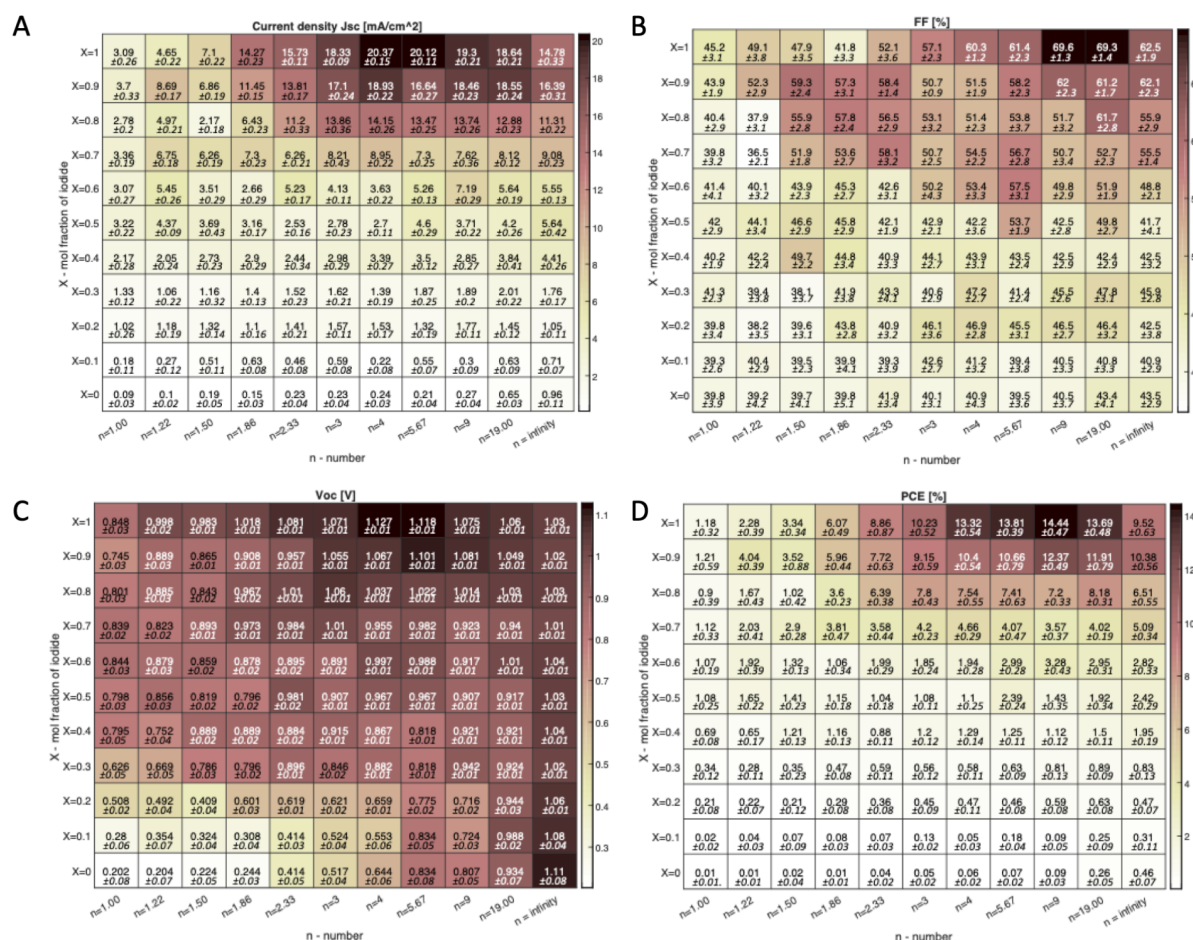

128

Figure 57: Photovoltaic performance heatmaps representing average device performance and standard deviation (each datapoint corresponds to a statistical average of 2 to 12 devices) derived from photocurrent-voltage curves. The data has been extracted from devices fabricated with our high-throughput perovskite deposition method. (A) Short-circuit current density, (B) open-circuit voltage, (C) power conversion efficiency, and (D) fill factor. Examples of the data and data extraction process can be found in Appendix D.

Using the perovskite precursor composition which yielded the highest PCE in presence of excess PbI$_2$ (n=9, χ=1), the subsequent optimization iteration was conducted. The samples still exhibited edge effects, known as "coffee rings",[25] which is in good agreement with previously reported publications.[13, 26-27] The "coffee ring" effects were investigated and mitigated in analogous deposition techniques[26, 28-31] via solvent engineering, surface wettability improvements or substrate temperature control.[32-35] As an incorporation of γ-butyrolactone (GBL) into the solvent mixture has been widely reported to increase the crystallization time-window and hence it improves the device performance for PSCs, especially the improvement is pronounced in deposition techniques where droplet spread is critical for film formation.[28, 36-40] Here, GBL lowered the vapor pressure of the precursor solution, thus slowing down the drying process and conversely resulting in more uniform films by better control of the nucleation rate. Starting with the highest performing composition with an excess PbI$_2$ from Figure 57 (n = 9, χ = 1), we screened the solvent composition by gradually replacing DMF/DMSO blend with an aliquot of GBL (see **Figure 58** for SEM micrograms of films). As expected, the introduction of GBL to the precursor solution improved the device performance associated with larger grain sizes. The table below summarizes the photovoltaic parameters for devices prepared with an increasing amount of GBL in the precursor solution. The total volume during the precursor solution preparation was fixed to 1 mL, DMF:DMSO volume fractions were set to 9:1. The replacement of 30 µL of DMF/DMSO blend with 30 µL of GBL leads to the highest efficiency of PCE= 15.9 %. The improved PCE derives from both an improvement in J_{SC} and V_{OC}. Once the best stoichiometry was identified (see Figure 42: n = 9, χ = 1) and the best solvent blend, the device fabrication was realized and subsequentially investigated. It shows the *J-V* curves of the champion device with neglectable hysteresis (< 0.1 %). The stabilized PCE of 15% after 200 hours (encapsulated device at maximum power point condition, 1 Sun in temperature of 25 °C) is presented in the Figure 59.

Photovoltaic properties of the champion devices of structure ITO|PEDOT:PSS|perovskite|PCBM|C60|BCP|Ag. All devices were measured under simulated solar light (1 Sun) through an aperture mask of size 0.16 cm^2 with a scan rate of 100 mV s^{-1} at 25 °C, RH 40%.

PSC device[a]	0 µL	10 µL	20 µL	30 µL	40 µL	50 µL	60 µL	70 µL	80 µL	90 µL	100 µL
V_{OC} [V]	1.07	1.08	1.1	1.1	1.06	1.05	0.99	0.88	0.66	0.56	0.62
J_{SC} [mA cm^{-2}]	19.29	18.74	19.71	20.82	19.44	17.73	12.32	13.71	8.35	6.29	5.54
FF	69.6	68.6	69.1	69.6	63.9	59.8	55.8	54.3	47.6	43.5	39.9
PCE [%]	14.3	13.9	14.9	15.9	13.2	11.7	6.8	6.5	2.6	1.5	1.4

[a] Values extracted from the *J-V* characterization; V_{OC} – open-circuit voltage, J_{SC} – short-circuit current density, FF – fill factor, PCE – power conversion efficiency.

The positive effect of the DMF/DMSO to GBL solvent participation (exchange) in the champion composition with excess lead iodide (see **Figure 59**) of n =9,χ =1 was further investigated using Time-Resolved PL (TRPL) on as-prepared fresh films on glass (see Figure 44). Samples with 0, 10, 20, 30 and 40 µL of GBL were found to have profoundly longer fluorescence lifetimes, which led to conclusion that the presence of GBL during crystallization suppresses non-radiative charge-carrier recombination by the formation of better-quality films (Figure 58).
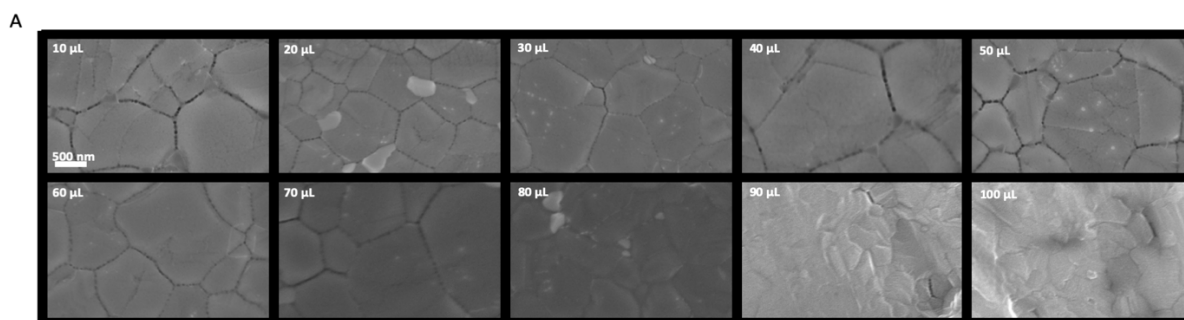
Figure 58: (A) SEM micrograms illustrating surface morphology of the films obtained by solvent exchange: DMF/DMSO replaced with GBL (exchanged volume in top left corner of each microgram).

With further samples (more GBL participation) was observed that the fluorescence lifetime was reduced. Experiment lifetimes confirm previous reports where the poor quality of films induced recombination mechanisms and trap-states.[84-85]
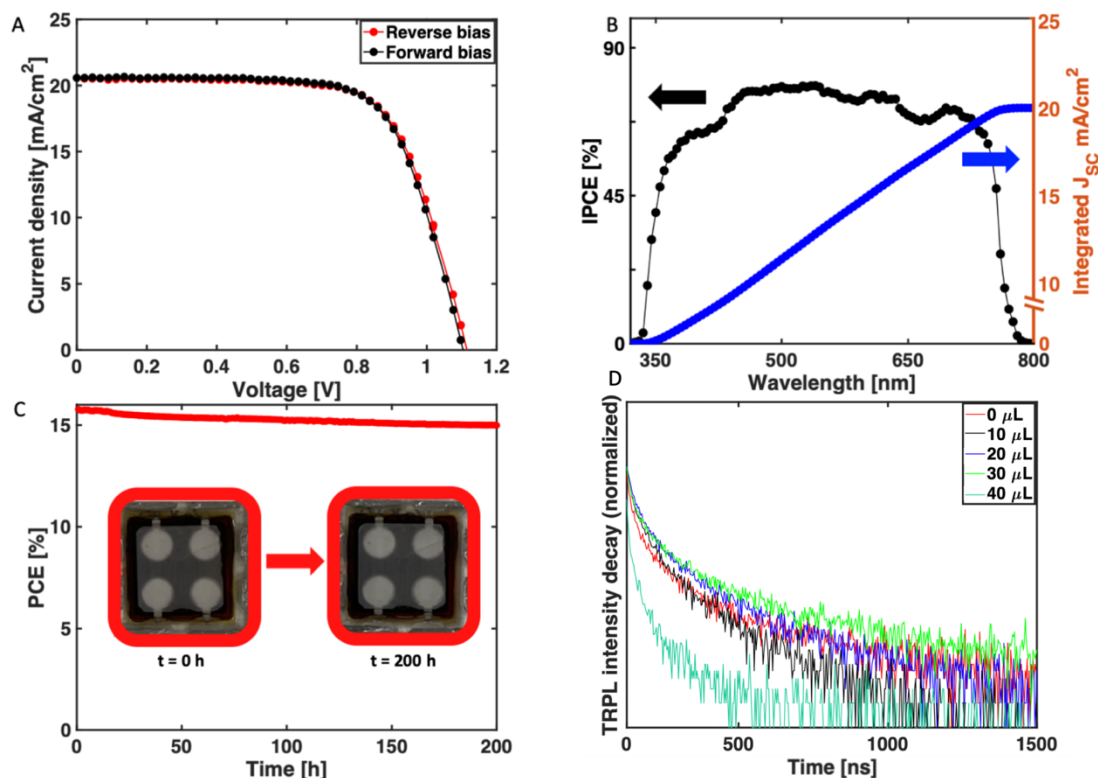
Figure 59: The solvent engineering approach for solar cell performance investigation and improvement. (A) J-V curve of the champion device. (B) Incident photon to charge carrier efficiency (IPCE) and integrated photocurrent. (C) Stability testing of encapsulated devices under 1 Sun, maximum power point tracking (MPPT) over 200 hours. (D) Time-resolved photoluminescence decay (TRPL), excitation at 400 nm, emission >700 nm indicating that 30 µL significantly improves, but excess (> 40 µL) of GBL hinders perovskite performance.

4.5 Conclusions and Future Outlook

This work demonstrated a simple, combinatorial high-throughput fabrication system for the quasi-2D R-P subclass perovskite solar cell fabrication which allowed the discovery and study of numerous samples, produced with a high degree of reproducibility and accuracy. The fast-automated deposition of homogeneously mixed precursor solution with carefully chosen stoichiometry obtained by timed volumetric mixing allowed for rapid testing of compounds

span from strictly 2D to strictly 3D, representing n numbers equal to: 1.00, 1.22, 1.50, 1.86, 2.33, 3.00, 4.00, 5.67, 9.00, 19.00 and ∞. This study presents an extraordinarily fast, easy, and relatively inexpensive method for acquiring a large PSCs property library required both for systematic and reproducible reporting. The system can be also utilized for the optimization techniques (solvent engineering, stoichiometric lead iodide excess) of a potentially scalable compound which are found by a systematic approach. Importantly, the films obtained by such an approach follow a newly developed quasi-2D R-P equation which translates to an exact composition heatmap, hence a potentially outstanding sample can be magnified, narrowed, and explored more thoroughly to unveil its promise. The approach succeeded in optimization of the device by discovering potentially highly efficient candidates and narrowing down the optimization study in order to boost specifically chosen features. Alongside the system points that multiple parameters can be chosen for further optimization e.g. wider bandgap materials that perform worse in terms of photocurrent generation. The system allowed for a remarkable reduction of the "coffee ring" effect which can potentially shine a new light on that issue and pave a new way of reducing material waste in other known scalable fabrication techniques. We can envisage a multitude of studies and future outlook which can be accomplished with this or similar robots; namely compound stability, crystallinity, surface roughness, topology studies, mostly oriented on tandem perovskite-silicon solar cell applications. The essential methodology is scalable and represents an extension of previously reported studies where the compositions were resulting from lengthy, often nonsystematic, erroneous, and manual studies. Beneficially, the system ushers an inexpensive, combinatorial, and highly accurate way of solar cell device film fabrication.

5. Surfactant- and Polymer-Enhanced High-Throughput Fabrication and Optimization of Quasi-2D Ruddlesden-Popper Perovskite Solar Cells

5.1 Context and motivation

The previous chapter provided a good insight into cHTR systems and allowed the successful production of multiple RPP films. The focus was on the development of 2DRP films which are structurally layered, quasi-2D Ruddlesden-Popper perovskites. [43] As was previously explained, they offer a potential solution to PSC stability issues.[44] It is reiterated in this paragraph that the 2DRP crystals **(Figure 60),** with the general formula $R_2(MA)_{n-1}M_nX_{3n+1}$, are formed by large halides and bulky aliphatic or aromatic cations that intercalate between well-defined inorganic octahedral "packs" of $[MX_6]_4^-$ due to van der Waals forces from the aliphatic groups.[45] Like their 3D counterparts, 2DRPs have easily tuneable band gaps,[46] can be solution-processed,[47] and exhibit commercially competitive device PCE of ~17-18 %.[48-49] The dielectric mismatch of organic and inorganic components creates a favorable environment for the formation of quantum wells and barriers,[50] generating an excellent perovskite for excitonic phenomena.[51-53]

However, there is a lack of studies exploring the improvement of stability for an existing more stable subgroup of perovskites for example through polymer framework incorporation known in ABX_3 perovskites. Hence the aim of this study is to explore this niche.
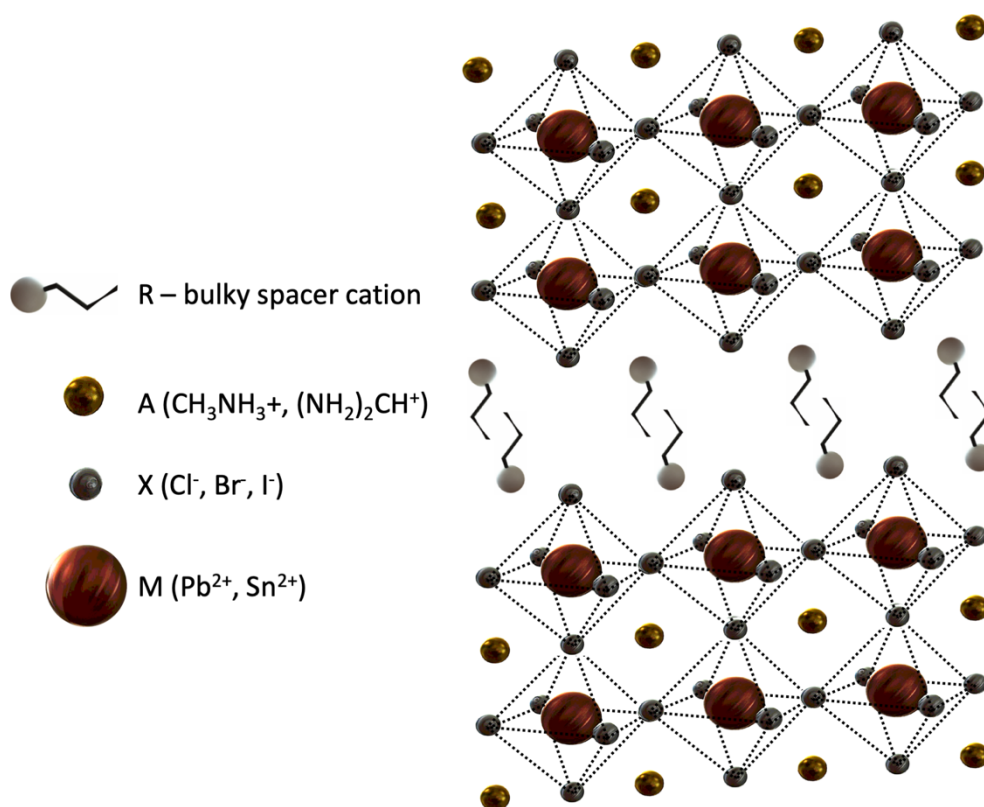
Figure 60: Crystal structure of quasi-2D Ruddlesden-Popper perovskite where R+ (bulky cation spacer) intercalates in the crystal lattice resulting in the enhancement of the structure stability.

Crystals of 2DRP[54] confer a stability increase by virtue of the hydrophobic aliphatic layers of its alternating structure that limit water ingress,[50, 55] and like 3D PSCs, their properties can be enhanced with a range of perovskite property-modifying additives.[56] For example, polyvinylpolypyrrolidone (PVP),[57-58] which is widely employed in ABX$_3$ PSCs, exhibits hydrogen bonding between its carbonyl groups and the protic polar species present in the 2DRP, leading to the creation of a polymer framework around the crystal structure that furthers enhances stability[59-61] As mentioned in the previous chapter, the use of R$^+$ in the crystal lattice relaxes the GTF,[62] resulting in potentially hundreds of thousands of undiscovered, yet highly-performing, compositions.[63-65] In this study, the perovskite precursor solution and stock solution of a particular additive is mixed. In order to address the behavior of polymers or surfactants, a more mechanical yet precise mixing pathway was required. By harnessing an ultrasonic piezoelectric microfluidic mixer, highly reproducible, spin-coating free perovskite films could be fabricated with intervals of stability increasing additive and spread enhancing protein concentrations. As stated in Chapter 4, 2DRP perovskite precursor solutions at molar

concentrations below 0.7 M crystalize into uniform and highly crystalline films via a low-temperature deposition technique called drop-casting.[13, 66] This extraordinary phenomenon of 2DRP (spin-coating free) film formation via drop-casting originates from the mechanism that drives the spread of the precursor solution, and subsequentially facilitates crystallization. Unlike their ABX_3 counterparts, there are few 2DRP studies focused on crystallization or spread mechanisms (e.g., using surfactants), providing an opportunity for discovery of film formation enhancement agents that can generate high-performing perovskites with superior stability. The drop-cast 2DRP perovskite film quality depends on a number of factors, such as precursor molarity, substrate temperature, and roughness, hydrophilicity or hydrophobicity of the perovskite adjacent charge-transporting layer and spread of such precursor, and environmental conditions (pressure, humidity, temperature, atmosphere)[67-68]. Given these factors, this study focused on the development of inexpensive, yet highly controllable and rapidly deployable techniques that expand the mechanism of perovskite drop-casting in air for rapid combinatorial screening of 2DRPs. in this chapter, the automated cHTR screening deposition platform is described that fabricates multiple perovskite film compositions via carefully aliquoted, microfluidic-mixed precursors and stock solution volume ratios. This system allows for fully controllable, synergistic mixing and casting of well-defined precursor solutions and modifying additives at the same time. In contrast with the work reported in the previous chapter, instead of creating heatmaps, iteratively screened performance was used that allowed for optimization and development of the champion recipe. **Figure 61** shows the workflow that guided this study.

1. Ruddlesden-Popper perovskite possible combinations
2. Fabrication outcomes

   Best Candidates

3. Accurate and reproducible recipe

   Fully Controlled Pristine Best Performers

4. Fully Refined, Tested and Confirmed Recipe
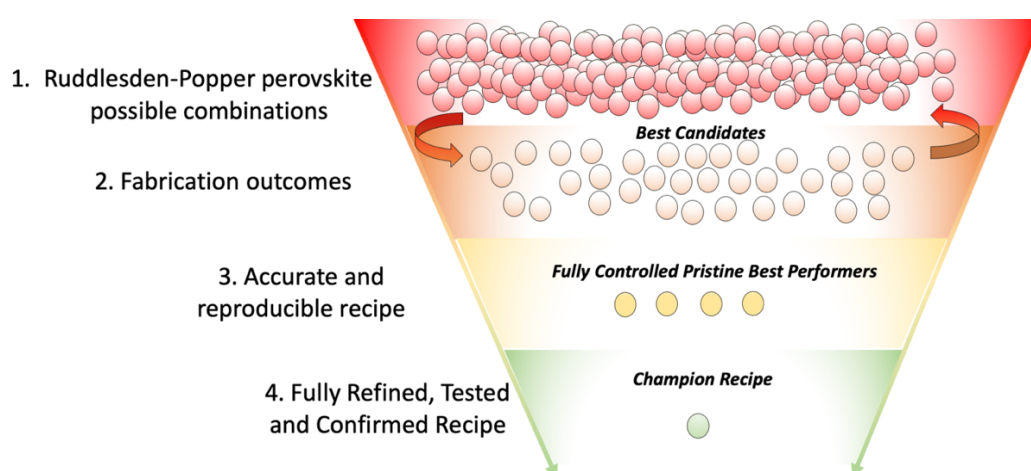
   Champion Recipe

Figure 61: Illustration of the process workflow with cHTR enhancement for narrowing down and accelerating the 2DRP recipe optimization. Each circle represents a batch of experiments.

5.2 System design

The cHTR approach developed here significantly enhances the simple, but often irreproducible, hand-held drop-casting methodology.[27-28] Unlike the previous study that focused on GB-inert atmosphere deposition, all films were produced in the air. This system consists of a programmable syringe pump for exact volume dispensation and volume-to-volume precursor solution mixing. Importantly, the system is capable of thoroughly mixing two precursor solutions prior to the deposition with an interconnected ultrasonic piezoelectric microfluidic mixer (see Appendix C for details). The outlet from this mixer is directly connected to a blunt needle that dispenses the aliquoted volume perpendicularly and centrally onto the substrate. (see **Figure 62** for more details). The deposition process is split into five key steps (see Figure 62B). First, the precursor solution droplet is formed at the end of the needle tip and the strong polarity of the precursor[29-30] as well as the surface tension,[31] keeps its teardrop shape. Second, the surface tension is broken once contact is established between the substrate and the droplet, and the syringe stroke aids solution flow. Subsequently, Tanner's law of droplet spread on solid surface[32] dynamically drives the isotropic distribution of the liquid precursor. The spread is influenced by the substrate type, temperature, roughness, and the hydrophobicity or hydrophilicity of the charge transporting layer (given that the film is produced directly for the PSCs). To probe the hydrophobicity properties, a range of surfactant concentrations was screened, aiming for the increased spreading induced by Marangoni flow.[33-34] Next, with the surface evenly wetted, solvent evaporation causes an increase in precursor concentration to its crystallization point. Finally, a nitrogen (N_2) gas stream is applied to quickly decrease the solution temperature and accelerate solvent removal, thereby inducing rapid and uniform crystallization. Such gas quenching reduces momentarily the solution temperature and accelerates the solvent vapor removal. Using an XYZ stage (see Figure 62c), the deposition system then continues to make an array of films of a variety of compositions.
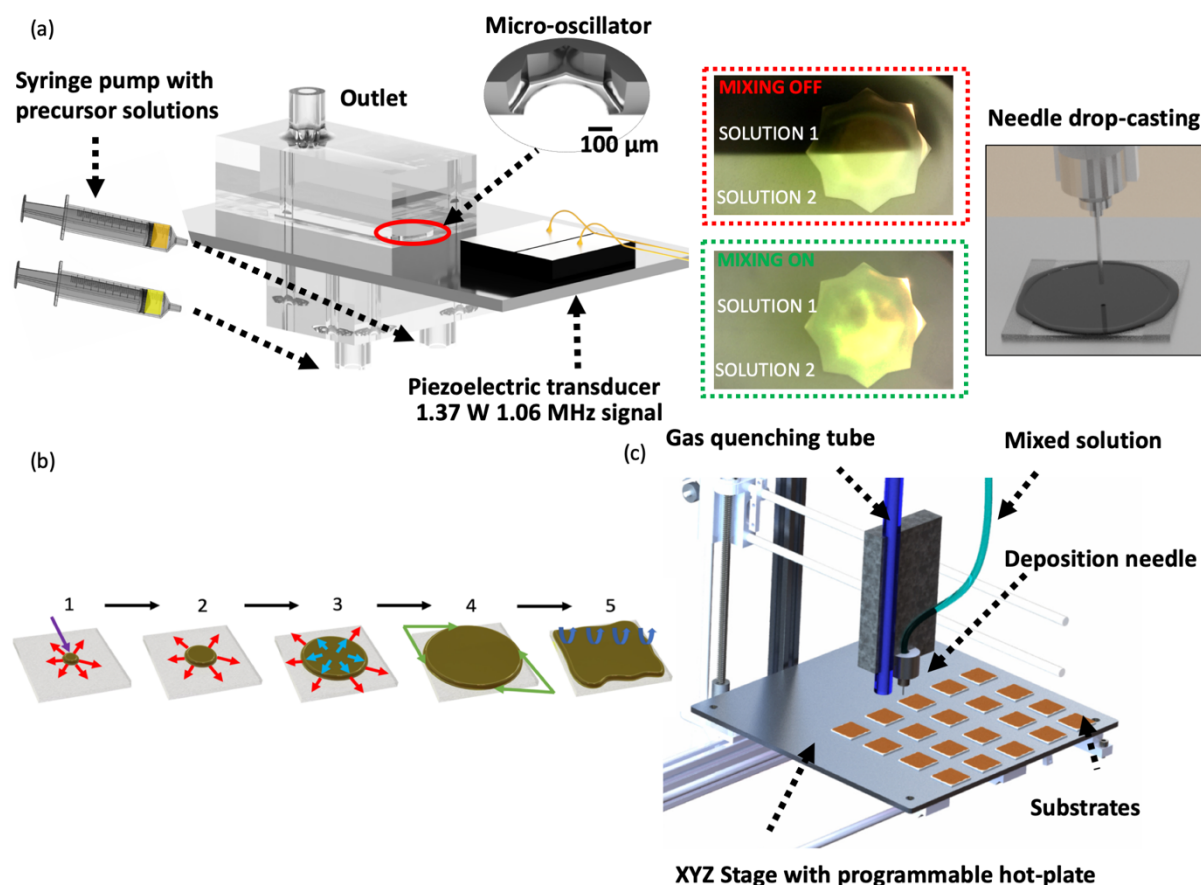
Figure 62: High-throughput automated deposition system for quasi-2D Ruddlesden-Popper (2DRP) perovskite optimization. (a) Conceptual overview of the deposition: two preloaded syringes introduce precursor solutions, the microfluidic mixer activates and mixes the two precursors and delivers it through a single outlet to the needle positioned directly above the preheated substrate. The central picture shows the ultrasonic microfluidic mixer used for this study for rapid solution preparation prior to deposition: the solutions are mixed in the chamber and the piezoelectric vibration element ensures complete mixing at a high flow rate. (b) Precursor solution deposition and crystallization mechanism split into five major steps: deposition with isometric spread caused by syringe stroke (1-2), surface tension drive the solution to the edge of the substrate (3), the solution's contact with the edge guides the solution allowing for further spread (4), solvent evaporation leads to an increase in precursor concentration to it crystallization point, causing the rapid film formation. (5), the row: i, ii and iii shows typical area useful for solar cell depending on the solution spread. (c) Illustration of the system used for the deposition of multiple compositions on an array of substrates.

5.3 Results and Discussion

5.3.1 2DRP perovskite base for high-throughput study

First, the drop-casted 2DRP perovskite films were explored via manual deposition (see **Figure 63**). These reference films, fabricated via use of a hand drop-casting technique, allowed for a better understanding of the key steps involved to the atmospheric deposition. The tests were commenced with different bulky R cations in the precursor solution: n-butylammonium iodide (n-BAI), iso-butylammonium iodide (iso-BAI) and tetra-butylammonium iodide (tert-BAI).
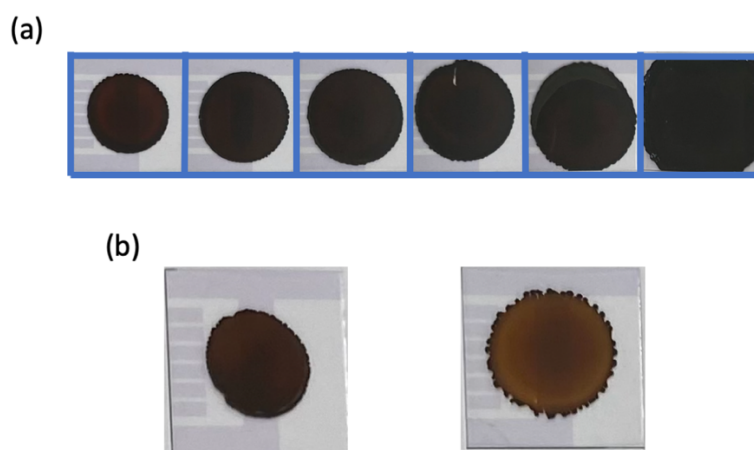
Figure 63: The optimization processes for finding the optimal precursor solution volume. (a) The sequential increase of precursor solution volume using pure n-BAI based 2DRP precursor solution: 3,4,5,6,7, and 8 µL respectively. (b) Impact of surfactant induced Tanner's spread in (iso-BA)$_2$MA$_{3.04}$Pb$_4$I$_{13}$Cl$_{0.04}$ (0.35 M) sample formation (left: volume of 2 µL pure, volume of 2 µL with 0.5% DLP).

The presence of the different bulky R cations allowed the following values to be found: the optimum precursor solution volume (8 µL), the position of the needle above the substrate (center +/- 0.5 mm), and the distance between the deposition needle tip and substrate face (0.2 mm).

The precursor solution stoichiometry was fixed at R$_2$MA$_{3.04}$Pb$_4$I$_{13}$Cl$_{0.04}$ (0.35 M), which corresponds to previously reported highly efficient 2DRP PSCs.[13, 27] The precursor solutions were additive-free to act as a reference. In line with previous reports,[28-31] to obtain large and

compact grains, each precursor solution was pre-heated to ~40 °C, and the substrate was pre-heated to 60 °C.[27, 32] The deposition area was first subjected to a high-flow N_2 stream prior the deposition to minimize local humidity to ~20-30 % RH; the quenching N_2 gas flow was set to 15 L min^{-1} and the precursor solution aliquots were pre-set to 8 μL. The films were subsequently brought to 95 °C for 30 minutes of post-annealing.

The precursor spread diameter was tested on three different glass substrates with transparent electrode: ITO, FTO, and AZO. The results revealed that only ITO substrate allowed for the precursor spread, which was attributed to the lowest surface energy and root mean square (RMS) surface roughness amongst the three substrates (please see Figure 42 for more details).[33-34] The AZO and FTO cannot be wetted using this technique, hence they were excluded from further tests. The study continued with the same fabrication method on ITO only.

For these ITO-based films, the key data was extracted, namely, optoelectronic, crystallographic, and physical characteristics: photoluminescence (PL), UV-Vis absorption, and X-ray diffraction (XRD) (see **Figure 64**). Further, there were cross-sectional scanning electron microscopy (SEM) micrographs, topographical atomic force microscopy (AFM) images, and in-plane images of the films obtained. Lastly, the reference batch of full PSC devices was fabricated and characterized.
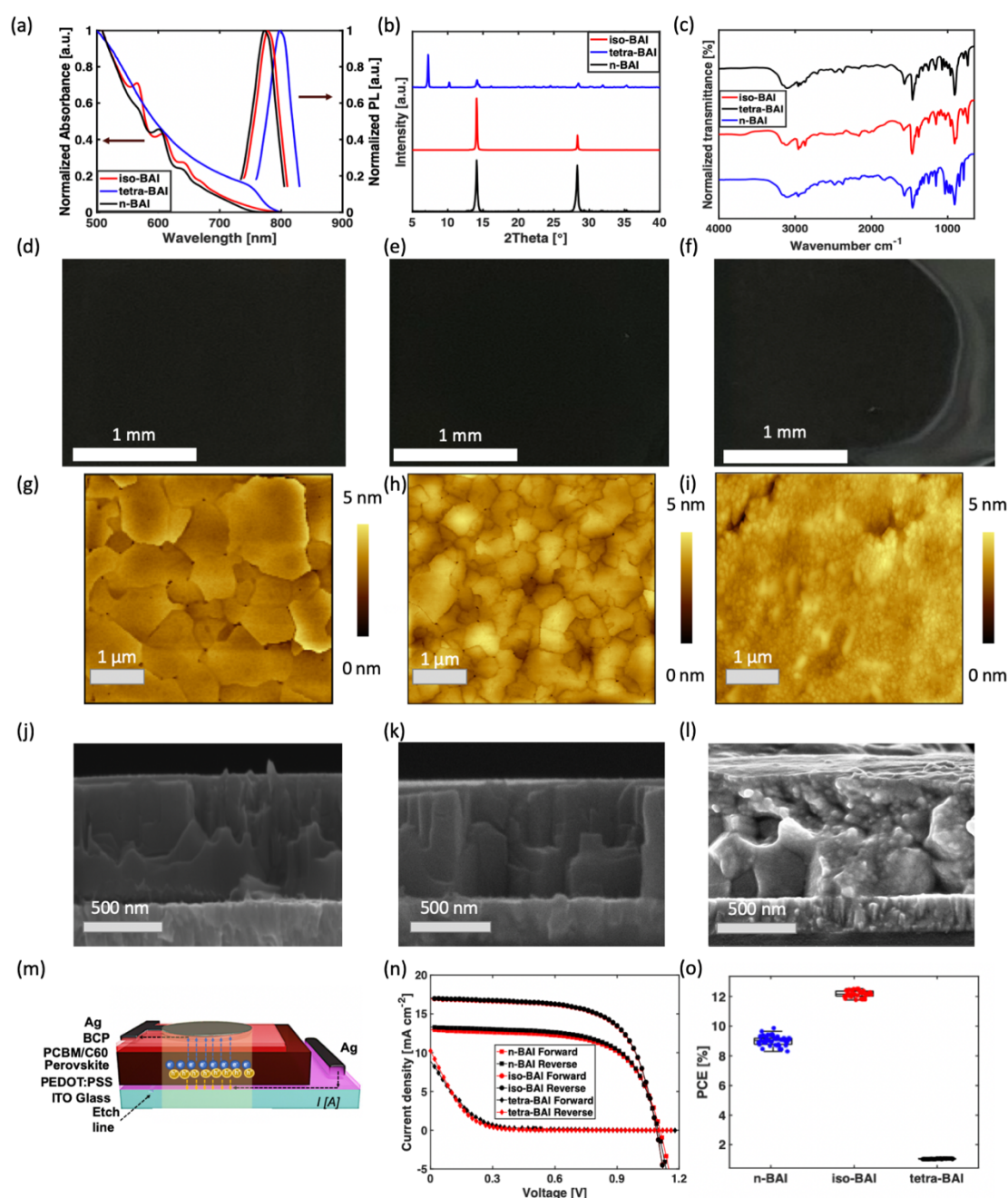
Figure 64: Initial pre-screening of three different bulky BA cations; iso-BAI, n-BAI, and tetra-BAI. (a) UV-vis absorption and steady-state photoluminescence (PL), (b) X-Ray diffraction (XRD) patterns, (c) Fourier-Transform Infrared Spectroscopy (FTIR), (d,e,f) macro photographs of n-BAI, iso-BAI, tetra-BAI 2DRP films, respectively, (g,h,i) atomic force microscopy (AFM) scans of n-BAI, iso-BAI, tetra-BAI 2DRP films, respectively, (j,k,l) scanning electron microscopy (SEM) cross-sectional micrograms of n-BAI, iso-BAI, tetra-BAI 2DRP films, respectively. (m) p-i-n device architecture, (n-o) PCE distribution and J-V characteristics of champions, respectively.

UV-vis and steady-state PL spectroscopy measurements were performed to determine the absorption and emission of RPP films with different R cations. The iso-BAI and n-BAI films exhibited absorption onsets at 775 nm and 757 nm, which correspond to absorption

bandgaps of ~1.64 and 1.62 eV, respectively. The tetra-BAI sample exhibited absorption onset at ~784 nm which corresponds to a bandgap of 1.56 eV.

Importantly, the UV-vis measurements revealed the quasi-2D nature of iso- and n-BAI films, expressed by the existence of the excitonic peak representing multiple mixed phases (n = 2, 3, and 4) corresponding to previously reported characteristic UV-vis peaks[10-12]. In this case, these occurred at 572 nm, 605 nm, and 640 nm for n-BAI sample and 572 nm, 609 nm, and 643 nm for iso-BAI sample. The UV-vis absorption spectrum shows that the tetra-BAI sample does not produce quasi-2D peaks. This is consistent with previous reports[13-14] of 3D perovskite films (MAPbX$_3$) with tetra-BAI cation additives, where the tetra-BAI does not incorporate into the crystal but forms a capping layer on top of the perovskite.

The characteristic emission peaks occurred at 782 nm for n-BAI sample, and 784 nm for an iso-BAI sample while, notably, the emission maximum for the tetra-BAI sample occurred at 798 nm. The PL measurements further confirmed the difference between iso-BAI and n-BAI samples versus tetra-BAI sample. XRD patterns of the films were consistent with previously reported peaks at ~14.2° and ~28.3° 2θ for iso-BAI and n-BAI samples corresponding to (110) and (220) tetragonal perovskite crystal planes.[12, 15-17] Remarkably, in the n-BAI sample case, the latter peak is approximately three times larger than in iso-BAI sample, suggesting that the iso-BAI sample film obtained with this method forms an intercalated layer.[11, 16]

Finally, in agreement with previous works,[7] the two distinctive peaks were taken to be strongly vertically oriented perovskite crystals. Unlike some reports suggest,[13, 18] in the case of the tetra-BAI sample crystal pattern lacks such a degree of crystallinity. All the peaks in the tetra-BAI sample can be assigned to ABX$_3$ perovskite and tetra-BAI salt, further indicating that tetra-BAI does not incorporate into the crystal lattice of a RPP. This is confirmed by the peak at ~7.5° 2θ which is reported to be due to tetra-BAI rather than quasi-2D functional spacer cation.

The presented FTIR interferogram contained bands from methyl group asymmetric and symmetric stretching vibrations at 2950 cm^{-1} and 2860 cm^{-1}, respectively. Bending vibrations associated with NH$_3^+$ are observed at ~1570 cm^{-1}, while another band at ~1460 cm^{-1} is

assigned to $CH_2NH_3^+$ bending in all perovskite samples studied. Additionally, stretching vibrations of various CH_3^- groups and C-C bonds are also observed at ~1380 cm^{-1} and ~1150 cm^{-1}, respectively. All samples produce an intense band at ~900 cm^{-1} that corresponds to the stretching of the C-N bond.

The photographs of representative films allowed for visual assessment of film quality and served as a reference for the spread measurements. Conspicuously the tetra-BAI sample, like n-BAI and iso-BAI samples, forms dark perovskite films; however, a matte-grey tetra-BAI residue on top of the tetra-BAI sample film is visible. Figure 64g-i presents the AFM images of the surface scan of the films in the central part of samples, both n-BAI and iso-BAI sample films have visible crystal grain boundaries and grains of size roughly 400-500 nm, however the tetra-BAI sample film exhibits densely packed grains (about 20-30 nm) which are attributed to the tetra-BAI capping layer formed on the film. Subsequentially, the cross-sectional SEM micrograms (Figure 64j-l) of those films reveal highly crystalline, formed n-BAI and iso-BAI sample films that are consistent with previously reported RPP films.[19] The tetra-BAI sample film cross-section also reveals the presence of a thick capping layer of tetra-BAI salt.

5.3.2 Automated Fabrication and Optimization of Ruddlesden-Popper Perovskite

Encouraged by a high degree of reproducibility in producing 2DRP perovskite candidate films, the automated deposition was pre-set to mimic the hand-held approach. Most experimental deposition conditions and parameters were tracked to serve as an additional productivity measure and reproducibility check. Fully automated study employed direct modification of the following variables: the concentration of the spread-increasing surfactant 1,2-diacyl-sn-glycero-3-phosphocholine (DLP); the concentration of the moisture-resistance increasing polymer polyvinylpolypyrrolidone (PVP); the precursor solution molarity; the solvent addition (DMSO and GBL); electrode fabrication method (electron-beam and thermal evaporation); and substrate temperature variation. Films spread diameter (photograph) and thickness (cross-sectional SEM) were measured. From these films, the PSCs were fabricated and photovoltaic properties such as PCE, open-circuit voltage (V_{OC}), short circuit current density (J_{SC}), and fill factor (FF) were obtained. Thus, the list of fabrication parameters for devices (**Figure 65)** served as an estimation of the best recipe.
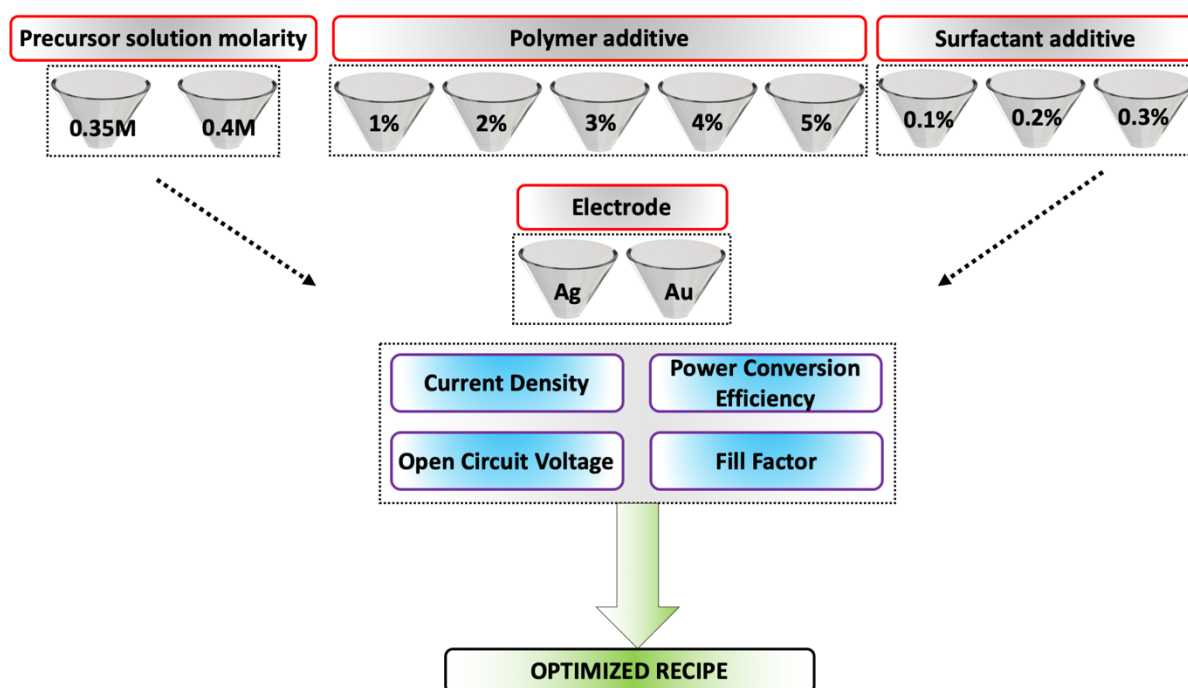
Figure 65: Fabrication workflow with employed variables using high-throughput perovskite film fabrication system.

5.3.3 Characterization results

In order to examine the performance of the RPP devices, analogous devices were prepared using the drop-casting approach. If not specified otherwise the following standard fabrication conditions were used for the fabrication of the RPP solar cells reported in this chapter: (iso-BA)$_2$MA$_{3.04}$Pb$_4$I$_{13}$Cl$_{0.04}$ (0.35 M): the piezoelectrically mixed, homogeneous precursor solutions (volume of 8 μL) were deposited in air on preheated (60 °C) poly(3,4-ethylenedioxythiophene) polystyrene sulfonate (PEDOT:PSS)-coated indium tin oxide (ITO, active area is defined to 0.1 cm^2) glass substrates using a blunt needle attached to a robotic head controllable in a XYZ direction. After the average spread time (~10 s), the gas valve triggers and gently opens the gas flow that dries the precursor solution. The freshly made film is gas-quenched with a uniform N$_2$ stream for 2 minutes. After the deposition of all intended films, the hotplate enters the post-annealing stage by increasing (ramping 5 °C per minute) the temperature to 100 °C and then naturally cools down back to RT. The devices are immediately transported to the GB through the antechamber where 5 times the vacuum evacuation is executed. The layer of phenyl-C61-butyric acid methyl ester (PC$_{61}$BM) was spin-

coated on top, and then layers of C60, bathocuproine (BCP) were evaporated in a single-vacuum session consecutively, finally a electrode was evaporated. The architecture of the PSC devices can be seen on **Figure 66**.
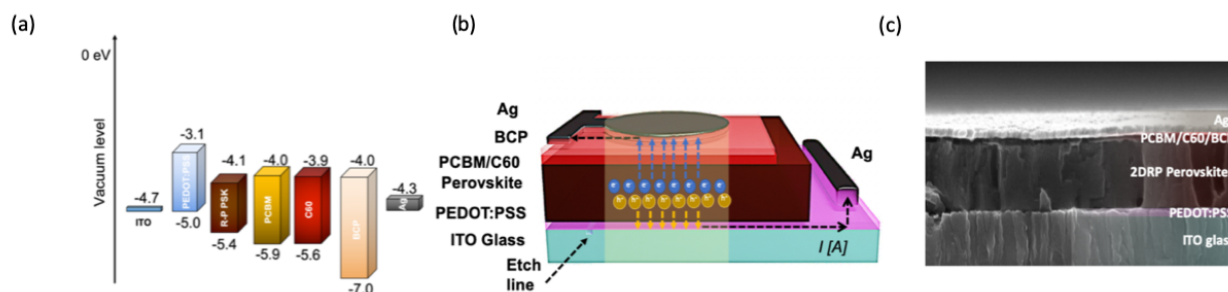

Figure 66: Inverted (p-i-n) solar cells fabricated with cHTR method in air. a) Energy level diagram with the alignment of the specific layers employed in this study, (b) schematic of inverted (p-i-n) architecture used in this study which allows for spin-coating-free 2DRP perovskite film fabrication, (c) cross-sectional SEM image of the device used in this study.

5.3.3.1 Precursor solution molarity impact

The increase of precursor solution molarity from 0.35M to 0.4M was explored in order to determine how specific characterization parameters J_{SC}, V_{OC}, PCE, and FF are affected. The precursor solution reference was highlighted with green and plotted throughout all studies to serve as a side by side comparison for better readability across all the modifications. Firstly, the contribution effects of increased molarity were assessed. The increase of molarity caused reduction of the J_{SC} spread from: low of ~15.7 mA cm^{-2}, high of ~19.8 mA cm^{-2} to low of ~16.5 mA cm^{-2} to high of ~19.7 mA cm^{-2} . The mean J_{SC} increased from ~17.9 mA cm^{-2} to 18.6 mA cm^{-2}. The FF only slightly increased from 0.63 to 0.65 however the spread also increased, and V_{OC} remained similar at ~1.1 V. The PCE increase mainly was caused by the increase of J_{SC}, the spread remained similar, however the mean increased from ~12.4% to 13.1%. This leads to conclusion that higher molarity caused the current density increase which goes in line with previous reports of 2DRP. The distributions of characteristics can be seen and compared in **Figure 67**.
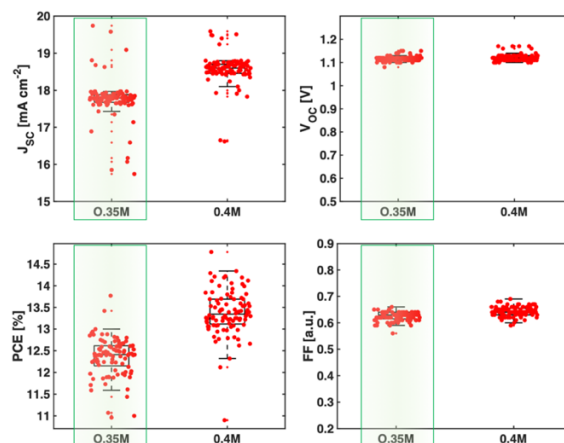
Figure 67: The J_{SC}, V_{OC}, PCE, and FF metrics comparison of 2DRP devices fabricated with the (iso-BA)$_2$MA$_{3.04}$Pb$_4$I$_{13}$Cl$_{0.04}$, precursor solutions with two molarities: 0.35M and 0.4M. Volume of 8 µL drop-casted on ITO/PEDOT:PSS substrates preheated to 60 °C, Ag electrode was thermally evaporated. Each batch contains of 96 PSCs.

5.3.3.2 Metal electrode impact

The impact of the metal deposition technique and metal type was explored in order to determine how the specific characterization parameters J_{SC}, V_{OC}, PCE, and FF are affected. The thermal evaporation does not require the samples to be removed from the GB and layers: C60/BCP/Ag were deposited in a single-step evaporation, hence this study also examines the impact of the PSC being removed from the GB and subjected to high vacuum deposition twice. This is because it was recently found that multiple vacuum processes have a degrading impact on the overall performance of 2DRP.[86-87] The J_{SC} was impacted in case of the e-beam evaporation, and for Ag samples the mean was reduced to ~17.1 mA cm^{-2}, and for Au it was significantly reduced to 14.1 mA cm^{-2}. For Ag e-beam sample the V_{OC} remained similar, however for Au e-beam devices the V_{OC} suffered on average from slight loss of 0.08 V. The FFs for the Ag e-beam samples were on average higher by 0.03, however for Au e-beam sample they remained similar. The overall PCE remained similar for Ag thermal and Ag e-beam samples, with a slight mean increase of ~0.1 %, whereas in case of the Au sample the PCE dropped to ~9.5 %. The impact of the Au electrode on the p-i-n structure agrees with the results of a previous report.[88] The Au Entire batch of solar cells was tested and the performance data was extracted for comparison purpose in **Figure 68**.
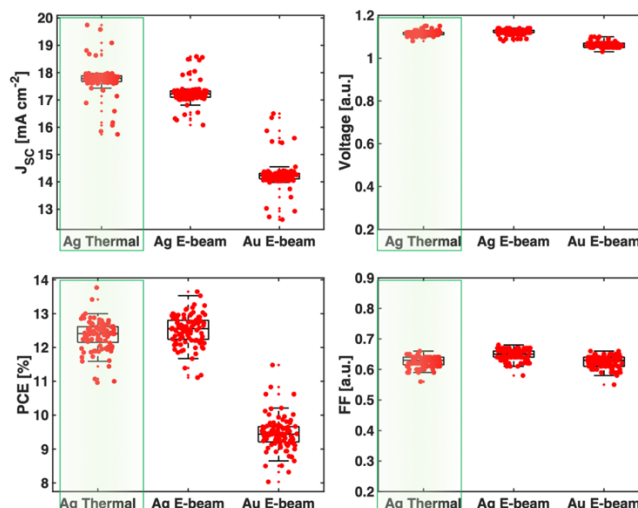
Figure 68: The J_{SC}, V_{OC}, PCE, and FF metrics comparison of 2DRP devices fabricated with (iso-BA)$_2$MA$_{3.04}$Pb$_4$I$_{13}$Cl$_{0.04}$, precursor solutions (0.35M) with different top electrodes: Ag thermally deposited, Ag and Au deposited with the e-beam evaporator. Volume of 8 µL drop-casted on ITO/PEDOT:PSS substrates preheated to 60 °C. Each batch contains of 96 PSCs.

5.3.3.3 Polymer additive impact

The impact of the long-chained PVP additive that acts mechanistically as a framework around the 2DRP crystals was investigated. In order to test the influence of this polymer on J_{SC}, V_{OC}, PCE, and FF a batch of drop-casted films was fabricated. The samples with 1 and 2% of PVP exhibited slight increase in PCE, FF and V_{OC}. The 1 and 2% PVP samples had marginally lower J_{SC} than the reference, however their J_{SC} parameter spread was significantly narrower indicated better reproducibility. The samples with higher concentrations of PVP (3,4, and 5%) had similar parameter spread and were severely impaired in comparison with the 0 % PVP reference resulting in decrease in all parameters. The resulting slight increase in PCE for sample of 1 and 2% PVP goes in line with previous reports.[89-90] The parameters can be seen and compared in **Figure 69**.

Figure 69: The J_{SC}, V_{OC}, PCE, and FF metrics comparison of 2DRP (iso-BA)$_2$MA$_{3.04}$Pb$_4$I$_{13}$Cl$_{0.04}$, (0.35M) devices fabricated with different PVP concentrations: 0,1,2,3,4, and 5%. Volume of 8 µL drop-casted on ITO/PEDOT:PSS substrates preheated to 60 °C. Ag electrode thermally evaporated. Each batch contains of 96 PSCs.

5.3.3.4 Surfactant impact

The impact of the surfactant additive that acts as a precursor solution spread inducing agent was investigated. In order to test the influence of this polymer on J_{SC}, V_{OC}, PCE, and FF a batch of drop-casted films was fabricated. In general, the samples with DLP exhibited decrease in PCE, and V_{OC}. Only for 0.1% and 0.3% of DLP a slight increase of FF was observed. The standard deviation of V_{OC} was observed in case of 0.1% DLP. Unlike the previous reports,[91] besides slight increase in the precursor spread and small positive impact on standard deviation, the use of DLP did not improve performance. The parameters can be seen and compared in **Figure 70**.
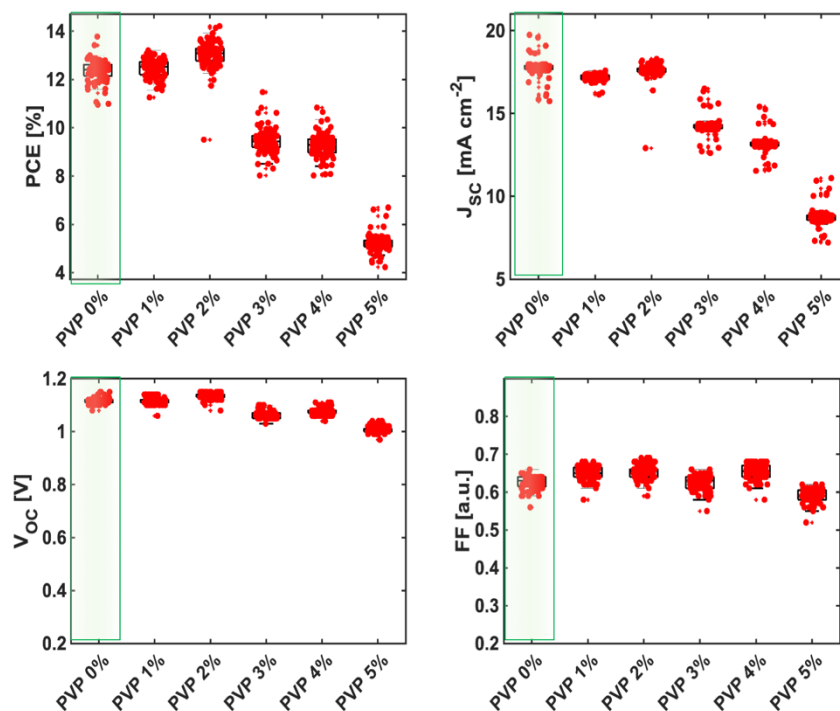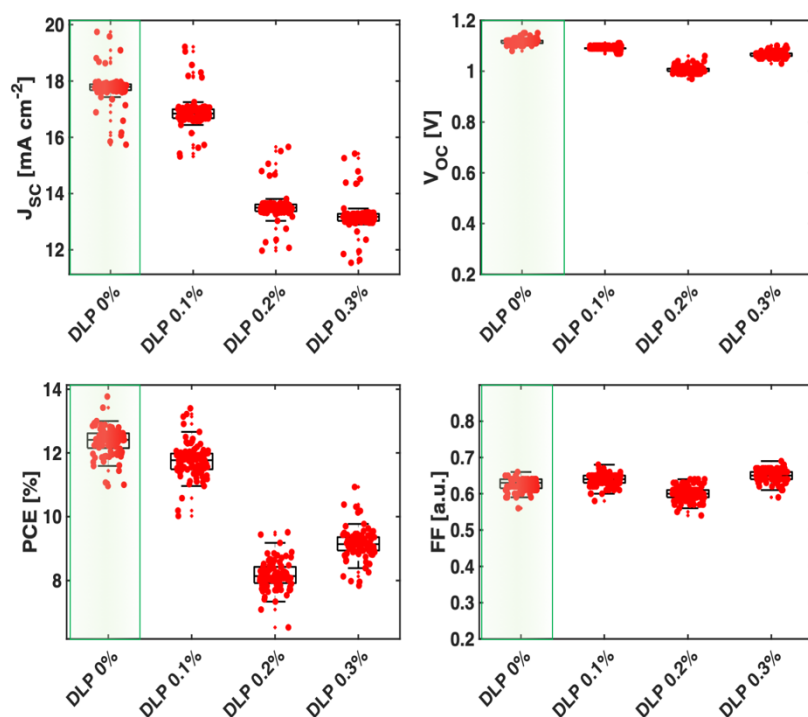
Figure 70: The J_{SC}, V_{OC}, PCE, and FF metrics comparison of 2DRP (iso-BA)$_2$MA$_{3.04}$Pb$_4$I$_{13}$Cl$_{0.04}$, (0.35M) devices fabricated with different DLP concentrations: 0.1, 0.2, and 0.3%. Volume of 8 μL drop-casted on ITO/PEDOT:PSS substrates preheated to 60 °C. Ag electrode thermally evaporated. Each batch contains of 96 PSCs.

5.3.3.5 Solvent impact

The impact of the solvent exchange that facilitates the crystallization mechanism of 2DRP was investigated here. In order to test the influence of solvents on J_{SC}, V_{OC}, PCE, and FF a batch of drop-casted films was fabricated. The samples with DMSO exhibited increase in PCE, FF and V_{OC}. However, the samples with GBL exhibited on average ~1 mA cm^{-2} loss. Similarly to previous reports on solvent screening,[92-93] the DMF-DMSO solvent system resulted in the best performance, whereas the DMF-GBL system worsen the overall performance. The unary DMF solvent system facilitates fast evaporation, often resulting in random-oriented perovskite grains, pinholes and dislocations. The DMF-DMSO binary solvent system typically retards the evaporation rate. In this case it facilitated heterogeneous nucleation at the precursor solution-gas interface,[93] forming a large grain, densely packed layer on the top surface of the film (see Figure 63). The DMF-GBL system exhibited even slower evaporation rate than DMF-DMSO one. The extended evaporation time results in forming of the top nucleation layer which traps the residual solvent that upon full crystallization forms voids,[94-95] hence the observed drop in the current-density. Parameters can be seen and compared in **Figure 71**.
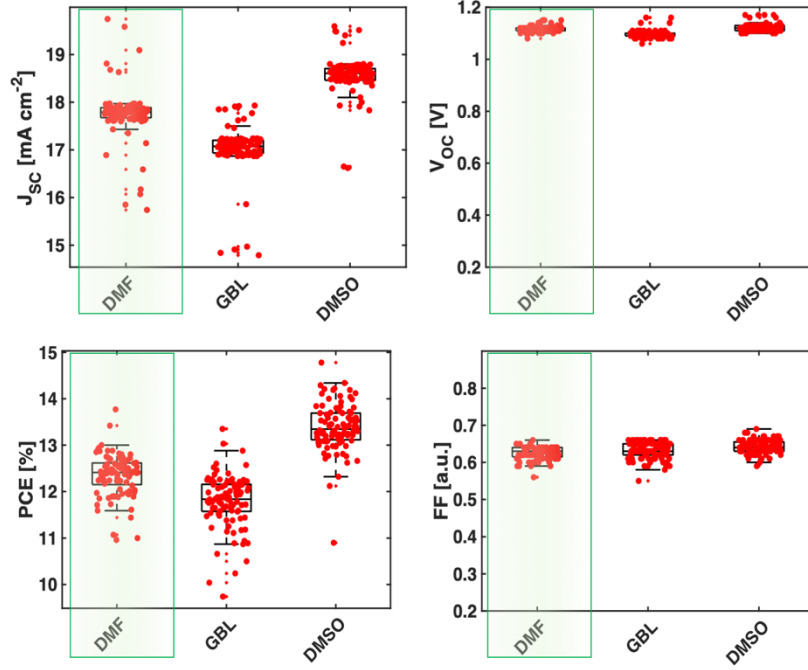
Figure 71: The J_{SC}, V_{OC}, PCE, and FF metrics comparison of 2DRP (iso-BA)$_2$MA$_{3.04}$Pb$_4$I$_{13}$Cl$_{0.04}$, (0.35M) devices fabricated with different solvent volume replacement: no solvent replacement (DMF only), GBL (~30 µL replaced), and DMSO (~30 µL replaced). Volume of 8 µL drop-casted on ITO/PEDOT:PSS substrates preheated to 60 °C. Ag electrode thermally evaporated. Each batch contains of 96 PSCs.

5.3.4 Optimized fabrication protocol

In the final part of this study, the results from all automated studies were analyzed to develop and investigate new precursor solution and fabrication parameters. By carefully selecting only the fabrication parameters that increased the energy conversion efficiency, the optimal fabrication parameter batch was fabricated. All the solar cells were tested for performance (PCE, V_{OC}, J_{SC} and FF). The optimal device is based on films of (0.4M) iso-BA$_2$MA$_{3.04}$Pb$_4$I$_{13}$Cl$_{0.04}$ with: 0.1% DLP; 1% PVP; DMSO; electrode of Ag e-beam. The champion fabricated from this material exhibited the highest PCE of ~15.1 % and demonstrated a low hysteresis index (HI) <0.4 % where:

$$HI_{PSC} = \pm \left(\frac{PCE_{Reverse} - PCE_{Forward}}{PCE_{Reverse}} \right) \times 100 \%.$$

As in the initial manual study, all the cHTR produced, 2DRP precursor solutions formed densely packed, compact films with visibly vertical highly crystalline grains (Fig 66c), with similar morphology to previously reported quasi-2D perovskite films.[96-98] The solar cell characteristics of the champion device prepared for the optimal fabrication protocol are

summarized in **Figure 72**. The devices were subsequently tested in a climatic chamber (ATLAS SC400), for over 240 hours under 1 Sun illumination at 25 °C and relative humidity of 40%, using 2-wire sense technique under constant bias. This study of the fully encapsulated in the GB device revealed that the optimal 2DRP PSC produces stable output power with a PCE of ~15 % and negligible (~0.2%) PCE loss.
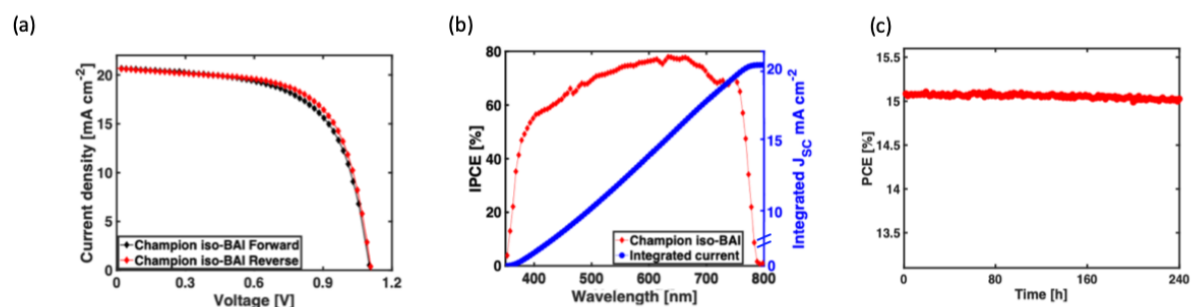
Figure 72: Champion 2DRP PSC fabricated using an automated system according to the ML-refined recipe. (a) J-V characterization of the champion device, (b) IPCE measurement with current density integration curve, and (c) long term (240 h) maximum power point tracking (MPPT) under continuous 1 Sun illumination (encapsulated devices, relative humidity (RH) of 40%, temperature of 25 °C).

5.4 Conclusions and Future Outlook

This chapter has presented a precise and reproducible perovskite film fabrication technique that allows for rapid, combinatorial studies and screening of potentially hundreds of thousands of compositions. This system can be easily adopted, and can serve as an inexpensive, cross-reference tool for stable perovskite material fabrication in near ambient conditions. This automated approach reduces the sample-to-sample variation of manually produced materials, resulting in higher quality materials and great stability. The polymer, surfactant and solvent additives elucidate the contributions key fabrication parameters make to device performance characteristics, aiding the process of device improvement. Notably, the combination of automated perovskite film fabrication and gradual screening can rapidly generate 2D perovskites with improved device performance.

Importantly, this study revealed that some parameters and additives can be synergistically screened which further accelerates progress in perovskite photovoltaics. In particular, the use of stability improvement polymer (PVP) was demonstrated for the first time in 2DRP drop-casted perovskite material space. In comparison with manual fabrication, the cHTR methodology provides great improvements in the reproducibility and reliability of device manufacture. Moreover, all materials are made in similar conditions to manual drop-casting methods and hence can serve as a state-of-the-art comparison setup.

These results paved the way for rapid, large-scale discovery studies where each fabrication step can be carefully recorded and the complete protocol can be reliably reproduced without the variability inherent in manual drop-casting methods. Such complex dissection of the fabrication process and automation makes it possible to create data libraries that serve as cross-research group reference points and can serve in future as training data for computational models. In future, automated fabrication combined for example with ML modelling could allow for the discovery and fabrication of optimal, efficient 2DRP films with multiple other optimizing agents, solvents or surfactants. The high reproducibility and stability resulting from prediction and models based on cHTR obtained data could be incorporated into devices with very good efficiencies and high long-term environmental stability that can readily translate to the industrialization of PSCs.

6. High-throughput direct deposition of high-quality low-temperature inorganic hole transporting materials for perovskite solar cells

6.1 Chapter context and motivation

The cHTR perovskite film fabrication for large-scale screening allows for the preparation of highly reproducible films. Simultaneously, the cHTR research focus on other layers than the perovskite. In the nutshell, the device quality is highly dependent on separate quality of each layer and all the layers acting together in the form of the device. Hence, the cHTR requires scalable techniques to produce the entire device, and thus substrates, CTLs and electrodes need to be precisely made. The design and preparation of a reproducible substrate (patterned glass with conductive transparent layer) is fully commercialized and requires only mechanical design to be accomplished. Similarly, most metal electrodes use one of standardized evaporation processes (thermal or e-beam evaporation, or RF sputter) that cover uniformly large area. The difficulty from the cHTR point of view lays in the adjacent to perovskite layer CTLs. Unfortunately, as described in literature review and reiterated here, the most efficient perovskite light absorber will not be useful without efficient charge extraction and selectivity.[38] In this chapter in order to achieve an efficient PSC, the study on cHTR employable CTL layer is conducted.

6.1.1 Efficient and stable CTL

As outlined in the thesis introduction, PSC devices can be divided conceptually into two architectures: back-contact PSC (where the absorption layer is located on top of both electrodes) or sandwich structure which contains further subgroups of flexible solar cells, mesoscopic, planar, and n-i-p or p-i-n.[40] In general, the common point among the n-i-p PSC design is the fact that the transparent, conductive cathode is further covered in a separate (pre-perovskite) process with ETLs. For example, some ETLs are semiconductors (TiO_2, WO_3,

ZnSnO$_4$, SnO$_2$ or ZnO layer) or insulators (Al$_2$O$_3$, ZrO$_2$). They generally require high-temperature annealing > 450 °C to form a mesoscopic (scaffolding) layer that allows for better charge extraction and mobility. This high-temperature annealing, unfortunately, excludes the use of flexible substrates. Alternatively, the research approach employs inverted architecture (p-i-n), the transparent conductive anode is coated with HTL PEDOT:PSS, NiOx, CuSCN, CuI, CuOx, MoOx, graphene oxide (GO) or reduced GO (rGO) and then after that perovskite layer is deposited.[41-42] The PSC device is completed subsequently with ETLs. There are certain requirements that should serve as aims when it comes to HTL/ETL development or optimization: the material needs to be deposited in the simplest process possible, ideally omitting or improving upon the currently used fabrication steps, the material needs to be a good candidate that does not put in jeopardy the PSC efficiency, needs to be stable in a long term application and must be commercially viable in terms of its cost and cost of the adjacent layers (compatible to it substrates, electrodes and perovskites). Moreover, the solution-processing brings the potential final price of PSC modules to a competitive price point at parity with the SSC. Hence our aim, important for the context of this chapter, is the cost, scalability, stability, and fabrication conditions.

6.1.2 Inorganic, inexpensive and scalable CTL for stable PSCs

Another important consideration is the simplicity of material application, synthesis, and low-temperature processing. To address the abovementioned causes and problems we have chosen to focus our work on the development of a ligand-modified nickel oxide (NiOx) HTL. We focused on the development of directly (microfluidically) premixed prior to the deposition dispersions of NiOx nanoparticles (NPs) due to the excellent properties of this material. NiOx is a commonly known simple inorganic metal oxide. NiOx film has high optical transmittance (almost transparent films), the valence band energy level is compatible with perovskite and thus promotes strong hole current movement. In order to serve as an HTL, the NiO film has to be of excellent quality. The electronic configuration of NiOx is nontrivial because convoluted oxidation states do not allow for direct distinction between NiO (II) or NiO (III). However, beyond the atomic scale, it performs selective charge separation essentially conducting hole current. Uniform and compact films enabled functional NiOx film realization

and served as a great hole mobility medium. We chose to develop a new ligand-modified NiOx NPs for low-temperature processing.

6.1.3 System design for cHTR-ready and easily scalable CTL

There are multiple ways to fabricate such a layer, however the most likely to gain the commercial attention is the low-temperature, vacuum-free methodology that can be sufficiently scaled and applied for a range of inexpensive, flexible, and light polymer substrates such as polyethylene napthalate (poly(ethylene 2,6-napthalate) (PEN) or polyethylene terephthalate (PET). Such substrates usually exhibit low glass-liquid transition temperature (T_g) which causes irreversible degradation and melting. For PET the T_g is around ~80 °C and for PEN is ~130 °C. However, there exist some ways to improve T_g to even 150 °C.[43] Hence, solution-processed and low-temperature deposition emerges to be an option for those types of substrates. In this cHTR system, three NiOx dispersions: NiO-OA, NiO-HBA and NiO-BF$_4$ were employed. The substrates were vacuum mounted on the spin-coated chuck and the dispersion was pushed through the multi-staged inverted Tesla valve to mimic ultrasonic dispersion premixing and allowing for exact aliquot definition. The programmable syringe pump controlled by a bespoke MATLAB algorithm (Chemyx 4000) was pre-set to timely push two pre-loaded syringes simultaneously (1 substrate equivalent volume per 2 minutes to allow dead volume purging, mounting, and spin-coating). The workflow is presented in the **Figure 73**, and the photograph of the system can be seen in the **Figure 74**. The next paragraph present the reported study and provides results of this system employed for PSCs fabrication.
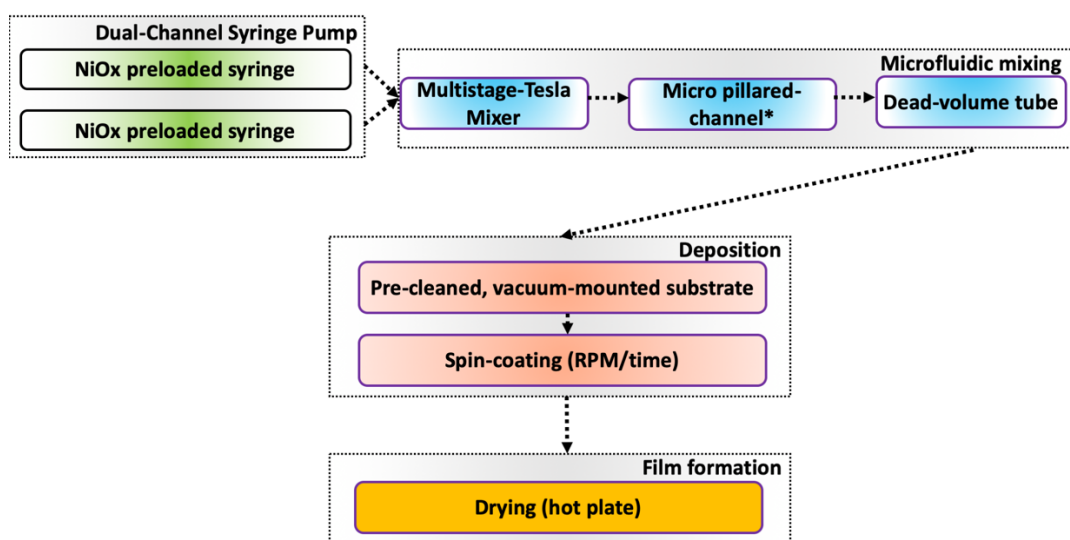
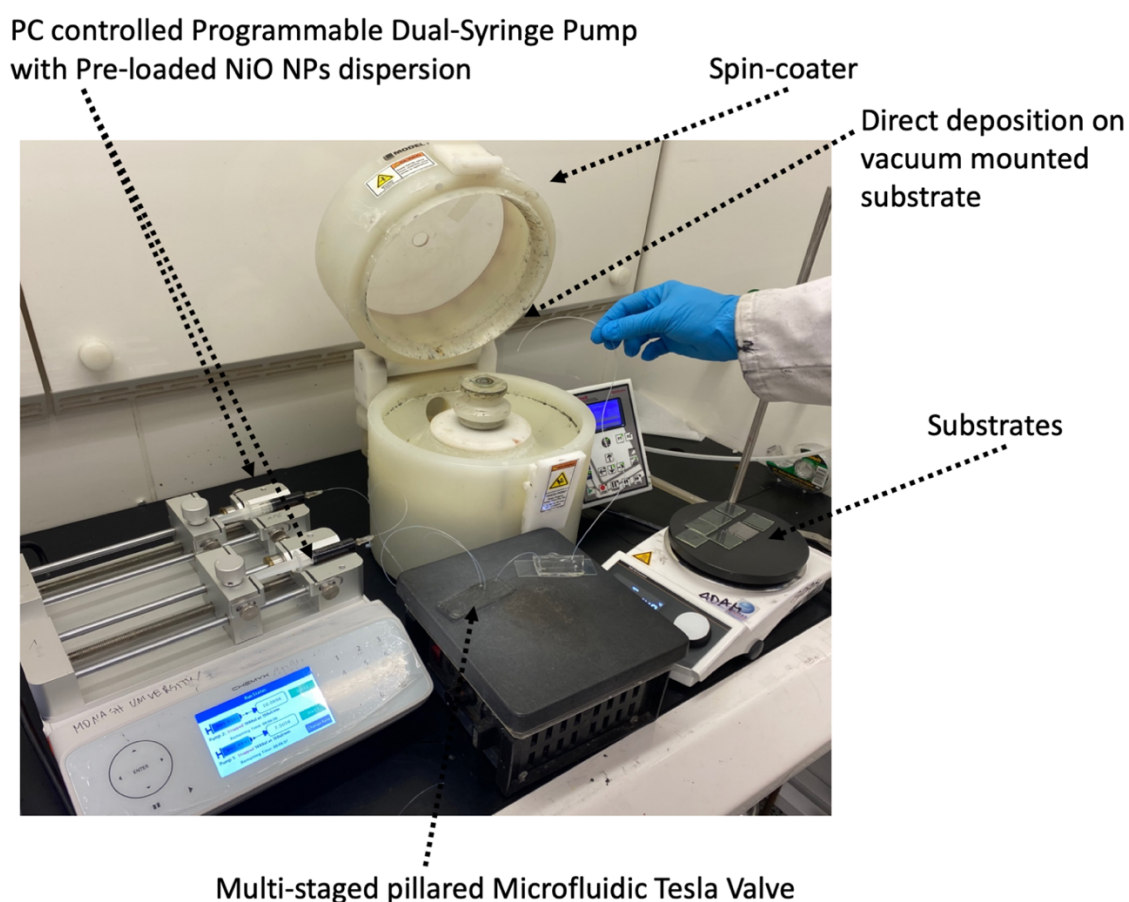*Figure 73: Schematic presenting the method adopted for the NiOx film deposition used in this study.*

Figure 74: Picture of the fabrication setup located in the fume hood. From left: the programmable stroke timing externally triggered dual syringe pump with preloaded syringes containing colloidal NiOx dispersions in DMF.

RESEARCH ARTICLE

Microfluidic Processing of Ligand-Engineered NiO Nanoparticles for Low-Temperature Hole-Transporting Layers in Perovskite Solar Cells

Monika Michalska, Maciej Adam Surmiak, Fatemeh Maasoumi, Dimuthu C. Senevirathna, Paul Chantler, Hanchen Li, Bin Li, Tian Zhang, Xionfeng Lin, Hao Deng, Naresh Chandrasekaran, T. A. Nirmal Peiris, Kevin James Rietwyk, Anthony S. R. Chesman, Tuncay Alan, Doojin Vak, Udo Bach,* and Jacek J. Jasieniak*

Nickel oxide (NiO) is used as a hole-transporting layer (HTL) in perovskite solar cells (PSCs) because of its high optical transmittance, intrinsic p-type doping, and suitable valence band energy level. However, fabricating high-quality NiO films typically requires high-temperature annealing, which limits their applicability for low-temperature, printable PSCs. Herein, the need for such postprocessing steps is circumvented by coupling 4-hydroxybenzoic acid (HBA) or trimethyloxonium tetrafluoroborate (Me_3OBF_4) ligand-modified NiO nanoparticles (NPs) with a Tesla-valve microfluidic mixer to deposit high-quality NiO films at a temperature $<150\,°C$. The NP dispersions and the resulting thin films are thoroughly characterized using a combination of optical, structural, thermal, chemical, and electrical methods. While the optical and structural properties of the ligand-exchanged NiO NPs remain comparable with those possessing the native long-chained aliphatic ligands, the ligand-modified NiO thin films exhibit dramatic reductions in surface energy and an increase in hole mobilities. These are correlated with concomitant and significant enhancements in performance and stability factors of PSCs when the ligand-modified NiO NPs are used as HTL layers within p$-$i$-$n device architectures.

1. Introduction

Intensive research into metal halide perovskite solar cells (PSCs) has rapidly brought this technology into a lucrative commercial spotlight.[1] However, it is still not clear how the tremendous promise of PSCs achieving low-cost and high-efficiency photovoltaic devices will be realized. Of the possible fabrication methods that might be suitable, printing is an efficient, fast, and scalable approach that is compatible with the solution-based perovskite deposition process.[2] The typical supporting substrate for such printed devices is polyethylene teraphthalate (PET), a low-cost, transparent polymer with a practical upper processing temperature limit of $150\,°C$.[3,4] Its use necessitates low-temperature processing of all the layers within the completed PSC devices. While hybrid lead halide perovskites are inherently amendable to these temperature

M. Michalska, Dr. D. C. Senevirathna, P. Chantler, H. Li, Dr. B. Li, H. Deng, Dr. N. Chandrasekaran, Dr. T. A. N. Peiris, Prof. J. J. Jasieniak
Department of Material Science and Engineering
Monash University
Clayton, Victoria 3800, Australia
E-mail: jacek.jasieniak@monash.edu

M. Michalska, M. A. Surmiak, Dr. T. Zhang, Dr. X. Lin, Dr. T. A. N. Peiris, Dr. K. J. Rietwyk, Prof. U. Bach, Prof. J. J. Jasieniak
ARC Center of Excellence in Exciton Science
Monash University
Clayton, Victoria 3800, Australia
E-mail: udo.bach@monash.edu

M. Michalska, M. A. Surmiak, Dr. A. S. R. Chesman, Dr. D. Vak, Prof. U. Bach
CSIRO Manufacturing
Clayton, Victoria 3168, Australia

The ORCID identification number(s) for the author(s) of this article can be found under https://doi.org/10.1002/solr.202100342.

DOI: 10.1002/solr.202100342

M. A. Surmiak, Dr. T. Zhang, Dr. X. Lin, Dr. K. J. Rietwyk, Prof. U. Bach
Department of Chemical Engineering
Monash University
Clayton, Victoria 3800, Australia

Dr. F. Maasoumi
Faculty of Science
Engineering and Technology
Swinburne University of Technology
Hawthorn, Victoria 3122, Australia

H. Deng, Dr. T. Alan
Department of Mechanical and Aerospace Engineering
Faculty of Engineering
Monash University
Clayton, Victoria 3800, Australia

Dr. A. S. R. Chesman
Melbourne Centre for Nanofabrication
Clayton, Victoria 3168, Australia

limits, complying with these for the other layers within a PSC remains challenging.

The conventional architecture of a PSC consists of a transparent conductive substrate serving as a bottom electrode, on which the perovskite film is sandwiched between the two charge-transporting layers (CTL) and is capped with a top metallic electrode.[5–7] The CTLs function to selectively extract charges from the ambipolar perovskite light absorber.[8,9] These can be in the form of n-type electron-transporting layers (ETLs) or p-type hole-transporting layers (HTLs) and depending on the device fabrication sequence can achieve either p−i−n or n−i−p architectures.[10] The ETLs typically constitute organic molecules, such as fullerene (C_{60}),[11,12] [6,6]-phenyl C_{61}-butyric acid methyl ester (PCBM),[13] or inorganic materials, such as titanium dioxide (TiO_2),[14] tin oxide (SnO_2),[15] or zinc oxide (ZnO).[16] Meanwhile, the HTLs are typically chosen from inorganic copper oxides (CuO or Cu_2O),[17] copper iodide (CuI),[18] copper tiocyanide (CuSCN),[19] molybdenum oxide (MoO_x),[20] tungsten oxide (WO_x),[21] and nickel oxide (NiO),[22] as well as organic materials, such as spiro-OMeTAD [2,2′,7,7′-tetrakis(*N,N*-di-p-methoxyphenyl-amine) 9,9′-spirobifluorene],[23] regioregular poly(3-hexylthiophene-2,5-diyl) (P3HT),[24] and poly(triarylamine) (PTAA).[25] While organic HTLs offer many advantages, such as tunable electronic levels[26] and low-temperature processing via thermal- or solution-based methods,[27] they are also expensive[28] and sensitive to ambient conditions (oxygen, humidity),[29] limiting their potential to be used in commercial applications. Inorganic HTLs are usually less sensitive to external conditions[30] and much easier to synthesize,[31] rendering them more cost effective than their organic counterparts.[28] However, the deposition of these materials often requires high-temperature processing or the use of solvents that are incompatible with the perovskite layer, which is problematic in n−i−p structures. Their use is therefore typically limited to p−i−n architectures, for which the HTL is deposited prior to the perovskite layer.[32,33]

Among the inorganic HTL candidates, NiO is the most widely used for the fabrication of PSCs.[34] It possesses an optical bandgap of ≈3.6 eV to give it high optical transmittance across the visible region, it is intrinsically p-type, and has a deep valence band (VB) edge of ≈5.4 eV, which is compatible with most common perovskites.[35] One of the most used approaches for obtaining NiO thin films has been based on sol−gel processing. This relies on organic or inorganic nickel salt precursors that are deposited and processed at temperatures of up to 500 °C to drive thermalization and condensation of the ligands and precursors, respectively.[36,37] We have also shown that chemical bath processing is another suitable method for NiO deposition, which beneficially enables microstructurally textured HTLs to be deposited to permit efficient charge extraction from the perovskite layer.[38] The clear need for high-temperature processing to form cubic NiO across these methods makes them incompatible with low-temperature processing requirements.

To avoid such high-temperature film annealing, crystalline NiO has to be formed prior to deposition on a substrate (for instance, via calcination).[39] Then, post-treatment at moderate temperatures is often applied to evaporate the solvent. Typically, the obtained NiO nanopowders are dispersed in a water-based medium, but recently, alternative NiO synthetic approaches for low-temperature deposition have been also studied. Liu et al. explored NiO nanoparticles (NPs) prepared using a high-temperature liquid synthesis with long-chained aliphatic ligands as low-temperature-processable HTLs.[40] In this approach, the NiO NPs dispersed in chlorobenzene (CBZ) were spin coated to form n−i−p and p−i−n-structured PSCs. Critical to their successful use was the need for a UV−ozone treatment of the films to remove the aliphatic ligands from the as-deposited NiO film. This treatment enabled the highest PCEs of up to 15.9% to be achieved for the p−i−n devices. In an alternative approach, Tang et al. harnessed identical NiO dispersions to deposit NP thin-films that were then annealed at 500 °C to thermalize the ligands and yield PSCs with a PCE of up to 15.4%.[41]

In this work, we study the use of ligand-exchange reactions to replace the long alkyl-chained ligands used for the synthesis of NiO NPs with alternative ligands. These act to improve the electrical properties of the as-cast NiO films and omit the need for subsequent high-temperature or UV−ozone processing steps. In general, ligand-exchange methods are commonly used in NP synthesis. For instance, stable dispersions of metal oxide NPs in polar solvents can be achieved using ligands containing organic substitutes, such as carboxylic acids,[42] thiols,[43] mercaptocarboxylic acids,[44] or inorganic substitutes like hydrazine,[45] chalcogenides ($S^{2−}$, $Se^{2−}$, $Te^{2−}$),[46] or halides ($Cl^−$, $Br^−$, $I^−$).[47] Here, we focus on two facile approaches that have been widely applied to different NPs to render them dispersible in polar solvents. The first of these involves a tetrafluoroborate salt, where surface modification of NPs is achieved using $BF_4^−$ ions.[48] Dong et al. applied this approach utilizing nitrosonium tetrafluoroborate ($NOBF_4$) as the exchange ligand to a wide range of nanocrystals, including Fe_3O_4, FePt, CoPt, TiO_2, and Bi_2S_3.[49] A further comparison between $NOBF_4$ and Et_3OBF_4 ligands indicated that $NOBF_4$ oxidizes chalcogenides, resulting in unstable products.[48] This suggests that trialkyloxonium tetrafluoroborate salts are the most appropriate to yield stable dispersions. Khanzada et al. applied this approach to exchange oleic acid (OA) and oleylamine (OLA) surface ligands from Cu_2ZnSnS_4 (CZTS) nanocrystals with trimethyloxonium tetrafluoroborate (Me_3OBF_4).[50] The PSC fabricated using such ligand-modified CZTS as HTLs showed a 26.2% relative improvement in PCE to achieve 15.4%. This increase in performance was attributed to enhanced photoconductivity and mobility of the modified HTL.

While Me_3OBF_4 is a promising NiO ligand-exchanging agent, it does require dimethylformamide (DMF) as a dispersion solvent, which can make processing challenging. As such, here, we also consider an alternate organic ligand in the form of 4-hydroxybenzoic acid (HBA). This approach has been used by Wang and coworkers for magnetic NPs (e.g., FePt, FeO_x), where OLA and trioctylphosphine ligands were exchanged with small-molecule ligands, such as HBA, 3-(4-hydroxyphenyl)propionic acid (HPP), or gallic acid (GAL).[51] The enhanced steric hindrance provided by these aromatic ligands over other shorter alkyl-chained counterparts provides a distinct advantage for ensuring greater dispersion stability. Furthermore, the presence of the hydrophilic −OH terminal groups enables H-bonding sites that act to stabilize dispersions in solvents of moderate polarity.

While these ligand-exchange approaches have been widely applied, they have not been used to modify the surface chemistry and dispersion of NiO NPs. As such, here we apply HBA and
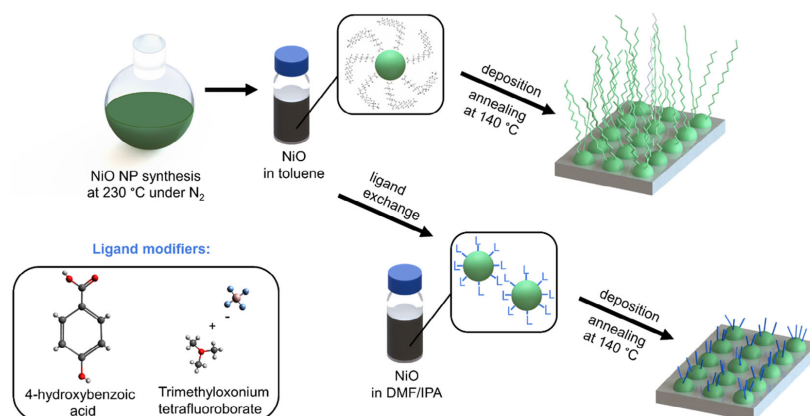
157

Figure 1. The ligand-exchange approach applied in the study. NiO NPs were synthesized via the heat-up method and dispersed in a nonpolar solvent (toluene). The NiO dispersion is stabilized by long alkyl-chained OA ligands. The as-synthesized NPs can be deposited form thin films, incorporating the charge-insulating OA. The OA can be exchanged with shorter ligands in the form of 4-hydroxybenzoic acid or trimethyloxonium tetrafluoroborate, resulting in the formation of stable NiO colloids in polar solvents. Such NiO dispersion can then be deposited to form thin NiO films at a low processing temperature of 140 °C.

trimethyloxonium tetrafluoroborate (Me$_3$OBF$_4$) as two different surface ligand modifiers of OA-capped NiO NPs (see **Figure 1**). These particles have been analyzed using X-ray diffraction (XRD), UV−vis spectroscopy, thermogravimetric analysis (TGA), scanning electron microscopy (SEM), and transmission electron microscopy (TEM). The deposition of these particles as thin films has been assisted using a novel Tesla-valve-like pillar microfluidic (MF) mixer on the dispersion directly prior to deposition.[52] This approach is found to promote high-pressure mixing of low-volume liquids, thereby yielding homogeneous dispersions of NiO NPs just prior to the deposition process to enable highly conformal films. Consistent with lower tunneling barriers,[53] field-effect transistor (FET) measurements of the surface-modified NiO showed appreciable enhancements to the hole mobility for short-chained ligands compared with neat OA. Moreover, the cubic NiO NP films were assessed as HTLs within p−i−n PSCs. Me$_3$OBF$_4$-modified NiO devices showed the highest performance, reaching champion PCEs of 17.9%, whereas HBA led to devices with a PCE of 17.5%. These performance metrics are significantly higher than UV−ozone-treated NiO OA HTLs that reached PCEs of 16% in PSCs. Importantly, device stability testing under maximum power point (MPP) conditions further showed that good stability was achieved across all NiO films, although negligible efficiency changes were only observed for the Me$_3$OBF$_4$ NiO HTLs.
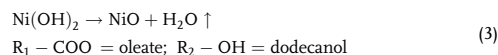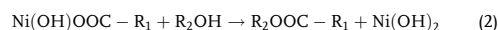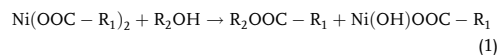
2. Results and Discussion

2.1. Ligand Engineering of NiO

We synthesized NiO NPs following a well-known heat-up method.[54] This approach takes advantage of alkali fatty acid salts, in our case sodium oleate, as a protecting ligand to avoid

the reduction of Ni^{2+} during the NP growth. It is understood that such protecting ligands bind to NiO surfaces to lower their reactivity, thus preventing surface reduction of Ni^{2+} to Ni^0. This is validated by the XRD pattern shown in **Figure 2**a, which confirms pure cubic NiO (according to JCPDS card 04-0835) when the synthesis was conducted in the presence of NaOA, whereas metallic Ni (according to JCPDS card 45-1027) is seen as a major impurity when NaOA is absent.

The overall reaction can be described by the following mechanisms.

$$Ni(OOC - R_1)_2 + R_2OH \rightarrow R_2OOC - R_1 + Ni(OH)OOC - R_1 \tag{1}$$

$$Ni(OH)OOC - R_1 + R_2OH \rightarrow R_2OOC - R_1 + Ni(OH)_2 \tag{2}$$

$$Ni(OH)_2 \rightarrow NiO + H_2O \uparrow$$
$$R_1 - COO = oleate; \ R_2 - OH = dodecanol \tag{3}$$

In the first step of the NiO synthesis, the nickel precursor reacts with an alcohol (Equation (1)), forming an ester and hydroxylated nickel intermediate product. In the second step (Equation (2)), the hydroxylated intermediate product condenses to form nickel hydroxide and the ester. In the final step (Equation (3)), nickel hydroxide condenses to form nickel oxide and water vapor. The resulting NPs are dispersible in nonpolar solvents due to the presence of OA ligands acting as capping agents at the NP surface. Such colloidal dispersions can then be deposited to form thin films (Figure 1). However, when annealing the films at moderate temperatures (140 °C in our study), the presence of residual OA ligands and its decomposition products in the films prevents their utilization as effective hole transport layers without any postdeposition treatment.
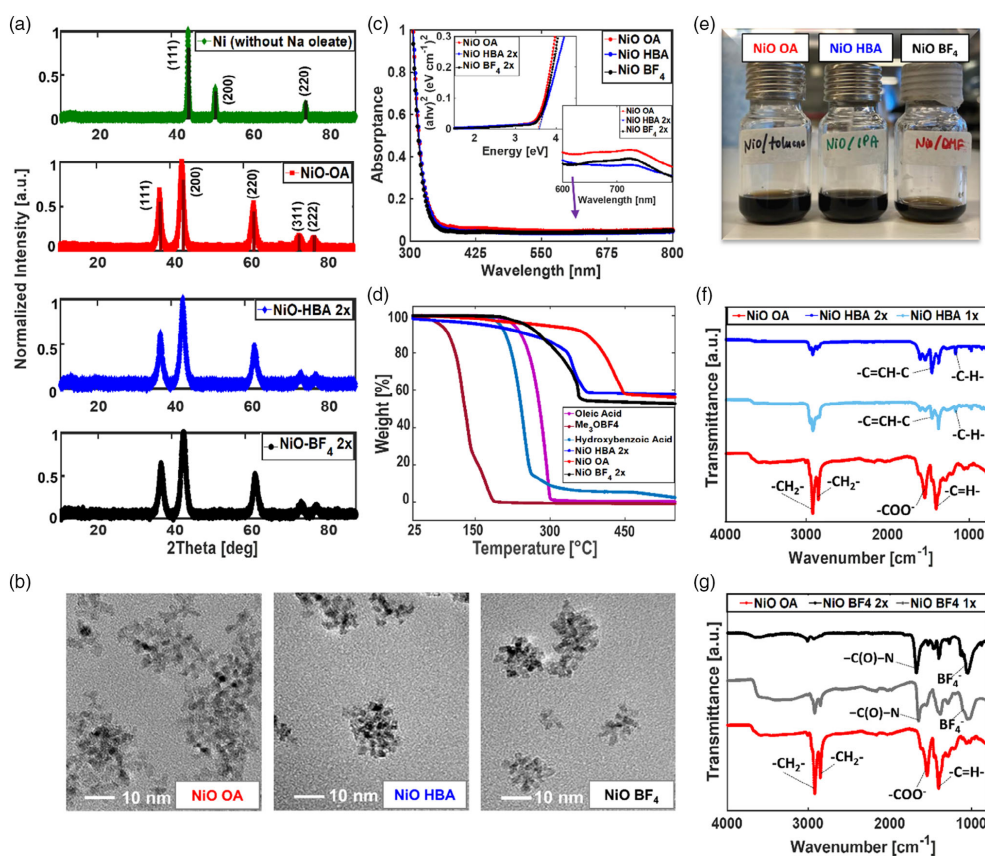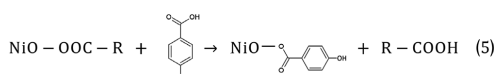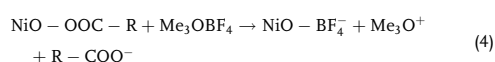
Figure 2. NiO material properties. NiO OA, NiO HBA, and NiO BF$_4$ analysis based on the following approaches: a) XRD, b) TEM, and c) UV−vis spectroscopy. Top inset: Tauc plot. Bottom inset: Magnified UV−vis spectra from 600 to 800 nm. d) TGA and e) NiO dispersions. NiO OA in toluene, NiO HBA in IPA, and NiO BF$_4$ in DMF. f,g) FTIR spectroscopy.

The proper selection of capping ligands affects the dispersibility of NPs in organic solvents. Typically, long alkyl-chained ligands create stable colloidal dispersions in nonpolar liquids, whereas ligands containing more hydrophilic terminating groups, or inorganic ligands, favor dispersion in more polar solvents.[55,56] By exchanging the long alkyl-chained ligands, not only does solvent compatibility for a colloidal system change, but also the organic fraction in the NP dispersion can be significantly decreased.[57] The latter acts to improve the resulting charge transport properties of such colloids when deposited as thin films.[58–60] To achieve this, we have investigated the use of HBA and Me$_3$OBF$_4$ to displace the native oleate surface chemistry on the NiO NPs (see Figure 1 for a general ligand-exchange overview and Experimental Section for synthetic details). The associated ligand-exchange reactions are presented in Equation (4) and (5).

$$NiO - OOC - R + Me_3OBF_4 \rightarrow NiO - BF_4^- + Me_3O^+$$
$$+ R - COO^- \tag{4}$$

$$NiO - OOC - R + \text{(HOOC-C}_6\text{H}_4\text{-OH)} \rightarrow NiO-O_2C\text{-C}_6\text{H}_4\text{-OH} + R - COOH \tag{5}$$

It is worth noting that in the case of Me$_3$OBF$_4$, the actual ligand present at the NiO surface is the anion, BF$_4^-$, which is then stabilized by the highly polar solvent DMF.[50] In case of the HBA, the conjugate base of HBA plays the role of the surface ligand.[51]

The ligand-exchanged NiO powders were analyzed using XRD (see Figure 2a). No differences in phase or texture were found for either NiO BF$_4$ or NiO HBA NPs when compared with unmodified NiO OA. Scherrer analysis based on the XRD patterns

provides an estimated crystal size of all investigated NiO NPs to be 4.9 nm. TEM was further conducted to confirm the NiO NP size (Figure 2b). In all three cases the average particle sizes were determined to be in the range of 3–4 nm (see Figure S1, Supporting Information), which is comparable with the estimations provided by Scherrer analysis.

To probe the optical properties of the dispersed NPs, absorption spectra of NiO OA, NiO BF$_4$, and NiO HBA dispersions in toluene, DMF, and IPA, respectively, were measured using UV−Vis spectroscopy (Figure 2c). Tauc plot analysis (top inset) indicates the samples all possess similar optical bandgap values of ≈3.62 eV. Despite these high optical bandgaps, the dispersions appear brown in color (Figure 2e). This arises from optically active intraband transitions on nickel, inducing a broad absorption across the visible region with a shoulder appearing at ≈700 nm (Figure 2c, bottom inset).[61–63]

To understand the thermal properties of the NiO OA, NiO BF$_4$, and NiO HBA NPs, TGA was conducted under a nitrogen atmosphere (see Figure 2d). A double-ligand-exchange protocol was applied to these samples to maximize ligand-exchange effectiveness (vide infra). For completeness, TGA results of single-ligand-exchanged NiO powders are included in Figure S2, Supporting Information. To complement these measurements, the thermal properties of the neat ligands were measured. These show that OA and HBA start to thermalize at 280 and 250 °C, respectively, whereas Me$_3$OBF$_4$ starts to decompose at only 70 °C. In comparison, the samples with a given surface ligand exhibit proportionately higher thermalization temperatures compared with the neat ligands. For NiO OA, NiO BF$_4$, and NiO HBA, the thermalization temperatures of the ligands are found to be 390, 270, and 340 °C. Notably, both substituent ligands (BF$_4$ and HBA) decompose at lower temperatures compared with OA. However, for applications of these particles where processing is conducted under mild temperatures, 140 °C for 2 min in our case, the surface ligands will be retained across all surface chemistries studied here.

The investigated NiO solids after ligand modification, NiO HBA and NiO BF$_4$, were dispersed in IPA and DMF, respectively, while NiO OA was dispersed in toluene as a control sample (Figure 2e). All of the colloidal dispersions appeared to be stable for at least 30 days in their respective solvents with no evidence of even partial precipitation.

Using Fourier-transform infrared (FTIR) spectroscopy, we probed the chemistry of the dry powders of the NiO NPs before and after the ligand modification process (Figure 2f,g). In both cases, double-ligand-exchange procedures (NiO HBA 2 × or NiO BF$_4$ 2 ×) significantly decrease the intensity of the characteristic vibrations of OA at ≈2919 and 2852 cm^{-1} associated with asymmetric and symmetric stretching, respectively, of the methylene group in the OA chain.[64] A similar suppression of transmittance for the 1598 and 1545 cm^{-1} bands, which correspond to asymmetric and symmetric stretching, respectively, is consistent with the decrease in the signal from the carboxylate group. Naturally, the stretching vibrations could not be entirely suppressed in the case of NiO HBA, as the carboxylate group is present in HBA as well. In comparison, single ligand exchange (NiO HBA 1 × or NiO BF$_4$ 1 ×) is less effective in stripping the native OA ligands, confirming the need for a multistep ligand-exchange process. Notably, the presence of residual OA peaks, even after two ligand exchanges, is indicative of incomplete ligand exchange arising

from the varying reactivities of surface binding sites.[65] For the HBA ligand modification (Figure 2f), aromatic rings are confirmed by the appearance of aromatic ring stretching at 1456 cm^{-1}, together with aromatic in-plane bend at 1150 cm^{-1} and additional out-of-plane bends in the range between 900 and 600 cm^{-1}. We also notice that aromatic C−H stretches coming from HBA at frequency 3000 cm^{-1} may interfere with asymmetric stretches from OA, making the analysis ambiguous.[66,67] For Me$_3$OBF$_4$ modification (Figure 2g), the peak absorption at 1056 cm^{-1} is characteristic of adsorbed BF$_4^{-}$.[68] Notably, the prevalent feature at ≈1650 cm^{-1} corresponds to an amide group[68] from residual solvent (DMF). It arises because of the relatively low drying temperature of 70 °C used during the sample preparation for FTIR analysis.

To further investigate the chemical composition of the NiO NPs with varying surface chemistry, X-ray photoelectron spectroscopy (XPS) was conducted of Ni 2p and O 1s (see Figure S3, Supporting Information). These results indicate that NiO is most likely accompanied by NiO(OH)$_2$ and oxygen defects, although no significant changes across the redox states are observed following ligand exchange.

2.2. Deposition and Characterization of NiO NP Thin Films

We now turn to the deposition of the NPs as thin films that are suitable for integration into PSCs. Here, we have used a novel deposition method that harnesses a MF mixer to dramatically improve the final NiO thin-film quality (**Figure 3**a). Within this system, the dispersions are preloaded into syringes and dispensed through the MF directly onto suitable substrates that are vacuum mounted on a spin coater. Immediately after deposition (see Figure S4, Supporting Information), the substrates are spun and subsequently annealed on a hot plate. The NiO dispersions were optimized in concentration to provide ≈30 nm-thick films following spin coating. To ensure reproducibility of the prepared dispersions and resulting film thicknesses, we utilized an ink calibration curve (see Figure S5, Supporting Information). This curve was further used to ensure that adequate NiO dispersion concentrations were used when preparing films from ligand-modified NiO materials.

UV−Vis spectra were acquired for the pristine NiO OA, modified NiO BF$_4$, and NiO HBA after single- (1×) and double (2×)-ligand exchange as thin films on ITO glass (Figure 3b, inset). The resulting Tauc plots (Figure 3b) reveal the samples to possess a bandgap of ≈3.62 eV, which is in line with the previous bandgap values obtained for the liquid NiO samples. For completeness, we also compared the transmittance properties of the investigated NiO thin films on ITO/glass substrate (see Figure S6, Supporting Information). These show a slight improvement in transparency of the ligand-modified NiO films. For the use of such NiO thin films as HTLs within a p−i−n PSC configuration, the deposition of the perovskite material from DMF and/or DMSO solvent(s) is required. As such, the HTLs have to be stable to this deposition process, while also supporting good wettability of the perovskite precursor solution. Of the NP dispersions, NiO OA NPs are dispersable only in nonpolar solvents and NiO HBA does not disperse well in DMF (see Figure S7, Supporting Information). Therefore, to assess
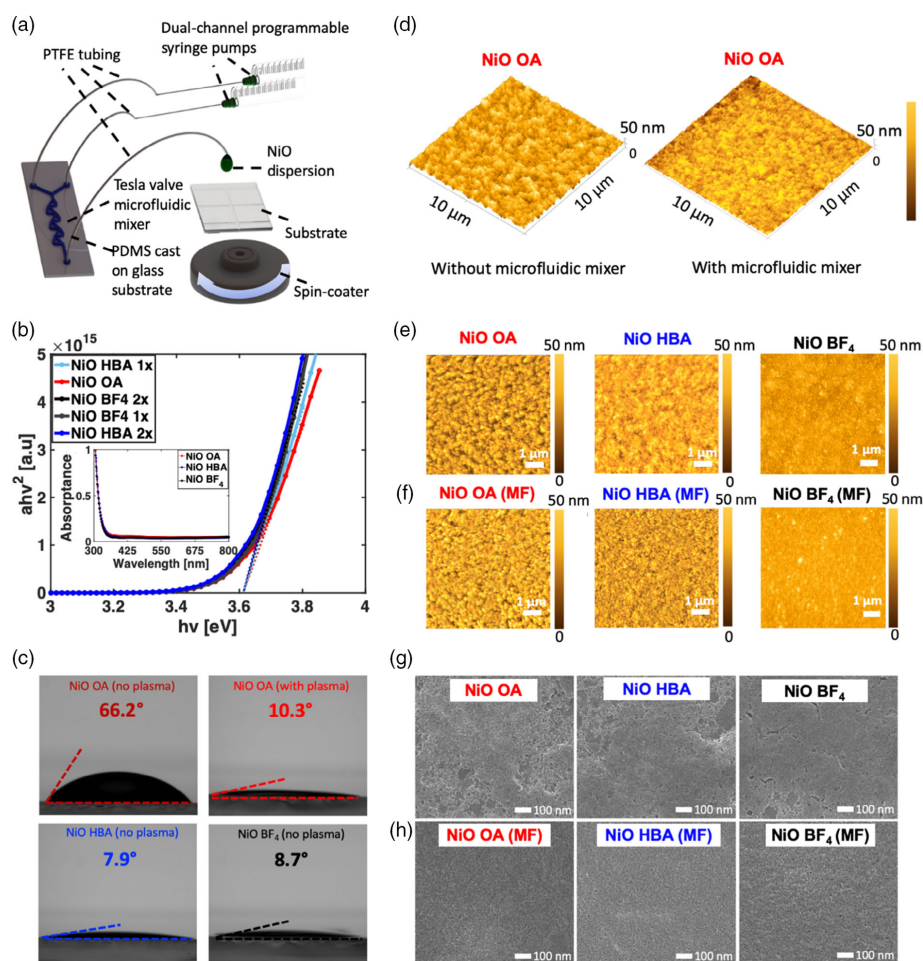
160

Figure 3. MF mixing-enhanced preparation of agglomerate-free nickel oxide films. a) Schematic view of the programmable dual-syringe pump-dispensing mechanism. b) Tauc plots of NiO thin films before and after ligand modifications and the resulting bandgap position. Inset: the normalised UV-Vis absorptance of the NiO films on ITO substrates. c) Contact angle measurements on NiO OA films without plasma treatment, NiO OA films with plasma treatment, NiO BF$_4$, and NiO HBA films without plasma treatment. d) AFM scans of NiO OA films before (left) and after (right) MF mixing. e,f) AFM scan of NiO OA, HBA, and NiO BF$_4$ films before and after MF mixing, respectively. SEM images of NiO films made of dispersions g) before and h) after MF mixing.

the stability of the NiO BF$_4$ thin films, DMF was spin coated onto the NiO films, mimicking the way we normally deposit the perovskite solution on NiO HTLs. We observe no variation in the optical properties of the final NiO BF$_4$ film (see Figure S8, Supporting Information).

As previously mentioned, NiO HTLs with OA ligands are typically plasma treated to remove the charge-insulating ligands and increase the wetting of highly polar perovskite precursor

solutions. Here we further report the impact of the exchanged ligands and pristine film quality on perovskite precursor solution wettability. Static contact angle (CA) measurements were carried out with DMSO as a wetting agent (Figure 3c). The pristine NiO thin film with OA ligands without plasma treatment exhibits a hydrophobic nature with a large CA of 66.2°. After 2 min of UV plasma treatment, which is the standard processing time for NiO OA HTLs applied during fabrication of PSCs, the CA

161

of NiO OA noticeably decreases to 10.3°. As shown in Figure S9, Supporting Information, homogeneous perovskite film formation could only be achieved on the NiO OA HTLs following plasma treatment. In comparison, the CAs for both ligand-modified NiO HBA and NiO BF$_4$ thin films were 7.9° and 8.7°, respectively, without plasma treatment. These results not only reveal the hydrophilic nature of the NiO HBA and NiO BF$_4$ HTLs but more importantly showcase that additional post-treatment procedures are unnecessary. This permits a simpler and more cost-effective NiO deposition process where the oxidation states of the NiO are retained.

In Figure 3d, atomic force microscopy (AFM) images of the NiO OA in toluene deposited onto indium tin oxide (ITO) on glass substrates with and without the MF mixer are shown. Despite the high quality of the NiO dispersions in the solvent, a significant improvement in the root mean square (RMS) surface roughness for an area of $10 \times 10\,\mu m$ is observed when adopting the MF mixer, with a reduction from ≈ 23.7 to $\approx 14.3\,nm$, respectively. Similarly, we also observe RMS value reductions for the NiO HBA and NiO BF$_4$ NP films using the MF approach down to ≈ 8.8 and $\approx 7.9\,nm$, respectively (see Figure 3e,f). From these results, it is evident that the use of the MF premixing results in less agglomeration of the NiO NPs and higher-quality coatings. This is due to the known effect of micropillared MF mixing,[69,70] which acts to increase the local pressure within the inverted multistaged Tesla valves[71] to provide a similar mixing phenomenon to vortexing or ultrasonication.[72,73] As a result, the NiO NPs become more homogeneously dispersed immediately prior to deposition.[74,75] Compared with the NiO HTL quality commonly found in previous reports,[76–79] the introduced MF mixing method yields far superior film quality outcomes, which is critical for their use as HTLs.

In addition to AFM analysis, SEM was used to evaluate the morphology of the NP films with different ligand systems and also the impact of the MF mixer on the film quality. NiO films (with OA, HBA, and BF$_4$ ligands) spin coated on ITO without and with MF mixing are shown in Figure 3g,h, respectively. The films made of unmixed dispersions exhibit uneven coverage of the ITO, whereas a significant improvement in the film quality is observed for those made using the MF system. Notably, no prominent differences are observed for NiO films with different ligands, indicating that these structural differences are inherent to the deposition approach. These outcomes confirm that direct MF mixing facilitates the formation of well-dispersed NO dispersions for high-quality thin HTL films.

As a final comparison, the electronic properties of the NiO NP films deposited using the MF mixer were investigated via fabrication and measurements (see Supporting Information) of p–n–p-type FETs. A comparison of the transfer curves across the different NiO NP films and a summary of their electrical characteristics are shown in Figure S10, Supporting Information. All the samples exhibited p-type characteristics, consistent with NiO featuring Ni^{3+}.[80] Meanwhile a comparison of the extracted hole mobilities shows that the NiO BF$_4$ and HBA samples exhibited values of $>0.04\,cm^2\,V^{-1}\,s^{-1}$, whereas that for the standard NiO OA films possessed a value that was ten times smaller at $\approx 0.004\,cm^2\,V^{-1}\,s^{-1}$. This result can be explained simply by considering that substitution of long ligands with shorter counterparts boosts electronic coupling, which enhances carrier

hopping rates to improve carrier mobility and conductivity.[81] An analogous improvement of carrier mobility was observed for CZTS in PSCs, where OLA ligands were exchanged with BF$_4^-$.[82]

2.3. The Performance of PSC Devices with NiO NP HTLs

The colloidal NiO OA, NiO BF$_4$, and NiO HBA films were utilized as HTLs within planar p–i–n heterojunction PSCs of structure ITO|NiO|perovskite|PC$_{61}$BM|C$_{60}$|BCP|Ag. All the investigated NiO HBA and NiO BF$_4$ films were fabricated using double-ligand-exchanged dispersions. Cross-sectional SEM of the devices presented in **Figure 4**a shows that all the investigated NiO films were densely packed HTLs of $\approx 30\,nm$ in thickness, while supporting similar microstructured perovskite layers of $\approx 400\,nm$. Figure 4b shows the energy-level diagram of the functional layers in the investigated devices. Ultraviolet photoelectron spectroscopy (UPS) was used to determine the relevant VB maxima and Fermi levels of all the NiO samples studied here (see Figure S11, Supporting Information). The conduction band minima were calculated from the bandgaps obtained via Tauc plots for NiO films. Little difference across the assessed NiO samples was observed from these measurements.

The solar cell characteristics of devices prepared for each NiO surface chemistry are shown in Figure 4c–e. All device measurements were taken using a four-wire sense measurement technique.[76,77] Each of the devices exhibited a low hysteresis index($HI_{PSC} = \pm \frac{(PCE_{reverse} - PCE_{forward})}{PCE_{reverse}} \times 100\%$), which was negligible for NiO HBA and NiO BF$_4$, while being $\approx 1\%$ for NiO OA. The characteristics of the champion solar cell devices across each of the investigated NiO films are shown in Figure 4c and summarized in **Table 1**. We report that devices based on NiO BF$_4$ films exhibit the highest overall PCE of $\approx 17.9\%$, followed by $\approx 17.5\%$ for NiO HBA and finally NiO OA, with a PCE of $\approx 16\%$. A notable improvement in short-circuit current (J_{sc}), fill factor (FF), and open-circuit voltage (V_{oc}) is observed for the surface-modified samples. To the best of our knowledge, the devices fabricated using NiO BF$_4$ mark the highest PSC efficiency achieved to date using low temperature ($<150\,°C$).[53,79,83–85] The incident photon-to-current efficiency (IPCE) measurements of these devices are shown in Figure 4d. Integrated photocurrent approximations are in good agreement with those obtained from $J–V$ measurements. The spectral efficiency reduction in the case of NiO OA is pronounced throughout the entire spectral region compared with both NiO HBA and NiO BF$_4$. The efficiency distribution for the ensemble of devices in Figure 4e further shows that, despite its champion efficiency, NiO BF$_4$-based devices exhibited a slightly lower mean efficiency compared with the NiO HBA due to their large performance variance. For completeness, we also include $J–V$ characteristics of devices with NiO HTLs after single-ligand exchange compared with the unmodified NiO HTLs (see Figure S12, Supporting Information). The champion devices of NiO HBA and NiO BF$_4$ exhibited lower PCE values of 16.2% and 16.7%, respectively, compared with double-ligand-exchanged samples (see Table 1). The improved device performance indicates that the residual OA ligands present in the single-ligand exchange samples do indeed have an adverse effect on the devices.
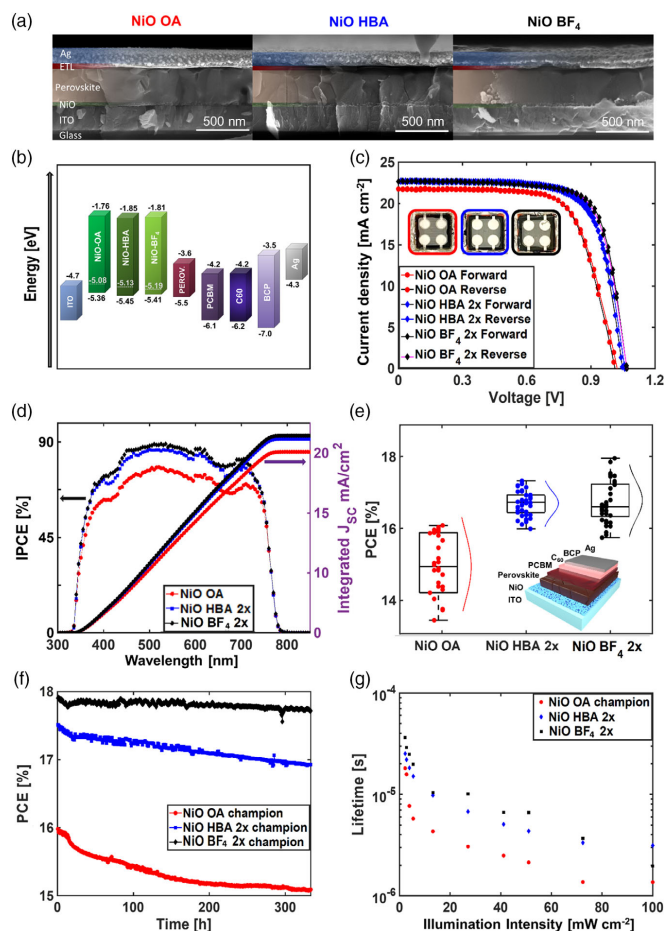
Figure 4. Characterization of PSC devices prepared using the various colloidal NiO films investigated here. a) Cross-sectional SEM images of the investigated inverted PSC devices with NiO OA, NiO BF$_4$, and NiO HBA ligands. b) Energy-level diagram of the NiO HTLs analyzed in this study, including their Fermi Levels. c) Current−voltage ($J−V$) characteristics (inset: pictures of measured and encapsulated devices from left, NiO OA, NiO HBA, and NiO BF$_4$). d) Incident photon-to-current efficiency (IPCE). e) PCE extracted from the three types of devices with different HTLs. Inset: A schematic of the device structure. f) MPP tracking under continuous 1 Sun illumination (encapsulated devices, RH of 40%, temperature of 25 °C). g) TPV lifetime versus illumination intensity.

These results are consistent with the reduction in insulating OA ligands from the NiO HTLs being beneficial for charge transfer, enabling an improvement in overall device performance. However, it is also expected that the exchanged ligands act as passivating layers for the perovskite/HTL boundary. Substitution of halide in perovskite by BF$_4^−$ anion is a well-known approach for improved performance of the light-absorbing layer,[86] but other anions (such as halides) are often introduced to passivate interstitial lead or halide vacancies in perovskite.[81] Typically, bromide[82] or chloride[83] anions are

beneficial for the perovskite film formation and passivation of grain boundaries, respectively. Recent studies have also confirmed the beneficial impact of NaF at the perovskite/HTL interface, where F$^−$-formed hydrogen bonds with organic cations hinder the diffusion of those cations in the light-absorbing layer.[4,87] Furthermore, fluorine was also found to efficiently passivate the perovskite surface to improve the intergrain charge transport.[85]

Encouraged by our results, we undertook stability measurements of the devices. We opted for an independent, parallel,

163

Table 1. Photovoltaic properties of the champion devices with three different types of HTLs. The device structure is ITO|NiO|perovskite|PCBM|C60|BCP|Ag. All devices were measured under simulated solar light (1 Sun) through an aperture mask of size 0.16 cm^2 with a scan rate of 100 mV s^{-1} at 25 °C, RH 40%.

PSC device	Scan direction	V_{OC} [V]	J_{SC} [mA [cm]$^{-2}$]	FF	PCE [%]
NiO OA[a)]	Forward	1.02	20.1	0.67	16.0
–	Reverse	1.03	20.1	0.69	16.1
NiO HBA	Forward	1.05	21.9	0.74	17.5
	Reverse	1.05	22.0	0.75	17.5
NiO BF$_4$	Forward	1.05	22.1	0.76	17.9
	Reverse	1.07	22.1	0.77	17.9

[a)]Values extracted from the champion *J*–*V* characterization, V_{OC}–open-circuit voltage, J_{SC}–short-circuit current density, FF–fill factor, PCE–power conversion efficiency.

and simultaneous testing of the devices under MPP condition.[76,86] MPP tracking was conducted on glass-encapsulated devices to avoid moisture/oxygen degradation. Figure 4f shows the champion device's long-term MPP stability under constant illumination. After a commonly reported initial PCE drop,[87] all the PSCs showed a decay of less than 7% relative to the first measured PCE. The NiO BF$_4$-based devices exhibited the most stable operation, with a relative (absolute) PCE drop of ≈1% (≈0.2%). This promising result indicates that the stability and FF of NiO HTLs is intricately coupled to the presented surface chemistry and that it is significantly more stable than typical organic counterparts, which are well known to be prone to abrupt degradation.[34,88]

Finally, we carried out transient photovoltage decay (TPV) measurements to determine charge carrier lifetime and probe the slow recombination processes. Our custom-built TPV setup relies on monitoring the open-circuit voltage dynamics under periodically illuminated devices with varying intensities through neutral density (ND) glass filters. The nonradiative recombination mechanisms are revealed by comparing our three NiO HTLs in Figure 4g to elucidate the superior properties of ligand-exchanged HTLs. The TPV revealed that in all three cases (NiO OA, NiO HBA, and NiO BF$_4$) there is a reduction in carrier lifetime with an increase in light intensity. Nonetheless, the two ligand-exchanged devices show comparatively higher carrier lifetimes than the NiO OA samples at each intensity (approximately half). Longer carrier lifetimes are correlated with slower recombination rates, which translate to higher V_{oc} and FF, as is observed for our devices. The enhanced recombination rate within the NiO OA-based device is consistent with the OA species on the NiO, reducing its hole mobility and hampering efficient charge extraction.

3. Conclusion

In conclusion, we have demonstrated a unique methodology for the facile preparation of low-temperature, highly reproducible, and solution-processable NiO NP HTLs. It harnesses a ligand-

exchange step to replace the native OA surface chemistry on the NPs with either 4-hydroxybenzoic acid or trimethyloxonium tetrafluoroborate. The solar cell devices fabricated with our ligand-exchanged NiO HTLs used a multistaged Tesla-valve-like MF mixing system directly prior to their deposition to afford high-quality thin films. When these NiO HTLs were used within inverted (p−i−n) Cs$_{0.17}$FA$_{0.83}$PbBr$_{0.55}$I$_{2.45}$ PSCs, the devices exhibited stabilized PCEs of 17.9% and 17.1% for the ligand-exchange NiO HTLs, respectively, which were superior in comparison with control devices harnessing the native surface chemistry and a postprocessing oxygen−plasma treatment step (PCE of 16.1%). Furthermore, while all NiO HTLs exhibited good photostability factors, a significant enhancement was observed for the ligand-exchange NiO HTLs, which, for NiO-BF$_4$, showed a 0.2% reduction in efficiency over a 300 h testing period compared with 0.9% for the NiO-OA-based PSCs. These findings showcase the importance of ligand engineering of NiO NPs for achieving efficient hole-transporting materials and its prospects for developing low-temperature-processable and high-stability PSCs. Future work will consider the printability of these dispersions to achieve fully printed flexible inverted PSCs. In addition, the dispersion of the NiO-HBA in IPA opens up further opportunities toward developing low-temperature-processable standard PSCs.

4. Experimental Section

Materials: OA (90%), nickel (II) acetate tetrahydrate (Ni(ac)$_2$ 4H$_2$O, 98%), Me$_3$OBF$_4$ (95%), 1-octadecene (ODE, 90%), OA (technical grade 90%), 4-hydroxybenzoic acid (HBA, 99%), anhydrous ethanol (EtOH, 99.5%), toluene (99.5%), hexane (anhydrous, 95%), 2-propanol (IPA, 99.5%), chlorobenzene (CBZ, anhydrous 99.8%), 1,2-dichlorobenzene (DCB, anhydrous, 99%), N,N-dimethylformamide (DMF, anhydrous, 99.8%), dimethyl sulfoxide (DMSO, anhydrous, 99.9%), and acetonitrile (ACN, 99.5%) were purchased from Sigma Aldrich. 1-dodecanol (DOD, 98%) and lead bromide (PbBr$_2$, 99.9%) were purchased from Alfa Aesar. Formamidinium iodide (FAI) and methylammonium bromide (MABr) were purchased from Greatcell Solar. Sodium oleate (NaOA, 97%) and lead iodide (PbI$_2$, 99.99%) were purchased from TCI. [6,6]-Phenyl-C61-butyric acid methyl ester (PCBM) was purchased from 1-Material. All materials were used as received without further purification.

NiO NPs Synthesis: Nickel oxide NPs were synthesized following a modified method by Liang et al.[89] Briefly, Ni(ac)$_2$ 4H$_2$O (0.5 mmol), NaOA (0.2 mmol), 1-dodecanol (DOD) (3 mmol), OA (1 mmol), and octadecene (ODE) (4 mL) were added sequentially to a tree-neck round-bottomed flask, mounted to a Schlenk line, mixed, degassed, and heated to 110 °C and kept for 30 min under vacuum.[89] Briefly, Ni(ac)$_2$ 4H$_2$O (0.5 mmol), NaOA (0.2 mmol), 1-dodecanol (DOD) (3 mmol), OA (1 mmol), and octadecene (ODE) (4 mL) were added sequentially to a tree-neck round-bottomed flask, mounted to a Schlenk line, mixed, degassed, and heated to 110 °C and kept for 30 min under vacuum. When the precursors were fully dissolved, the temperature was increased to 235 °C, and the reaction was conducted for 2 h under N$_2$. The green reaction solution naturally cooled down to room temperature, then was precipitated with a mixture of acetone and ethyl acetate (1:1), and centrifuged at 5000 rpm for 5 min. The supernatant was decanted and the solid product was then dissolved in 30 mL of a nonpolar solvent (hexane, toluene) and centrifuged to precipitate impurities. In the final step, the NiO NPs present in the supernatant were precipitated with 30 mL of ethanol (EtOH) and centrifuged at 5000 rpm for 5 min. The dark-green wet solid was then air dried at 70 °C for 4 h and dispersed in a nonpolar solvent (CBZ, toluene, hexane) to a concentration of 15 mg mL^{-1}.[83–89] For the XRD analysis, the dried product was taken.

Ligand-Exchange Routes: 4-hydroxybenzoic acid (HBA) ligand modification was conducted following the exchange route with small ligands.[66] Typically, 50 mg of dry NiO NPs and 500 mg of HBA were added to 20 mL of EtOH and sonicated for 1 h till a clear-brown dispersion was obtained. Then the ligand-exchanged NiO NPs were precipitated with an excess of an antisolvent, such as hexane, and centrifuged. The purification was then conducted by washing with ethanol:hexane (1:2) mix, 2–3 times. The final NiO HBA product was then dispersed in isopropanol (IPA) for single-ligand exchange route (1×) or dried at 50 °C for XRD analysis. For double-ligand exchange (2×), the wet NiO solid obtained after 1× ligand exchange was added to another solution of 500 mg HBA in 20 mL of EtOH, and the ligand exchange was repeated following the steps described earlier.

The ligand stripping with Me$_3$OBF$_4$ salt was conducted following the procedure developed by Rosen et al.[48] Briefly, 150 mg of Me$_3$OBF$_4$ was dissolved in 10 mL of ACN. In a separate vial, 20 mg of NiO NPs was dissolved in 10 mL of hexane; then, the two dispersions were mixed, forming a two-phase system. After 10 s of vortexing, a midphase of ligand-stripped NiO NPs was formed. To isolate the product, the entire system was centrifuged, then washed with toluene, and finally purified by washing with toluene : DMF (1:2) mixture. The final NiO BF$_4$ NPs (after single-ligand exchange, 1×) were dispersed in DMF or dried at 70 °C for XRD analysis. For double-ligand exchange (2×), the wet NiO solid obtained after 1× ligand exchange was again added to 10 mL of hexane. In a separate vial, 150 mg of Me$_3$OBF$_4$ was dissolved in 10 mL of ACN and the ligand-exchange procedure was repeated according to the protocol described earlier.

Solar Device Preparation: The perovskite precursor solution was prepared in a N$_2$-filled glovebox by mixing PbI$_2$ (0.88 mmol), PbBr$_2$ (0.22 mmol), FAI (0.83 mmol), and CsI (0.17 mmol), a precursor solution in a 1 mL mixture (4:1 v v^{-1}) of anhydrous DMF and dimethyl sulfoxide (DMSO). The perovskite precursor solution was stirred overnight until fully dissolved, forming a clear yellow solution. Preparation of the NiO hole transport material: About 15 mg of dried NiO OA NPs were dissolved in 1 mL of toluene, whereas for the ligand-exchanged NPs, 15 mg of NiO BF$_4$ or 15 mg of NiO HBA were dissolved in separate vials in 1 mL of DMF or IPA, respectively.

Solar Cell Fabrication: The ITO-coated glass substrates were designed in house[77] and commercially prepared by Latech Singapore. Cleaning Sequence: Ultrasonication baths with 2% (volume ratio) Hellmanex solution, MilliQ water (18 MΩ), and ethanol (each for 15 min) were prepared and treated with UV plasma cleaning for 10 min and immediately transferred to a fume hood where NiO dispersions were spin coated at 3000 rpm for 30 s and annealed at 140 °C for 2 min. NiO OA samples were plasma treated for 2 min and directly transported to a N$_2$-filled glovebox for perovskite deposition. For the perovskite film deposition, 40 µL cm^{-2} of perovskite precursor solution was spread onto the substrates and then spin coated, following a two-step program at 1000 rpm for 10 s, with a ramping speed of 1000 rpms^{-1}, and then at 5000 rpm for 30 s with a ramping speed of 2000 rpm. About 110 µL of chlorobenzene (CBZ) was poured onto the substrate 5 s before the end of the second step. The substrates were then annealed at 100 °C for 1 h. After cooling, the PCBM solution (10 mg µL^{-1}) in CBZ was deposited on the perovskite layer and spin coated at 3000 rpm for 30 s; subsequently, 20 nm of (C60-Ih)[5,6]fullerene (C60), followed by 5 nm of bathocuproine (BCP) and 60 nm of Ag, was evaporated through a shadow mask, yielding four unique devices on one substrate, each with an area of 0.16 cm^2. To avoid perovskite degradation, the control devices were encapsulated with commercially obtained encapsulation glass and UV glue (Luminescence Technology Corp. LT-U001) under N$_2$ atmosphere.

FET Preparation: In a cleanroom facility (Class 10 000), silicon substrates (diameter: 100 mm, grown by Czochralski method, orientation <1−0−0>, type P, boron doped, resistivity: 0.001–0.002 Ohm cm^{-1}, 525 µm, single-side polished, 3000 Å of thermal oxide, Silicon Valley Microelectronics, Inc) were diced up to 10 × 10 mm square substrates using a wet dicing process (Disco DAD321) and subsequently cleaned by sonication in the following sequence: Milli-Q water–10 min, acetone–20 min, isopropanol–10 min. The top oxide layer was etched

off using deep reactive ion etching (DRIE) and conformal 150 nm of SiO$_2$ was deposited using electron beam evaporation (0.1 Å s^{-1}). The substrates were cleaned with IPA ultrasonication and dried at 120 °C for 30 min and subsequently transported to a nitrogen glovebox, where NiO dispersions were deposited. Typically, 0.5 mL of each NiO dispersion was dispensed directly on the substrate before spin coating (3000 rpm for 30 s) and then annealed at 140 °C for 2 min. Substrates were moved to an electron beam evaporator and 65 nm of Au was evaporated through a shadow mask. Such devices were subsequently measured using a probe station (Signatone WL-1160RF) combined with an Agilent B2902A Precision Source/Measure Unit. Device characterization results were calculated and fit using the Igor script.

MF Mixer: MF mixer molds were fabricated on 4 and 6 in. master silicon wafers using a photolithography technique and utilizing SU-8 photoresist. In a Class 100 cleanroom, poly(dimethylsiloxane) (PDMS, Sylgard 184, Dow Corning, USA) was mixed with crosslinker at a mass proportion of 10:1 (Thinky Mixer Are-310) and was cast onto the wafer. The mixture was vacuum degassed and cured at 75 °C for 4 h. The PDMS cast was removed mechanically from the wafer and the inlet and outlets were bored using a 1 mm-diameter Uni-Core Punch Tool (Ted Pella, Inc. USA). The soda-lime glass substrate was cleaned using the same bath procedure as the ITO glass earlier. The cast and glass substrate were oxygen plasma treated for 20 s (Harrick PDC-32 G-2 230 V) and then immediately bonded onto each other by the use of a compression plate. Silicone tubing (Gecko Optics, Perth, Australia) was inserted into the inlet and outlet of the mixer to interface with PTFE (Tygon Tubing) tubing connected with syringes.

Optical Properties: Transmission and reflection spectra were obtained on a Perkin Elmer Lambda 1050 UV−vis−NIR spectrophotometer equipped with an integrating sphere (150 mm InGaAs Integrating Sphere) relative to a standard of known reflectivity. These two measurements were then used to calculate the absorbance (A) according to the equation $A = 100 − (R + T)$. Photoelectron spectroscopy in Air (PESA) measurements were carried out using a Riken Keiki AC-2 spectrometer. For all samples, a power intensity of 20 nW was used. Photographs were taken using a Canon EOS 450 D with an EFS 60 macrolens.

Surface Morphology: AFM measurements were carried out on a Dimension Icon (Veeco) in air. Chromium−platinum-coated conductive probes (ElectriMulti75-G, BudgetSensors) were used for the scans. The scanning area and scanning rate were 10 × 10 µm at 0.5 Hz, respectively. Grain cluster size was refit and scans were levelized by Gwyddion software. The top-view NiO film morphology was characterized by JEOL 7001F FEGSEM and the perovskite device cross sections were characterized by FEI Magellan 400 FEGSEM.

X-Ray Diffraction: XRD patterns were collected with a Bruker D8 Advance Diffractometer with a Cu Kα X-ray tube at 40 kV and 40 mA and with a step size of 0.02° and 0.8 s per step.

X-Ray Photoelectron Spectroscopy and Ultraviolet Photoelectron Spectroscopy: XPS analysis was conducted on Thermo Scientific Nexsa Surface Analysis System with monochromated Al Kα X-ray (1486.6 eV), using a 40 eV pass energy for the high-resolution narrow scans. Ultraviolet photoelectron spectroscopy was conducted using Al Kα and He (I) source (21.21 eV) with pass energies of 200 eV (50 eV for narrow scan) and 3 eV that were used to emit X-ray and UV photons, respectively. The measurements were carried out with a chamber pressure below $5.0 × 10^{-8}$ Torr. The work function was determined directly from the secondary cut-off energy through the relation Work Function = 21.21− Secondary Cut-Off Energy.

Transmission Electron Microscopy: TEM images were taken by a FEI Tecnai G2 T20 transmission electron microscope equipped with a LaB$_6$ electron source under the voltage of 200 kV. The NiO NPs were deposited from diluted dispersions onto carbon-coated copper TEM grids (Proscitech).

IPCE: Incident photon-to-current efficiency (IPCE) spectra were measured using an in-house-built Keithley 2400 Source Meter under 300 W xenon-lamp irradiation with an Oriel Cornerstone 260¼ m monochromator. The monochromatic photon flux was measured through a calibrated silicon cell (Peccell Technologies). To ensure perpendicular light orientation, a custom-made printed circuit board was built to position the substrate.

Transient Photovoltage: TPV decay measurements were accomplished using an in-house-built system by illuminating solar devices with a constant background intensity high-power white light-emitting diode (Thorlabs MWWHL3). A light perturbation was delivered by a Kingbright L7104VGCH light-emitting diode (465 nm wavelength) triggered by a signal generator (Agilent 33533A). A pulse width of 2 μs was chosen for perturbation with the rise and fall times of the light emitting diodes (LED) to be <100 ns measured using a Thorlabs DET10A M^{-1} Si photodetector. The transient response of the solar cell under test was recorded on an Agilent DSOX 3032A (DOSC). For TPV measurements, solar cells were connected with the termination of 1 MΩ to achieve open-circuit condition. The intensity of the background LED was changed to achieve different V_{OC} conditions. To measure the transient photocurrent response, the device was connected to the DOSC with a 50 Ω termination to achieve a short-circuit condition. The LED intensity was verified and calibrated to correspond to $J-V$ curves achieved under specific ND-filtered light as a fraction of a 1 Sun AAA-simulated light (ABET 3000 solar simulator).

Fourier-Transform Infrared Spectroscopy: FTIR measurements were carried out on a Thermo Scientific Nicolet 6700 FTIR spectrometer with a Smart iTR Attenuated Total Reflectance (ATR) Sampling Accessory. A typical measurement consisted of 16 scans that were later averaged into a single figure with a resolution of 4 cm^{-1}.

Thermogravimetric Analysis: TGA was conducted using Mettler Toledo Thermogravimetric Analyser 2 Star System. Nitrogen gas was used during the analysis at 40 mL min^{-1} rate and cell gas at 20 mL min^{-1} at a temperature ramp rate of 10 K min^{-1} from 25 to 500 °C. Samples were heated in alumina crucibles.

Contact Angle: CA measurements were obtained using a Contact Angle System OCA (Dataphysics). Dimethylformamide was dropped onto samples with a dosing volume of 3.5 μL and a dosing rate of 1 μL s^{-1}.

Solar Devices Performance: The current−density ($J-V$) curves of the devices were measured using a fully automated combinatorial high-throughput solar cell measurement system that was reported by Surmiak et al. previously.[83] To simulate solar light, an ABET 3000 solar simulator with a xenon-arc lamp, fed with 1000 W input power, was used. The light intensity was calibrated using a professional reference silicon cell with an IR cut-off filter (KG5, Schott). The $J-V$ curves were measured using a BioLogic VMP3 potentiostat in a four-wire sense configuration. All measurements ($J-V$ dark, $J-V$ light, stability, and MPP tracking) were taken automatically without human interaction, using a high-throughput measurement technique. There was a 5 min break applied, where the devices were cooled down by a laminar flow of N$_2$. The voltage step was set to 10 mV s^{-1}, the starting voltage was reversed, and no bias conditioning or light soaking was applied. The working area of the devices was set to 0.16 cm^2. The initial performance measurement was followed by the long stability testing. All champion devices were aged and measured simultaneously inside ATLAS SC3 340 MHG climate chamber using an in-house-made 20-channel custom parallel real-time measurement system based on Osilla Xtralien X200 source-measure units. The voltage step was set to 10 mV s^{-1}, the starting voltage was reversed, no bias conditioning or light soaking was applied, and MPP tracking was based on perturb−observe algorithm.[6,90] The test conditions were 1 Sun, 25 °C, and relative humidity (RH) of 40%. The devices were encapsulated and a shadow mask was mounted to limit working area of the devices to 0.16 cm^2.

Supporting Information

Supporting Information is available from the Wiley Online Library or from the author.

Conflict of Interest

The authors declare no conflict of interest.

Data Availability Statement

Research data are not shared.

[1] M. Jeong, I. W. Choi, E. M. Go, Y. Cho, M. Kim, B. Lee, S. Jeong, Y. Jo, H. W. Choi, J. Lee, J.-H. Bae, S. K. Kwak, D. S. Kim, C. Yang, *Science* **2020**, *369*, 1615.

[2] C. Zuo, A. D. Scully, W. L. Tan, F. Zheng, K. P. Ghiggino, D. Vak, H. Weerasinghe, C. R. McNeill, D. Angmo, A. S. R. Chesman, M. Gao, *Commun. Mater.* **2020**, *1*, 33.

[3] T. M. Schmidt, T. T. Larsen-Olsen, J. E. Carlé, D. Angmo, F. C. Krebs, *Adv. Mater.* **2015**, *5*, 1500569.

[4] H. Su, M. Zhang, Y.-H. Chang, P. Zhai, N. Y. Hau, Y.-T. Huang, C. Liu, A. K. Soh, S.-P. Feng, *ACS Appl. Mater. Interfaces* **2014**, *6*, 5577.

[5] I. Hussain, H. P. Tran, J. Jaksik, J. Moore, N. Islam, M. J. Uddin, *Emergent Mater.* **2018**, *1*, 133.

[6] M. Saliba, J.-P. Correa-Baena, C. M. Wolff, M. Stolterfoht, N. Phung, S. Albrecht, D. Neher, A. Abate, *Chem. Mater.* **2018**, *30*, 4193.

[7] J. M. Ball, M. M. Lee, A. Hey, H. J. Snaith, *Energy Environ. Sci.* **2013**, *6*, 1739.

[8] Y. Chen, W. Tang, Y. Wu, R. Yuan, J. Yang, W. Shan, S. Zhang, W.-H. Zhang, *Solar RRL* **2020**, *4*, 2000344.

[9] F. Wang, M. Yang, Y. Zhang, J. Du, D. Han, L. Yang, L. Fan, Y. Sui, Y. Sun, X. Meng, J. Yang, *Chem. Eng. J.* **2020**, *402*, 126303.

[10] P. Roy, N. Kumar Sinha, S. Tiwari, A. Khare, *Solar Energy* **2020**, *198*, 665.

[11] L. Hu, S. Li, L. Zhang, Y. Liu, C. Zhang, Y. Wu, Q. Sun, Y. Cui, F. Zhu, Y. Hao, Y. Wu, *Carbon* **2020**, *167*, 160.

[12] D. Liu, Q. Wang, C. J. Traverse, C. Yang, M. Young, P. S. Kuttipillai, S. Y. Lunt, T. W. Hamann, R. R. Lunt, *ACS Nano* **2018**, *12*, 876.

[13] L. Zhou, J. Chang, Z. Liu, X. Sun, Z. Lin, D. Chen, C. Zhang, J. Zhang, Y. Hao, *Nanoscale* **2018**, *10*, 3053.

[14] Y. Rong, Y. Hu, S. Ravishankar, H. Liu, X. Hou, Y. Sheng, A. Mei, Q. Wang, D. Li, M. Xu, J. Bisquert, H. Han, *Energy Environ. Sci.* **2017**, *10*, 2383.

[15] Q. Jiang, X. Zhang, J. You, *Small* **2018**, *14*, 1801154.

[16] P. Zhang, J. Wu, T. Zhang, Y. Wang, D. Liu, H. Chen, L. Ji, C. Liu, W. Ahmad, Z. D. Chen, S. Li, *Adv. Mater.* **2018**, *30*, 1703737.

[17] C. Zuo, L. Ding, *Small* **2015**, *11*, 5528.

[18] S. Uthayaraj, D. Karunarathne, G. Kumara, T. Murugathas, S. Rasalingam, R. Rajapakse, P.amoorthy. Ravirajan, D. Velauthapillai, *Materials* **2019**, *12*, 2037

[19] V. E. Madhavan, I. Zimmermann, A. A. B. Baloch, A. Manekkathodi, A. Belaidi, N. Tabet, M. K. Nazeeruddin, *ACS Appl. Energy Mater.* **2020**, *3*, 114.

[20] T. H. Schloemer, J. A. Raiford, T. S. Gehan, S. Moot, S. Nanayakkara, S. P. Harvey, R. C. Bramante, S. Dunfield, A. E. Louks, A. E. Maughan, L. Bliss, M. D. McGehee, M. F. A. M. van Hest, M. O. Reese, S. F. Bent, J. J. Berry, J. M. Luther, A. Sellinger, *ACS Energy Lett.* **2020**, *5*, 2349.

[21] L. Zhou, Y. Zuo, T. K. Mallick, S. Sundaram, *Sci. Rep.* **2019**, *9*, 8778.

[22] L. Xu, X. Chen, J. Jin, W. Liu, B. Dong, X. Bai, H. Song, P. Reiss, *Nano Energy* **2019**, *63*, 103860.

[23] M. Hu, X. Wu, W. L. Tan, B. Tan, A. D. Scully, L. Ding, C. Zhou, Y. Xiong, F. Huang, A. N. Simonov, U. Bach, Y.-B. Cheng, S. Wang, J. Lu, *ACS Appl. Mater. Interfaces* **2020**, *12*, 8260.

[24] M. Jiang, J. Yuan, G. Cao, J. Tian, *Chem. Eng. J.* **2020**, *402*, 126152.

[25] Y. Kim, E. H. Jung, G. Kim, D. Kim, B. J. Kim, J. Seo, *Adv. Mater.* **2018**, *8*, 1801668.

[26] Y. Liu, Z. Hong, Q. Chen, H. Chen, W.-H. Chang, Y. M. Yang, T.-B. Song, Y. Yang, *Adv. Mater.* **2016**, *28*, 440.

[27] S. A. Ok, B. Jo, S. Somasundaram, H. J. Woo, D. W. Lee, Z. Li, B.-G. Kim, J. H. Kim, Y. J. Song, T. K. Ahn, S. Park, H. J. Park, *Nat. Commun.* **2018**, *9*, 4537.

[28] A. Urbina, *J. Phys. Energy* **2020**, *2*, 022001

[29] H. D. Pham, L. Xianqiang, W. Li, S. Manzhos, A. K. K. Kyaw, P. Sonar, *Energy Environ. Sci.* **2019**, *12* 1177.

[30] P.-K. Kung, M. H. Lin, P. Y. Lin, Y. H. Chiang, C. R. Chan, T. F. Guo, P. Chen, et al., *Adv. Mater.* **2018**, *5*, 1800882.

[31] Q. Wu, S. Mao, Z. Wang, Y. Tong, Y. Lu, Y. Hao, *Nano Sel.* **2020**, *1*, 111.

[32] W. Chen, Y. Wu, J. Fan, A. B. Djurišić, F. Liu, H. W. Tam, A. Ng, C. Surya, W. K. Chan, D. Wang, Z.-B. He, *Adv. Mater.* **2018**, *8*, 1703519.

[33] X. Yin, Z. Yao, Q. Luo, X. Dai, Y. Zhou, Y. Zhang, Y. Zhou, S. Luo, J. Li, N. Wang, H. Lin, *ACS Appl. Mater. Interfaces* **2017**, *9*, 2439.

[34] A. C. Nkele, A. C. Nwanya, N. M. Shinde, S. Ezugwu, M. Maaza, J. S. Shaikh, F. I. Ezema, *Int. J. Energy Res.* **2020**, *44*, 9839.

[35] X. Yin, Y. Guo, H. Xie, W. Que, L. B. Kong, *Solar RRL* **2019**, *3*, 1900001.

[36] N. Kumar, H. B. Lee, S. Hwang, J.-W. Kang, *J. Mater. Chem. A* **2020**, *8*, 3357.

[37] C. C. Boyd, R. C. Shallcross, T. Moot, R. Kerner, L. Bertoluzzi, A. Onno, S. Kavadiya, C. Chosy, E. J. Wolf, Jérémie. Werner, J. A. Raiford, C. de Paula, A. F. Palmstrom, Z. J. Yu, J. J. Berry, S. F. Bent, Z. C. Holman, J. M. Luther, E. L. Ratcliff, N. R. Armstrong, M. D. McGehee, *Joule* **2020**, *4*, 1759.

[38] J. Sun, J. Lu, B. Li, L. Jiang, A. S. Chesman, A. D. Scully, T. R. Gengenbach, Y.-B. Cheng, J. J. Jasieniak, *Nano Energy* **2018**, *49*, 163.

[39] M. Najafi, F. Di Giacomo, D. Zhang, S. Shanmugam, A. Senes, W. Verhees, A. Hadipour, Y. Galagan, T. Aernouts, S. Veenstra, R. Andriessen, *Small* **2018**, *14* 1702775.

[40] Z. Liu, A. Zhu, F. Cai, L. Tao, Y. Zhou, Z. Zhao, Q. Chen, Y.-B. Cheng, H. Zhou, *J. Mater. Chem. A* **2017**, *5*, 6597.

[41] J. Tang, D. Jiao, L. Zhang, X. Zhang, X. Xu, C. Yao, J. Wu, Z. Lan, et al., *Solar Energy* **2018**, *161*, 100.

[42] K. V. Korpany, D. D. Majewski, C. T. Chiu, S. N. Cross, A. S. Blum, et al., *Eur. J. Inorg. Chem.* **2015**, *2015*, 2889.

[43] X. Peng, T. E. Wilson, A. P. Alivisatos, P. G. Schultz, et al., *Angew. Chem.* **1997**, *36*, 145.

[44] D. Wawrzynczyk, A. Bednarkiewicz, M. Nyk, J. Cichos, M. Karbowiak, D. Hreniak, W. Strek, M. Samoc, *J. Nanosci. Nanotechnol.* **2012**, *12*, 1886.

[45] D. V. Talapin, C. B. Murray, *Science* **2005**, *310*, 86.

[46] A. Nag, V. M. Kovalenko, J. S. Lee, W. Liu, B. Spokoyny, D. V. Talapin, *J. Am. Chem. Soc.* **2011**, *133*, 10612.

[47] D. Bederak, N. Sukharevska, S. Kahmann, M. Abdu-Aguye, H. Duim, D. N. Dirin, M. V. Kovalenko, G. Portale, M. A. Loi, *ACS Appl. Nano Mater.* **2018**, *1*, 6882.

[48] E. L. Rosen, D. R. Buonsanti, L. Anna, R. Buonsanti, A. Llordes, A. M. Sawvel, D. J. Milliron, B. A. Helms, et al., *Angew. Chem. Int. Ed.* **2012**, *51*, 684.

[49] A. Dong, X. Ye, J. Chen, Y. Kang, T. Gordon, J. M. Kikkawa, C. B. Murray, et al., *J. Am. Chem. Soc.* **2010**, *133*, 998.

[50] L. S. Khanzada, I. Levchuk, Y. Hou, H. Azimi, A. Osvet, R. Ahmad, M. Brandl, P. Herre, M. Distaso, R. Hock, W. Peukert, M. Batentschuk, C. J. Brabec, et al., *Materials* **2016**, *26*, 8300.

[51] X. Liang, Q. Yi, S. Bai, X. Dai, X. Wang, Z. Ye, F. Gao, F. Zhang, B. Sun, Y. Jin, et al., *Nano Lett.* **2014**, *14*, 3117.

[52] C.-C. Hong, J.-W. Choi, C. H. Ahn, *Lab Chip* **2004**, *4*, 109.

[53] G. Mallick, J. Labh, L. Giri, A. C. Pandey, S. P. Karna, *AIP Adv.* **2017**, *7*, 085007.

[54] X. Liang, Q. Yi, S. Bai, X. Dai, X. Wang, Z. Ye, F. Gao, *Nano Lett.* **2014**, *14*, 3117.

[55] C. A. Fernandez, J. G. Bekhazi, E. M. Hoppes, G. E. Fryxell, C. Wang, J. T. Bays, M. G. Warner, R. J. Wiacek, R. S. Addleman, et al., *Langmuir* **2009**, *25*, 4900.

[56] S. R. Tulsani, S. Ganguly, A. K. Rath, et al., *J. Mater. Sci. Mater. Electron.* **2019**, *30*, 16234.

[57] S. Shaw, T. F. Silva, P. Mohapatra, D. Mendivelso-Perez, X. Tian, F. Naab, C. L. Rodrigues, E. A. Smith, L. Cademartiri, *Phys. Chem. Chem. Phys.* **2019**, *21*, 1614.

[58] E. L. Rosen, A. M. Sawvel, D. J. Milliron, B. A. Helms, *Chem. Mater.* **2014**, *26*, 2214.

[59] J.-S. Lee, M. V. Kovalenko, J. Huang, D. S. Chung, D. V. Talapin, *Nat. Nanotechnol.* **2011**, *6*, 348.

[60] J. J. Jasieniak, B. I. MacDonald, P. Mulvaney, *Nanomater. Polym. Devices* **2015**, 357.

[61] A. Hagfeldt, G. Boschloo, *J. Phys. Chem. B* **2001**, *105*, 5585.

[62] W. Kleemann, T. Tsuboi, *J. Phys. Condens. Matter* **1994**, *6*, 8625.

[63] L. Kumari, W. Z. Li, C. H. Vannoy, R. M. Leblanc, D. Z. Wang, *Cryst. Res. Technol.* **2009**, *44*, 495.

[64] J. Huang, W. Liu, D. S. Dolzhnikov, L. Protesescu, M. V. Kovalenko, B. Koo, S. Chattopadhyay, E. V. Shenchenko, D. V. Talapin, et al., *ACS Nano* **2014**, *8*, 8537.

[65] V. Chechik, A. Caragheorgheopol, *Phys. Chem. Chem. Phys.* **2008**, *10*, 5029.

167

[66] X. Wang, R. D. Tilley, J. J. Watkins, et al., *Langmuir* **2014**, *30*, 1514.

[67] J. Coates, *Encyclopedia of Analytical Chemistry: Applications, Theory and Instrumentation*, Wiley **2006**.

[68] W. Q. Feng, Y.-H. Lu, Y. Chen, Y. W. Lu, T. Yang, et al., *J. Therm. Anal. Calorim.* **2016**, *125*, 143.

[69] Y.-J. Ko, S.-M. Ha, H.-J. Kim, D.-H. Lee, Y. Ahn, *J. Solid Mech. Mater. Eng.* **2008**, *2*, 445.

[70] P. M. Valencia, P. A. Basto, L. Zhang, M. Rhee, R. Langer, O. C. Farokhzad, R. Karnik, *ACS Nano* **2010**, *4*, 1671.

[71] J. P. Martins, G. Torrieri, H. A. Santos, *Expert Opin. Drug Delivery* **2018**, *15*, 469.

[72] A. A. S. Bhagat, I. Papautsky, *J. Micromech. Microeng.* **2008**, *18*, 085005.

[73] C. Fan, Y. Luo, T. Xu, Y. Song, X. Zhang, *Nanoscale* **2021**, *13*, 739.

[74] T. V. Thi, A. K. Rai, J. Gim, J. Kim, *J. Power Sources* **2015**, *292*, 23.

[75] P. M. Ponnusamy, S. Agilan, N. Muthukumarasamy, T. S. Senthil, G. Rajesh, M. R. Venkatraman, D. Velauthapillai, *Mater. Charact.* **2016**, *114*, 166.

[76] W. Nie, H. Tsai, J.-C. Blancon, F. Liu, C. C. Stoumpos, B. Traore, M. Kepenekian, O. Durand, C. Katan, S. Tretiak, J. Crochet, P. M. Ajayan, M. Kanatzidis, J. Even, A. D. Mohite, *Adv. Mater.* **2018**, *30*, 1703879.

[77] J. W. Jung, C.-C. Chueh, A. K. Y. Jen, *Adv. Mater.* **2015**, *27*, 7874.

[78] Z. Liu, J. Chang, Z. Lin, L. Zhou, Z. Yang, D. Chen, C. Zhang, S. Liu, Y. Hao, *Adv. Mater.* **2018**, *8*, 1703432.

[79] Q. He, K. Yao, X. Wang, X. Xia, S. Leng, F. Li, *ACS Appl. Mater. Interfaces* **2017**, *9*, 41887.

[80] H. Lee, Y.-T. Huang, M. W. Horn, S.-P. Feng, *Sci. Rep.* **2018**, *8*, 5590.

[81] Y. Liu, M. Gibbs, J. Puthussery, S. Gaik, R. Ihly, H. W. Hillhouse, M. Law, et al., *Nano Lett.* **2010**, *10*, 1960.

[82] L. S. Khanzada, I. Levchuk, Y. Hou, H. Azimi, A. Osvet, R. Ahmad, M. Brandl, P. Herre, M. Distaso, R. Hock, W. Peukert, M. Betentschuk, C. J. Brabec, et al., *Adv. Funct Mater.* **2016**, *26*, 8300.

[83] M. A. Surmiak, T. Zhang, J. Lu, K. J. Rietwyk, S. R. Raga, D. P. McMeekin, U. Bach, *Solar RRL* **2020**, *4*, 2000097.

[84] K.-C. Wang, J.-Y. Jeng, P.-S. Shen, Y.-C. Chang, E. W.-G. Diau, C.-H. Tsai, T.-Y. Chao, H.-C. Hsu, P.-Y. Lin, P. Chen, T.-F. Guo, T.-C. Wen, *Sci. Rep.* **2014**, *4*, 4756.

[85] M. I. Hossain, A. K. M. Hasan, W. Qarony, M. Shahiduzzaman, M. A. Islam, Y. Ishikawa, Y. Uraoka, N. Amin, D. Knipp, M. Akhtaruzzaman, Y. H. Tsang, *Small Methods* **2020**, *4*, 2000454.

[86] J. Zhang, S. Wu, T. Liu, Z. Zhu, A. K. Y. Jen, et al., *Adv. Funct. Mater.* **2019**, *29*, 1808833.

[87] N. Li, S. Tao, Y. Chen, X. Niu, C. K. Onwudinanti, C. Hu, Z. Qiu, Z. Xu, G. Zheng, L. Wang, Y. Zhang, L. Li, H. Liu, Y. Lun, J. Hong, X. Wang, Y. Liu, H. Xie, Y. Gao, Y. Bai, S. Yang, G. Brocks, Q. Chen, H. Zhou, *Nature Energy* **2019**, *4*, 408.

[88] S. Ruan, M.-A. Surmiak, Y. Ruan, D. P. McMeekin, H. Ebendorff-Heidepriem, Y.-B. Cheng, J. Lu, C. R. McNeill, *J. Mater. Chem. C* **2019**, *7*, 9326.

[89] X. Liang, Q. Yi, S. Bai, X. Dai, X. Wang, Z. Ye, F. Gao, F. Zhang, B. Sun, Y. Jin, et al., *Nano Lett.* **2014**, *14*, 3117.

[90] L. Rakocevic, F. Ernst, N. T. Yimga, S. Vashishtha, T. Aernouts, T. Heumueller, C. J. Brabec, R. Gehlhaar, J. Poortmans, *Solar RRL* **2019**, *3*, 1800287.

Supporting Information

Microfluidic Processing of Ligand-Engineered NiO Nanoparticles for Low-Temperature Hole Transporting Layers in Perovskite Solar Cells

Monika Michalska (F C-A), Maciej Adam Surmiak (F C-A), Fatemeh Maasoumi, Dimuthu C. Senevirathna, Paul Chantler, Hanchen Li, Bin Li, Tian Zhang, Xionfeng Lin, Hao Deng, Naresh Chandrasekaran, T. A. Nirmal Peiris, Kevin James Rietwyk, Anthony S. R. Chesman, Tuncay Alan, Doojin Vak and Udo Bach*, Jacek J. Jasieniak*
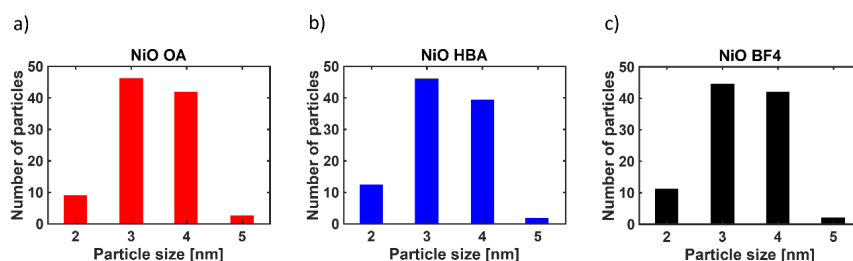

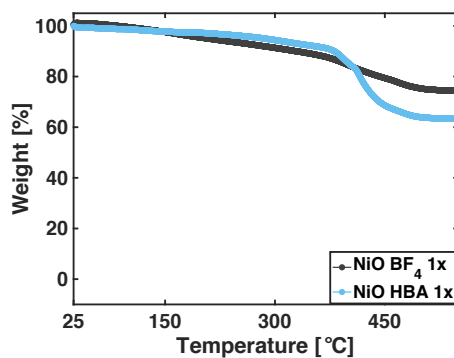**Figure S1:** Histogram of NiO NP size distribution. a) NiO OA, b) NiO HBA, c) NiO BF$_4$.

Figure S2: TGA analysis of single ligand-exchanged NiO powders.

Section 1. XPS of NiO NPs

Given that Ni is known to exhibit a complex and overlapping photoelectron spectrum, we do not provide a quantitative analysis of its components.[94] Qualitatively, the Ni 2p$_{3/2}$ peaks across all surface chemistries were comparable (**Figure S3 a**), with the main signature at ~854 eV, the broad satellite peak at ~862 eV and a peak at ~856 eV. These combined signatures are most likely NiO with some Ni(OH)$_2$.[94] The comparable photoelectron spectra across the samples confirms that the ligand exchange process does not alter the oxidation state of the Ni within the NiO NPs.

Figure S3 b, shows the O 1s region of the various NiO NPs. These scans, similarly to Ni 2p$_{3/2}$, also correspond to multiple contributions, with the main peak at ~529 eV that most likely corresponds to NiO and a broader peak at ~531 eV which may originate from the NiO crystal lattice, hydroxides or oxygen defects in the oxide crystal.[4-56] Thus, despite that we can observe significant changes in spectral intensity in the case of Ni HBA 2×, we do not provide quantitative analysis of the O 1s region. However, we can confirm that no significant changes in the position and shape of the O 1s peaks across the different surface chemistries can be observed.
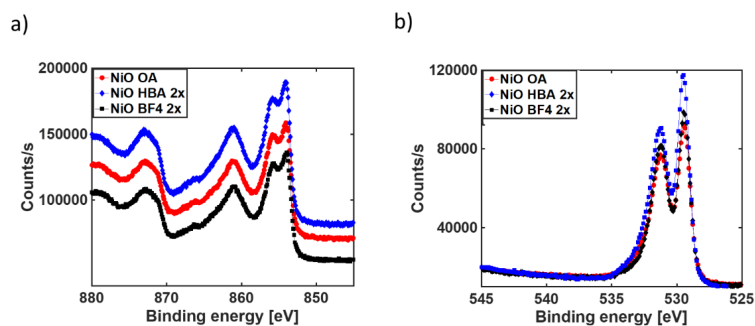

a)

b)

Figure S3: Comparison of NiO materials' properties with different surface ligands. a and b) XPS Ni2p and O1s spectra of NiO thin films (with OA, or BF_4^-, and HBA ligands after double ligand exchange), respectively.

Figure S4: Picture of the fabrication setup located in the fume hood (from left: dual syringe pump with preloaded NiO_x dispersions, microfluidic mixers, spin-coater and annealing plate). The computer-controlled syringe pump triggers the simultaneous push of two syringes which are preloaded with equal amount of thoroughly mixed and ultrasonically shaken dispersions, the tubing is connecting both syringes to the inverted-multistage Tesla valve and pushes the solutions through it (the channels inside of the Tesla valve have micropillars (1-3 µm), the Tesla valves can be connected in series for better mixing or the tube can be directly positioned above the substrate. The aliquoted amount (typically 50 to 100 µL) is being deposited and the spin-coater with pre-programmed speed and time begins the spin-coating. The substrate is subsequentially removed from the vacuum chuck and placed on the hot-plate.
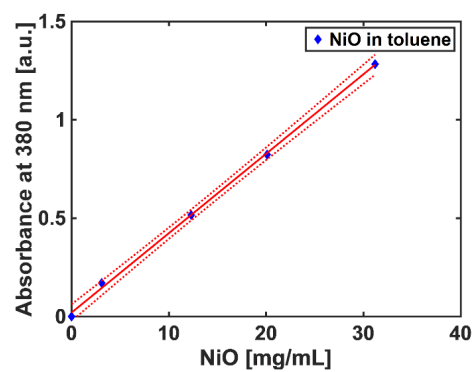
Figure S5: Calibration curve for NiO OA in toluene. A relation between NiO OA
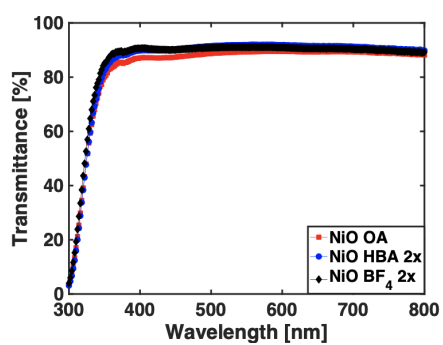
concentration and absorption at 380 nm.

Figure S6: Comparison of NiO thin films' transmittance on ITO substrates.
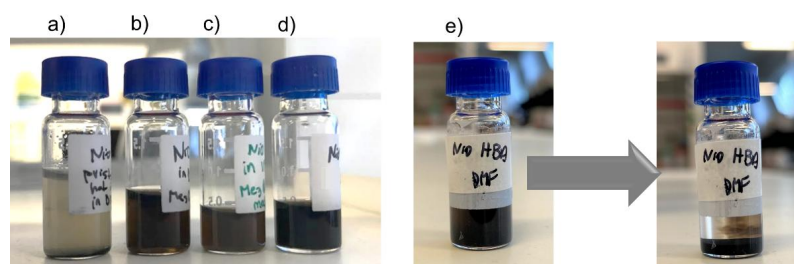
Figure S7: Dispersibility comparison of the investigated NiO NPs (at concentration of 10 mg/1 mL). a) Unstable dispersion of NiO OA NPs in polar solvent, DMF. b, c) Stable dispersions of NiO BF$_4$ NPs in polar solvents, DMF and IPA, respectively. d) Stable control dispersion of NiO OA in nonpolar solvent, toluene. e) Sedimentation of NiO HBA dispersion in DMF, that appears after 1 day.
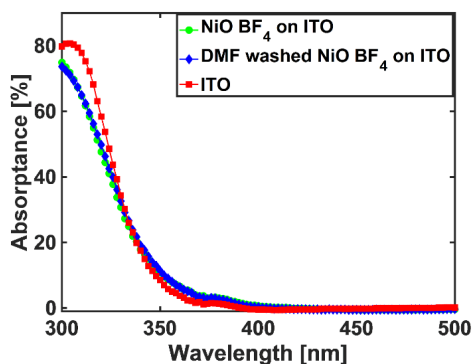

Figure S8: UV-VIS Absorbance of NiO BF$_4$ films on ITO before and after DMF treatment.
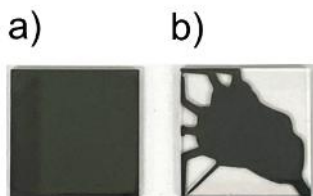
Figure S9: Comparison of perovskite wettability on NiO OA HTLs. a) Perovskite film spin-coated on NiO OA HTL after 2 minutes of plasma treatment. b) Perovskite film spin-coated on NiO OA HTL without plasma treatment.

Section 2. Hole mobility study on NiO HTLs

The electronic properties of NiO films deposited using the MF mixer were investigated via fabrication and measurements of p-n-p type field effect transistors (FETs). To explore the

hole transporting property of the NiO films, we investigated FETs built on a commercially acquired p-type Si substrate with a layer of SiO$_2$ (**see Figure S10a**). Similarly to others,[1-2] we avoided high-K dielectric layers (Al$_2$O$_3$) to not artificially enhance the carrier mobility by reduction of the activation energy for carrier transition. In order to directly lower the required gate voltage at the interface, we used deep reactive ion etching to remove thermally grown SiO$_2$ and then controllably deposited a fresh SiO$_2$ layer using electron beam evaporation to achieve a conformal and high-quality gate dielectric. NiO dispersions were spin-coated on this dielectric layer.[76] The measurements were focused on extracting field effect driven hole mobility in the saturation region ($\mu_{h,FE}$), threshold voltages (V_{th}), ratios between switching current ($I_{on/off}$) and subthreshold swings (*SS*). In order to extract hole mobility, we measured currents between drain and source. The main driving equation and calculated $\mu_{h,FE}$ according to Equation 6 is given below:

$$I_{DS} = \left(\frac{W C_i \mu_{h,FE}}{2L}\right)(V_G - V_{TH})^2 \tag{6}$$

where I_{DS} is the current between drain and source, $\mu_{h,FE}$ is the hole mobility in the saturation region, W is the width of the channel, L is the length of the channel, C is the aerial capacitance of gate dielectric material, V_g is the gate voltage, and V_{th} is the threshold voltage.

A comparison of the transfer curves across the different NiO NP films (fixed step size and drain-source voltage of $V_{DS} = 10$ V) and a summary of their electrical characteristics are shown in Figure S4b-f.[3] The NiO HBA exhibited a $\mu_{h,FE}$ of ~0.041 cm^2 V^{-1} s^{-1}, $I_{on/off}$ of ~3 x 10^4, *SS* of ~4 V dec^{-1} and V_{th} of ~4 V. Meanwhile, the NiO BF$_4$ showed a $\mu_{h,FE}$ of ~0.044 cm^2 V^{-1} s^{-1}, $I_{on/off}$ of ~2.9 x 10^4, *SS* of ~2.8 V dec^{-1} and V_{th} of ~5.6 V. While the mobility and I$_{on/off}$ characteristics across these samples were comparable, the standard NiO OA films exhibited

the lowest values with respect to all extracted parameters. We attribute these lower parameters, namely $\mu_{h,FE}$ of ~0.004 cm^2 V^{-1} s^{-1}, $I_{on/off}$ of ~0.7 x 10^4, SS of ~1.5 V dec^{-1} and V_{th} of ~1.3 V, to the charge-insulating properties of the OA ligands compared to NiO HTLs with HBA or BF$_4^-$ ligands. These results support the choice of the alternative ligands, HBA and BF$_4$, was relevant for the modification of NiO, as both of them improved the electric properties of the HTLs, thus the application of the NiO HBA and NiO BF$_4$ should be beneficial for the perovskite devices.
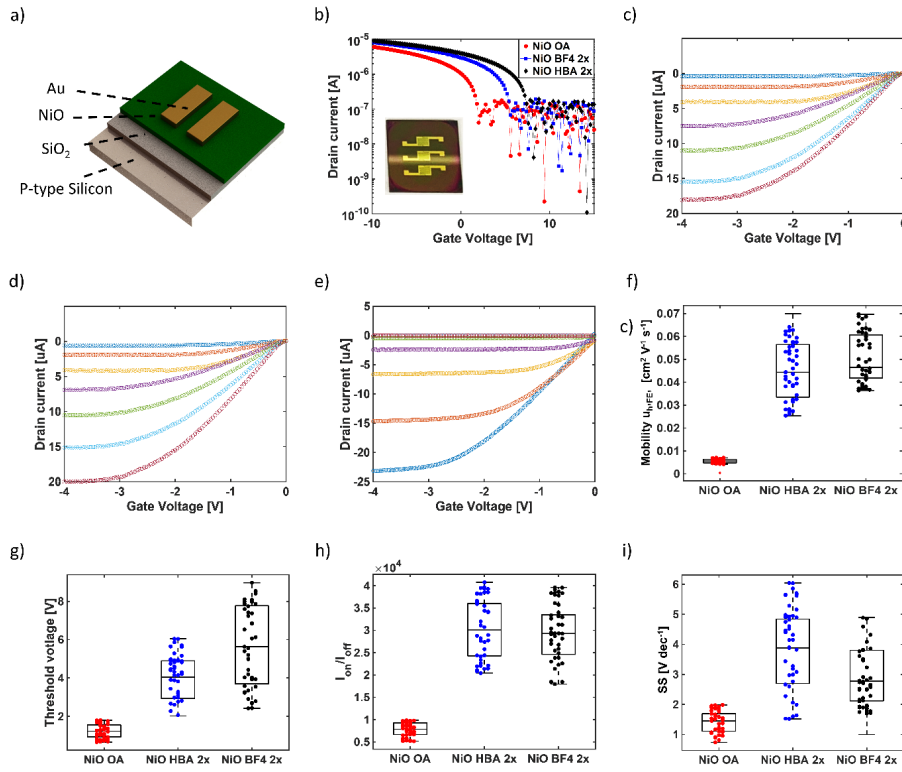

Figure S10: FET systematic study of hole mobility in NiO films at fixed conditions and fabrication steps. a) FET device architecture used in this study; b) typical transfer curves (V_{DS} = 10 V) inset is a device photograph; c) typical output curve for NiO OA device; d) typical

output curve for NiO HBA device; e) typical output curve for NiO BF$_4$ device; comparison of

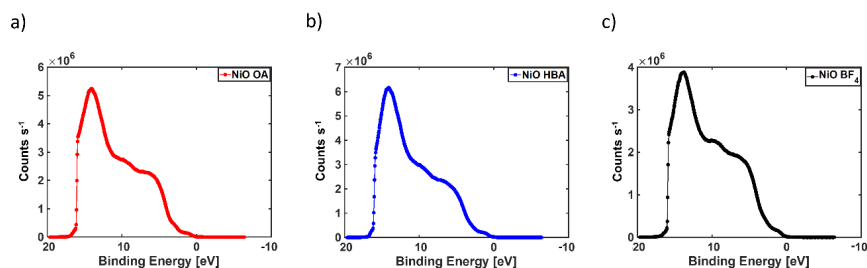f) hole mobility, g) threshold voltage, h) switching current ratio, and i) subthreshold swing.

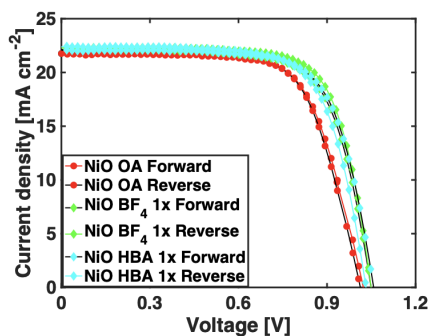**Figure S11**: UPS spectra of NiO films. a) NiO OA; b) NiO HBA; c) NiO BF$_4$.

Figure S12: Current-voltage (I-V) characteristics of the PSC devices with NiO HTLs after a single ligand-exchange procedure compared to the NiO HTLs with unmodified ligands.

References

1.   Shimotani, H.; Suzuki, H.; Ueno, K.; Kawasaki, M.; Iwasa, Y., p-type field-effect transistor of NiO with electric double-layer gating. *Applied Physics Letters* **2008,** *92* (24), 242107.
2.   Matsubara, K.; Huang, S.; Iwamoto, M.; Pan, W., Enhanced conductivity and gating effect of p-type Li-doped NiO nanowires. *Nanoscale* **2014,** *6* (2), 688-692.
3.   Lee, H.; Huang, Y.-T.; Horn, M. W.; Feng, S.-P., Engineered optical and electrical performance of rf–sputtered undoped nickel oxide thin films for inverted perovskite solar cells. *Scientific Reports* **2018,** *8* (1), 5590.
4.   Norton, P. R.; Tapping, R. L.; Goodale, J. W., A photoemission study of the interaction of Ni(100), (110) and (111) surfaces with oxygen. *Surface Science* **1977,** *65* (1), 13-36.
5.   Hagelin-Weaver, H. A. E.; Weaver, J. F.; Hoflund, G. B.; Salaita, G. N., Electron energy loss spectroscopic investigation of Ni metal and NiO before and after surface reduction by

6.3 Conclusions and Future Outlook

A cHTR-ready pathway for novel ligand modifications of newly developed NiOx NPs was presented. The novel ligand-modified NPs dispersions were thoroughly investigated employing multiple characterization methods, including cHTR performance assessment explained in detail in Chapter 7. The dispersions were thoroughly pre-mixed using an inverted multi-staged Tesla valve (μFM) with mixing inducing micro-pillars (diameter 1-5 μm). NPs in a form of nonaqueous dispersion were deposited directly on the solid surface using automated dual-syringe pumps and mixing system. Typically, the NPs require a thorough ultrasonic shake (approximately 10-15 minutes) prior the deposition to break the agglomerations, upon multiple depositions from the vial it was observed that NPs tend to agglomerate, resulting in reduced NiOx film quality. It is not viable to shake the colloids and then deposit each time hence such a microfluidic approach is desired. This method allowed for high-pressure, rapid mixing of low dispersion volumes, acting as an agglomeration breaking step that ensures perfectly pre-mixed droplet at each time directly prior the deposition. The capabilities of such μFM were harnessed and employed in such application for the first time to the best of my knowledge. This allowed for reducing the impacts of NPs agglomeration and dispersion sedimentation over time. Moreover, the dispersions formed topographically uniform films which are far more superior than the ones without mixing. The improved electronic properties of NiOx films were investigated through the employment of in-house built field-effect transistors (FETs) for hole mobility study, and finally, their compatibility and performance were assessed in PSC devices. This inorganic NiOx film resulted from employment of novel NPs deposited in low-temperature process using unique technique allowed for superior electronic properties, stability, and operation of the PSC devices under MPP condition with marginal efficiency loss. Importantly, the microfluidically enhanced deposition allowed for a better solution spread across the substrate, this circumvents the need for the oxygen plasma treatment step. This study outcomes can be directly employed in printable PSCs due to abovementioned advantages. The follow up studies would be preferred to automate completely the deposition and harness this capability in completely inert atmosphere. In doing so, it is likely that such approach can further minimize human factor in the sample preparation and the scalable mixing method based on agglomeration-breaking approach would be highly desirable enhancement for commercial HTL fabricators.

7. High-throughput characterization of perovskite solar cells

7.1 Chapter context

Measurement of energy conversion efficiency and other fundamental PV performance parameters such as V_{OC}, J_{SC} and FF under simulated sunlight is the most widely applied characterization technique in solar cell research. The characterization of PSC by recording the photocurrent density – voltage curve under illumination has been shown to be a non-trivial and often time-consuming matter. The work in this chapter is motivated by the following 3 goals:

- Improve the accuracy of the PV measurement
- Increase the reproducibility of the process steps used to fabricate conventional PSCs.
- Automate and accelerate the throughput of the PV characterization by use of parallel measurement techniques.

7.1.1 PV measurements and accuracy

The characterization of materials for photovoltaics always converges to the most critical and quintessential test: the performance check. This provides the definitive answer to the reasoning behind the development of any concept related to photovoltaics – it is a real application. In order to not miss potentially promising candidates for PV materials, the characterization must be accurate.[42] The performance data plays a crucial role in each scientific communication, and usually serves as the proof-of-concept verification or review of future applicational potential.[43-44] As aforementioned in the introductory section, intrinsic structural properties, transient effects (hysteresis) stemming from the ionic nature of the crystal or degradation mechanisms of perovskite pose certain limitations and force specific to perovskite measurement protocols.[45] The incorrect measurement protocol itself in fact can stimulate the transient effects. Due to the voltage bias, illumination, and temperature, the

crystal lattice ions activate their movements.[99-100] This alters the electric field, promoting recombination. The photogenerated free charges then can momentarily have a different path if the bias is applied "forward" and "reverse". The key recombination spots tend to reveal themselves at perovskite/CTL interfaces or grain boundaries which additionally can trap/recombine some of the free charges.[46] Unfortunately, the state-of-the-art *J-V* characterization is not simply a trivial bias application and current measurement under the simulated 1 Sun conditions. It is obviously caused by the lack of standardized measurement (however over the course of this thesis the first major consensus related to the measurements occurred in 2020[47]) on the best measurement approach. The need for reproducible, accurate, and trustworthy measurement solutions is evident. cHTR film fabrication systems and skilled manual researchers produce samples that evidently degrade (unencapsulated) within hours in external conditions. Hence, the system has to be rapid, measurement protocol bespoke (adjustable), definite and precise. Some of the potential underlying problems can be found in **Figure 75**.
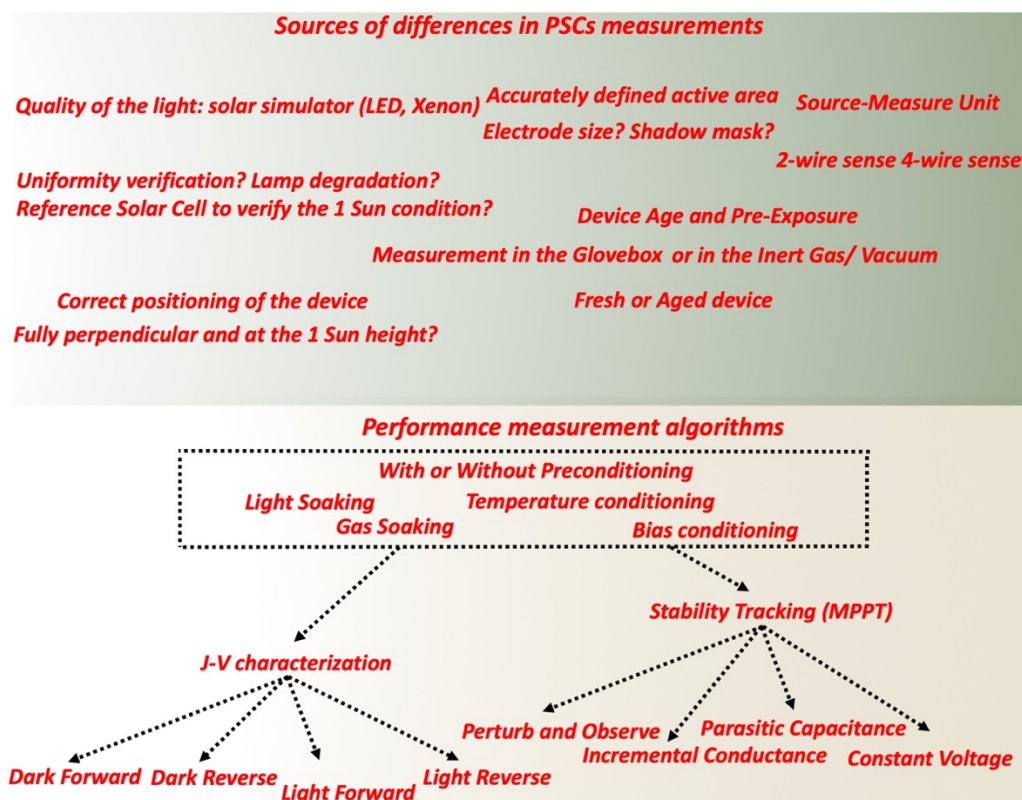

Figure 75: Workflow of the PSC performance assessment requirements and problems associated with it.

7.1.2 System design

The PSC substrate design is non-trivial and plays a critical role in all of solar cell tests. In this research it was compared that the manually prepared substrate yields much lower results. In the **Figure 76** can be found comparison between the old, manual fabrication pathway and newly designed by the author substrate for cHTR characterization.
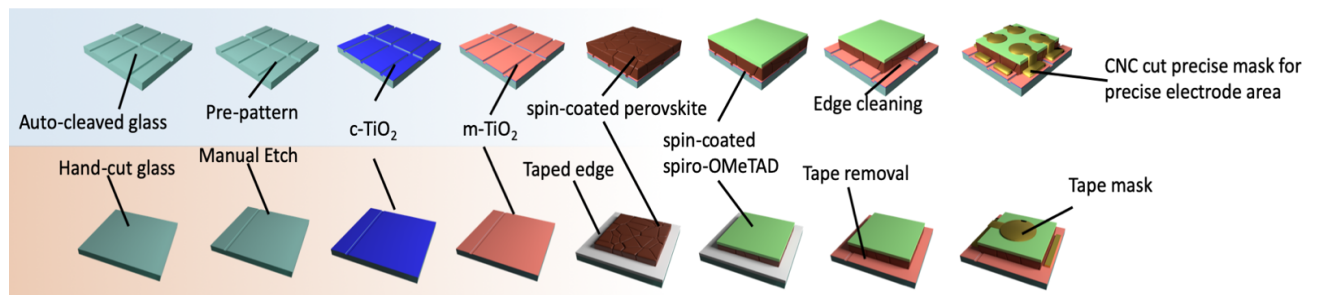

Figure 76: Comparison between the fabrication processes which are usually reported. Top: method of PSC fabrication for the automated measurements. Bottom: commonly reported designs or simply a "manual" PSC.

The fabrication process based on standardized device allows for unification of tests, better control of the electrode positioning and perfect shadow-masking of the device under test. Finally, such design allows for encapsulation of all 4 devices at once. In the **Figure 77**, the digital photograph of fully constructed PSC can be seen.
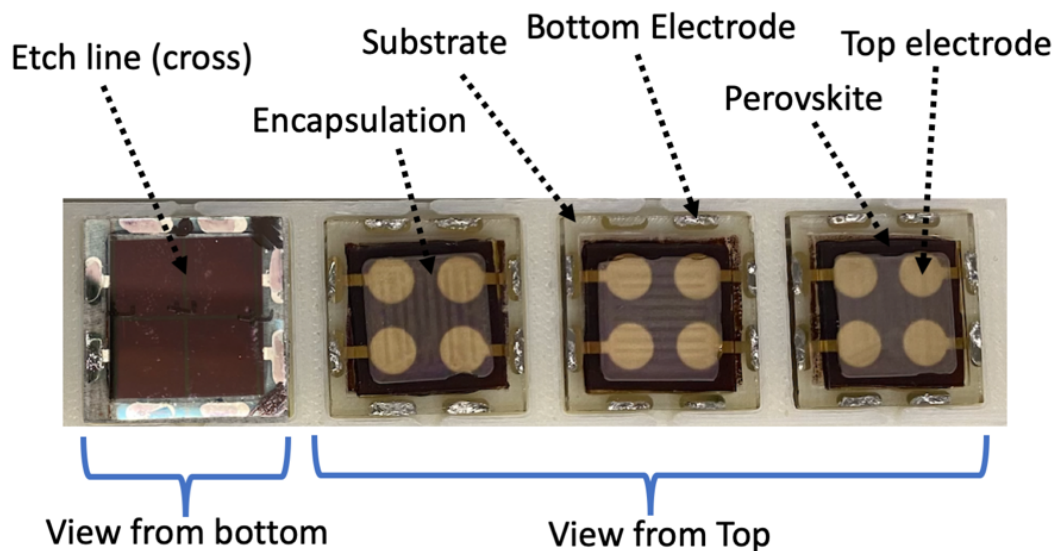

Figure 77: Example of perovskite solar cells commonly used in Renewable Energy Laboratories at Monash University (design is developed by the author of this thesis and will be discussed in Chapter 7).

7.1.3 Measurement protocol

Having the unified substrate and fabrication protocol, the next step was to develop an open-protocol that allows the researcher for reproducible, accurate and trackable characterization of PSCs whilst still being flexible for various types of solar cells. In the **Figure 78**, the the flow diagram of the newly developed cHTR characterization setup is presented. The system ultimately can be pre-defined to execute any sort of described in previous paragraph performance characterization measurements simultaneously. The acquired performance data is presented in real-time in a form of self-populating graphs, followed by a standardized data file generation. The raw data can be directly employed into the database or ML algorithms in future.

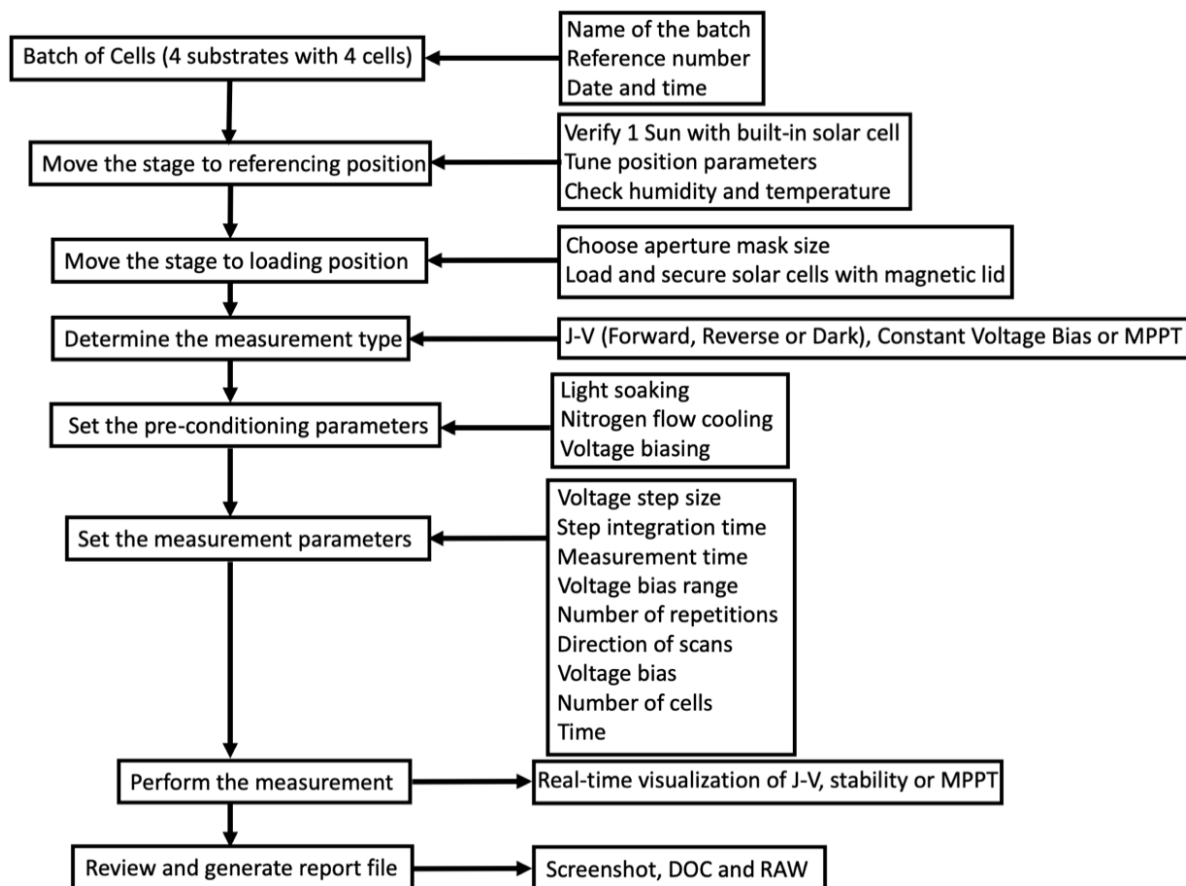*Figure 78: cHTR characterization setup workflow diagram.*

Unlike the sequential measurement approaches this cHTR setup can perform up to 16 solar cell measurements parallel, in real-time giving excellent, unique comparison of PSCs data generated without any of the PSCs being exposed to pre-conditioning for longer than other samples). The next paragraph contain published results of this chapter work.

7.2 Results and Discussion

High-Throughput Characterization of Perovskite Solar Cells for Rapid Combinatorial Screening

Maciej Adam Surmiak, Tian Zhang, Jianfeng Lu, Kevin James Rietwyk, Sonia Ruiz Raga, David Patrick McMeekin, and Udo Bach*

To discover the ideal perovskite material for solar cell application, a large parameter space (composition, surrounding condition, fabrication technique, etc.) must first be explored. Therefore, screening this parameter space using a rapid combinatorial screening approach can drastically speed up the rate of discovery. During the last decade, these discoveries and optimization processes of perovskite materials have been achieved using simple lab-scale deposition techniques and characterization methods, resulting in a substantial time-consuming process, slowing the rate of progress in the field of photovoltaics. Thus, the benefits of developing fully automated, high-throughput characterization techniques become apparent. Herein, a high-throughput solar cell testing system that enables parallel, real-time, and comprehensive measurements is detailed, allowing for 16 solar cells to be characterized simultaneously. The importance of measurement reproducibility, condition verification, and structured data postprocessing is shown.

1. Introduction

In the past decade, there has been a drastic upheaval in the research of photovoltaics with the introduction of solution-processed solar cells, particularly inorganic–organic hybrid lead halide perovskite materials. Perovskite materials have a general ABX_3 chemical formula, where A is a cation, B is a divalent metal ion, and X is a halide. Moreover, by adjusting the chemical composition of the A-site cation, commonly, (methylammonium, and formamidinium, or caesium), the B-site metal cation (lead or tin), or the X-site anions (iodide, bromide, chloride) we can

M. A. Surmiak
Department of Chemical Engineering
Monash University
Clayton, Victoria 3800, Australia

M. A. Surmiak, Dr. T. Zhang,[+] Dr. J. Lu,[+] Dr. K. J. Rietwyk,[+]
Dr. S. R. Raga,[+] Dr. D. P. McMeekin,[+] Prof. U. Bach
ARC Centre of Excellence for Exciton Science
Monash University
Clayton, Victoria 3800, Australia
E-mail: udo.bach@monash.edu

The ORCID identification number(s) for the author(s) of this article can be found under https://doi.org/10.1002/solr.202000097.

[+]Present address: Department of Chemical Engineering, Monash University, Clayton, Victoria 3168, Australia

fine-tune the optoelectronic properties of this novel semiconductor. Perovskite solar cells (PSCs) have achieved significant power conversion efficiencies that are currently competing with commercially available solar cells.[1] Their performance continuously improved over the past decade, reaching a certified power conversion efficiency (PCE) of 25.2%,[1] rivalling the all-time champion silicon solar cells (SCs) with record efficiencies of 26.1%.[1] However, the characterization of PSC is nontrivial due to their ionic movement within the material, resulting in a range of transient behaviors when attempting to measure their performance.[2] Due to this ionic movement within the film when a voltage bias is applied, a hysteric behavior is observed during the measurement of the current–voltage (J–V)[3–5] curve. To eliminate the effect of ionic motion when determining the true performance of the device, a maximum power point tracking (MPPT) technique is preferred over a J–V scan.[6] Furthermore, to mitigate the effect of heating caused by 1 Sun illumination, which can reach 35–40 °C, the device is held at 25 °C using a nitrogen gas flow,[7,8] when illuminated with a spectral irradiance of AM1.5G and a $1000\,\mathrm{W\,m^{-2}}$ power density using a lamp (xenon, quartz tungsten halogen, metal halide, or light-emitting diode)[9,10] and area-defining mask. The ionic behavior of lead halide perovskites causes a hysteric behavior in the J–V curve, depending on scan parameters such as scan direction, speed, settling time, and bias voltage range. These devices also demonstrate severe memory-like effects, where the performance is altered by past measurement such as light soaking, applied voltage bias, storage under specific atmospheres, and temperatures. Recently, Zimmermann et al., Pellet et al., and Rakocevic et al. addressed the complex challenges in reliability of the measurements.[6,11,12] Perovskite laboratories around the world have their own ad-hoc J–V measurement protocols, thus causing ambiguity when reporting the true performance of the solar.[11–16] Despite the aforementioned issues, J–V scans still remain a key characterization tool among the perovskite research community. The most reliable method for measuring a J–V curve is the dynamic J–V curve, where the current density for each voltage point is measured long enough to demonstrate stable current).[17] Although this method is highly accurate and only requires a sweep in a single direction, this approach takes longer to perform compared with a conventional J–V curve

(where the extracted current is stabilized over a period of time determined by the user). Therefore, the generally agreed best approach to determine the stabilised PCE is to track the evolution of the extracted current at maximum power point voltage over the course of typically 1–10 min. Similarly, to obtain a stabilised measurement of the short-circuit current density (J_{SC}) and open-circuit voltage V_{OC}, a time-depend approach can be utilised. Another approach to obtain a stabilized $J–V$ involves repeating the measurement of the $J–V$ curve until the curve stabilizes, thus accounting the impact of "light-soaking."[16,18,19] However, each method has their own shortcomings: therefore, to account for the fluctuation in maximum power point (V_{MPP}) over time, while also minimizing the measurement time, an MPPT is viable approach as a characterising method. Dunbar et al. recently reported an interlaboratory comparison on the measurement of PSCs that highlights the variability in measurement protocol across 10 laboratories.[15] One of the key findings was that the variability in measured PCE for each laboratory was primarily determined by light and voltage preconditioning, electrical measurement protocol, and inaccuracies in estimating the cell active area. The manual handling of the devices during the fabrication and characterization and the arbitrary choice of measurement parameters contribute to difficulties when comparing PCE from lab-to-lab. Therefore, to bolster research outcomes, it is preferred to automatize and standardize such routine electrical characterizations and develop MPPT algorithms to accurately report PCE. Only a few commercial solar cell measurements systems are available today; however, they usually do not achieve all three desired requirements for PSC research: 1) customisation of measurement parameters and protocols, 2) simultaneous measurement of several devices, and 3) a sample holder to precisely overlap the aperture mask with the counter electrodes. Due to lack of versatile commercial instruments crafted specifically for PSCs, many researchers decide to design their own characterization setups, based on programmable source-measure units (NI, Ossila, Keysight, or Keithley).[20–23] Some of the commercial products offer automated computation of key characterization parameters commonly found across solar cell research; however, these parameters are not necessarily tailored toward the specific needs of PSCs, such as light and bias preconditioning, or versatility in selecting $J–V$ parameters such dwell time or scan speed to mitigate the impact of the hysteretic behavior found in PSC. These measurement instruments were designed to cater to the solid-state solar cell industry, which do not exhibit strong transient behavior when being measured. Here, we present a systematic study using a versatile state-of-the-art high-throughput solar cell characterization system, capable of testing up to 16 solar cells simultaneously while maintaining a high level of reproducibility. We demonstrate the advantages of the system in terms of accuracy, speed, and reproducibility, with our results captured in less than one-tenth of the measurement time compared with conventional approaches. We believe that this system will provide a valuable guidance for researchers when characterizing PSC with hysteretic behavior and consequently will play an important role in developing future measurement system for the photovoltaics (PV) industry.[24–29]

2. Results and Discussion

At research-scale, solar cell devices are generally fabricated on individual substrates of area less than 5 cm² due to size limitations posed by laboratory equipment, and to reduce research costs. The laboratory fabrication process for PSC test cells typically involves the manual cutting of transparent conductive oxides (TCO) substrates by hand tools, which results in poorly controlled substrate shapes and sizes. The manual cutting and patterning require extra care and extensive cleaning and despite efforts of being precise manual cutting causes significant glass size difference ($\pm$ 1 to 3 mm) making the use of precise jig and masking impossible. To address these bottlenecks for high-throughput solar cell research, we combine a number of techniques to reduce the manual handling using a jig (positioning device)-based fabrication (Supporting Information, S1). First, we increased the number of solar cells per substrate. The old substrates were diced by hand from 100×100 mm of fluorine-doped tin oxide (FTO, $<14 \,\Omega\, sq^{-1}$) to $\pm 25 \times 25$ mm pieces. New ones are commercially ordered as precision-cut, prepatterned pieces covered with a thin film of FTO ($< 10 \,\Omega\, sq^{-1}$). For that, we have designed a new substrate architecture that can contain four individual solar cells electrically isolated from each other (see **Figure 1**A). Custom-made, precision-cut, prepatterned FTO glass substrates (accuracy ± 0.15 mm) were sourced from Latech Scientific Supply Pte. Ltd. (Singapore). The glass is cleaned in specially ordered trays which are placed in ultrasonic baths. Cleaned substrates are dried and placed in precisely milled jig. The automated way of spraying TiO_2 therefore allows minimizing discrepancy of layer thickness and quality from batch to batch. The electron transporting Layer (ETL)-covered substrates are therefore transported to glovebox where spin coating of perovskite precursor solution and hole transporting layer is performed. Later on, the substrates are placed in another precisely milled jig to evaporate Au electrodes making the alignment and masking procedure completely redundant, ensuring the same position of the electrodes across entire batch of solar cells. We have encompassed in the design that the tolerance buildup between each commercially purchased substrate (up to ± 0.15 mm), position in the measurement pocket (± 0.016 mm), and evaporation plate (± 0.01 mm) can negatively influence results, so therefore we have designed the connection printed circuit board (PCB) accordingly. The pin rows are positioned in the middle of 2 mm wide contact electrode areas; thus, the connection is always established. We highlighted the fabrication differences in fabrication step in **Table 1**.

2.1. Methodology

We designed a custom-made sample holder (Figure 1D) that allows for the simultaneous measurement of four substrates, containing four solar cells. The holder allows for precise alignment between the aperture mask and the active area; further details on the sample mounting are shown in Figure 1. In addition, the holder has built-in sensors for temperature and relative humidity, as well as a Si photodiode reference cell with KG5 filter. The chamber also has ports and lines for N_2 gas circulation, directed onto the solar cells to reduce the presence of oxygen and
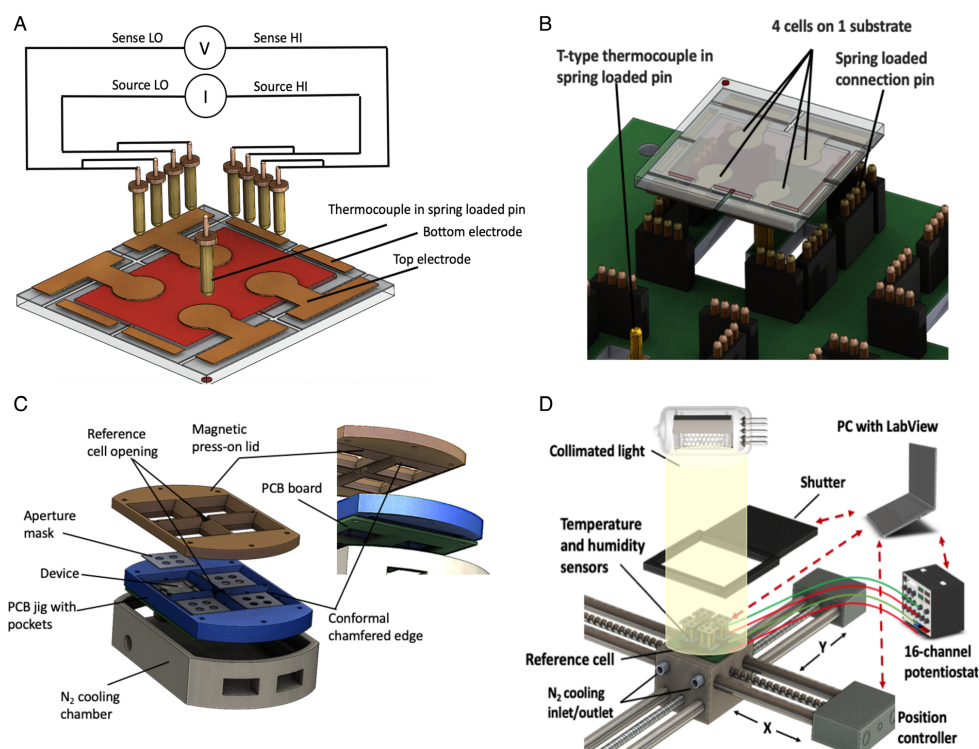
Figure 1. Schematic diagram of the high-throughput solar cell characterization system. A) A schematic showing a custom-designed prepatterned FTO substrate that is being probed in a 4WS configuration with spring-loaded pins. B) Close up of a single substrate slot, where each cell is connected with eight spring-loaded pins, and measured with a 4WS technique. C) Single measurement module consists of positioning jig where the substrates are mounted, the design allows the room for a thin 0.08 mm black dyed stainless-steel apertures masks. The masks are pressed against the solar cells by a magnetic force and the chamfered protrusion guides the magnetic lid in place restricting the movement of the cells and ensuring electrical connection between solar cells and spring-loaded probes. D) Sample holder consists of a PCB equipped with spring-loaded gold pins that provide electrical connection between the 16 solar cells and the potentiostat. The red dashed lines denote communication routes between PC and system parts.

moisture while simultaneously providing an active cooling during the measurement process. All sensors, photodiode, and N_2 valves are communicating with the computer through a microcontroller (ATmega 2560), giving full access to the end user. The 16 solar cells are connected to a commercially available, computer controlled, 16-channel potentiostat (Bio-Logic VMP3). The holder provides electrical contact by utilising a magnetic lid to press the solar cells onto the spring-loaded pins. The custom-built PCB board is mounted inside the sample to provide good contact connection between the pin and electrode. We have used a twofold-redundancy system to always achieve electrical contact connection. The sample holder is mounted on a motorized two-axis (x–y) stage that is connected to the PC through a second microcontroller. The moving stage allows the light intensity to be mapped using the reference Si solar cell, and then the solar cells are placed in the region with greatest illumination uniformity; this will be explained in detail in Section 2.3. Moreover, the

x–y moving stage could potentially host several sample holders to further increase the throughput of the solar simulator by sequentially measuring batches of 16 devices. The motorized stage is aligned with a commercial solar simulator (Abet Technologies Sun 3000 class AAA). The solar simulator is equipped with a software-operated built-in programmable light shutter wired to one of the microcontrollers. Finally, the system is controlled by a custom-made piece of LabView software; further details on the characteristics of the protocol are provided in Section 2.3; for picture, see Supporting Information, S2.

The devices were made in the following way, the substrates are cleaned using Hellmanex 2% de-ionized (DI) water solution, DI water, solvents: acetone, ethanol, isopropanol, respectively, and place in an ultrasonic bath for 15 min. Onto the FTO a compact layer 10–20 nm of TiO_2 is deposited using spray-pyrolysis. For this, 1 mL of bis(isopropoxide)-bis (acetylacetonate) titanium(IV) dissolved in 19 mL of anhydrous isopropanol at

Table 1. Comparison between fabrication steps of new and old design solar cell.

Variables	Alignment required	Old method	New method
Glass cutting	Y	Hand scribe and cut	Precision laser cut ($\pm$0.15 mm)
Pattern etching	Y	Manual	Laser pattern ($\pm$0.001 mm)
Compact TiO_2	Y	Manual	Automated spray inside of jig[a)]
Mesoporous TiO_2	N	Jig not required	Jig not required
Perovskite	N	Jig not required	Jig not required
Spiro-OMeTAD	N	Jig not required	Jig not required
Edge removal	Y	Solvent cleaning	Machine buffing
Gold evaporation	Y	Tape masking	CNC milled jig ($\pm$0.01 mm)
Shadow mask	Y	Manually placed	Guided and magnet-clamped

[a)]Jig—device used for positioning.

500 °C. Subsequently, a mesoporous TiO_2 layer 150–200 nm was spin-coated at 4000 RPM for 20 s with a ramp of 2000 RPM s^{-1} using a 30 nm of Dyesol 30 NR-D diluted in ethanol (30 NR-D:ethanol = 1:6, wt). After that the substrates were dried at 110 °C (10 min), and then they were annealed at 500 °C (30 min). This was followed by preparation of perovskite films prepared entirely in a N_2-filled glove box including spin coating and annealing and preparation of the precursor solutions. Perovskite precursor solutions were produced by dissolving formamidinium iodide (1.1 M (M = mole L^{-1})), PbI_2 (1.2 M), MABr (0.22 M), $PbBr_2$ (0.24 M), and CsI (0.07 M) in anhydrous dimethylformamide (DMF):dimethyl sulfoxide (DMSO) (4:1 v/v) to achieve a composition of $Cs_{0.05}FA_{0.79}MA_{0.16}PbI_{2.49}Br_{0.51}$ with a concentration 1.44 M. The perovskite film was fabricated by spin coating 80 L of the perovskite precursor solution per substrate using a two-step program: 1000 RPM for 10 s (1000 RPM s^{-1} ramp), followed by 6000 RPM for 20 s at (6000 RPM s^{-1} ramp). Then 200 L of chlorobenzene was poured onto the spinning substrate 5 s prior to the end of the second step. The samples were annealed in the dark at 100 °C (1 h) and then allowed to cool to 25 °C. After cooling, 80 L of a chlorobenzene solution containing spiro-OMeTAD (60 mM), 4-_tert_-butylpyridine (tBP; 198 mM), bis(trifluoromethanesulfonyl) imide (LiTFSI; 30 mM), with (1.8 mM) cobalt complex FK269(III), was spin-coated at 3000 RPM for 30 s (3000 RPM s^{-1} ramp). A gold (Au) counter electrode (80 nm) was then deposited on the HTM layer by thermal evaporation. To minimize the possibility of having unconnected cell, we used a row of four soft spring-loaded pins, having more pins also minimizes damaging of the 80 nm thick metal electrode. This allowed to minimize mechanical damage to the electrodes. Every solar cell is connected with eight pins in total. To address the issue of the unwanted contact resistance and cable resistance, we implemented a 4-wire sense (4WS) connection (see Figure 1A). The testing current is applied to the

outer pair of contacts and the voltage is measured with the inner pair, for each electrode. The measurement performed at high impedance, thus eliminating the current and voltage drop caused by the contact resistance and the resistance of the external measuring circuit.[15] To ensure precision, we designed a thin (0.08 mm) stainless steel opaque aperture mask with a laser-cut opening (0.16 cm^2 $\pm$ 0.001 cm^2), to create a precise and well-defined aperture to illuminate the device under test (DUT). Precise of fabrication of this aperture mask is essential to accurately control the active area of the illuminated device and to determine the PCE. We performed a study to establish the optimal ratio between the gold electrode and illumination mask diameter (see **Figure 2**). Similarly, it has been demonstrated in dye-sensitized solar cells (DSC) by Ito et al. that the aperture mask size in comparison with the electrode area impacted performance.[30] By masking the cells, we mitigate any artificial V_{OC} gains.[31]

A key concern with performing simultaneous characterization of multiple cells on a single substrate is the possibility of a crosstalk, i.e., current flow between adjacent cells, thus impacting the _J–V_ measurement. Despite the wide 0.5 mm pseudomoat separating the four cells of the patterned FTO glass substrate, lateral current leakage may potentially occur through the perovskite layer, or the HTM or ETL. We investigated case where one, two, three, and four cells are illuminated and one is completely covered (see **Figure 3**). The purpose was to exclude a crosstalk parasite effect from 1, 2, and 3 devices measured simultaneously. By scanning the _J–V_ across four cells with three exposed cells and one completely masked. We have also measured current below 0.01 mA cm^{-2}. The short-circuit current density of illuminated cells exceeds 20 mA cm^{-2}, whereas shaded cells exhibit no significant photocurrent, indicating that the design of the patterned substrate connections and masking is highly effective to impede the crosstalk, for the materials used (i.e., $Cs_{0.05}FA_{0.79}MA_{0.16}PbI_{2.49}Br_{0.51}$, TiO_2, and Li-TFSI-doped spiro-OMeTAD).[18,32]

2.2. Illumination and External Conditions

For research purposes, solar cells are measured under a standardized light source; this enables reproducibility and comparison among laboratories around the world. A xenon lamp light sources emits an electromagnetic spectrum that closely matches the sunlight that reaches the Earth surface after correction of spectral and intensity loss caused by atmospheric gases. This is achieved by using a filter that corrects the xenon spectra to AM1.5, corresponding to a zenith angle of 48.2° and adjusting the lamp power (100 mW cm^{-2}).[33] The highest class of solar simulators is AAA, which fulfils strict requirements including a uniformity of irradiance of less than 2% across the region of interest and exhibits spectral agreement with the AM1.5G solar spectral of within $\pm$25% at any wavelength. The overall irradiance of the solar simulator is typically determined using a certified reference Si solar cell with a KG filter.[34–36] However, as the lamp ages, the illumination intensity may fluctuate, thus regular monitoring of the actual irradiation power density with a calibrated reference cell prior to the measurements is advisable. To this end, we have integrated a reference Si solar cell in the x–y motorised stage and a simple LabView code, allowing the
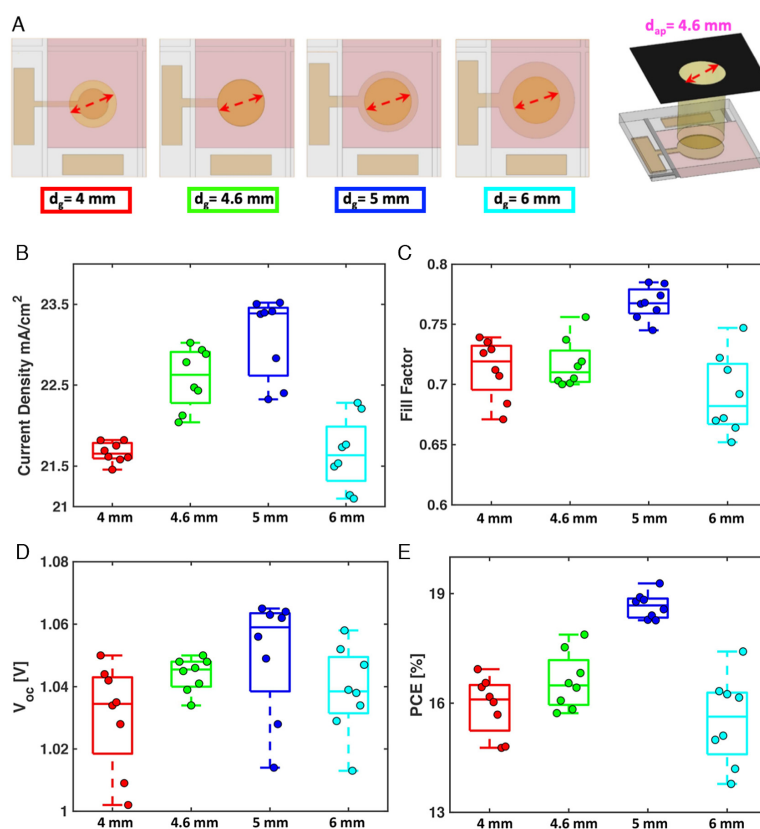
186

Figure 2. Influence of gold electrode diameter (d_g) on PSC performance. A) Schematic illustration of the measurement conditions. PSCs with four different gold electrode diameters, ranging from 4 to 6 mm, were fabricated and their photovoltaic performance tested, using a shadow mask with a fixed aperture (d_{ap}) of 4.6 mm (red double arrow). The mask was placed on top of the PSC to define the illumination area. B–E) Photovoltaic performance (short-circuit current density (B), fill factor (C), open-circuit voltage (D), and PCE (E)) as a function of gold electrode diameter. Every batch is composed of eight solar cells. Short-circuit current densities are calculated as the ratio of short-circuit photocurrent and the illumination area (πr_{ap}^2).

user to routinely map the illumination from the solar simulator and confirm that a 1 ± 0.02 Sun equivalent is maintained across the region of interest. An example is shown in **Figure 4**. The program identifies the x–y coordinates for the area with less deviation to 1 Sun intensity and automatically places the sample holder under that region to proceed with the electrical measurements. This ensures a comparable light intensity for each of the cells measured simultaneously and provides a useful tool for gauging the aging on the xenon lamp.

2.3. Electrical Characterization of PSCs

As we have mentioned, due to the hysteric behaviour of PSCs, we have designed the software to allow the end-user to vary each electrical parameter according to standard measurements, such as scan direction, initial voltage, end voltage, scan rate or scan speed, the number of sampling points or voltage step, and dwell time or settlement time. In addition, the following preconditioning options are available: set an applied voltage and/or open the shutter and light-soak for a certain time a priori to measurement, open the gas valve to purge the chamber, and cool the sample before measurement. The user can test stability of the cell by setting the bias voltage and measure the extracted current of up to 16 cells simultaneously. Finally, our software can automatically track the MPP (up to 16 devices in real-time parallel algorithm) where the MPP is sampled up to every 12 s to ± 10 mV around the previous value and obtains the real-time MPP. There have been a number of reports in the literature emphasizing that the evolution of MPPT varies drastically between different
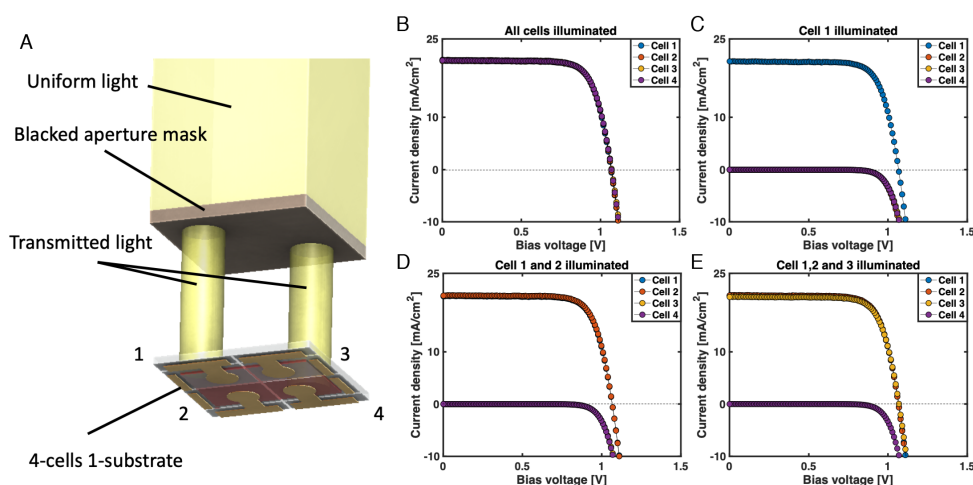
Figure 3. Evaluation of crosstalk between solar cells colocated on the same substrate. A) Schematic of a substrate with four solar cells during current–voltage measurement. The mask is precisely clamped on top of the measured device. B–D) Current density–voltage characteristics recorded in parallel for all four devices with specific cells illuminated with simulated AM1.5 (100 mW cm^{-2}) sunlight through a $d_{ap} = 4.6$ mm aperture mask as indicated.
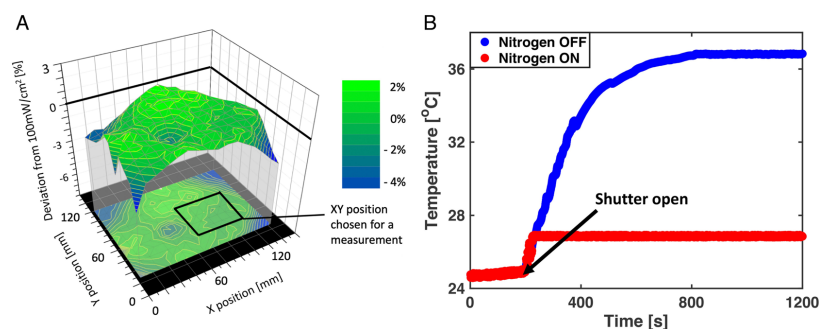

Figure 4. A) Spatial map of the relative solar intensity under the solar simulator. The ideal region for analysis is where the deviation is closest to 0%. B) Temperature of the substrate with and without N$_2$ cooling. The temperature fluctuations in the presence of N$_2$ gas flow are smaller and the temperature after opining the shutter remains at lower level than without active cooling.

architectures and for accurate tracking it is necessary to tune the tracking parameters.[11,12,14] Most importantly, we do not define a single set of parameters for all devices but rather we implemented the possibility to choose between different parameters (voltage step size, voltage dwell time, stabilized transient current test). The users can pick their own parameter set, which is specific for the measured solar cell composition. Furthermore, the user defines the light soaking and gas exposure time,[37] and aperture mask area[38] (protocol details and automatically produced statistics can be found in Supporting Information, S3 and S4). The temperature of substrates was measured before the measurement at 24.2 °C with the relative humidity of the room measured to be RH = 41.2%. Prior to performing

measurements, the solar cells are exposed to N$_2$ flow for 30 s. We have mapped (system has option of systematic mapping to establish the lamp aging intensity decay) the illumination area to ensure that we are under simulated air mass (AM) 1.5 solar illumination of 100 mW cm^{-2}. We have chosen 5 s of light soaking prior to scanning at 0 V bias voltage. The voltage was swept from −0.2 to 1.2 V at a scan speed of 80 mV s^{-1} with voltage steps of 10 mV. An *J–V* sweep was initially performed in the dark (solar simulator shutter closed) followed by forward and reverse scans under illumination. We have performed 4 separate tests of 16 solar cells using automated and manual methods. The obtained data from these measurements are shown in **Figure 5**. To demonstrate the effectiveness of the solar cell
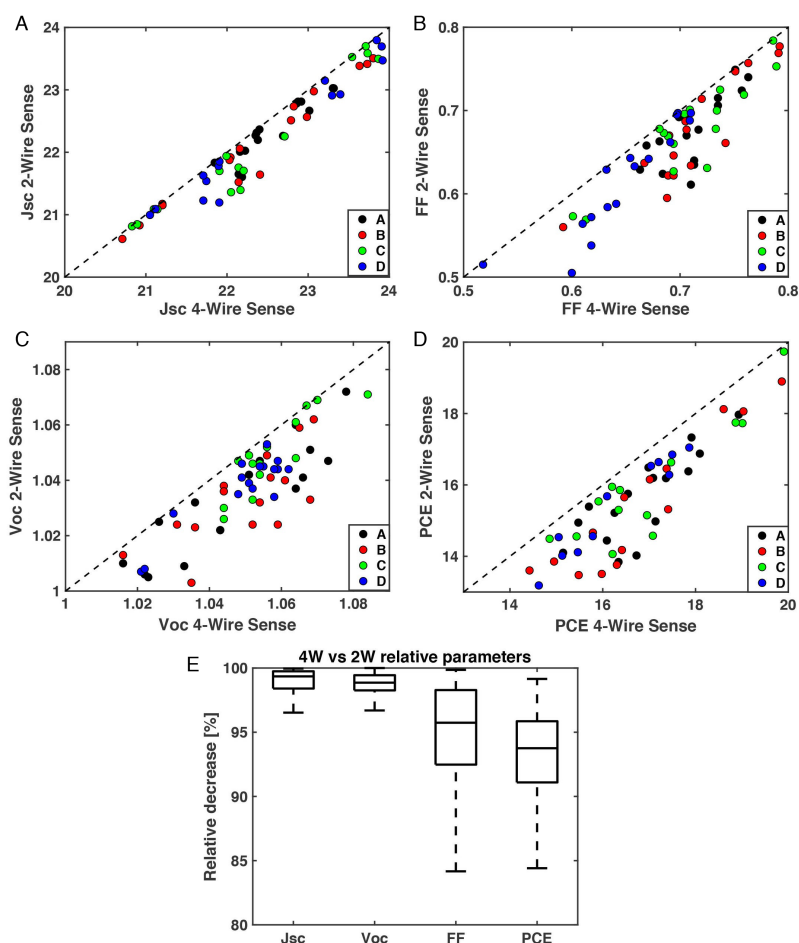
Figure 5. Comparison of metrics acquired using 2WS and 4WS technique. A) J_{SC}, B) fill factor, C) V_{OC}, and D) PCE of four different batches of 16 solar cells each (A, B, C, D). The diagonal line represents an equal measurement. E) Relative summary of parameter decrease. A reduced standard deviation on the FF obtained by the automated measurement demonstrates the superior reliability of the measurements made with minimum human interaction. We attribute the reduced performance of the manual measurement to the sum of several minor errors, such as misalignments between the shadow mask and the electrode, and nonperpendicularity between the the sample and the incoming light. In addition, the lack of N_2 cooling and longer exposure to humidity and light may contribute to slight degradation prior to the measurement.[14,15,17,39]

characterization system in terms of accuracy and speed, we proceed to compare the experimental results of 4 batches of 16 solar cell (batches are denoted with A, B, C, D in Figure 5), totalling 64 measurements using first the 16-channel system and comparing it to a single-cell manual clipping measurement where each cell is simply connected with alligator clip. An experienced researcher requires an average of 2 min for aligning and fixing the illumination mask, clipping the two electrodes, and placing it perpendicularly to the illumination beam of the solar simulator.

Afterward, an average of 2 min is consumed for sample data entry and running the $J–V$ measurement. This protocol, repeated 16 times, resulted in a total of 60 min for the manual measurements, whereas for the automated measurement the devices were mounted simultaneously measured within 5 min. This full automation designed to increase characterization speed is motivated by combinatorial screening to discover and optimize novel perovskite compounds. Saliba et al. presented a positively trending correlation between the number of fabricated and

189

characterized cells and their overall performance.[40] On average, a research laboratory can produce daily 10–20 cells per person hence by having an automatized measurement; we can not only speed up the characterization, but also make sure that the fabricated devices are treated equally and none of them needs to wait in queue to be characterized. As aforementioned, the negative impact of external conditions can significantly degrade the cells and potentially derail the research of a prospecting composition/material/architecture of PSC. The test cells and therefore the photocurrents are typically small. In our case, $I_{SC} < 4\,mA$. It is often perceived that the 4WS is not required, when measuring such small currents. However, the statistical data provide clear evidence that commonly overlooked parasite resistances influenced measurements. All data points come to sit underneath the diagonal indicative of a systematic underestimation of PV performance parameters when using 2-wire sense (2WS). In average this resulted in an underestimation of the PCE of 1–2%. This highlights the importance of using 4WS when measuring PSC test cells using contact pins. In case of 2WS, the resistances of test leads and contacts are unknown; therefore, the voltage drop caused by the sum of all resistances contributed by wires and contact affects the measurement.[41] According to the literature[42,43] the FF is governed by the following equations

$$FF_0 = \frac{V - \ln(V + 0.72)}{V + 1} \tag{1}$$

$$FF = FF_0[1 - R_S] x \left[1 - \frac{1}{R_{SH}}\right] \tag{2}$$

where V is a normalized V_{OC} corresponding to q/nk_BT (q—elementary charge; n—ideality factor; k_B—Boltzmann constant; T—absolute temperature); FF is strongly related to series resistance (R_S) and less to shunt resistance (R_{SH}). The differences in mechanisms between 2WS and 4WS, including bypassing of the test lead and contact resistance, are presented in Supporting Information, S5.

3. Conclusions

In our work, we have developed a high-throughput solar simulator-based system for PSCs for rapid combinatorial screening. This high-throughput solar cell characterization system is capable of performing measurements with high accuracy and allows for excellent versatility in terms of measurement protocols. The system provides rapid and reliable research-scale characterization for PSCs and other emerging solar cell technologies. Combined with the prepatterned FTO substrate, these automatic features can significantly increase the daily output of any research laboratory. We have shown the benefits of a 4WS method for measuring PSCs and its impact on the photovoltaic performance parameters. The system tackles commonly known issues found when measuring hysteretic PSCs and can potentially set a benchmark for PCS measurement protocols. We have demonstrated that by automating the solar simulator, we can potentially reduce the discovery time of novel perovskite materials. The high-throughput scanning improves the productivity of perovskite research laboratories, and removes human error by using a systematic and repeatable method of characterization of PSCs.

[1] N. R. E. L., Best Research-Cell Efficiency Chart, https://www.nrel.gov/pv/cell-efficiency.html (accessed: November 2019).
[2] C. Eames, J. M. Frost, P. R. F. Barnes, B. C. O'Regan, A. Walsh, M. S. Islam, *Nat. Commun.* **2015**, *6*, 7497.
[3] S. N. Habisreutinger, N. K. Noel, H. J. Snaith, *ACS Energy Lett.* **2018**, *3*, 2472.
[4] E. L. Unger, E. T. Hoke, C. D. Bailie, W. H. Nguyen, A. R. Bowring, *Energy Environ. Sci.* **2014**, *7*, 3690.
[5] H. J. Snaith, A. Abate, J. M. Ball, G. E. Eperon, T. Leijtens, N. K. Noel, S. D. Stranks, J. T.-W. Wang, K. Wojciechowski, W. Zhang, *J. Phys. Chem. Lett.* **2014**, *5*, 1511.
[6] N. Pellet, F. Giordano, M. Ibrahim Dar, G. Gregori, S. M. Zakeeruddin, J. Maier, M. Grätzel, *Prog. Photovolt. Res. Appl.* **2017**, *25*, 942.
[7] C.-Y. Chen, J.-H. Chang, K.-M. Chiang, H.-L. Lin, S.-Y. Hsiao, H.-W. Lin, *Adv. Funct. Mater.* **2015**, *25*, 7064.
[8] W. Tress, K. Domanski, B. Carlsen, A. Agarwalla, E. A. Alharbi, M. Graetzel, A. Hagfeldt, *Nat. Energy* **2019**, *4*, 568.
[9] S. T. Surface, f. R. S. S. I. D. N. a. H. o. T. ASTM G173 – 03, **2008**. http://www.astm.org/cgi-bin/resolver.cgi?G173 (accessed: November 2019).
[10] S. S. Testing, f. S. S. f. T. P. ASTM E927 – 10, http://www.astm.org/cgi-bin/resolver.cgi?E927 (accessed: November 2019).
[11] E. Zimmermann, P. Ehrenreich, T. Pfadler, J. A. Dorman, J. Weickert, L. Schmidt-Mende, *Nat. Photonics* **2014**, *8*, 669.
[12] L. Rakocevic, F. Ernst, N. T. Yimga, S. Vashishtha, T. Aernouts, T. Heumueller, C. J. Brabec, R. Gehlhaar, J. Poortmans, *Sol. RRL* **2019**, *3*, 1800287.
[13] A. J. Moulé, K. Meerholz, *Adv. Funct. Mater.* **2009**, *19*, 3028.
[14] E. Zimmermann, K. K. Wong, M. Müller, H. Hu, P. Ehrenreich, M. Kohlstädt, U. Würfel, S. Mastroianni, G. Mathiazhagan, A. Hinsch, T. P. Gujar, M. Thelakkat, T. Pfadler, L. Schmidt-Mende, *APL Mater.* **2016**, *4*, 091901.

190

[15] R. B. Dunbar, B. C. Duck, T. Moriarty, K. F. Anderson, Noel W. Duffy, C. J. Fell, J. Kim, A. Ho-Baillie, D. Vak, T. Duong, Y. Wu, K. Weber, A. Pascoe, Y.-B. Cheng, Q. Lin, P. L. Burn, R. Bhattacharjee, H. Wang, G. J. Wilson, _J. Mater. Chem. A_ **2017**, _5_, 22542.

[16] J. A. Christians, J. S. Manser, P. V. Kamat, _J. Phys. Chem. Lett._ **2015**, _6_, 852.

[17] R. B. Dunbar, W. Moustafa, A. R. Pascoe, T. W. Jones, K. F. Anderson, Y.-B. Cheng, C. J. Fell, G. J. Wilson, _Prog. Photovolt. Res. Appl._ **2017**, _25_, 533.

[18] N. Mundhaas, Z. J. Yu, K. A. Bush, H.-P. Wang, J. Häusele, S. Kavadiya, M. D. McGehee, Z. C. Holman, _Sol. RRL_ **2019**, _3_, 1800378.

[19] B. C. O'Regan, P. R. F. Barnes, X. Li, C. Law, E. Palomares, J. M. Marin-Beloqui, _J. Am. Chem. Soc._ **2015**, _137_, 5087.

[20] P. Measurements, Multichannel Solar Characterization Systems, http://www.pvmeasurements.com/Products/I-V-Measurements/solar-cell-i-v-data-acquisition-system.html (accessed: November 2019).

[21] C. S. N. Pellet, Multichannel Solar Characterization Setup, contact@candlelight-systems.com (accessed: November 2019).

[22] Ossila Solar characterization System, https://www.ossila.com/products/solar-cell-iv-test-system?variant=13633049100384 (accessed: November 2019).

[23] N. Instruments, 1-channel SMU, http://www.ni.com/en-au/support/model.pxi-4130.html http://www.ni.com/example/30918 (accessed: November 2019).

[24] Y. Li, et al., _Energy Environ. Sci._ **2019**, _12_, 2233.

[25] S. Sun, N. T. P. Hartono, Z. D. Ren, F. Oviedo, A. M. Buscemi, M. Layurova, D. X. Chen, T. Ogunfunmi, J. Thapa, S. Ramasamy, C. Settens, B. L. DeCost, A. G. Kusne, Z. Liu, S. I. P. Tian, I. M. Peters, J.-P. Correa-Baena, T. Buonassisi, _Joul_ **2019**, _3_, 1437.

[26] M. Saliba, _Adv. Energy Mater._ **2019**, _9_, 1803754.

[27] Y. Cai, W. Xie, Y. T. Teng, P. C. Harikesh, B. Ghosh, P. Huck, K. A. Persson, N. Mathews, S. G. Mhaisalkar, M. Sherburne, M. Asta, _Chem. Mater._ **2019**, _31_, 5392.

[28] S. Chen, L. Zhang, L. Yan, X. Xiang, X. Zhao, S. Yang, B. Xu, _Adv. Funct. Mater._ **2019**, _29_, 1905487.

[29] J. Li, P. Du, S. Li, J. Liu, M. Zhu, Z. Tan, M. Hu, J. Luo, D. Guo, L. Ma, Z. Nie, Y. Ma, L. Gao, G. Niu, J. Tang, _Adv. Funct. Mater._ **2019**, _29_, 1903607.

[30] S. Ito, M. K. Nazeeruddin, P. Liska, P. Comte, R. Charvet, P. Péchy, M. Jirousek, A. Kay, S. M. Zakeeruddin, M. Grätzel, _Prog. Photovolt. Res. Appl._ **2006**, _14_, 589.

[31] D. Kiermasch, L. Gil-Escrig, H. J. Bolink, K. Tvingstedt, _Joule_ **2019**, _3_, 16.

[32] Q. Chen, L. Chen, F. Ye, T. Zhao, F. Tang, A. Rajagopal, Z. Jiang, S. Jiang, A. K. Y. Jen, Y. Xie, J. Cai, L. Chen, _Nano Lett._ **2017**, _17_, 3231.

[33] ASTM E927-10, _Standard Specification for Solar Simulation for Terrestrial Photovoltaic Testing_, ASTM International, West Conshohocken, PA **2010**.

[34] H. J. Snaith, _Energy Environ. Sci._ **2012**, _5_, 6513.

[35] V. Shrotriya, G. Li, Y. Yao, T. Moriarty, K. Emery, Y. Yang, _Adv. Funct. Mater._ **2006**, _16_, 2016.

[36] Y. Wang, X. Liu, Z. Zhou, P. Ru, H. Chen, X. Yang, L. Han, _Adv. Mater._ **2019**, _0_, 1803231.

[37] C. Zhao, B. Chen, X. Qiao, L. Luan, K. Lu, B. Hu, _Adv. Energy Mater._ **2015**, _5_, 1500279.

[38] X. Xu, J. Shi, H. Wu, Y. Yang, J. Xiao, Y. Luo, D. Li, Q. Meng, _J. Renew. Sustainable Energy_ **2015**, _7_, 043104.

[39] A. K. Jena, A. Kulkarni, T. Miyasaka, _Chem. Rev._ **2019**, _119_, 3036.

[40] M. Saliba, J.-P. Correa-Baena, C. M. Wolff, M. Stolterfoht, N. Phung, S. Albrecht, D. Neher, A. Abate, _Chem. Mater._ **2018**, _30_, 4193.

[41] F. Fu, T. Feurer, Thomas P. Weiss, S. Pisoni, E. Avancini, C. Andres, S. Buecheler, Ayodhya N. Tiwari, _Nat. Energy_ **2016**, _2_, 16190.

[42] N. Park, H. Segawa, _ACS Photonics_ **2018**, _5_, 2970.

[43] M. A. Green, _Solid-State Electron._ **1981**, _24_, 788.

7.4 Conclusions and Future Outlook

Experimental results based on bespoke, yet highly reproducible and precise measurement algorithms should become a standard for the PV community. It is crucial for objective reporting to provide performance characteristics. The manual measurements of non-standardized PSC samples cause erroneous results and significantly extend the parameter screening time. Next generation, high-throughput systems, based on accurate, programmable, and trackable measurements help the research community to further PSC research. The automatization of standardized performance measurements and sample architectures combined in human-intervention free, cost-effective, and time-saving systems lead to universal tools that can be shared across research groups, thus enabling rapid discoveries.

8. Thesis Conclusion

The discovery of perovskites as a new class of PV solar energy harvesters has brought enormous promise and hope for cost-effective, easily manufactured, and highly versatile solar panels. At a high level, the first pilot PSC manufacturers and start-ups benefited from a decade of rapid PSC research, and commercialization of the technology is entering its initial phase. Unfortunately, despite having a marketable efficiency, the best known PSC compositions suffer from long-term stability problems. Fortunately, this new class of materials is versatile, with potentially millions of more efficient and stable PSC compositions yet to be discovered. The fabrication processes typically used in PSC research are manual, time-consuming and often inaccurate. An accelerated approach to materials discovery through automation has recently gained interest. The prediction-fabrication-measurement-analysis approach via automated methodologies and a collaborative database of recipes is key to the market realization of the PSC technology, however, it requires a uniform approach across all research groups to be universally applicable. There is also a notable lack of automation protocols or standardized intra-laboratorial reproducibility maximizing tools. This thesis presented an inexpensive film fabrication technique to study more stable, low-dimensional perovskites, charge transporting materials, measurement protocols and long-term data acquisition methods. The presented robotic fabrication methodology plays a key role in detailed and accurate compositional space generation. Owing to the layered structure of quasi-2D perovskites, a quarterly compositional screening map through the simultaneous variation of organic cations (MA^+ to BA^+), and halides (Br^- to I^-) has been achieved. Moreover, such a human-intervention-free film fabrication protocol can be directly utilized for other compositional spaces with different cations or halides. The cHTR system allowed for the fabrication of the PVP- and DLP-enhanced quasi-2D RP perovskite films in air, which are directly employable in PSC devices. Author would like to emphasize that presented techniques allow for multiple other materials being fabricated and characterized, potentially new bulky spacer cations or combinations of spacer cations would lead to further stability and performance developments. Simultaneously the MA^+ could have been replaced with Cs^+ or FA^+ based space, or even mixed to discover whether it would benefit the performance and stability. Furthermore, this bespoke cHTR protocol demonstrated how a rapid optimization

process with careful data recording can maximize a performance parameter of interest. In future, such rapid device fabrication protocols can be expanded and serve as a great discovery accelerator or parameter screening setups for emerging ML enhanced cHTR studies. Author also focussed efforts on a stable, inorganic and inexpensive charge-transporting layer for PSCs, which can be employed in low-temperature deposition processes. The unique inverted multi-stage Tesla-valve microfluid mixer for newly developed ligand-modified NiO NP precursor provided a new pathways for generation of a uniform, reproducible and plasma-treatment-free low-temperature NiO HTL films. Subsequently author developed fully human-intervention free rapid combinatorial, 4-wire sense, parallel measurement system for PSCs characterization. This cHTR characterization system demonstrated in this work allowed for multiple discoveries and projects to be realized in the Renewable Energy Laboratory at Monash University and inspired/affirmed similar work elsewhere. To benefit the research community oriented on characterization of the PSCs, the work is published in full and allows for easy adaptation. Finally, author provided a pathways for long-term stability testing and data acquisition of PSCs. This open-style approach allowed for tests in real-world conditions and provided important step-by-step engineering instruction for the research community. The perovskite solar panel realization is destined to gain a significant attention after years of single device investigations. In this work (Appendix A), with the most simple, commonly accessible tools the modular solar panel totalling of approximately ~450 cm^2 of active area was realized. The pathway step-by-step fabrication was proposed. This long-term real-world aging station allows for multiple follow up studies and easy adaptation at marginal costs.

8.1 Future Outlook

The recent story of perovskite has shown that potential and opportunity in novel PV materials. This work naturally points to some directions of future study, especially now, in 2021, when the PSC research field transitioned towards commercialization phase and the study focus shifted towards stable perovskites. The high PCE and stability of R-P perovskites is tempting. The ability to incorporate bulky cations as water repelling intercalating layers in the perovskite crystal structure whilst still maintaining highly ordered and efficient solar cell will definitely drive multiple new studies. Author can envisage that the RP or DJ perovskites

including multiple subgroups enhanced with polymers and other additives are yet to be discovered. It is evident that a tremendous amount of undiscovered compositions predicted with DFT/ML computations must be screened. Also these quasi-2D lower dimensional candidates have the potential of being ultimate perovskite material of future due to their superior stability and low-temperature processing. In terms of this work, the BA^+ organic cations were choice of this study and multiple Ruddlesden-Popper family quasi-2D perovskites were developed with novel technique automated drop-casting and microfluidic mixing technique, however the author points that multiple other bulky cations are still there to be employed or even mixed for binary bulky cation realizations. In addition, author notices a strong desire towards optimizing and testing these newly developed perovskite materials in large scale application. A "large scale" could be potentially executed on flexible substrate if the solutions were deposited with similar, yet more sophisticated instrumentation. The high-speed and large scale deposition techniques are currently employed and some of them even reached the early commercialization phase (roll-to-roll deposition or ink-jet printing). It is therefore necessary to carefully consider the low-temperature CTLs options (for example recently gaining a lot of interest SnO_2 NPs for ETLs) and improve their high-speed deposition methods (for example newly developed in this work NiO NPs in this work). Author suggests that a large scale, flexible substrate with two inorganic CTLs sandwiching a highly-stable, polymer enhanced (PVP or PVA) quasi-2D perovskite produced in completely inert atmosphere with immediate encapsulation could be a potentially great candidate for a commercial solar panel. Moreover, the newly developed precursor solutions utilizing binary or ever tertiary solvent systems for increased crystallization windows is destined to gain a significant research focus and potentially a commercial value. Ultimately when it comes to the large scale application author points that the current literature provides many insights into the cost calculation methods and one of the critical ones is to use inorganic, stable materials and lower the energy required for production of the solar panel, naturally this can be achieved by having a low-temperature processable materials. Interestingly, while extensive studies are performed or new materials are predicted, there is a very little initiative to develop a centralized database with the material properties. Potentially unlimited compositional space of highly performing candidates requires more efforts than just manual, low-throughput experiments. To dive into these opportunities there is a desire to develop and screen new materials, with a priority to as yet unrealized combinations of fabrication

parameters. In this work a glimpse of the power of high-throughput research, the capacity to produce and characterise new materials at previously unrealized rates was delivered. A natural direction for this to proceed in is the application of full automation. As shown here, this can occur for each of the key steps in material discovery including the development fabrication, characterisation and data analysis/management. Automation can be achieved through the development of new techniques that allow for the creation/analysis of high quality, continuous samples or more rapid management of discrete samples with minimal researcher intervention. While this can be implemented on a small scale, for isolated instruments, the advantage of automation can often be hindered by bottle-necks caused complementary techniques that require manual steps, sample loading and/or has restrictive sample requirements. For automated material discovery to be optimal it should be performed at a large scale on a dedicated system. Recently Monash University received multimillion dollar funding and began construction of a unique, world-class, high-throughput material discovery platform. The system, housed entirely in inert atmosphere, will employ robots to synthesise precursors solutions, prepare thin films and characterise a wide range of material properties including crystallography, optical absorption/reflection, electrical conductivity, etc. Experimentally measured data will be stored in a dedicated, searchable database along with sample metadata. The role of researcher will be redefined into the "data analyst/experiment designer" who based, on ML outcomes, will exploit the massive amounts of data to perform multidimensional analysis and propose new studies. The manual element is intended to be limited only to the process design and chemicals refill; instrument maintenance and control will be conducted by a dedicated engineer. While the highly versatile platform will greatly accelerate the rate of material discovery across countless fields, it has been designed with a PSC community in mind. It will further the discovery of new generation materials directly benefiting the community and promote renewable energy transformation across the globe.

8.2 Final remark

Beyond the stability problem that is being mitigated by many groups around the world, author acknowledges that the sustainability of perovskites is widely debated in terms of

environmental impact. The toxicity of ionic lead complexes or extremely hazardous solvents gained much more public awareness and most of the leading research organizations acknowledges these risks. Fortunately, the strategies around the encapsulation, recycling, substitution of lead with other material, or use of greener solvents were explored.[101] These developments only proved the need of cHTR systems. The combination of human-intervention free cHTR fabrication and characterization with computational modelling of exploration space will provide the most accurate, the fastest and arguably the best way for progress in photovoltaics.

9. Bibliography

1. Byrnes, L.; Brown, C.; Foster, J.; Wagner, L. D., Australian renewable energy policy: Barriers and challenges. *Renewable Energy* **2013,** *60*, 711-721.
2. IRENA.
3. IEA_UPDATE.
4. Rühle, S., Tabulated values of the Shockley–Queisser limit for single junction solar cells. *Solar Energy* **2016,** *130*, 139-147.
5. Hong, J.; Chen, W.; Qi, C.; Ye, L.; Xu, C., Life cycle assessment of multicrystalline silicon photovoltaic cell production in China. *Solar Energy* **2016,** *133*, 283-293.
6. Tang, Y.; Sun, H.; Yao, Q.; Wang, Y., The selection of key technologies by the silicon photovoltaic industry based on the Delphi method and AHP (analytic hierarchy process): Case study of China. *Energy* **2014,** *75*, 474-482.
7. Bukhary, S.; Ahmad, S.; Batista, J., Analyzing land and water requirements for solar deployment in the Southwestern United States. *Renewable and Sustainable Energy Reviews* **2018,** *82*, 3288-3305.
8. Dubey, S.; Jadhav, N. Y.; Zakirova, B., Socio-Economic and Environmental Impacts of Silicon Based Photovoltaic (PV) Technologies. *Energy Procedia* **2013,** *33*, 322-334.
9. Kojima, A.; Teshima, K.; Shirai, Y.; Miyasaka, T., Organometal Halide Perovskites as Visible-Light Sensitizers for Photovoltaic Cells. *Journal of the American Chemical Society* **2009,** *131* (17), 6050-6051.
10. Mishra, S.; Ghosh, S.; Singh, T., Progress in Materials Development for Flexible Perovskite Solar Cells and Future Prospects. *ChemSusChem* **2021,** *14* (2), 512-538.
11. NREL Best Research-Cell Efficiency Chart. (https://www.nrel.gov/pv/cell-efficiency.html.
12. Yoshikawa, K.; Kawasaki, H.; Yoshida, W.; Irie, T.; Konishi, K.; Nakano, K.; Uto, T.; Adachi, D.; Kanematsu, M.; Uzu, H.; Yamamoto, K., Silicon heterojunction solar cell with interdigitated back contacts for a photoconversion efficiency over 26%. *Nature Energy* **2017,** *2* (5), 17032.
13. Goldschmidt, V. M., Die Gesetze der Krystallochemie. *Naturwissenschaften* **1926,** *14* (21), 477-485.
14. Poglitsch, A.; Weber, D., Dynamic disorder in methylammoniumtrihalogenoplumbates (II) observed by millimeter-wave spectroscopy. *The Journal of Chemical Physics* **1987,** *87* (11), 6373-6378.
15. Calió, L.; Kazim, S.; Grätzel, M.; Ahmad, S., Hole-Transport Materials for Perovskite Solar Cells. *Angewandte Chemie International Edition* **2016,** *55* (47), 14522-14545.
16. Zhang, Y.; Liu, M.; Eperon, G. E.; Leijtens, T. C.; McMeekin, D.; Saliba, M.; Zhang, W.; de Bastiani, M.; Petrozza, A.; Herz, L. M.; Johnston, M. B.; Lin, H.; Snaith, H. J., Charge selective contacts, mobile ions and anomalous hysteresis in organic–inorganic perovskite solar cells. *Materials Horizons* **2015,** *2* (3), 315-322.

17.   Son, D.-Y.; Kim, S.-G.; Seo, J.-Y.; Lee, S.-H.; Shin, H.; Lee, D.; Park, N.-G., Universal Approach toward Hysteresis-Free Perovskite Solar Cell via Defect Engineering. *Journal of the American Chemical Society* **2018,** *140* (4), 1358-1364.

18.   Cho, A.-N.; Park, N.-G., Impact of Interfacial Layers in Perovskite Solar Cells. *ChemSusChem* **2017,** *10* (19), 3687-3704.

19.   Zhang, M.; Yun, J. S.; Ma, Q.; Zheng, J.; Lau, C. F. J.; Deng, X.; Kim, J.; Kim, D.; Seidel, J.; Green, M. A.; Huang, S.; Ho-Baillie, A. W. Y., High-Efficiency Rubidium-Incorporated Perovskite Solar Cells by Gas Quenching. *ACS Energy Letters* **2017,** *2* (2), 438-444.

20.   A Conversation with Michael Grätzel. *ACS Energy Letters* **2017,** *2* (7), 1674-1676.

21.   A Conversation with Henry Snaith. *ACS Energy Letters* **2017,** *2* (11), 2552-2554.

22.   Mohamad Noh, M. F.; Teh, C. H.; Daik, R.; Lim, E. L.; Yap, C. C.; Ibrahim, M. A.; Ahmad Ludin, N.; Mohd Yusoff, A. R. b.; Jang, J.; Mat Teridi, M. A., The architecture of the electron transport layer for a perovskite solar cell. *Journal of Materials Chemistry C* **2018,** *6* (4), 682-712.

23.   Qiu, W.; Merckx, T.; Jaysankar, M.; Masse de la Huerta, C.; Rakocevic, L.; Zhang, W.; Paetzold, U. W.; Gehlhaar, R.; Froyen, L.; Poortmans, J.; Cheyns, D.; Snaith, H. J.; Heremans, P., Pinhole-free perovskite films for efficient solar modules. *Energy & Environmental Science* **2016,** *9* (2), 484-489.

24.   Janker, L.; Tong, Y.; Polavarapu, L.; Feldmann, J.; Urban, A. S.; Krenner, H. J., Real-Time Electron and Hole Transport Dynamics in Halide Perovskite Nanowires. *Nano Letters* **2019,** *19* (12), 8701-8707.

25.   Limpert, S.; Bremner, S.; Linke, H., Reversible electron–hole separation in a hot carrier solar cell. *New Journal of Physics* **2015,** *17* (9), 095004.

26.   Yang, T. C.-J.; Fiala, P.; Jeangros, Q.; Ballif, C., High-Bandgap Perovskite Materials for Multijunction Solar Cells. *Joule* **2018,** *2* (8), 1421-1436.

27.   Chueh, C.-C.; Li, C.-Z.; Jen, A. K. Y., Recent progress and perspective in solution-processed Interfacial materials for efficient and stable polymer and organometal perovskite solar cells. *Energy & Environmental Science* **2015,** *8* (4), 1160-1189.

28.   Hörantner, M. T.; Nayak, P. K.; Mukhopadhyay, S.; Wojciechowski, K.; Beck, C.; McMeekin, D.; Kamino, B.; Eperon, G. E.; Snaith, H. J., Shunt-Blocking Layers for Semitransparent Perovskite Solar Cells. *Advanced Materials Interfaces* **2016,** *3* (10), 1500837.

29.   Mundhaas, N.; Yu, Z. J.; Bush, K. A.; Wang, H.-P.; Häusele, J.; Kavadiya, S.; McGehee, M. D.; Holman, Z. C., Series Resistance Measurements of Perovskite Solar Cells Using Jsc–Voc Measurements. *Solar RRL* **2019,** *3* (4), 1800378.

30.   Wu, B.; Fu, K.; Yantara, N.; Xing, G.; Sun, S.; Sum, T. C.; Mathews, N., Charge Accumulation and Hysteresis in Perovskite-Based Solar Cells: An Electro-Optical Analysis. *Advanced Energy Materials* **2015,** *5* (19), 1500829.

31.   Christians, J. A.; Manser, J. S.; Kamat, P. V., Best Practices in Perovskite Solar Cell Efficiency Measurements. Avoiding the Error of Making Bad Cells Look Good. *The Journal of Physical Chemistry Letters* **2015,** *6* (5), 852-857.

32.   Wang, Y.; Liu, X.; Zhou, Z.; Ru, P.; Chen, H.; Yang, X.; Han, L., Reliable Measurement of Perovskite Solar Cells. *Advanced Materials* **2019,** *31* (47), 1803231.

33.   Hishikawa, Y.; Shimura, H.; Ueda, T.; Sasaki, A.; Ishii, Y., Precise performance characterization of perovskite solar cells. *Current Applied Physics* **2016,** *16* (8), 898-904.

34.   Snaith, H. J.; Abate, A.; Ball, J. M.; Eperon, G. E.; Leijtens, T.; Noel, N. K.; Stranks, S. D.; Wang, J. T.-W.; Wojciechowski, K.; Zhang, W., Anomalous Hysteresis in Perovskite Solar Cells. *The Journal of Physical Chemistry Letters* **2014,** *5* (9), 1511-1515.

35.   Cimaroli, A. J.; Yu, Y.; Wang, C.; Liao, W.; Guan, L.; Grice, C. R.; Zhao, D.; Yan, Y., Tracking the maximum power point of hysteretic perovskite solar cells using a predictive algorithm. *Journal of Materials Chemistry C* **2017,** *5* (39), 10152-10157.

36.   Saliba, M.; Stolterfoht, M.; Wolff, C. M.; Neher, D.; Abate, A., Measuring Aging Stability of Perovskite Solar Cells. *Joule* **2018,** *2* (6), 1019-1024.

37.   De Bastiani, M.; Dell'Erba, G.; Gandini, M.; D'Innocenzo, V.; Neutzner, S.; Kandada, A. R. S.; Grancini, G.; Binda, M.; Prato, M.; Ball, J. M.; Caironi, M.; Petrozza, A., Ion Migration and the Role of Preconditioning Cycles in the Stabilization of the J–V Characteristics of Inverted Hybrid Perovskite Solar Cells. *Advanced Energy Materials* **2016,** *6* (2), 1501453.

38.   La-Placa, M.-G.; Gil-Escrig, L.; Guo, D.; Palazon, F.; Savenije, T. J.; Sessolo, M.; Bolink, H. J., Vacuum-Deposited 2D/3D Perovskite Heterojunctions. *ACS Energy Letters* **2019,** *4* (12), 2893-2901.

39.   Domanski, K.; Correa-Baena, J.-P.; Mine, N.; Nazeeruddin, M. K.; Abate, A.; Saliba, M.; Tress, W.; Hagfeldt, A.; Grätzel, M., Not All That Glitters Is Gold: Metal-Migration-Induced Degradation in Perovskite Solar Cells. *ACS Nano* **2016,** *10* (6), 6306-6314.

40.   Li, X.; Dar, M. I.; Yi, C.; Luo, J.; Tschumi, M.; Zakeeruddin, S. M.; Nazeeruddin, M. K.; Han, H.; Grätzel, M., Improved performance and stability of perovskite solar cells by crystal crosslinking with alkylphosphonic acid ω-ammonium chlorides. *Nat Chem* **2015,** *7* (9), 703-11.

41.   You, J.; Meng, L.; Song, T.-B.; Guo, T.-F.; Yang, Y.; Chang, W.-H.; Hong, Z.; Chen, H.; Zhou, H.; Chen, Q.; Liu, Y.; De Marco, N.; Yang, Y., Improved air stability of perovskite solar cells via solution-processed metal oxide transport layers. *Nature Nanotechnology* **2016,** *11* (1), 75-81.

42.   Grancini, G.; Nazeeruddin, M. K., Dimensional tailoring of hybrid perovskites for photovoltaics. *Nature Reviews Materials* **2019,** *4* (1), 4-22.

43.   Vasileiadou, E. S.; Wang, B.; Spanopoulos, I.; Hadar, I.; Navrotsky, A.; Kanatzidis, M. G., Insight on the Stability of Thick Layers in 2D Ruddlesden–Popper and Dion–Jacobson Lead Iodide Perovskites. *Journal of the American Chemical Society* **2021,** *143* (6), 2523-2536.

44.   Tremblay, M.-H.; Bacsa, J.; Zhao, B.; Pulvirenti, F.; Barlow, S.; Marder, S. R., Structures of (4-Y-C6H4CH2NH3)2PbI4 {Y = H, F, Cl, Br, I}: Tuning of Hybrid Organic Inorganic Perovskite Structures from Ruddlesden–Popper to Dion–Jacobson Limits. *Chemistry of Materials* **2019,** *31* (16), 6145-6153.

45.   Lai, Z.; Dong, R.; Zhu, Q.; Meng, Y.; Wang, F.; Li, F.; Bu, X.; Kang, X.; Zhang, H.; Quan, Q.; Wang, W.; Wang, F.; Yip, S.; Ho, J. C., Bication-Mediated Quasi-2D Halide Perovskites for High-Performance Flexible Photodetectors: From Ruddlesden–Popper Type to Dion–Jacobson Type. *ACS Applied Materials & Interfaces* **2020,** *12* (35), 39567-39577.

46.   Soe, C. M. M.; Stoumpos, C. C.; Kepenekian, M.; Traoré, B.; Tsai, H.; Nie, W.; Wang, B.; Katan, C.; Seshadri, R.; Mohite, A. D.; Even, J.; Marks, T. J.; Kanatzidis, M. G., New Type of 2D Perovskites with Alternating Cations in the Interlayer Space, (C(NH2)3)(CH3NH3)nPbnI3n+1: Structure, Properties, and Photovoltaic Performance. *Journal of the American Chemical Society* **2017,** *139* (45), 16297-16309.

47.   Li, X.; Hoffman, J.; Ke, W.; Chen, M.; Tsai, H.; Nie, W.; Mohite, A. D.; Kepenekian, M.; Katan, C.; Even, J.; Wasielewski, M. R.; Stoumpos, C. C.; Kanatzidis, M. G., Two-Dimensional Halide Perovskites Incorporating Straight Chain Symmetric Diammonium Ions, (NH3CmH2mNH3)(CH3NH3)n−1PbnI3n+1 (m = 4–9; n = 1–4). *Journal of the American Chemical Society* **2018,** *140* (38), 12226-12238.

48.   Zheng, K.; Pullerits, T., Two Dimensions Are Better for Perovskites. *The Journal of Physical Chemistry Letters* **2019,** *10* (19), 5881-5885.

49.   Hu, Z.; Lin, Z.; Su, J.; Zhang, J.; Chang, J.; Hao, Y., A Review on Energy Band-Gap Engineering for Perovskite Photovoltaics. *Solar RRL* **2019,** *3* (12), 1900304.

50.   Passarelli, J. V.; Mauck, C. M.; Winslow, S. W.; Perkinson, C. F.; Bard, J. C.; Sai, H.; Williams, K. W.; Narayanan, A.; Fairfield, D. J.; Hendricks, M. P.; Tisdale, W. A.; Stupp, S. I., Tunable exciton binding energy in 2D hybrid layered perovskites through donor–acceptor interactions within the organic layer. *Nature Chemistry* **2020,** *12* (8), 672-682.

51.   Kim, D.; Ahmadi, M., Elucidating the Spatial Dynamics of Charge Carriers in Quasi-Two-Dimensional Perovskites. *ACS Applied Materials & Interfaces* **2021**.

52.   Cheng, B.; Li, T.-Y.; Maity, P.; Wei, P.-C.; Nordlund, D.; Ho, K.-T.; Lien, D.-H.; Lin, C.-H.; Liang, R.-Z.; Miao, X.; Ajia, I. A.; Yin, J.; Sokaras, D.; Javey, A.; Roqan, I. S.; Mohammed, O. F.; He, J.-H., Extremely reduced dielectric confinement in two-dimensional hybrid perovskites with large polar organics. *Communications Physics* **2018,** *1* (1), 80.

53.   Lian, X.; Wu, H.; Zuo, L.; Zhou, G.; Wen, X.; Zhang, Y.; Wu, G.; Xie, Z.; Zhu, H.; Chen, H., Stable Quasi-2D Perovskite Solar Cells with Efficiency over 18% Enabled by Heat–Light Co-Treatment. *Advanced Functional Materials* **2020,** *30* (48), 2004188.

54.   Lai, X.; Li, W.; Gu, X.; Chen, H.; Zhang, Y.; Li, G.; Zhang, R.; Fan, D.; He, F.; Zheng, N.; Yu, J.; Chen, R.; Kyaw, A. K. K.; Sun, X. W., High-performance quasi-2D perovskite solar cells with power conversion efficiency over 20% fabricated in humidity-controlled ambient air. *Chemical Engineering Journal* **2022,** *427*, 130949.

55.   Jacobsson, T. J.; Correa-Baena, J.-P.; Halvani Anaraki, E.; Philippe, B.; Stranks, S. D.; Bouduban, M. E. F.; Tress, W.; Schenk, K.; Teuscher, J.; Moser, J.-E.; Rensmo, H.; Hagfeldt, A., Unreacted PbI2 as a Double-Edged Sword for Enhancing the Performance of Perovskite Solar Cells. *Journal of the American Chemical Society* **2016,** *138* (32), 10331-10343.

56.   Hoke, E. T.; Slotcavage, D. J.; Dohner, E. R.; Bowring, A. R.; Karunadasa, H. I.; McGehee, M. D., Reversible photo-induced trap formation in mixed-halide hybrid perovskites for photovoltaics. *Chemical Science* **2015,** *6* (1), 613-617.

57.   Barker, A. J.; Sadhanala, A.; Deschler, F.; Gandini, M.; Senanayak, S. P.; Pearce, P. M.; Mosconi, E.; Pearson, A. J.; Wu, Y.; Srimath Kandada, A. R.; Leijtens, T.; De Angelis, F.; Dutton, S. E.; Petrozza, A.; Friend, R. H., Defect-Assisted Photoinduced Halide Segregation in Mixed-Halide Perovskite Thin Films. *ACS Energy Letters* **2017,** *2* (6), 1416-1424.

58.   Eperon, G. E.; Paternò, G. M.; Sutton, R. J.; Zampetti, A.; Haghighirad, A. A.; Cacialli, F.; Snaith, H. J., Inorganic caesium lead iodide perovskite solar cells. *Journal of Materials Chemistry A* **2015,** *3* (39), 19688-19695.

59.   McMeekin, D. P.; Sadoughi, G.; Rehman, W.; Eperon, G. E.; Saliba, M.; Hörantner, M. T.; Haghighirad, A.; Sakai, N.; Korte, L.; Rech, B.; Johnston, M. B.; Herz, L. M.; Snaith, H. J., A mixed-cation lead mixed-halide perovskite absorber for tandem solar cells. *Science* **2016,** *351* (6269), 151.

60.   Poespawati, N. R.; Kevin, L.; Abuzairi, T.; R. W., P.; Sulistianto, J.; Rembianov In *Effect of Perovskite Precursors Molarity on Solar Cell Performance*, 2019 11th International Conference on Information Technology and Electrical Engineering (ICITEE), 10-11 Oct. 2019; 2019; pp 1-4.

61.   Rai, M.; Wong, L. H.; Etgar, L., Effect of Perovskite Thickness on Electroluminescence and Solar Cell Conversion Efficiency. *The Journal of Physical Chemistry Letters* **2020,** *11* (19), 8189-8194.

62.   Hong, L.; Hu, Y.; Mei, A.; Sheng, Y.; Jiang, P.; Tian, C.; Rong, Y.; Han, H., Improvement and Regeneration of Perovskite Solar Cells via Methylamine Gas Post-Treatment. *Advanced Functional Materials* **2017,** *27* (43), 1703060.

63.   Vasilopoulou, M.; Fakharuddin, A.; Coutsolelos, A. G.; Falaras, P.; Argitis, P.; Yusoff, A. R. b. M.; Nazeeruddin, M. K., Molecular materials as interfacial layers and additives in perovskite solar cells. *Chemical Society Reviews* **2020,** *49* (13), 4496-4526.

64.   You, P.; Liu, Z.; Tai, Q.; Liu, S.; Yan, F., Efficient Semitransparent Perovskite Solar Cells with Graphene Electrodes. *Advanced Materials* **2015,** *27* (24), 3632-3638.

65.   Rolston, N.; Bush, K. A.; Printz, A. D.; Gold-Parker, A.; Ding, Y.; Toney, M. F.; McGehee, M. D.; Dauskardt, R. H., Engineering Stress in Perovskite Solar Cells to Improve Stability. *Advanced Energy Materials* **2018,** *8* (29), 1802139.

66.   De Angelis, F., Celebrating 10 Years of Perovskite Photovoltaics. *ACS Energy Letters* **2019,** *4* (4), 853-854.

67.   Talapatra, A.; Uberuaga, B. P.; Stanek, C. R.; Pilania, G., A Machine Learning Approach for the Prediction of Formability and Thermodynamic Stability of Single and Double Perovskite Oxides. *Chemistry of Materials* **2021,** *33* (3), 845-858.

68.   Lee, B. D.; Park, W. B.; Lee, J.-W.; Kim, M.; Pyo, M.; Sohn, K.-S., Discovery of Lead-Free Hybrid Organic/Inorganic Perovskites Using Metaheuristic-Driven DFT Calculations. *Chemistry of Materials* **2021,** *33* (2), 782-798.

69.   Li, J.; Pradhan, B.; Gaur, S.; Thomas, J., Predictions and Strategies Learned from Machine Learning to Develop High-Performing Perovskite Solar Cells. *Advanced Energy Materials* **2019,** *9* (46), 1901891.

70.   Arya, S.; Mahajan, P.; Gupta, R.; Srivastava, R.; Tailor, N. k.; Satapathi, S.; Sumathi, R. R.; Datt, R.; Gupta, V., A comprehensive review on synthesis and applications of single crystal perovskite halides. *Progress in Solid State Chemistry* **2020,** *60*, 100286.

71.   Gu, E.; Tang, X.; Langner, S.; Duchstein, P.; Zhao, Y.; Levchuk, I.; Kalancha, V.; Stubhan, T.; Hauch, J.; Egelhaaf, H. J.; Zahn, D.; Osvet, A.; Brabec, C. J., Robot-Based High-Throughput Screening of Antisolvents for Lead Halide Perovskites. *Joule* **2020,** *4* (8), 1806-1822.

72.   Chen, S.; Hou, Y.; Chen, H.; Tang, X.; Langner, S.; Li, N.; Stubhan, T.; Levchuk, I.; Gu, E.; Osvet, A.; Brabec, C. J., Exploring the Stability of Novel Wide Bandgap Perovskites by a Robot Based High Throughput Approach. *Advanced Energy Materials* **2018,** *8* (6), 1701543.

73.   Li, Z.; Najeeb, M. A.; Alves, L.; Sherman, A. Z.; Shekar, V.; Cruz Parrilla, P.; Pendleton, I. M.; Wang, W.; Nega, P. W.; Zeller, M.; Schrier, J.; Norquist, A. J.; Chan, E. M., Robot-Accelerated Perovskite Investigation and Discovery. *Chemistry of Materials* **2020,** *32* (13), 5650-5663.

74.   Gouda, L.; Gottesman, R.; Tirosh, S.; Haltzi, E.; Hu, J.; Ginsburg, A.; Keller, D. A.; Bouhadana, Y.; Zaban, A., Vapor and healing treatment for CH3NH3PbI3−xClx films toward large-area perovskite solar cells. *Nanoscale* **2016,** *8* (12), 6386-6392.

75.   Rakocevic, L.; Ernst, F.; Yimga, N. T.; Vashishtha, S.; Aernouts, T.; Heumueller, T.; Brabec, C. J.; Gehlhaar, R.; Poortmans, J., Reliable Performance Comparison of Perovskite Solar Cells Using Optimized Maximum Power Point Tracking. *Solar RRL* **2019,** *3* (2), 1800287.

76.   Angmo, D.; DeLuca, G.; Scully, A. D.; Chesman, A. S. R.; Seeber, A.; Zuo, C.; Vak, D.; Bach, U.; Gao, M., A Lab-to-Fab Study toward Roll-to-Roll Fabrication of Reproducible Perovskite Solar Cells under Ambient Room Conditions. *Cell Reports Physical Science* **2021,** *2* (1), 100293.

77.   Zuo, C.; Scully, A. D.; Tan, W. L.; Zheng, F.; Ghiggino, K. P.; Vak, D.; Weerasinghe, H.; McNeill, C. R.; Angmo, D.; Chesman, A. S. R.; Gao, M., Crystallisation control of drop-cast quasi-2D/3D perovskite layers for efficient solar cells. *Communications Materials* **2020,** *1* (1), 33.

78.	Stoumpos, C. C.; Cao, D. H.; Clark, D. J.; Young, J.; Rondinelli, J. M.; Jang, J. I.; Hupp, J. T.; Kanatzidis, M. G., Ruddlesden–Popper Hybrid Lead Iodide Perovskite 2D Homologous Semiconductors. *Chemistry of Materials* **2016,** *28* (8), 2852-2867.

79.	Cao, D. H.; Stoumpos, C. C.; Farha, O. K.; Hupp, J. T.; Kanatzidis, M. G., 2D Homologous Perovskites as Light-Absorbing Materials for Solar Cell Applications. *Journal of the American Chemical Society* **2015,** *137* (24), 7843-7850.

80.	Thompson, S. M.; Paudel, B. J.; Jamal, T.; Walters, D. K., Numerical Investigation of Multistaged Tesla Valves. *Journal of Fluids Engineering* **2014,** *136* (8).

81.	Porwal, P. R.; Thompson, S. M.; Walters, D. K.; Jamal, T., Heat transfer and fluid flow characteristics in multistaged Tesla valves. *Numerical Heat Transfer, Part A: Applications* **2018,** *73* (6), 347-365.

82.	Uličná, S.; Dou, B.; Kim, D. H.; Zhu, K.; Walls, J. M.; Bowers, J. W.; van Hest, M. F. A. M., Scalable Deposition of High-Efficiency Perovskite Solar Cells by Spray-Coating. *ACS Applied Energy Materials* **2018,** *1* (5), 1853-1857.

83.	Wei, Z.; Chen, H.; Yan, K.; Yang, S., Inkjet Printing and Instant Chemical Transformation of a CH3NH3PbI3/Nanocarbon Electrode and Interface for Planar Perovskite Solar Cells. *Angewandte Chemie International Edition* **2014,** *53* (48), 13239-13243.

84.	Yuan, J.; Zhang, L.; Bi, C.; Wang, M.; Tian, J., Surface Trap States Passivation for High-Performance Inorganic Perovskite Solar Cells. *Solar RRL* **2018,** *2* (10), 1800188.

85.	Ren, Y.-K.; Shi, X.-Q.; Ding, X.-H.; Zhu, J.; Hayat, T.; Alsaedi, A.; Li, Z.-Q.; Xu, X.-X.; Yang, S.-F.; Dai, S.-Y., Facile fabrication of perovskite layers with large grains through a solvent exchange approach. *Inorganic Chemistry Frontiers* **2018,** *5* (2), 348-353.

86.	Hofstetter, Y. J.; García-Benito, I.; Paulus, F.; Orlandi, S.; Grancini, G.; Vaynzof, Y., Vacuum-Induced Degradation of 2D Perovskites. *Frontiers in Chemistry* **2020,** *8* (66).

87.	Babaei, A.; Zanoni, K. P. S.; Gil-Escrig, L.; Pérez-del-Rey, D.; Boix, P. P.; Sessolo, M.; Bolink, H. J., Efficient Vacuum Deposited P-I-N Perovskite Solar Cells by Front Contact Optimization. *Frontiers in Chemistry* **2020,** *7* (936).

88.	Liang, L.; Cai, Y.; Li, X.; Nazeeruddin, M. K.; Gao, P., All that glitters is not gold: Recent progress of alternative counter electrodes for perovskite solar cells. *Nano Energy* **2018,** *52*, 211-238.

89.	Xiong, H.; DeLuca, G.; Rui, Y.; Zhang, B.; Li, Y.; Zhang, Q.; Wang, H.; Reichmanis, E., Modifying Perovskite Films with Polyvinylpyrrolidone for Ambient-Air-Stable Highly Bendable Solar Cells. *ACS Applied Materials & Interfaces* **2018,** *10* (41), 35385-35394.

90.	Zuo, L.; Guo, H.; deQuilettes, D. W.; Jariwala, S.; De Marco, N.; Dong, S.; DeBlock, R.; Ginger, D. S.; Dunn, B.; Wang, M.; Yang, Y., Polymer-modified halide perovskite films for efficient and stable planar heterojunction solar cells. *Science Advances* **2017,** *3* (8), e1700106.

91.	Deng, Y.; Zheng, X.; Bai, Y.; Wang, Q.; Zhao, J.; Huang, J., Surfactant-controlled ink drying enables high-speed deposition of perovskite films for efficient photovoltaic modules. *Nature Energy* **2018,** *3* (7), 560-566.

92.	Seo, Y.-H.; Kim, E.-C.; Cho, S.-P.; Kim, S.-S.; Na, S.-I., High-performance planar perovskite solar cells: Influence of solvent upon performance. *Applied Materials Today* **2017,** *9*, 598-604.

93.	Zhang, J.; Zhang, L.; Li, X.; Zhu, X.; Yu, J.; Fan, K., Binary Solvent Engineering for High-Performance Two-Dimensional Perovskite Solar Cells. *ACS Sustainable Chemistry & Engineering* **2019,** *7* (3), 3487-3495.

94.   Liu, G.; Liu, Z.; Zeng, F.; Wang, X.; Li, S.; Xie, X., High performance two-dimensional perovskite solar cells based on solvent induced morphology control of perovskite layers. *Chemical Physics Letters* **2020,** *743*, 137186.

95.   Shin, M.; Kim, J.; Jung, Y.-K.; Ruoko, T.-p.; Priimagi, A.; Walsh, A.; Shin, B., Low-dimensional formamidinium lead perovskite architectures via controllable solvent intercalation. *Journal of Materials Chemistry C* **2019,** *7* (13), 3945-3951.

96.   Li, F.; Zhang, J.; Jo, S.; Qin, M.; Li, Z.; Liu, T.; Lu, X.; Zhu, Z.; Jen, A. K. Y., Vertical Orientated Dion–Jacobson Quasi-2D Perovskite Film with Improved Photovoltaic Performance and Stability. *Small Methods* **2020,** *4* (5), 1900831.

97.   Yang, R.; Li, R.; Cao, Y.; Wei, Y.; Miao, Y.; Tan, W. L.; Jiao, X.; Chen, H.; Zhang, L.; Chen, Q.; Zhang, H.; Zou, W.; Wang, Y.; Yang, M.; Yi, C.; Wang, N.; Gao, F.; McNeill, C. R.; Qin, T.; Wang, J.; Huang, W., Oriented Quasi-2D Perovskites for High Performance Optoelectronic Devices. *Advanced Materials* **2018,** *30* (51), 1804771.

98.   Xie, Y.; Yu, H.; Duan, J.; Xu, L.; Hu, B., Enhancing Device Performance in Quasi-2D Perovskite ((BA)2(MA)3Pb4I13) Solar Cells Using PbCl2 Additives. *ACS Applied Materials & Interfaces* **2020,** *12* (9), 11190-11196.

99.   Schwenzer, J. A.; Rakocevic, L.; Abzieher, T.; Rueda-Delgado, D.; Moghadamzadeh, S.; Gharibzadeh, S.; Hossain, I. M.; Gehlhaar, R.; Richards, B. S.; Lemmer, U.; Paetzold, U. W., Toward Stable Perovskite Solar Cell Architectures: Robustness Against Temperature Variations of Real-World Conditions. *IEEE Journal of Photovoltaics* **2020,** *10* (3), 777-784.

100.   Pockett, A.; Carnie, M. J., Ionic Influences on Recombination in Perovskite Solar Cells. *ACS Energy Letters* **2017,** *2* (7), 1683-1689.

101.   Schileo, G.; Grancini, G., Lead or no lead? Availability, toxicity, sustainability and environmental impact of lead-free perovskite solar cells. *Journal of Materials Chemistry C* **2021,** *9* (1), 67-76.

102.   Jošt, M.; Lipovšek, B.; Glažar, B.; Al-Ashouri, A.; Brecl, K.; Matič, G.; Magomedov, A.; Getautis, V.; Topič, M.; Albrecht, S., Perovskite Solar Cells go Outdoors: Field Testing and Temperature Effects on Energy Yield. *Advanced Energy Materials* **2020,** *10* (25), 2000454.

103.   Afzaal, M.; Yates, H. M.; Walter, A.; Nicolay, S., Improved FTO/NiOx Interfaces for Inverted Planar Triple-Cation Perovskite Solar Cells. *IEEE Journal of Photovoltaics* **2019,** *9* (5), 1302-1308.

104.   Saliba, M.; Correa-Baena, J.-P.; Wolff, C. M.; Stolterfoht, M.; Phung, N.; Albrecht, S.; Neher, D.; Abate, A., How to Make over 20% Efficient Perovskite Solar Cells in Regular (n–i–p) and Inverted (p–i–n) Architectures. *Chemistry of Materials* **2018,** *30* (13), 4193-4201.

105.   Kim, J. Y.; Lee, J.-W.; Jung, H. S.; Shin, H.; Park, N.-G., High-Efficiency Perovskite Solar Cells. *Chemical Reviews* **2020,** *120* (15), 7867-7918.

106.   Michalska, M.; Surmiak, M. A.; Maasoumi, F.; Senevirathna, D. C.; Chantler, P.; Li, H.; Li, B.; Zhang, T.; Lin, X.; Deng, H.; Chandrasekaran, N.; Peiris, T. A. N.; Rietwyk, K. J.; Chesman, A. S. R.; Alan, T.; Vak, D.; Bach, U.; Jasieniak, J. J., Microfluidic Processing of Ligand-Engineered NiO Nanoparticles for Low-Temperature Hole Transporting Layers in Perovskite Solar Cells. *Solar RRL* **2021,** *n/a* (n/a).

107.   Yang, D.; Yang, R.; Zhang, J.; Yang, Z.; Liu, S.; Li, C., High efficiency flexible perovskite solar cells using superior low temperature TiO2. *Energy & Environmental Science* **2015,** *8* (11), 3208-3214.

108.   Taylor, A. D.; Sun, Q.; Goetz, K. P.; An, Q.; Schramm, T.; Hofstetter, Y.; Litterst, M.; Paulus, F.; Vaynzof, Y., A general approach to high-efficiency perovskite solar cells by any antisolvent. *Nature Communications* **2021,** *12* (1), 1878.

109.   Chiang, C.-H.; Wu, C.-G., A Method for the Preparation of Highly Oriented MAPbI3 Crystallites for High-Efficiency Perovskite Solar Cells to Achieve an 86% Fill Factor. *ACS Nano* **2018,** *12* (10), 10355-10364.

110.   Babayigit, A.; D'Haen, J.; Boyen, H.-G.; Conings, B., Gas Quenching for Perovskite Thin Film Deposition. *Joule* **2018,** *2* (7), 1205-1209.

111.   Xin, C.; Zhang, J.; Zhou, X.; Ma, L.; Hou, F.; Shi, B.; Pan, S.; Chen, B.; Wang, P.; Zhang, D.; Chen, X.; Zhao, Y.; Bakulin, A. A.; Li, Y.; Zhang, X., Defects Healing in Two-Step Deposited Perovskite Solar Cells via Formamidinium Iodide Compensation. *ACS Applied Energy Materials* **2020,** *3* (4), 3318-3327.

112.   Ji, R.; Zhang, Z.; Cho, C.; An, Q.; Paulus, F.; Kroll, M.; Löffler, M.; Nehm, F.; Rellinghaus, B.; Leo, K.; Vaynzof, Y., Thermally evaporated methylammonium-free perovskite solar cells. *Journal of Materials Chemistry C* **2020,** *8* (23), 7725-7733.

113.   Bishop, J. E.; Read, C. D.; Smith, J. A.; Routledge, T. J.; Lidzey, D. G., Fully Spray-Coated Triple-Cation Perovskite Solar Cells. *Scientific Reports* **2020,** *10* (1), 6610.

114.   Kim, Y. Y.; Yang, T.-Y.; Suhonen, R.; Kemppainen, A.; Hwang, K.; Jeon, N. J.; Seo, J., Roll-to-roll gravure-printed flexible perovskite solar cells using eco-friendly antisolvent bathing with wide processing window. *Nature Communications* **2020,** *11* (1), 5146.

115.   Trudeau, C.; Beaupré, P.; Bolduc, M.; Cloutier, S. G., All inkjet-printed perovskite-based bolometers. *npj Flexible Electronics* **2020,** *4* (1), 34.

116.   Howard, I. A.; Abzieher, T.; Hossain, I. M.; Eggers, H.; Schackmar, F.; Ternes, S.; Richards, B. S.; Lemmer, U.; Paetzold, U. W., Coated and Printed Perovskites for Photovoltaic Applications. *Advanced Materials* **2019,** *31* (26), 1806702.

117.   Surmiak, M. A.; Zhang, T.; Lu, J.; Rietwyk, K. J.; Raga, S. R.; McMeekin, D. P.; Bach, U., High-Throughput Characterization of Perovskite Solar Cells for Rapid Combinatorial Screening. *Solar RRL* **2020,** *4* (7), 2000097.

118.   Giordano, F.; Petrolati, E.; Brown, T. M.; Reale, A.; Carlo, A. D., Series-Connection Designs for Dye Solar Cell Modules. *IEEE Transactions on Electron Devices* **2011,** *58* (8), 2759-2764.

119.   Cai, L.; Liang, L.; Wu, J.; Ding, B.; Gao, L.; Fan, B., Large area perovskite solar cell module. *Journal of Semiconductors* **2017,** *38* (1), 014006.

120.   Gao, L.; Chen, L.; Huang, S.; Li, X.; Yang, G., Series and Parallel Module Design for Large-Area Perovskite Solar Cells. *ACS Applied Energy Materials* **2019,** *2* (5), 3851-3859.

Appendix A

A. Perovskite solar cell experimental testing platform in a form of solar panel

A.1 Introduction and motivation

After a decade of intensive research, in 2021 perovskite solar cell (PSC) technology entered commercialization phase. However, a full market debut is yet to be realized, as the first perovskite products are limited to specialized applications. To date only a few perovskite modules were reported, moreover the fabrication details were only briefly detailed.[102] There is a noticeable underreporting in designing, processing and testing of such perovskite concepts. The PSC panel technology starts evolving and thus requires intensive efforts and tests to describe long-term behavior of interconnected PSCs in real-world application. Most of research communication focuses on fundamental material or fabrication improvements, demonstrating their results using simulated conditions, small sample area and size.[102] Herein, it is demonstrated how to build a perovskite solar panel that serves as the device aging station with a typical research size module using commonly available in research environment techniques. It is presented in great detail how the concept of the perovskite solar panel can be realized and tested in real-world conditions without the need to use an expensive climatic chambers. Importantly, this work provides a starting point for the broader research community who look to enter PSC research or want to improve their data output with an inexpensive tool that can serve as a great testbench equipment for further developments. This chapter also demonstrates the concept of perovskite solar panel realization using a modular techniques that reach beyond a single PSC sample. In this chapter a step-by-step protocol of perovskite prototype panel fabrication is delivered. This work intention is to provide, a simple, laboratory-based instruction for fabrication of the modules.

A.2 System design and protocol

Our module prototype consists of inter-connected 224 PSCs (with a total active area of ~448 cm^2). The perovskite solar panel prototype works as an inexpensive, real-world aging station for direct performance data acquisition. The modular design allows for easy size expansion and multiple study of PSC operation under load in various connections (series, parallel or hybrid). Furthermore, we demonstrate conceptual use by employment of the same PSC modules with different type of electrodes, gold (Au) and carbon (C). See figures below for more details on realization of our panel prototype.

A.2.1 Substrate preparation
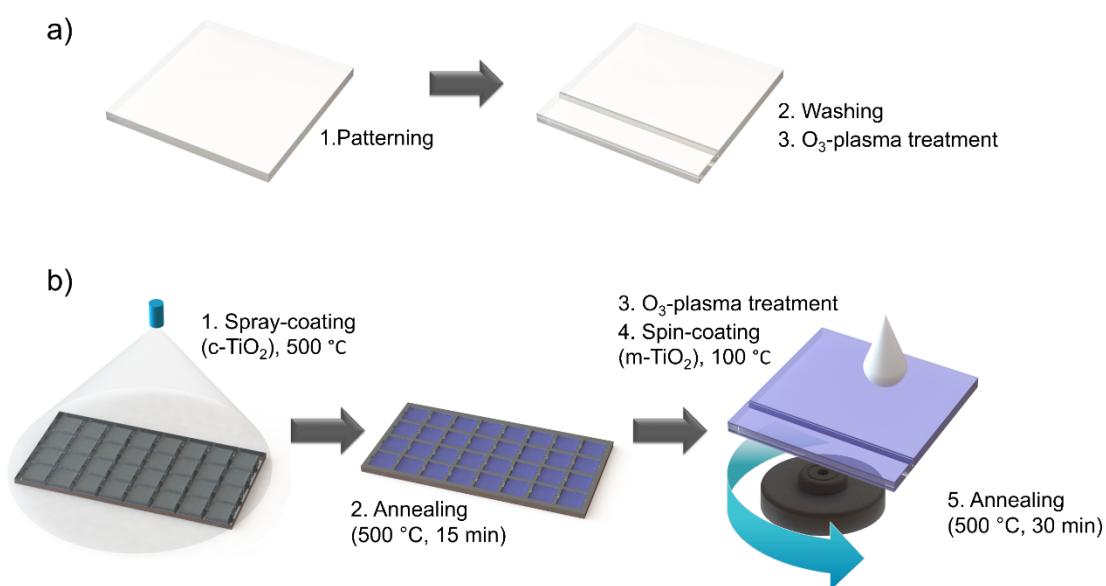
Figure A1: Substrate handling and ETL deposition. a) FTO glass preparation. b) Deposition of the TiO2 layers.

The fabrication process starts with the application of the chosen device pattern onto a substrate. For perovskite solar cells a typical glass substrate will be covered with either FTO (fluorine-doped tin oxide) or ITO (indium-doped tin oxide) serving as bottom electrode. Each

cell consists of a working and counter electrode, which need to be separated to prevent from short-circuit. However, depending on a design (and more importantly, PSC working area), one substrate can hold multiple cells. A pattern can be made using various methods involving use of, for example, laser or etching solvents. In this study, we have used commercially patterned FTO substrates, with each substrate carrying one solar cell of ~2 cm^2 working area.
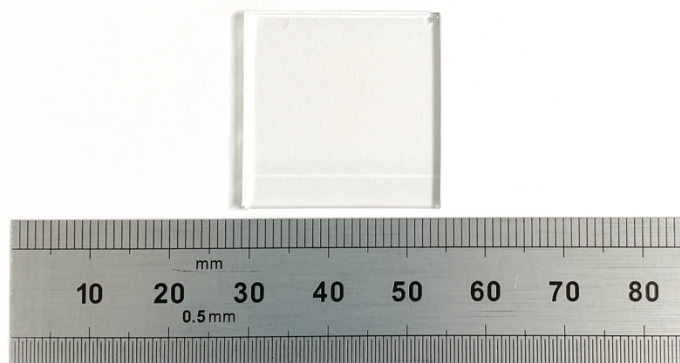
Figure A2: A commercially ordered FTO glass substrate with an etch line that defines the top electrode connection area and the cell position on the substrate.

The next step is the substrate cleaning. Appropriate cleanness of the substrates is crucial for the final performance of the solar cells. There are various washing procedures involving, for instance, the use of acids and bases,[103] but more often detergents and organic solvents.[104] The typical laboratory procedure for the substrate (**Figure A3**) consists of the following steps:

1. Washing in detergent (Hellmanex®) 2% water solution in ultrasonic bath for 15 min.

2. Washing (x2) in MilliQ water in ultrasonic bath for 15 min (or till no detergent residuals are noticeable).

3. Washing in acetone in ultrasonic bath for 15 minutes.

4. Washing in isopropanol (IPA) in ultrasonic bath for 15 minutes.

5. Drying the substrates with N_2 blow

6. Prior to the deposition of the first layer, O_3-plasma treatment for 15 minutes (Figure 67)
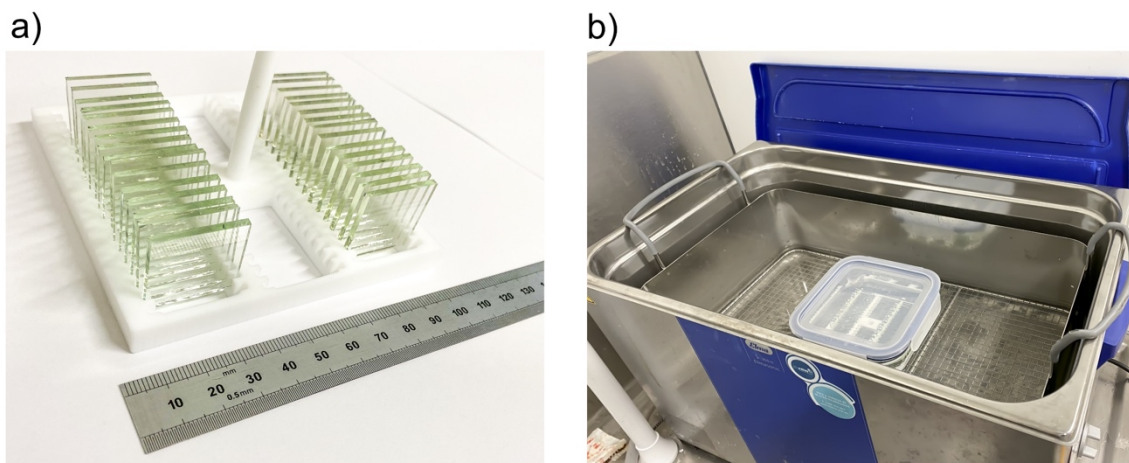
Figure A3: Wet-cleaning of the glass substrates. a) FTO glass on a 3D-printed holder. b) Glass substrates in a holder immersed in a detergent during ultrasound treatment.
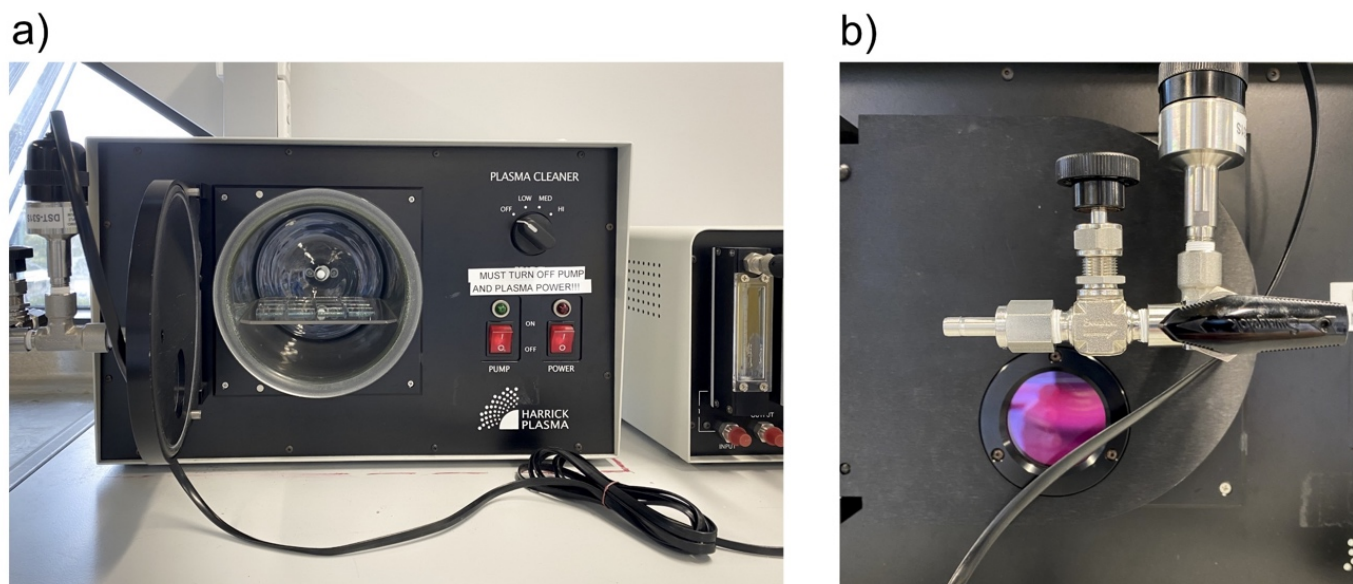
Figure A4: Plasma treatment for organic residue removal and surface activation (allowing better wettability).

A.2.2 Deposition of bottom charge transporting layer

Dry and plasma-treated substrates were ready for the deposition of the first charge transporting layer (**Figure A4**). In case of fabricating the "standard" n-i-p devices, the first charge transporting layer (CTL) is the electron transporting material (ETM), while in the "inverted" p-i-n devices, the first deposited is the hole transporting material (HTM).[105] This protocol focuses on the n-i-p architecture, but previously a procedure for the p-i-n PSC fabrication was presented, and such inverted devices can also be applied in a solar panel.[106]

Here, the SnO_2 was used for 1 batch of 16 devices, thus please see Experimental Methods in Chapter 3 for SnO_2 fabrication details. For the rest of the substrates TiO_2 was employed as the bottom electron transporting layer (ETL) for PSCs, due to its band gap position closely matching the perovskite, and high optical transmittance.[107] The common approach of TiO_2 fabrication involves 2 steps; formation of a thin compact film, followed by deposition of a thick mesoporous layer. The compact layer (c-TiO_2) uniformly covers the FTO surface, while the porous one (m-TiO_2), due to large active area, is later infiltrated by the perovskite, improving the charge extraction mechanism. The ~20 nm thick TiO_2 compact layer is formed by spray deposition of a mix containing 1 mL of titanium diisopropoxide bis(acetylacetonate) (TAA) solution in 4.75 mL of IPA on FTO substrates placed on a hotplate (set to 500 °C). After the deposition, the substrates were left on the hotplate for 10-15 minutes to ensure formation of the crystalline anatase phase of TiO_2. Then the substrates were left to cool naturally to prevent cracking. Prior to deposition of the m-TiO_2 the substrates were plasma-cleaned again to remove any organic residuals from the surface. The TiO_2 paste is diluted in anhydrous ethanol (EtOH) 1:9 and stirred for 1 hour. Finally, the dispersion was spin-coated onto the FTO/c-TiO_2/m-TiO_2 substrates at 6000 RPM for 30 seconds and placed on a hotplate set to 100 °C to dry-off the solvent. The dried films are then annealed at 500 °C for 30 minutes. See Figures A5-A7 for photos. The prepared films are ready for perovskite precursor solution deposition.
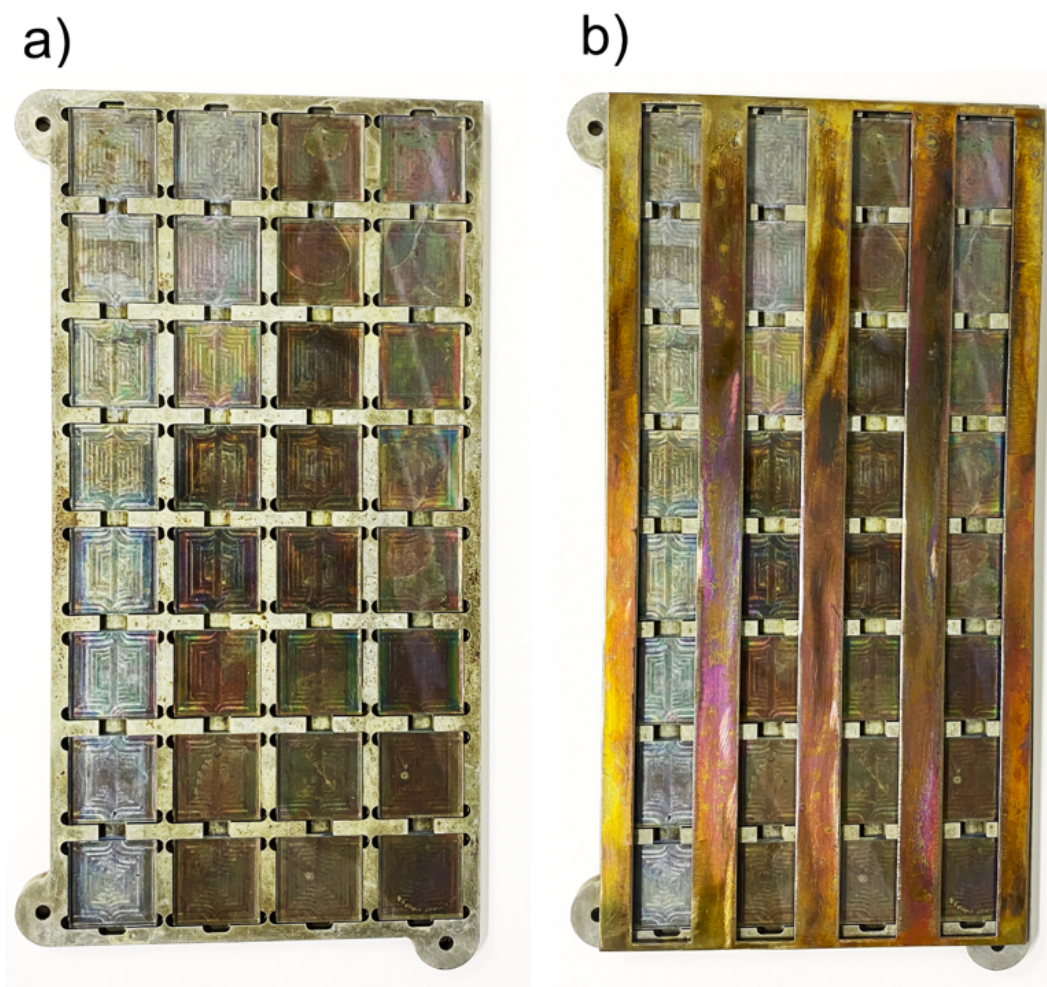
Figure A5: Marine grade stainless steel plate for equal temperature gradient with (a) rebates cut to the substrate size and depth, and (b) stainless steel mask that allows for masking the top electrode contact area. The design STEP file can be shared by the author upon request.
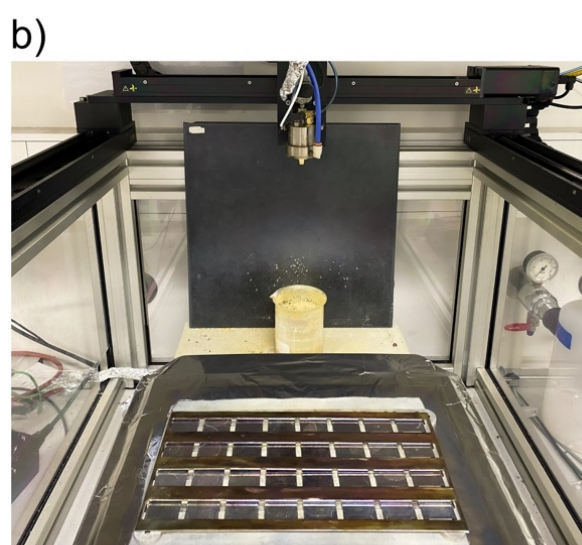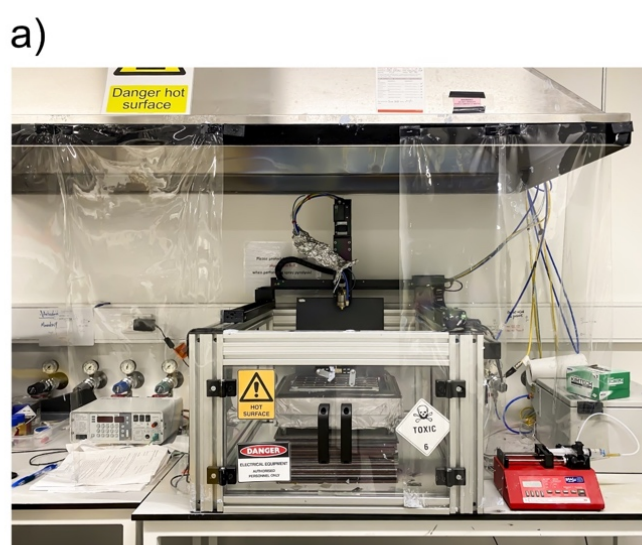
Figure A6: Ultrasonic automated commercial spray-pyrolysis system for transparent compact TiO2 layer. The system allows number of passes, nozzle pressure, height and PID controlled hot -plate temperature (including the ramping settings) to be set.

a)

b)
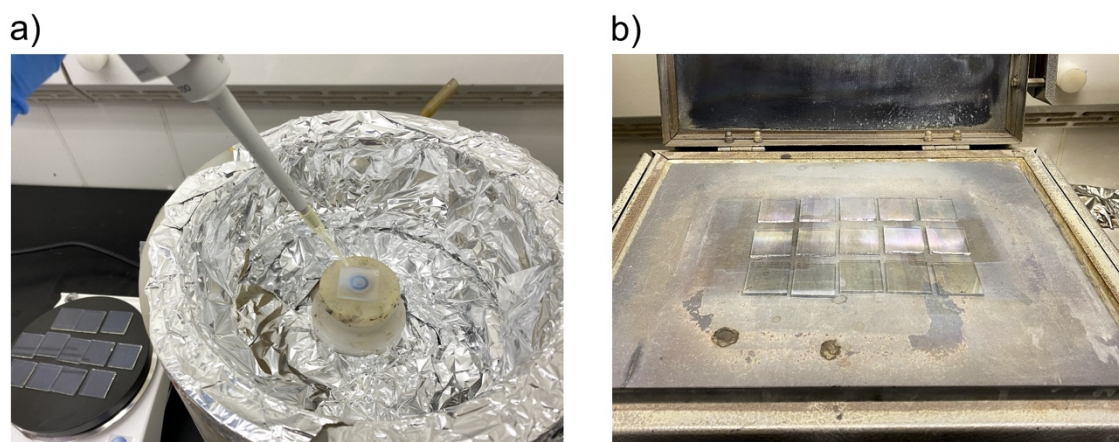
Figure A7: Spin-coating and air annealing (500 °C) of the mesoporous TiO$_2$ layer.

A.2.3 Perovskite layer deposition

Over the years, various perovskite deposition approaches have been developed, such as the antisolvent method,[108] gas-quenching,[109-110] 2-step deposition,[111] evaporation,[112] spray-coating,[113] or printing.[114-116] For small-scale fabrication, solution-processing is the most popular-method-owing to its simplicity. This fabrication process employs the antisolvent method (Figure A8).
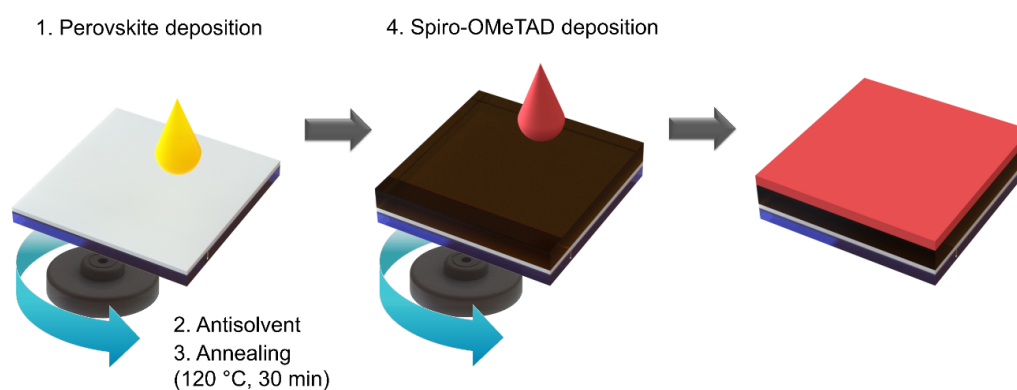
Figure A8: 2-step deposition: First, spin-coating of perovskite precursor, followed by antisolvent, annealing, and spiro-OMeTAD spin-coating.

The mixed cation halide $Cs_{0.05}FA_{0.81}MA_{0.14}PbI_{2.55}Br_{0.45}$ perovskite solution was prepared under inert conditions by dissolving the precursor salts in DMF:DMSO (4:1) solvent mix. The FTO/c-TiO_2/m-TiO_2 substrates were plasma-cleaned for 5 min, then transferred to N_2-filled glove box. 50 μL of the perovskite solution was cast onto a substrate and spun at 1000 rpm (200 RPM s^{-1} acceleration) for 10 seconds, then at 6000 RPM (800 RPM s^{-1} acceleration) for 20 seconds. At 5 seconds before the end of the second step, 150-200 μL of chlorobenzene (CBZ) was pipetted onto the perovskite film to induce crystallization. The substrate is then transferred onto a hot plate and annealed at 120 °C for 30 minutes (the formed perovskite film is typically dark-brown and has a reflective, mirror-like surface, see Figures below). Then the substrates are cooled down to room temperature and the last CTL can be deposited. A Spiro-OMeTAD solution was prepared by mixing 73 mg of Spiro-OMeTAD with 5.4 μL TBP, 8.4 μL Co complex and 17.4 μL LiTFSI in 1 ml of CBZ. The HTL was deposited at 3000 RPM for 30 seconds. No post-treatment was required. Before finishing the devices with top contacts, the edge of each cell was removed to ensure the correct connection to both (working and counter) electrodes. We used a solvent method, where a mix of DMF:CBZ:IPA (1:1:1) was used to wipe off the deposited films, typically with soaked cotton swabs.
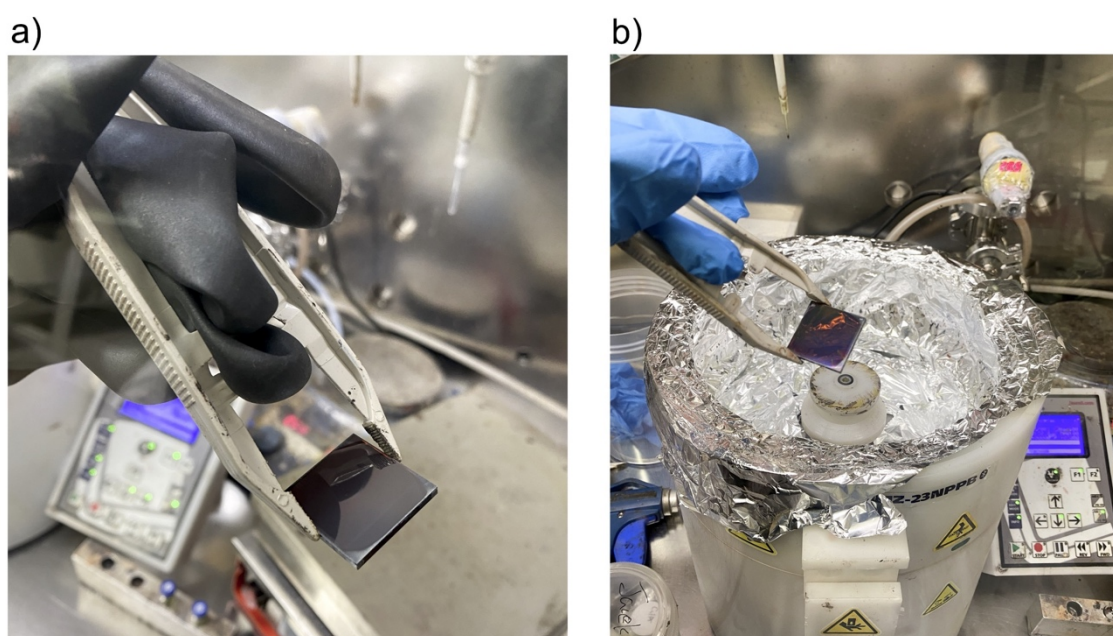
Figure A9: a) Perovskite film after annealing. b) Spiro-OMeTAD layer formed on the perovskite film.

A.2.4 Panel realization

The PSCs are completed by deposition of the top contacts followed by encapsulation. Typically, metal electrodes, such as gold (for n-i-p structures) or silver (for p-i-n), are evaporated. Carbon films can be deposited by pressing or printing. Our protocol uses a Au thermal evaporation and C cold-pressing method. All Au substrates were covered with "shadow masks" and placed on a metal array then transferred to the thermal evaporator containing the gold source. Gold evaporation is conducted at high vacuum (~6x10^{-6} Torr) to thickness ~80 nm.
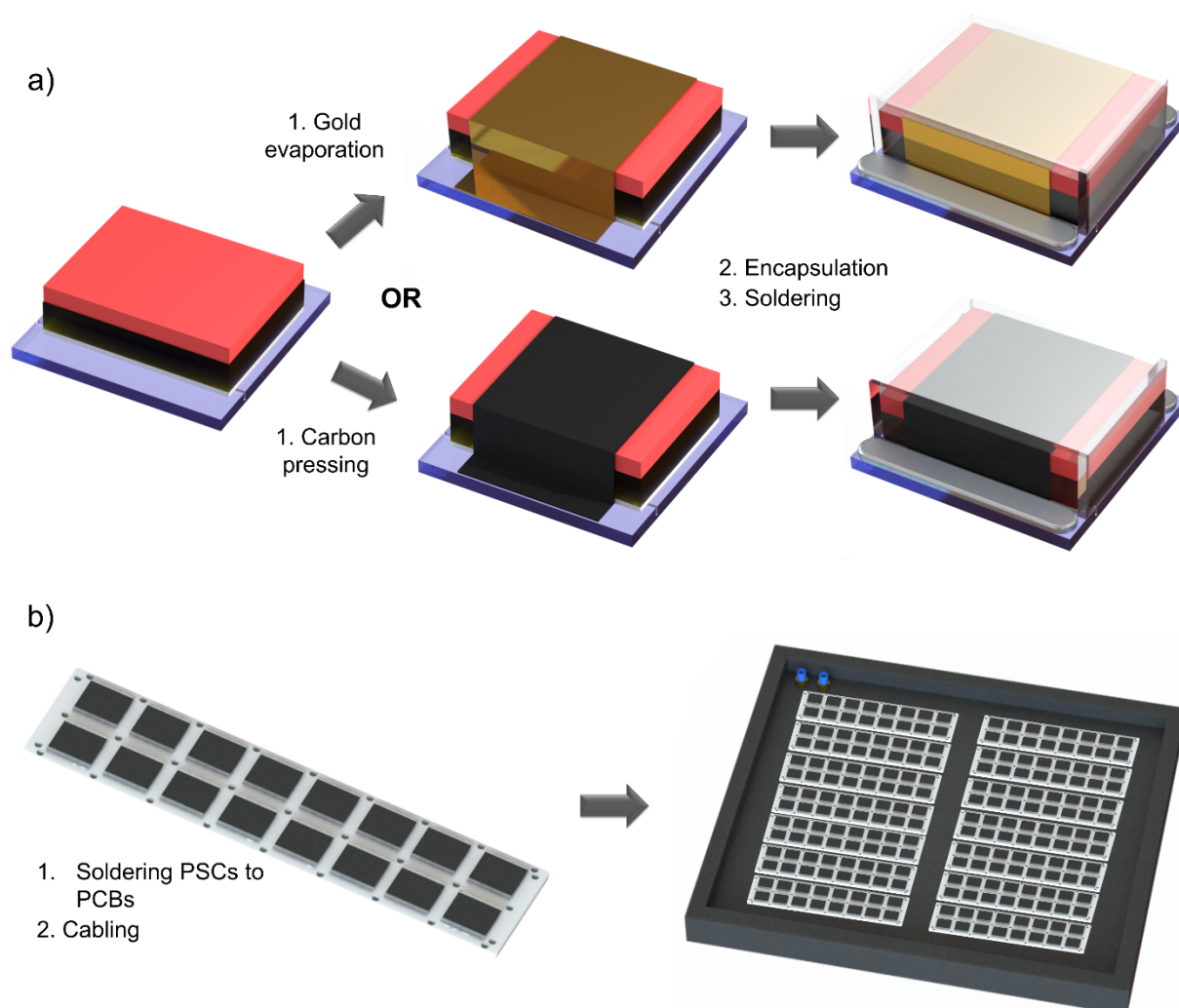
Figure A10: The solar panel completion. a) Top electrode deposition, encapsulation, and soldering of PSCs. b) Soldering of the single PSCs to PC boards and their assembly in the panel.

A.2.4.1 Gold evaporation

The Au evaporation method is a standard laboratory sample preparation method, it can be viewed in the **Figures A11-12**

a)   b)
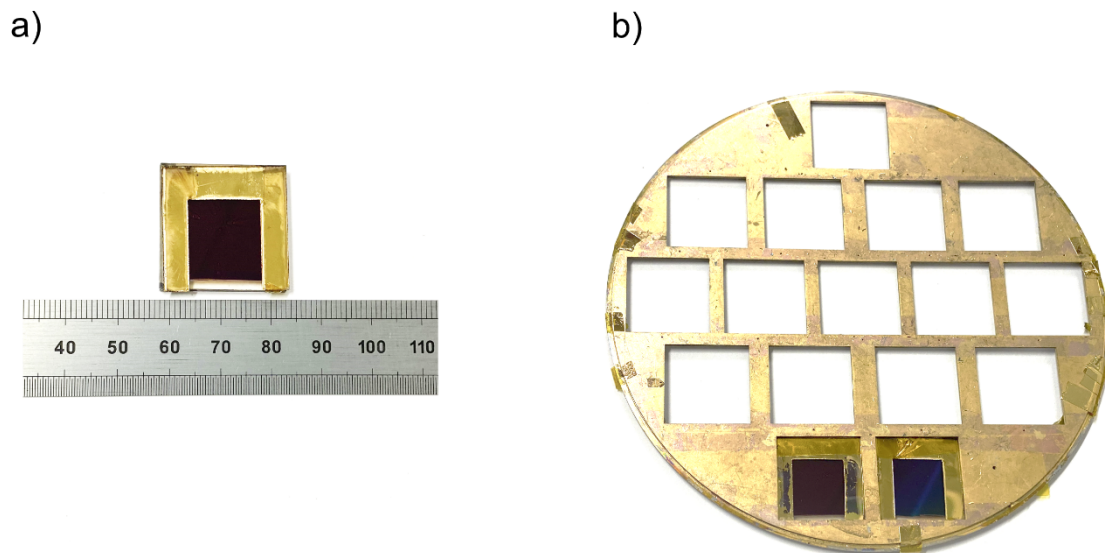
Figure A11: Evaporation of metal electrode. A) Solar cell is masked to expose the area designated as top electrode whereas the bottom electrode area is masked to avoid short-circuit. B) Masked solar cells are placed into the evaporation jig.
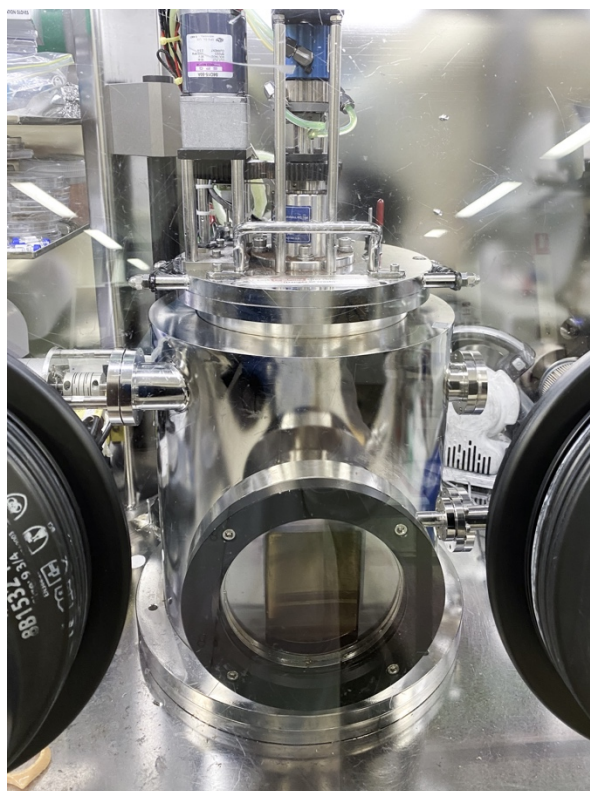
Figure A12: The metal evaporator inside of the glovebox.

A.2.4.2 C-pressing method

The C-cold pressing method contains of the steps that can be viewed in the **Figures A13-14**.

a)

b)

c)

d)

e)

f)

g)

h)

i)
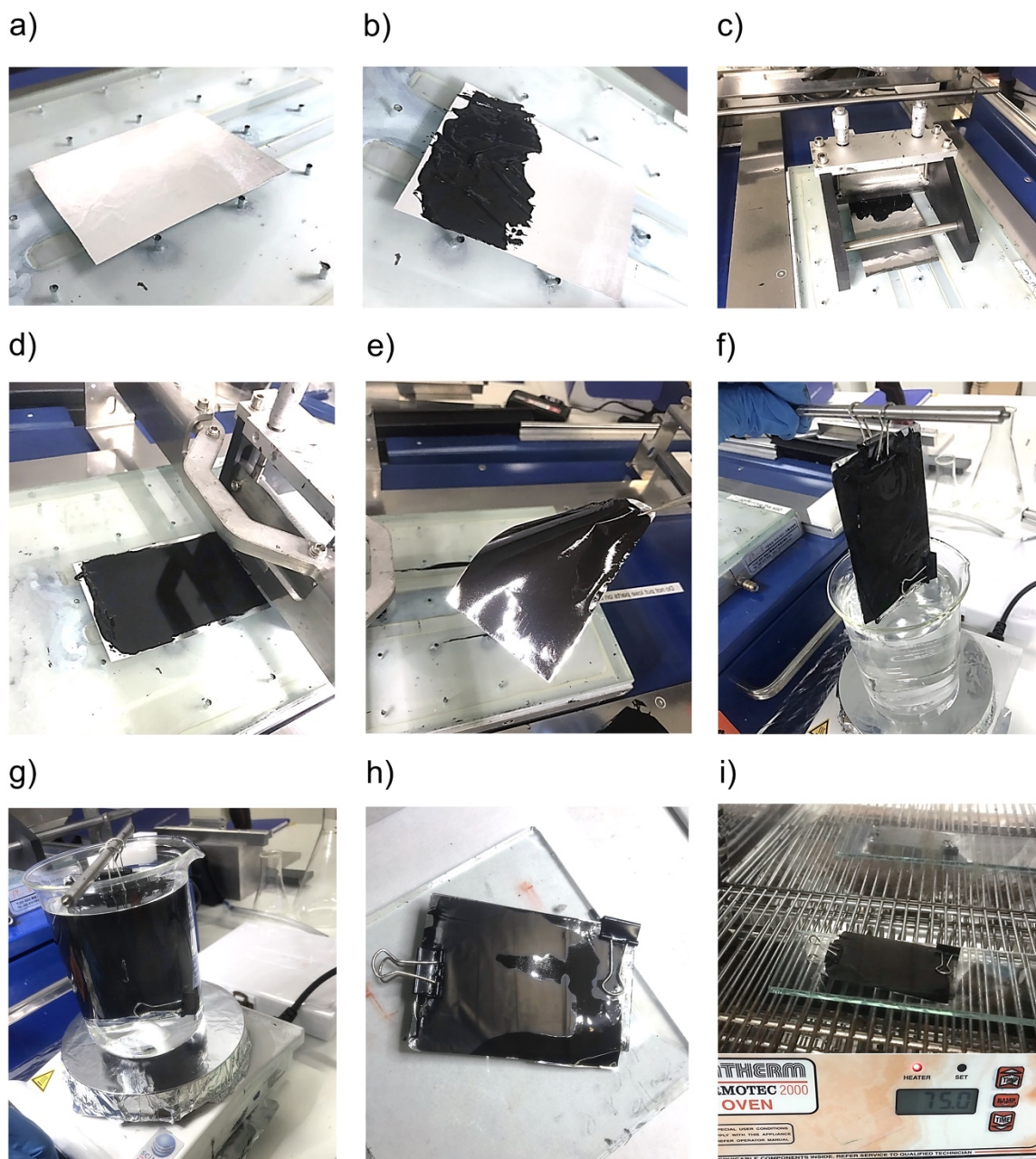
Figure A13: Carbon electrode preparation. a) Cleaning of the aluminum foil with ethanol. b) Carbon paste spread on the pre-cleaned Al foil. c) Doctor-blading. d) Carbon paste evenly deposited on the Al foil. e) Flexible Al foil with the carbon film. f) The electrode is mounted to a glass slide and immersed in ethanol. g) 30 min of stirring at room temperature. h) Air-dying at RT. i) Drying at 75 °C for 2 h.
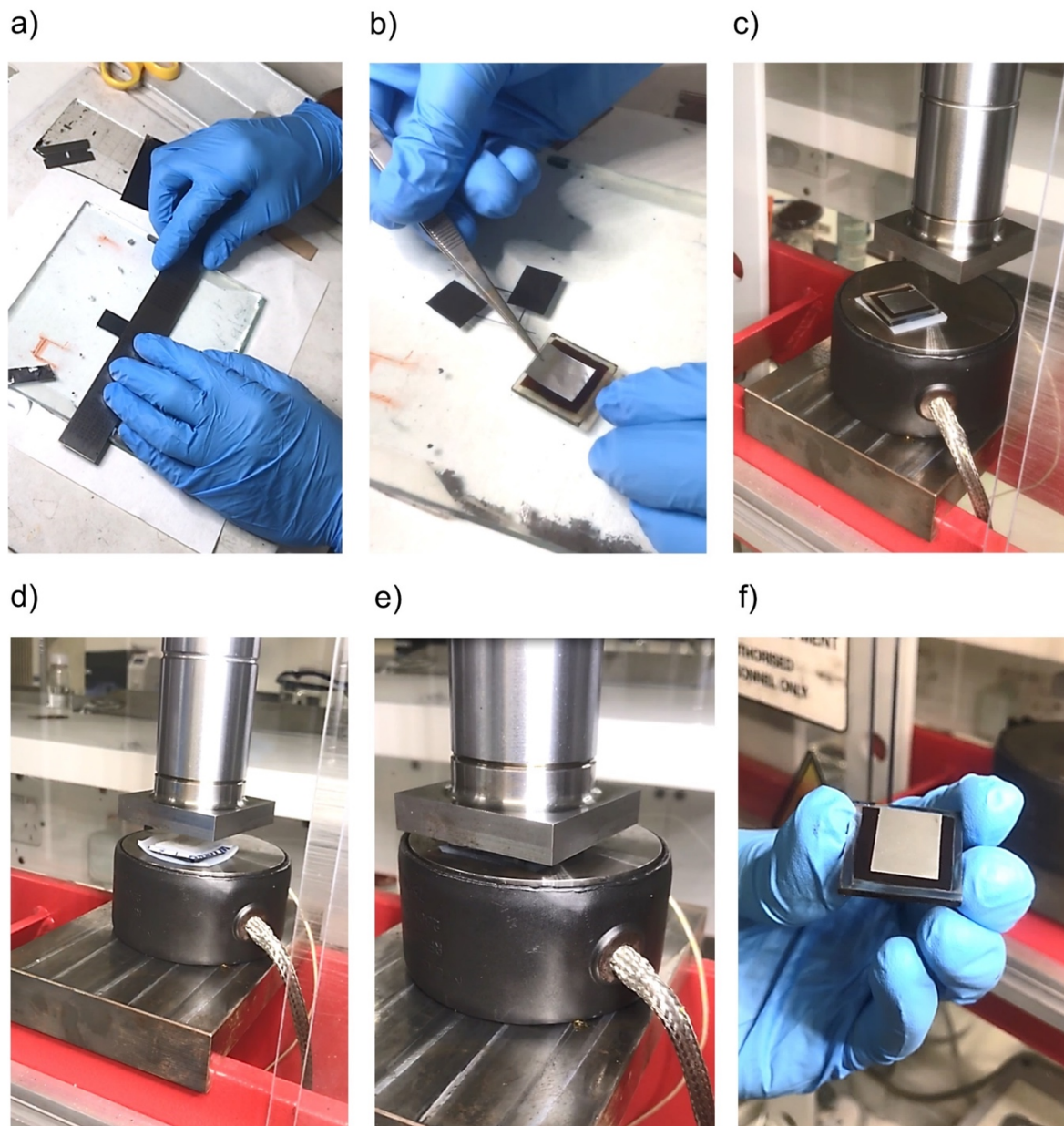
Figure A14: Carbon electrode deposition on the perovskite solar cells. a) Cutting of the dried electrodes. b) Placing the electrodes on the PSCs. c-d) Mounting the PSC into a hydraulic press. e) Pressing at 20 MPa for 2 min. f) Final Al-supported C electrode on a PSC.

A.2.4.3 Module encapsulation

The final devices were aimed to have the electrode size as close as possible to ensure the same active area. The side-by-side comparison can be seen in **Figure A15**.
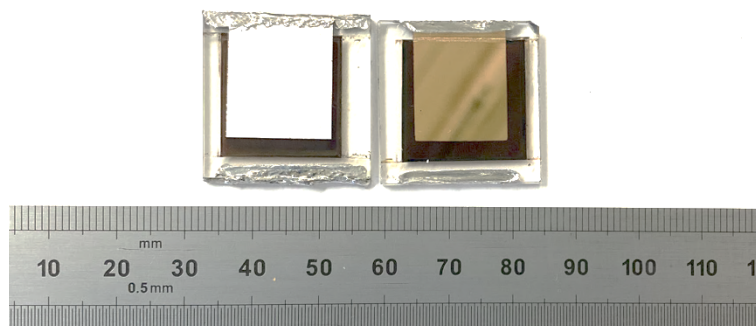
Figure A15: Complete perovskite solar cells with top contact.

The next step was to build the modules of 8 PSCs interconnected in series on one PCB board. For the encapsulation process the PDMS casting method was used. The PCB boards are commercially made to the order from dual-sided copper/FR4® 1.6 mm plates. Upon receival, they are cleaned with similar steps to the one used for glass (besides water and detergent), dried in 100 °C in N_2, and left under vacuum for 1 hour. The specific design of the PCB boards allows for full exposure of solar cell and thick (~1.6 mm) encapsulation inside of the cavity that is created once the solar cell is soldered into the PCB board.
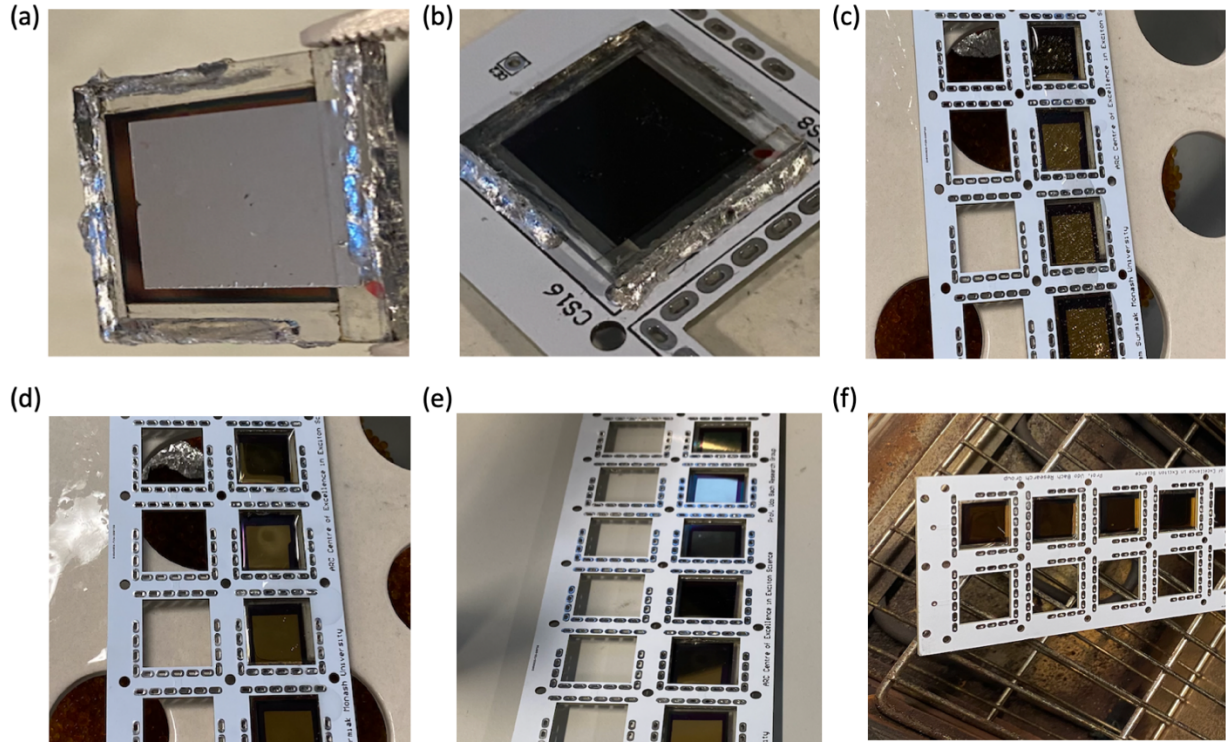
Figure A16: Modular design for the data acquisition, 8 solar cells in one rung in series connection. (a) Top and bottom electrodes are soldered and solder is distributed around the edges (ultrasonic soldering iron is required to solder to glass edge) (b) the solar cell is placed in the position and soldered around, (c) the pre-mixed PDMS with curing agent is casted on the soldered rung of 8 devices, the PCB board together with top of the solar cell creates a small cavity that is filled with PDMS, (d) the mixed, uncured casts in the cavities are placed into vacuum dome for vacuum treatment (removes air bubble, allows the PDMS to penetrate into the FR4 PCB boards through the cutout edge), (e) the vacuum dried PDMS-filled modules are cured in the electric oven for 60 minutes at 50 °C.

A.2.4.4 Panel enclosure

In total 28 PCB boards with 56 rungs of 8 solar cells connected in series were exposed to 12 week test. The commercially cut and provided solar panel frame (Tindo Solar Pty Ltd) was used in order to enclose the modules. The enclosure was filled with N_2. The bottom of the frame was chosen to be 8 mm double-side metal bonded high density polyethylene (HDPE) board, and the top was 5 mm acrylic. The modules were laid next to each other and the cables were run alongside to enable access to each rung. Unlike the commercial solar panels, these

rungs were not connected into a single cable outlet. The cables needed to be easily accessible and had the same length to ensure similar series resistance.
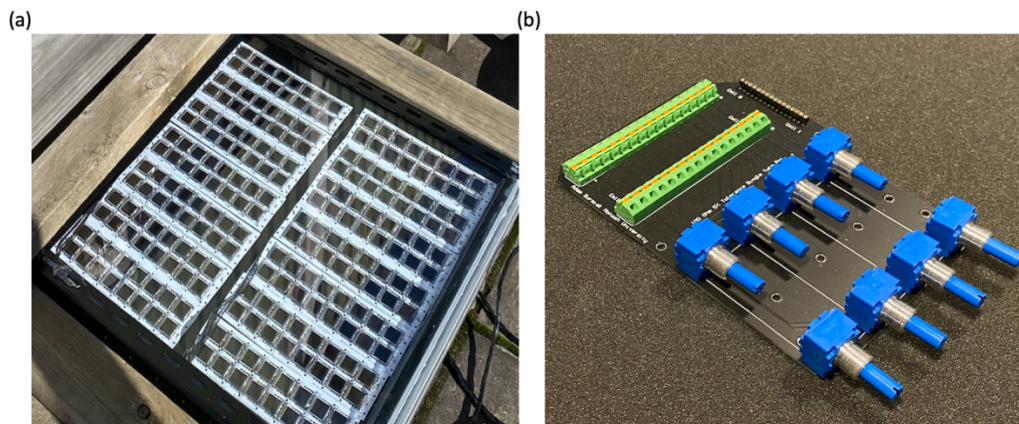

Figure A17: The solar panel prototype built out of 448 devices in the form of aging station in real-world application.(a) A view of solar panel mounted on the top of Monash University Building 27 Clayton Campus rooftop, the panel was not tilted due to the safety policies. (b) Example of the ballast potentiometers developed by author used to keep solar cells in ~MPP if not measured. Due to circumstances in Victoria constant monitoring/access was not permitted.

A.3 Tests and data acquisition propositions

The protocol presented in this paragraph remains a proposition of the potential way forward. Depending on the particular study, different approaches can be employed. From the engineering perspective, the visible comparison between the degradation mechanisms was chosen to be elaborated.

A.3.1 Initial characterization of the solar cells

For this study 23 solar cells with each type of the electrode were selected and measured under the 1 Sun solar simulated light. The purpose of this test was solely to establish the overarching beginning efficiency. This permits for the estimation of the potential maximum power output from the panel. It can be seen that the samples with Au electrodes exhibited ~0.5 % higher average PCE than the C based samples. The performance distribution can be seen in the Figure 84.
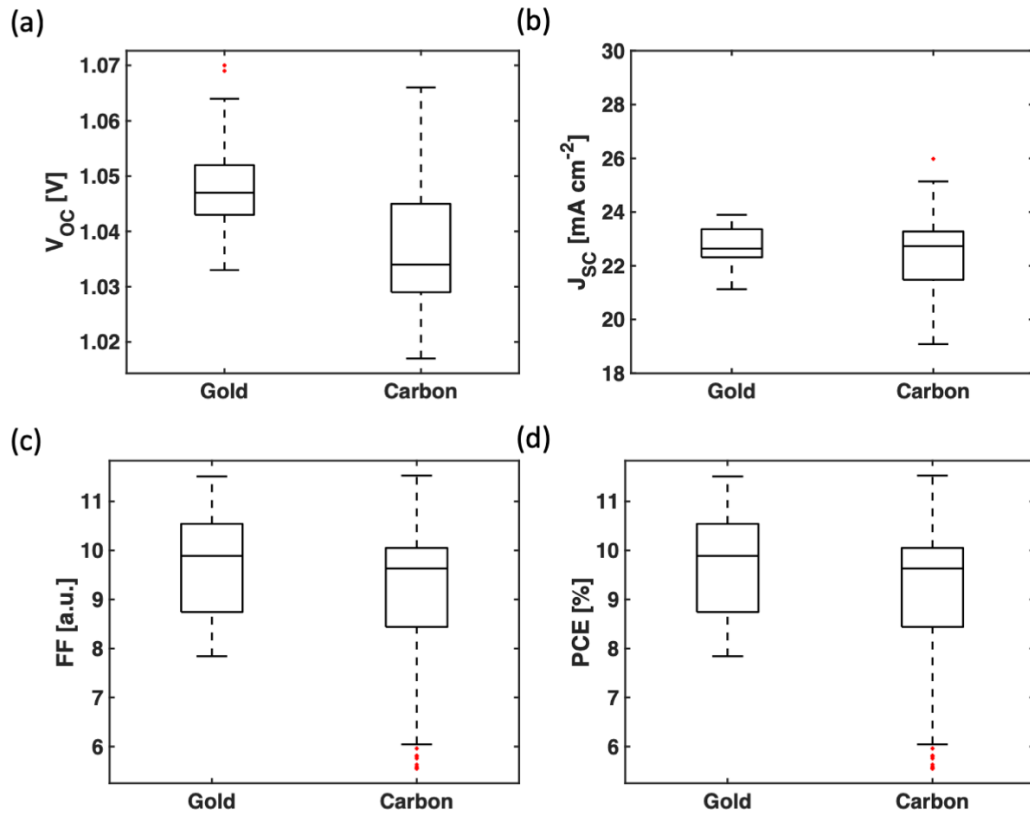
Figure A18: The initial performance extracted from 92 randomly selected samples of gold- and carbon devices under 1 Sun illumination. The area of each PSC was shadow masked to ~2 cm². Author notices that the irregular size of electrodes can contribute to the overall current due to the edge effects.[117]

A.3.2 Characterization of the module

From similar case studies,[118-120] it is understood that the characterization of interconnected modules is realized through the power tracking mechanisms. In this study the modules were initially tested for their current output under 1 Sun condition for seconds.
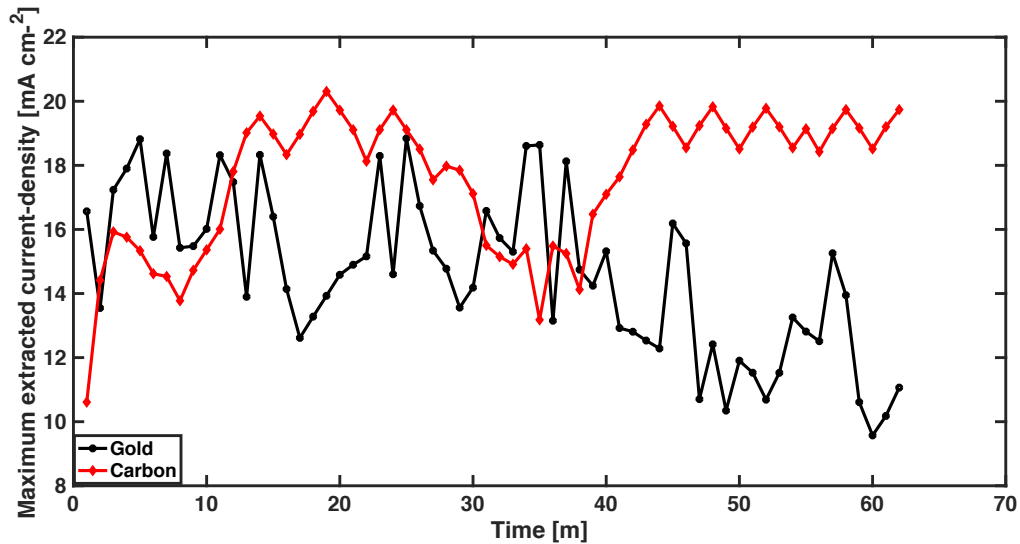
Figure A19: The initial current-density extracted from devices made with gold and carbon electrodes. Each rung consists of 8 devices, interconnected in series. 1 Sun conditions (unencapsulated) for 1 hour.

The gold electrode samples initially exhibited higher performance (for approximately 10 minutes). For next 30 minutes the carbon electrode was performing better, however at around 35 minutes into the test the current density of gold lowered to ~12 mA cm^{-2}/rung of 8 devices, the carbon run stabilized after 1 hour at around 19 mA/rung of 8 devices.

A.3.3 Long term data acquisition example

For the long term testing, the panel was mounted on the rooftop. For the measurement on the physical roof the author chosen a sunny day and allowed the measurement to run for 160 minutes. The figure A20 present a sample outcome of the current generation with the perovskite modules (8 carbon and 8 gold samples). The current measurement protocol was realized with the programmable source-measure unit (Ossila X200) using 2-wire sense method. Each module has been equipped with two wires that allow for easy access and the data extraction.
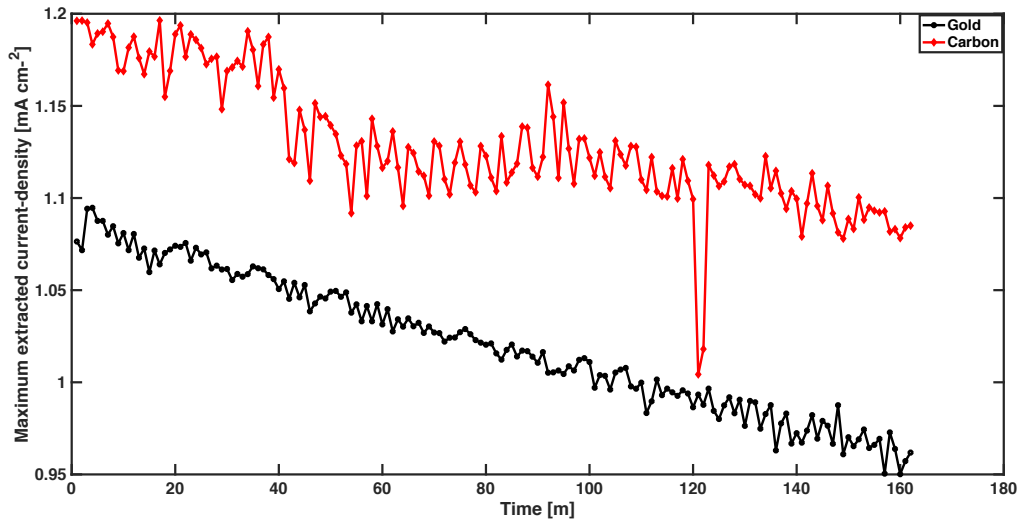
Figure A20: A sample comparison of current extraction from carbon- and gold-based rungs of 8 devices.

The current density oscillated in case of Au and carbon samples oscillated at around 1 mA/rung of 8 devices, overall the carbon-based samples exhibited better performance than the gold ones in this particular PCB module.

A.4 Conclusions and future outlook

In this work a step-by-step engineering solution for perovskite solar panel in the form of long-term aging station was presented. All the devices were based on spin-coated $Cs_{0.05}FA_{0.81}MA_{0.14}PbI_{2.55}Br_{0.45}$ perovskite film. The long-term testing station allows for inexpensive, research scale application of the perovskite solar cell devices. The real-life realization of the solar panel is a non-trivial task and requires a lot of carefully chosen steps. Typically, the equipment and resources spent on the novel material panel realizations limit the research and hence there is a significant gap on the panel realizations. Moreover, the expensive aging stations and solar simulators do not provide all environmental conditions, for example: heavy rain/hailing/wind, staining/bleaching, vibrations are not part of the laboratory based tests. Moreover, in this work the overall cost of used materials is estimated on AUD1000 which is multiple times less than the commercial environmental chambers. The resulting efficiency of solar modules provides the details of impact of multiple conditions; amongst the others: uncertainty of the irradiation at the particular moment of the test, losses resulting from manual handling, multiple connections between the devices and SMU, air-processing of the devices, random effects induced by a manual spin-coating, the acrylic enclosure losses such as reflections of diffusion, series resistance of leads used for the test. This work shows that the collaborative efforts (in total 14 PCBs were populated by 7 independently working researchers) allowed for fabrication of reasonably similar devices in terms of the performance. In future, a multiple follow up studies can be proposed from this initial work, for example: 24/7 performance monitoring, the device size increase, different deposition methods, different substrates, various encapsulation pathways, influence of various enclosures on the performance.

Appendix B

Author permits the CAD and PCB design to be reasonably requested by the non-for-profit entities and provides non-for-profit collaborative consultation related to the design and realization of PV characterization tools.

B. Printed Circuit Boards
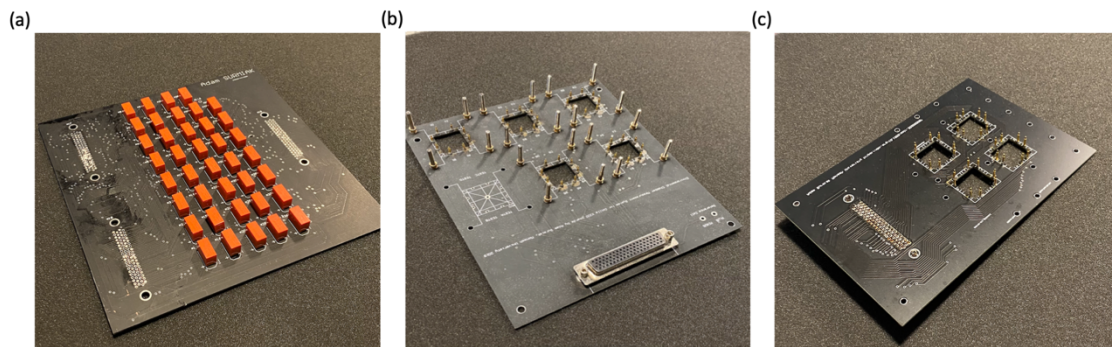
B.1 Solar Device Characterization Testing setups

Figure B1: Printed circuit boards used at Renewable Energy Laboratories Monash Univeristy developed by the author. (a) relay board for simultaneous physical switching of 78 connections. The relay cannot be based on the semiconductor, it must be physical connection. Author points that for 2-wire measurements all the copper path size and weight has to be equal to introduce similar series resistance. (b) long term aging board that allows for screw-mounting of the solar cells. Author points that black finish of the majority of PCB is non-UV resistant and requires package to avoid bleaching. (c) Soft, spring loaded connections allowing for simultaneous 4-wire sense measurements. This particular board allows for clamping mechanism from the top due to the cut-outs or for contacting the solar cells developed by the author from underneath.
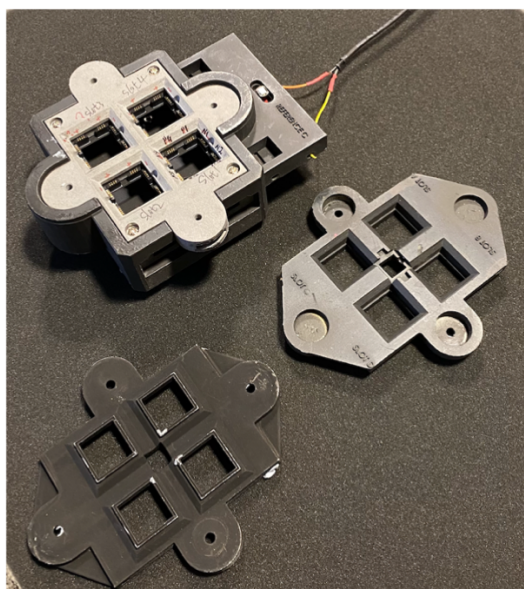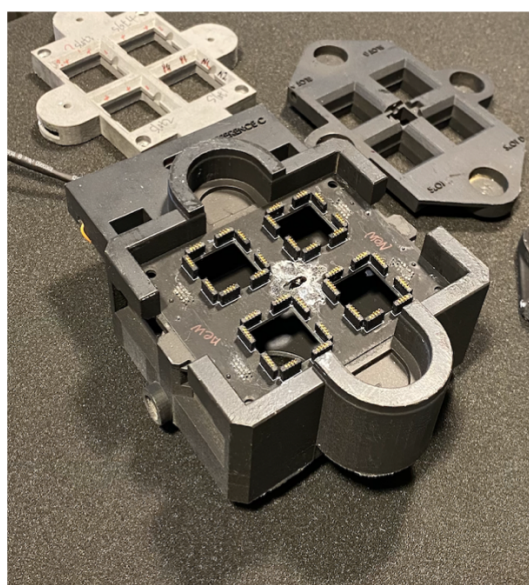
Figure B2: 16-channel potentiostat XY-stage measurement chamber. (a) The overview of one of the first prototypes. (a) the travelling stage with replacement positioning jigs (permitting the reference Si cell to be located centrally). The slot allows for the substrate to be positioned with a standard laboratory tweezers. The shadow mask is placed on top of the substrate and the clamping lid ensures the correct positioning. The neodymium magnets sitting in the pockets force ideal position at each time and provide enough pressure on the pins to connect the device. The soft, spring-loaded pins allow for the 4-wire sense measurements and have double-redundancy (8 pins interconnected into 4 measurement points). (b) View without the positioning jig and clamp of one of prototypes. The gas tube connector visible there delivers uniform flow to all substrates from underneath. The space there allows for temperature and humidity measurement. This modular design allows for multiple enhancements and expansions. Author shares that alumide, nylon or PEEK were found to sustain extensive heat and 1 Sun light exposure.
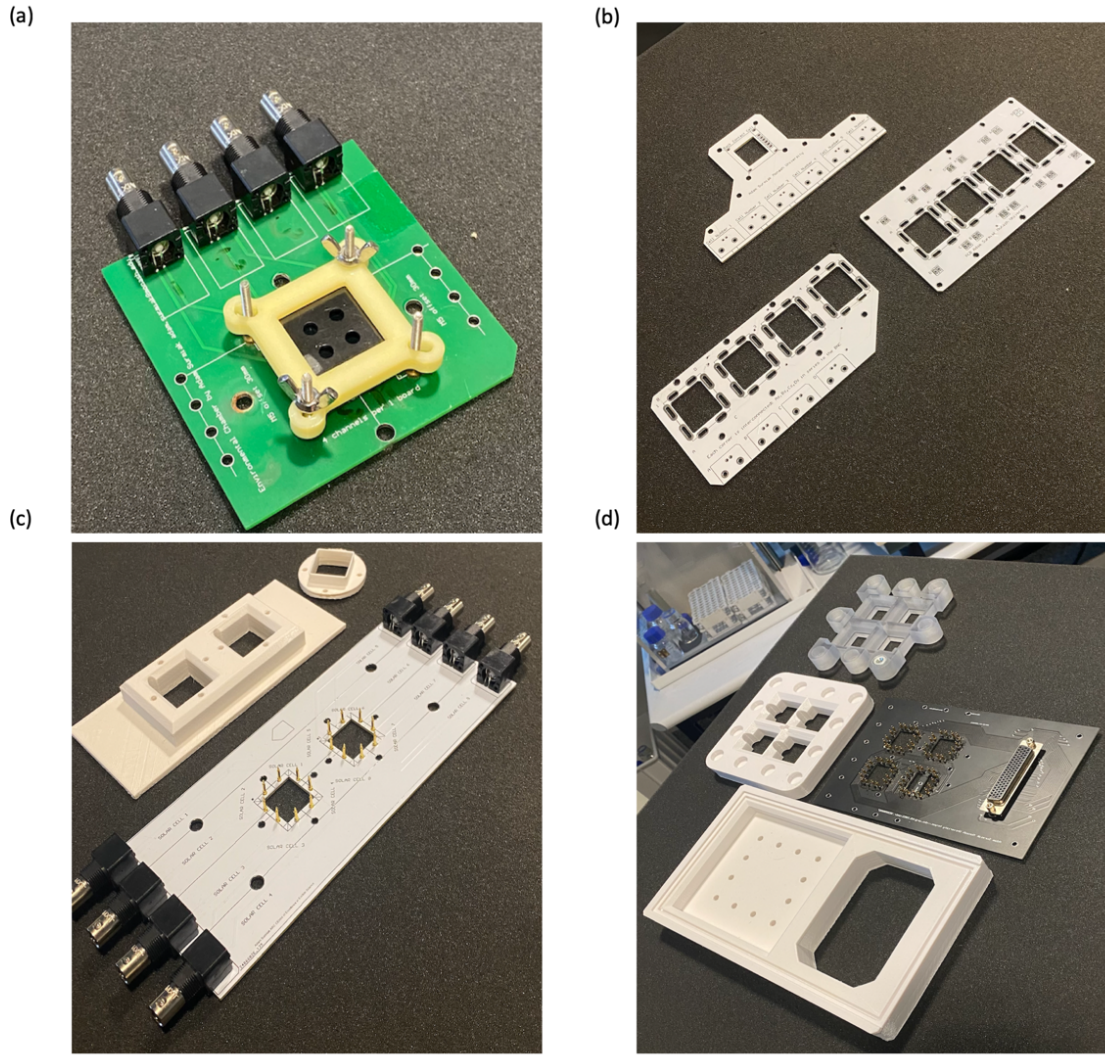
Figure B3: Various design used throughout the study. (a) one of the characterization extensions with mounted and shadow-masked encapsulated PSC utilized for a long term study in Chapter 6. Author points that the inexpensive design allows for a mounting of the device whilst still in the glovebox. In such way the device can be directly transported from the GB to the characterization chamber in the seal-tight vacuum bag. (b) Top left: back-contact solar cell design similar to the (a), two rectangular PCBs are used for long-term study of series and parallel connections compatible with 4 in 1 substrate design developed by the author.(c) evolution of (a) for a long term comparison study between two devices (allows to ensure that the conditions presumed are as close as possible, and (d) prototype of new 16-channel rapid characterization setup evolution from Chapter 7 for easy to mount extensions, currently the goal is to characterize up to 8 batches of 16 solar cells and add freezing and voltage decay functionalities..

Appendix C

The micromixer used in this work is a piezoelectric actuated active acoutofluidic mixer and microfluidic T-junctions. It is capable to rapidly and effectively homogenies solutions within 8 milliseconds. The core of the mixer is a silicon micro-oscillator chip with a natural frequency at 1.06 MHz, created using a modified deep reactive ion etching (DRIE) process. The process started from a photolithography process, in a class 100 clean room, that patterns a 50 μm layer of SU8 photoresist as masking layer on a 500 μm thick, <100> crystal orientation, double side polished silicon die, to selectively expose the area to be etch, and protects other areas from the subsequent DRIE process. After creating the masking layer, the silicon die is loaded into a plasma etching machine (Oxford Instruments PLASMALAB100 ICP380) and subjected to close to 1000 cycle of the modified Bosch process, this part of the process is conducted in a class 10,000 clean room. The Bosch process creates a 500 μm radius star-shaped through hole on the silicon die, with a variable thickness membrane structure at the edge of the hole that has a triangular cross-section. The residue SU8 masking layer is then removed from the die by submerging it in 80 °C sulfuric acid for 3 hours. The chip is then assembled between two PDMS chips for fluidic connection, where the bottom chip has two opening to allow inflow of two separate fluid into the mixer, and the top chip has one opening to allow outflow of the mixed solution. The PDMS chips contains a single straight channel that is 5 mm long, 2 mm wide, and 100 μm tall, with 1.5 mm diameter in/outlet at one or both ends of the channel. They are fabricated using standard soft-lithography techniques, where a mold is fabricating by patterning the channel shape on a silicon wafer using SU8 photoresist by photolithography process in a class 100 cleanroom, then pouring 1:10 ratio mixture of curing agent and PDMS on the mold and degas in a vacuum chamber to remove bubble, and subsequently baked for 4 hours on a 70°C hotplate to allow crosslinking of the PDMS. The cured PDMS is then removed from the mold and trimmed to desired size with a scalpel blade, and bonded with the silicon micro-oscillator chip. The bonding between the silicon chip and PDMS chips are created by activating the surface of the PDMS by treating it with air/oxygen plasma in a plasma cleaner (PDC-32G-2, Harrick Plasma) at 0.6-0.8 Torr pressure for 21 seconds then immediately bring in contact with the silicon chip to form Si-O-Si bond at the interface. A piezoelectric transducer (PZ26, Ferroperm Piezo-ceramics, Meggitt Pty) is adhered directly on the silicon chip with epoxy glue (Araldite 5 Minute Epoxy Adhesive, Selleys). and connected with to a function generator (Stanford Research Systems DS345) and amplifier (T&C Power Conversion, Inc.

AG 1006). During operation, a 1.06 MHz 1.37 W sinusoidal electric signal is provided to the piezoelectric transducer which cause the variable thickness membrane structure to resonates and rapidly homogenies solutions in the though hole of the Si-chip though strong acoustic streaming.
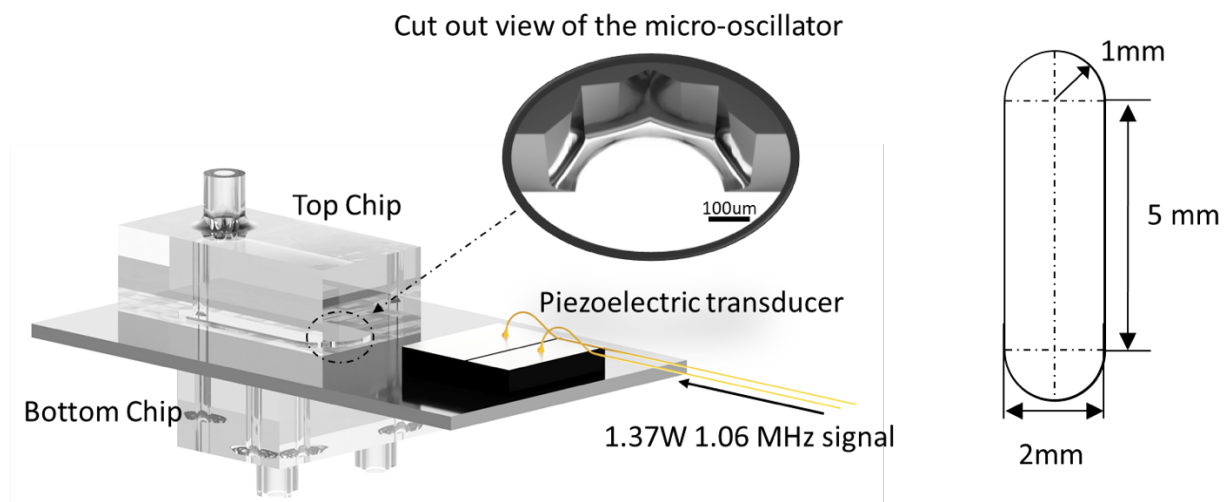

Figure C1: Overview of the piezoelectric mixer with detailed dimensions.

Appendix D

In this appendix the examples of the data extraction will be presented.

D.1 XRD data point processing example

The XRD diffraction patterns were taken using commercial instrument, the background noise was programmatically removed for all the samples. The diffractograms were not normalized for the calculation purposes (Figure D1 provides normalized data). The FWHM procedure was programmatically run over all the samples and the outcome for the datapoint was averaged over the number of samples produced from the specific perovskite composition film.


```
figure(3)
%draw an empty figure window

data = K3; %take the raw data (counts) from XRD for y vector

x = W1; %take the angle for x vector

plot(x, data) %plot raw XRD measurement

% search for the half maximum
halfMax = (-min(data) + max(data)) / 2;
% Find point where the data drops below half max
index1 = find(data >= halfMax, 1, 'first');
% Find point where the data drops above the half max
index2 = find(data >= halfMax, 1, 'last');

%get the FWHM from the difference between these indexes (in other words
%project the length on the x axis from where I get the data point

fwhmx = x(index2) - x(index1);
fwhmx = (fwhmx/180)*pi;

%Sherrer equation, I left it here but I did not use it for the heatmap
beta = fwhmx;
% theta =
K = 0.9; %constant paramter
lambda = 1.78E-10; %angstrom
hT= 4.53/2;
hT = (hT/180)*pi;
tau = (K*lambda)/(beta*cos(hT));
```
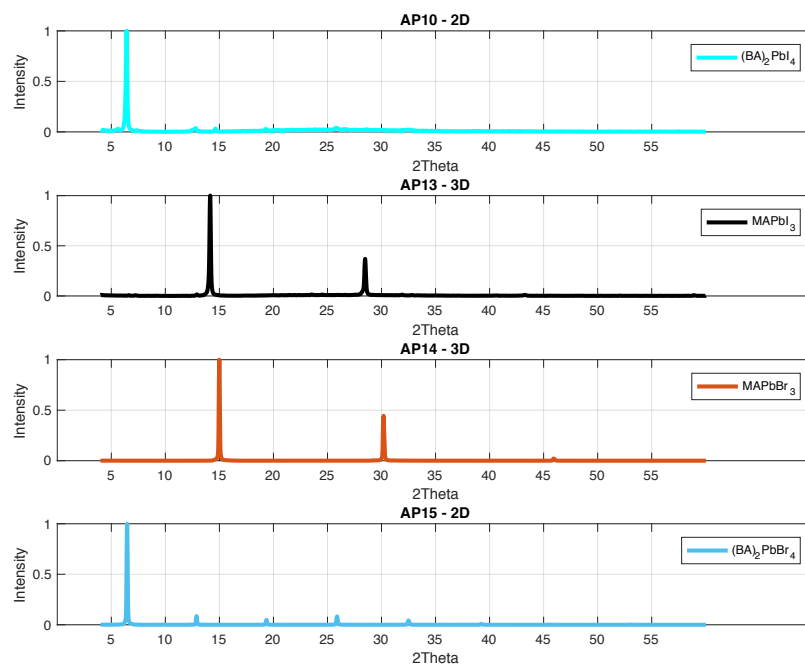
Figure D1 Normalized diffraction patterns of the films. The background subtraction was applied by the commercial instrument software.

D.2 PESA data point processing example

In the case of PESA data, the commercial program provided with the instrument calculated automatically the datapoints provided in the heatmap. The plotted data presents some of the typical data curves.
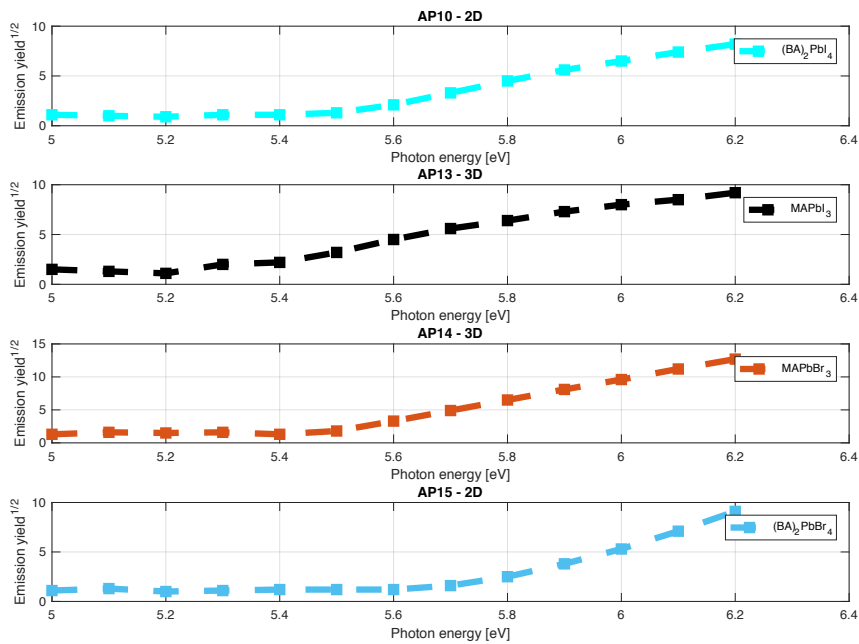
Figure D2 Pure corners measured by the PESA system and plotted as the example. The datapoint is derived from the onset where the linear regression is employed to find the intersection point. Author does not provide code here as the exact datapoint is generated by the commercial instrument built in program.

D.3 UV-vis data point processing example

Each datapoint was measured and calculated using commercial instrument. Each film was measured multiple times to ensure a correct data distribution. The transmission and absorption measurements were taken respectively. Each data point was calculated using the same wavelength range, the counts were normalized and the averaged onset of all the films produced for a specific sample composition) served as the datapoint for the heatmap.

Programming example:

```
%wavelength vector
W = ROWAP14toAP13.Wave;

%normalization of each transmission measurement
normT1 = T1 – min(T1(:));
T1 = normT1 ./ max(normT1(:));
normT2 = T2 – min(T2(:));
T2 = normT2 ./ max(normT2(:));
normT3 = T3 – min(T3(:));
```

```matlab
T3 = normT3 ./ max(normT3(:));
normT4 = T4 – min(T4(:));
T4 = normT4 ./ max(normT4(:));
normT5 = T5 – min(T5(:));
T5 = normT5 ./ max(normT5(:));
normT6 = T6 – min(T6(:));
T6 = normT6 ./ max(normT6(:));
normT7 = T7 – min(T7(:));
T7 = normT7 ./ max(normT7(:));
%normalization of each reflection measurement
normR1 = R1 – min(R1(:));
R1 = normR1 ./ max(normR1(:));
normR2 = R2 – min(R2(:));
R2 = normR2 ./ max(normR2(:));
normR3 = R3 – min(R3(:));
R3 = normR3 ./ max(normR3(:));
normR4 = R4 – min(R4(:));
R4 = normR4 ./ max(normR4(:));
normR5 = R5 – min(R5(:));
R5 = normR5 ./ max(normR5(:));
normR6 = R6 – min(R6(:));
R6 = normR6 ./ max(normR6(:));
normR7 = R7 – min(R7(:));
R7 = normR7 ./ max(normR7(:));
normR8 = R8 – min(R8(:));
R8 = normR8 ./ max(normR8(:));


%UV vis absorption calculation
Y1 = 100 – R1 – T1;
Y2 = 100 – R2 – T2;
Y3 = 100 – R3 – T3;
Y4 = 100 – R4 – T4;
Y5 = 100 – R5 – T5;
Y6 = 100 – R6 – T6;
Y7 = 100 – R7 – T7;
Y8 = 100 – R8 – T8;

%plotting
figure(1)
set(gcf,'color','w');
subplot(8,1,1);
str = '#0AD1F9';
color = sscanf(str(2:end),'%2x%2x%2x',[1 3])/255;
plot(W,Y1,'Color', color); hold on;
set(findall(gca, 'Type', 'Line'),'LineWidth',3);
title('AP15 to AP10')
ylabel('Counts')
xlabel('Theta')
legend({'1/8','65C, 10% Humidity'},'Location','northeast')
grid on
subplot(8,1,2);
str = '#13C4E8';
color = sscanf(str(2:end),'%2x%2x%2x',[1 3])/255;
plot(W,Y2,'Color', color); hold on;
set(findall(gca, 'Type', 'Line'),'LineWidth',3);
title('AP15 to AP10')
ylabel('Counts')
xlabel('Theta')
legend({'2/8','65C, 10% Humidity'},'Location','northeast')
grid on
subplot(8,1,3);
```

```matlab
str = '#23B6D4';
color = sscanf(str(2:end),'%2x%2x%2x',[1 3])/255;
plot(W,Y3,'Color', color); hold on;
set(findall(gca, 'Type', 'Line'),'LineWidth',3);
title('AP15 to AP10')
ylabel('Counts')
xlabel('Theta')
legend({'3/8','65C, 10% Humidity'},'Location','northeast')
grid on
subplot(8,1,4);
str = '#2AA3BC';
color = sscanf(str(2:end),'%2x%2x%2x',[1 3])/255;
plot(W,Y4,'Color', color); hold on;
set(findall(gca, 'Type', 'Line'),'LineWidth',3);
title('AP15 to AP10')
ylabel('Counts')
xlabel('Theta')
legend({'4/8','65C, 10% Humidity'},'Location','northeast')
grid on
subplot(8,1,5);
str = '#2C6C79';
color = sscanf(str(2:end),'%2x%2x%2x',[1 3])/255;
plot(W,Y5,'Color', color); hold on;
set(findall(gca, 'Type', 'Line'),'LineWidth',3);
title('AP15 to AP10')
ylabel('Counts')
xlabel('Theta')
legend({'5/8','65C, 10% Humidity'},'Location','northeast')
grid on
subplot(8,1,6);
str = '#9BB321';
color = sscanf(str(2:end),'%2x%2x%2x',[1 3])/255;
plot(W,Y6,'Color', color); hold on;
set(findall(gca, 'Type', 'Line'),'LineWidth',3);
title('AP15 to AP10')
ylabel('Counts')
xlabel('Theta')
legend({'6/8','65C, 10% Humidity'},'Location','northeast')
grid on
subplot(8,1,7);
str = '#BDDF0F';
color = sscanf(str(2:end),'%2x%2x%2x',[1 3])/255;
plot(W,Y7,'Color', color); hold on;
set(findall(gca, 'Type', 'Line'),'LineWidth',3);
title('AP15 to AP10')
ylabel('Counts')
xlabel('Theta')
legend({'1/8','65C, 10% Humidity'},'Location','northeast')
grid on
subplot(8,1,8);
str = '#E1E109';
color = sscanf(str(2:end),'%2x%2x%2x',[1 3])/255;
plot(W,Y8,'Color', color); hold on;
set(findall(gca, 'Type', 'Line'),'LineWidth',3);
title('AP15 to AP10')
ylabel('Counts')
xlabel('Theta')
legend({'7/8','65C, 10% Humidity'},'Location','northeast')
grid on
```

Visual inspection of the typical data calculation where the onset was programmatically calculated for further processing.
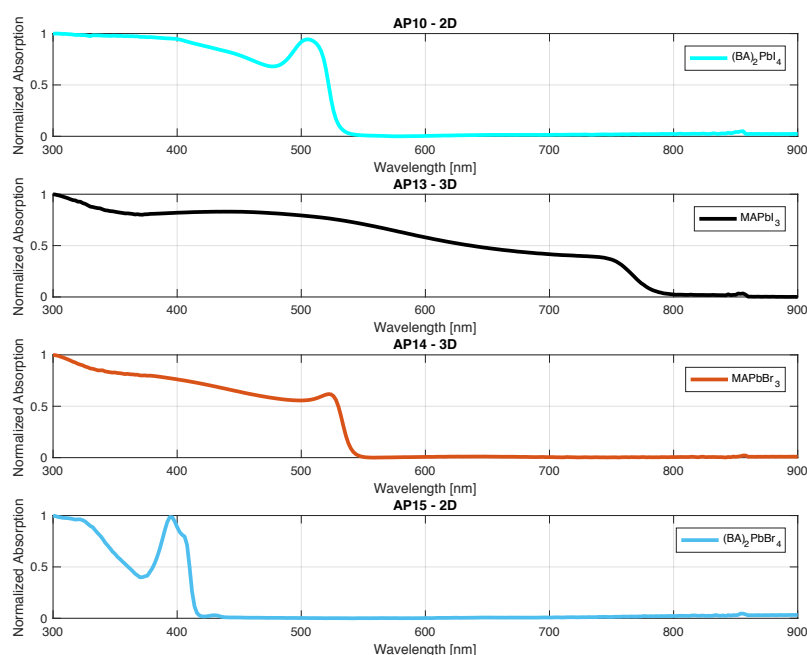

Figure D3: Each datapoint was derived as the absorption onset (programmatically) which was further calculated using Tauc method. The estimated intersection point was gathered and averaged over the number of samples fabricated from the same perovskite precursor solution.

D4 PL data point processing example

The raw intensity was obtained using commercial instrument. The data was pre-processed by the instrument and pure PL intensity and wavelength was obtained. The data was further normalized and the peak position (wavelength) was programmatically calculated as the index of the maximum value. Here is presented how these points were extracted from the raw data:

```
%wavelength
W1 = purePLall.W1;
W2 = purePLall.W2;
W3 = purePLall.W3;
W4 = purePLall.W4;

%raw PL intensity
AP10 = purePLall.AP10;
AP13 = purePLall.AP13;
AP14 = purePLall.AP14;
AP15 = purePLall.AP15;
```

```matlab
%normalization of PL intensity
normAP10 = AP10 - min(AP10(:));
AP10 = normAP10 ./ max(normAP10(:));
normAP13 = AP13 - min(AP13(:));
AP13 = normAP13 ./ max(normAP13(:));
normAP14 = AP14 - min(AP14(:));
AP14 = normAP14 ./ max(normAP14(:));
normAP15 = AP15 - min(AP15(:));
AP15 = normAP15 ./ max(normAP15(:));

%plotting figure
figure(1)
set(gcf,'color','w');
subplot(4,1,1);
plot(W1,AP10,'Color', 'c'); hold on;
set(findall(gca, 'Type', 'Line'),'LineWidth',3);
title('AP10 - 2D')
ylabel('Normalized Emission')
xlabel('Wavelength [nm]')
legend({'(BA)_2PbI_4','65C, 10% Humidity'},'Location','northeast')
grid on
subplot(4,1,2);
plot(W2,AP13, 'Color', [0.0, 0.0, 0.0]); hold on;
set(findall(gca, 'Type', 'Line'),'LineWidth',3);
title('AP13 - 3D')
ylabel('Normalized Emission')
xlabel('Wavelength [nm]')
legend({'MAPbI_3','65C, 10% Humidity'},'Location','northeast')
grid on
subplot(4,1,3);
plot(W3,AP14, 'Color', [0.8500, 0.3250, 0.0980]); hold on;
set(findall(gca, 'Type', 'Line'),'LineWidth',3);
title('AP14 - 3D')
ylabel('Normalized Emission')
xlabel('Wavelength [nm]')
legend({'MAPbBr_3','65C, 10% Humidity'},'Location','northeast')
subplot(4,1,4);
plot(W4,AP15, 'Color', [0.3010, 0.7450, 0.9330]); hold on;
title('AP15 - 2D')
ylabel('Normalized Emission')
xlabel('Wavelength [nm]')
set(findall(gca, 'Type', 'Line'),'LineWidth',3);
legend({'(BA)_2PbBr_4','65C, 10% Humidity'},'Location','northeast')
grid on
```
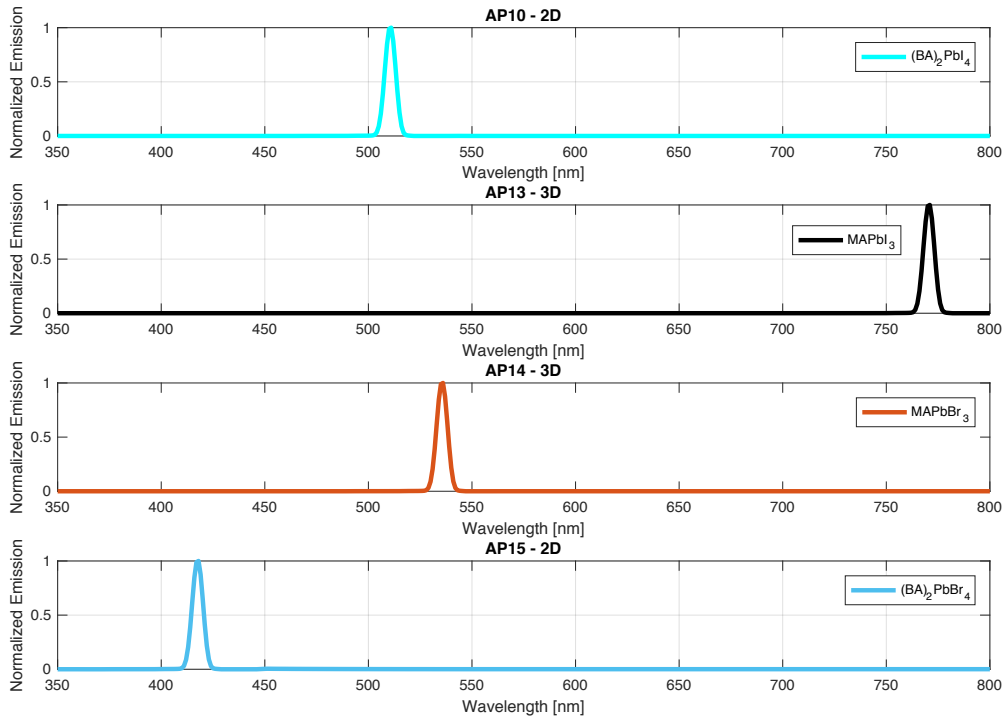
Figure D4: Each datapoint was derived as the index of the curve maximum (programmatically). The calculated maximum index was gathered and averaged over the number of samples fabricated from the same perovskite precursor solution.

D.5 J-V data point processing example

For the datapoint generation in regards to heatmap the standard way of plotting J-V curves was employed. First, the raw data was normalized to the shadow mask area, then dark, light reverse and light forward curves were plotted. The PCE (1), FF (2), J_{SC} (3) and V_{OC} (4) were programmatically calculated using the equations which could be found on https://www.pveducation.org/ and were provided in the literature review. The datapoint was averaged over the number of samples produced with the same perovskite precursor solution.
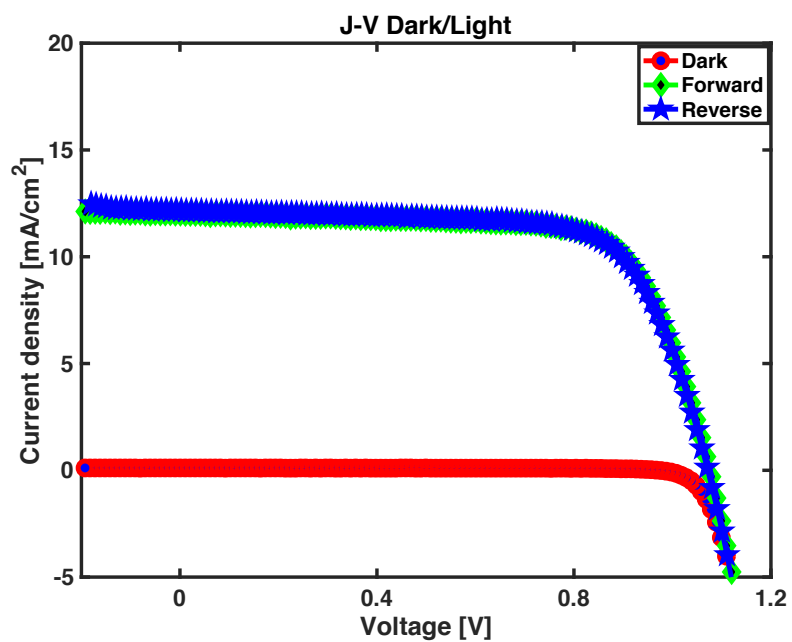
Figure D5: Typical J-V curve plotted for a single datapoint for one of the samples from x = 0.9 n=1. Dark measurement was not used for the heatmap.

-EOF-